Multiband Channel Estimation for Precise Localization in Wireless Networks Algorithms, Simulations and Experiments

Kazaz, T.

DOI
10.4233/uuid:5d618877-1001-4897-ac80-2f5bbb10489a

Publication date
2022

Document Version
Final published version

Citation (APA)
Kazaz, T. (2022). *Multiband Channel Estimation for Precise Localization in Wireless Networks: Algorithms, Simulations and Experiments*. [Dissertation (TU Delft), Delft University of Technology]. https://doi.org/10.4233/uuid:5d618877-1001-4897-ac80-2f5bbb10489a

Important note
To cite this publication, please use the final published version (if applicable).
Please check the document version above.

MULTIBAND CHANNEL ESTIMATION FOR PRECISE LOCALIZATION IN WIRELESS NETWORKS

ALGORITHMS, SIMULATIONS AND EXPERIMENTS

MULTIBAND CHANNEL ESTIMATION FOR PRECISE LOCALIZATION IN WIRELESS NETWORKS

ALGORITHMS, SIMULATIONS AND EXPERIMENTS

Dissertation

for the purpose of obtaining the degree of doctor
at Delft University of Technology,
by the authority of the Rector Magnificus, Prof. dr. ir. T.H.J.J. van der Hagen,
chair of the Board for Doctorates,
to be defended publicly on Thursday 23, June 2022 at 15:00 o'clock

by

Tarik KAZAZ

Master of Science in Electrical Engineering,
University of Sarajevo, Sarajevo, Bosnia and Herzegovina,
born in Teslić, Bosnia and Herzegovina.

This dissertation has been approved by the

promotor: Prof. dr. ir. A. J. van der Veen
promotor: Dr. ir. G. J. M. Janssen

Composition of the doctoral committee:

Rector Magnificus,	chairperson
Prof. dr. ir. A. J. van der Veen	Delft University of Technology, promotor
Dr. ir. G. J. M. Janssen	Delft University of Technology, promotor
Independent members:	
Prof. dr. ir. H. Steendam	Ghent University, Belgium
Prof. dr. ir. M. J. Bentum	Eindhoven University of Technology
Prof. dr. ir. K. Witrisal	Graz University of Technology, Austria
Dr. J. Romme	IMEC Holst Centre
Prof. dr. ir. F. A. Kuipers	Delft University of Technology
Prof. dr. A. Yarovoy	Delft University of Technology, reserve member

The research in this thesis was financially supported by Netherlands Organization for Scientific Research (NWO) and Koninklijke KPN N.V. (KPN) under "SuperGPS" project with number 13970.

Keywords: Multipath Channel Estimation for Localization, Array Signal Processing, Time-Delay Estimation, Subspace Based Methods, Multiband Ranging, Localization in Wireless Networks

Printed by: Ipskamp Printing | www.proefschriften.net

Front and Back: Designed based on illustration from www.shutterstock.com with permission of Shutterstock under the standard license.

ISBN 978-94-6366-559-9

An electronic version of this dissertation is available at
http://repository.tudelft.nl/.

To my father and mother,
for being my life guides
and for all the sacrifices they did.

To my Aybüke,
for being my best friend
and for all the laughs
and love she brings.

To my brother,
for being there whenever I need.

To my Ayten and Faruk,
for all their care
and support.

CONTENTS

Summary 1

Samenvatting 3

1 Introduction 5
- 1.1 Brief History of Radio Localization . . . 7
- 1.2 Why GNSS Localization is Not Good Enough? . . . 9
- 1.3 Localization in the Multipath Radio Channel . . . 12
- 1.4 Scope and context of this thesis . . . 13
  - 1.4.1 SuperGPS . . . 14
  - 1.4.2 Problem Statement and Research Goals . . . 14
- 1.5 Outline . . . 16
- 1.6 List of contributions . . . 20
  - 1.6.1 Thesis Related Contributions . . . 20
  - 1.6.2 Other Contributions . . . 21

2 Principles of Radio Localization 23
- 2.1 Introduction . . . 24
- 2.2 Inferring Location from Multipath Radio Channels . . . 24
- 2.3 Measurements for Two-step Localization Methods . . . 25
  - 2.3.1 Time-delay measurements . . . 26
  - 2.3.2 Received signal strength . . . 32
  - 2.3.3 Direction of arrival (DOA) . . . 34
- 2.4 Algorithms for Two-step Localization Methods . . . 36
  - 2.4.1 Nonlinear Estimation . . . 37
  - 2.4.2 Linear Estimation Methods . . . 39
  - 2.4.3 Direct Location Estimation (DLE) . . . 41
- 2.5 Conclusions . . . 42

3 Multipath Time-Delay Estimation and Super-Resolution Problems 45
- 3.1 Introduction . . . 46
- 3.2 Time-Delay Estimation for Localization . . . 46
- 3.3 Super-resolution Problems . . . 49
- 3.4 Super-Resolution Spectral Estimation . . . 51
  - 3.4.1 Discrete Data Model . . . 51
  - 3.4.2 Maximum Likelihood Estimation . . . 53
  - 3.4.3 Subspace Based Estimation . . . 54
  - 3.4.4 Sparse Estimation Methods . . . 58
- 3.5 Conclusions . . . 64

4 Multiband Time-Delay Estimation for Ranging and Localization 67
4.1 Introduction . . . 68
4.2 Data Model . . . 70
4.2.1 System Model . . . 70
4.2.2 Multiband Channel Probing . . . 71
4.2.3 Discrete Data Model . . . 72
4.3 Multiband time-delay estimation . . . 74
4.3.1 Algorithm Outline . . . 74
4.3.2 Weighting . . . 76
4.3.3 Data Extensions . . . 76
4.3.4 Noise Reduction . . . 78
4.3.5 Estimation of Amplitudes and Algorithm Summary . . . 79
4.4 Gaussian Cramér-Rao Bound . . . 79
4.5 Numerical Experiments . . . 82
4.6 Conclusions . . . 88

5 Multiresolution Time-Delay Estimation 91
5.1 Introduction . . . 92
5.2 Data Model . . . 93
5.3 Multiresolution Time-Delay Estimation . . . 93
5.3.1 Singleband Time-Delay Estimation Algorithm . . . 93
5.3.2 Multiresolution Time-Delay Estimation Algorithm . . . 94
5.3.3 Data Extensions . . . 96
5.3.4 Algorithm Summary . . . 97
5.4 Numerical Experiments . . . 97
5.5 Conclusions . . . 101

6 Joint RF Chain Calibration and Time-Delay Estimation 103
6.1 Introduction . . . 104
6.2 Problem Formulation and Data Model . . . 105
6.2.1 Discrete-time signal model . . . 105
6.2.2 Data Model . . . 106
6.3 Joint Calibration and Time-Delay Estimation . . . 106
6.3.1 Assumptions . . . 107
6.3.2 Algorithm . . . 108
6.4 Numerical Experiments . . . 111
6.5 Conclusions . . . 112

7 Joint Ranging and Synchronization for Narrowband Transceivers 113
7.1 Introduction . . . 114
7.2 Problem Formulation and Signal Model . . . 115
7.2.1 Frequency synthesizer model . . . 116
7.2.2 Signal model . . . 116
7.3 Communication Protocol and Data Model . . . 117
7.3.1 Classical PDoA ranging protocol . . . 117
7.3.2 2-D PDoA ranging and synchronization protocol . . . 119

7.4 Joint Clock-skew and Range Estimation . . . 119
7.5 Gaussian Cramér Rao Bound . . . 121
7.6 Numerical Experiments . . . 122
7.7 Conclusions . . . 123

8 Multiband Time-Delay Estimation and Localization Experiments 125
8.1 Introduction . . . 126
8.2 Overview of IEEE 802.11be Training Signals and Channel Estimation . . . 126
8.3 Datasets . . . 128
8.4 Experiments . . . 129
8.4.1 Influence of System Parameters $\{f_{c,i}\}_{i=1}^{L}$ and B . . . 130
8.4.2 Performance of Positioning and Ranging . . . 133
8.5 Conclusions . . . 135

9 Conclusions and Future Research Directions 137
9.1 Conclusions and Summary of Main Results . . . 138
9.2 Suggestions for Future Research . . . 141

Bibliography 145

Glossary of Notation and Abbreviations 167

Acknowledgments 171

Curriculum Vitæ 173

SUMMARY

OVER the last two decades, we have witnessed a tremendous evolution of wireless communication systems. For example, the data rates in mobile wireless systems have increased from a few tens of kilobits per second to 10 gigabits per second between the first and last, i.e., fifth generation (5G). The main enablers for this growth are signal processing and radio frequency (RF) hardware innovations, which led to more efficient modulation and coding schemes and high-performance RF transceivers. Following these trends, future wireless systems such as 6G and WiFi-7 aim for even higher data rates, requiring higher frequency ranges, wider bandwidths, and massive antenna arrays. These developments pave the way toward joint communication and sensing RF systems with very high range, Doppler, and angular resolutions. In particular, favorable signal and RF transceiver properties such as large bandwidth will enable precise RF localization in rich scattering environments such as indoor or urban canyons where multipath effects severely impair the performance of traditional localization systems like GNSS (Global Navigation Satellite Systems). At the same time, the wide range of emerging applications in areas of autonomous navigation, assisted living, and Internet-of-Things require precise localization, often to cm-level degree accuracy. Therefore, it is evident that new localization approaches and signal processing algorithms that can exploit signal and transceiver properties of emerging wireless systems are needed to solve the problem of precise localization in multipath environments and lead the way to novel applications.

The goal of this thesis is to design signal processing algorithms and protocols that will enable precise ranging in multipath environments while using practical single-antenna RF transceivers. In the first part of this thesis, we introduce a multiband channel model to describe multipath channel measurements collected over multiple separate frequency bands using narrowband and wideband RF transceivers. This model shows that multiband channel measurements have multiple shift-invariance property and that by increasing the frequency aperture of the multiband measurements, we can improve the resolution of multipath time-delay estimation. We use this property of the measurements to develop high-resolution time-delay estimation algorithms based on subspace estimation. To illustrate the performance of these algorithms, we perform extensive numerical experiments which demonstrate that the proposed algorithms are statistically efficient and that multiband time-delay estimation enables precise ranging in multipath environments.

However, the aforementioned results also show that the proposed algorithms are sensitive to errors introduced by hardware impairments of RF transceivers and imperfect calibration. In the second part of the thesis, we focus on the problem of joint RF transceiver calibration and high-resolution time-delay estimation. For example, in practical scenarios, the frequency response of RF transceivers might not be known nor calibrated, and performing time-delay estimation without calibrating these effects will lead

to biased estimates. We show that the problem of joint RF transceiver calibration and time-delay estimation can be formulated as a particular case of covariance matching, which after reformulation, can be solved using a simple group Lasso algorithm. Likewise, due to imperfections of oscillators used in RF transceivers, the mobile and anchor nodes are usually not frequency synchronized. This frequency offset severely deteriorates the performance of multiband ranging methods. To solve this issue, we design a two-way protocol for collecting multiband channel measurements and a weighted least squares-based algorithm that enable joint clock synchronization and ranging.

Finally, in the last part of the thesis, we validate our modeling assumptions and illustrate the performance of the multiband time-delay estimation algorithms by considering practical scenarios of localization in future WiFi-7 networks. For these experiments, we use real indoor multipath channel measurements collected in a hospital and a university building environment. The results of the experiments show that using multiband channel measurements with a total bandwidth of 320 MHz, the absolute ranging error is smaller than 4 cm in 80% of the cases. Likewise, using the same scenario setup and three anchors to localize the mobile node, it is observed that the positioning error is below 24 cm in 95% of the cases. These results show that by using the advanced signal processing techniques to design estimation algorithms and channel measurement protocols that can exploit the properties and degrees of freedom offered by future wireless systems and RF transceivers, decimeter-level accurate positioning is achievable.

The signal processing models presented in this thesis are common to the wide area of array signal processing applications, such as radar and ultrasound imaging. Therefore, the results presented in this thesis impact these application areas as well.

SAMENVATTING

De afgelopen twee decennia zijn we getuige geweest van een enorme evolutie van draadloze communicatiesystemen. Zo zijn de datasnelheden in mobiele draadloze systemen gestegen van enkele tientallen kilobits per seconde tot 10 gigabits per seconde tussen de eerste en de laatste, d.w.z. vijfde generatie (5G). De belangrijkste aanjagers van deze groei zijn signaalverwerking en radiofrequentie (RF) hardware innovaties, die hebben geleid tot efficiëntere modulatie- en coderingstechnieken en RF zendontvangers met hoge prestaties. In het verlengde van deze trends streven toekomstige draadloze systemen zoals 6G en WiFi-7 naar nog hogere datasnelheden, waarvoor hogere frequentiebereiken, hoge bandbreedtes en massale antenne-arrays nodig zijn. Deze ontwikkelingen effenen de weg naar gezamenlijke RF-systemen voor communicatie en detectie met zeer afstands-, Doppler- en hoekresolutie. Met name gunstige signaal- en RF-zendontvangereigenschappen zoals een grote bandbreedte zullen nauwkeurige RF-lokalisatie mogelijk maken in omgevingen met veel verstrooiing, zoals binnenshuis of in stedelijke gebieden, waar multipad-effecten de prestaties van traditionele lokalisatiesystemen en GNSS ernstig aantasten. Tegelijkertijd vereisen de vele opkomende toepassingen op het gebied van autonome navigatie, begeleid wonen en het internet-van-dingen nauwkeurige lokalisatie, vaak tot op cm-niveau. Daarom is het duidelijk dat nieuwe lokalisatiebenaderingen en signaalverwerkingsalgoritmen die de signaal- en zendontvangereigenschappen van opkomende draadloze systemen kunnen benutten, nodig zijn om het probleem van precieze lokalisatie in multipad-omgevingen te verlichten en de weg te bereiden voor nieuwe toepassingen.

In dit proefschrift is het ons doel om signaalverwerkingsalgoritmen en protocollen te ontwerpen die nauwkeurige afstandsmetingen in multipad omgevingen mogelijk maken terwijl realistische RF zendontvangers met één antenne worden gebruikt. In het bijzonder introduceren we in het eerste deel van dit proefschrift een multiband kanaalmodel om multipad kanaalmetingen te beschrijven die zijn verzameld over meerdere afzonderlijke frequentiebanden met gebruikmaking van smalbandige en breedbandige RF zendontvangers. Dit model laat zien dat multibandkanaalmetingen een meervoudige verschuivingsinvariantie-eigenschap hebben en dat we, door de frequentie-opening van de multibandmetingen te vergroten, de resolutie van de multipad tijdvertragingsschatting kunnen verbeteren. Wij gebruiken deze eigenschap van de metingen om hogeresolutie tijd-vertraging schattingsalgoritmen te ontwikkelen gebaseerd op subspace schatting. Om de prestaties van deze algoritmen te illustreren, voeren we uitgebreide numerieke experimenten uit die aantonen dat de voorgestelde algoritmen statistisch efficiënt zijn en dat multiband tijdvertragingsschatting nauwkeurige ranging in multipad omgevingen mogelijk maakt.

De bovengenoemde resultaten tonen echter ook aan dat de voorgestelde algoritmen gevoelig zijn voor fouten die worden geïntroduceerd door hardwarematige beperkingen van RF-zendontvanger en onvolmaakte kalibratie. In het tweede deel van het proef-

schrift richten we ons op het probleem van gezamenlijke RF-zendontvangerkalibratie en tijdvertragingsschatting met hoge resolutie. In praktische scenario's kan het bijvoorbeeld voorkomen dat de frequentierespons van RF-zendontvangers niet bekend of gekalibreerd is, en dat het uitvoeren van tijdvertragingsschattingen, zonder voor deze effecten te kalibreren, zal leiden tot vertekende schattingen. Wij tonen aan dat het probleem van gezamenlijke RF zendontvangerkalibratie en tijdvertragingsschatting kan worden geformuleerd als een bijzonder geval van covariantiematching, dat na herformulering kan worden opgelost met behulp van een eenvoudig groeps-Lasso algoritme. Als gevolg van onvolkomenheden in de oscillatoren die in RF-zendontvangers worden gebruikt, zijn de mobiele en ankerknooppunten gewoonlijk niet frequentiesynchroon. Dit frequentieverschil verslechtert de prestaties van multiband afstandsmethodes aanzienlijk. Om dit probleem op te lossen, ontwerpen we een twee-weg protocol voor het verzamelen van multiband kanaalmetingen en een gewogen kleinste kwadraten-gebaseerd algoritme dat gezamenlijke kloksynchronisatie en afstandsmetingen mogelijk maakt.

Tenslotte, in het laatste deel van het proefschrift, valideren we onze modelveronderstellingen en illustreren we de prestaties van de multiband tijdvertragingsschattingsalgoritmen door praktische scenario's van lokalisatie in toekomstige WiFi-7 netwerken te beschouwen. Voor deze experimenten gebruiken we echte inpandige multipad-kanaal metingen verzameld in een ziekenhuis en een universiteitsgebouw. De resultaten van de experimenten tonen aan dat bij gebruik van een enkele snapshot multiband kanaalmeting met een totale bandbreedte van 320 MHz, de absolute afstandsfout kleiner is dan 4 cm in 80% van de gevallen. Evenzo, gebruikmakend van dezelfde scenario-opstelling en drie ankers om het mobiele knooppunt te lokaliseren, wordt waargenomen dat de positioneringsfout kleiner is dan 24 cm in 95% van de gevallen. Deze resultaten tonen aan dat door gebruik te maken van geavanceerde signaalverwerkingstechnieken om schattingsalgoritmen en kanaalprotocollen te ontwerpen die gebruik kunnen maken van de eigenschappen en vrijheidsgraden van toekomstige draadloze systemen en RF-transceivers, nauwkeurige plaatsbepaling op decimeterniveau haalbaar is.

De signaalverwerkingsmodellen die in dit proefschrift worden gepresenteerd zijn algemeen voor het brede gebied van array signaalverwerkingstoepassingen, zoals radar en ultrasone beeldvorming. Daarom hebben de resultaten die in dit proefschrift worden gepresenteerd ook gevolgen voor deze toepassingsgebieden.

1

INTRODUCTION

"Fix your course to a star and you can navigate through any storm."

— Leonardo da Vinci

1

HUMANS possess a powerful sensing system that lets us observe physical phenomena around us and make meaning from these observations. As I am writing these pages, I am using: ears to listen to sound, i.e., music, coming from headphones, eyes to see what I am typing on the screen of the laptop, sense of touch to feel the keys on the keyboard, and at the same time, I feel thermal energy dissipating from the laptop using temperature receptors on my hands. In essence, all of what we sense around us are different forms of energy generated from various sources in our environment. This energy stimulates our sensing and nervous system, and then these stimuli are processed by the brain, which infers meaning.

Over the centuries, we have mastered physics and mathematics and developed a powerful signal processing framework that allows us to describe the physical phenomena around us using equations and functions, i.e., mathematical models. The energy that is emitted by various sources we have described by mechanical and electromagnetic waves. For example, we have described sound as mechanical waves created by vibrations of an object (e.g., the loudspeakers of our phone or the motor of a car passing next to us) with frequencies from 20 Hz to 20 kHz. These waves stimulate our hearing system, and finally, their stimuli are processed by our brain, which infers meaning from them. This ability is often existential and allows us to sense our environment, react on time, and protect our lives. For example, by using our hearing system, we can detect an approaching car while cycling, allowing us to maneuver and prevent colliding with it.

Like sound, we have described the propagation of light and heat radiated from our environment as electromagnetic waves. These signals cover a large range of frequencies, i.e., spectrum, most of which we can not sense directly. However, over the years, we mastered how to use them for many useful applications that improve our quality of life and are inevitable parts of our modern society. We invented advanced sensing systems composed of devices that can produce these waves and sensors that can acquire them. In particular, electromagnetic waves that cover frequencies from 3 kHz to 3 THz, known as radio frequency (RF) waves, are widely used in wireless communications and radar applications.

For example, we use RF waves to exchange Netflix video between our phone and a WiFi router. However, to extract useful information from collected observations of RF waves, i.e., signals, first, their propagation is described using an appropriate signal model. Then, signal processing is used to develop clever algorithms that process acquired signals and infer valuable information from them, such as extracting Netflix video from the radio signals.

In this thesis, we use signal processing to model the propagation of the radio frequency (RF) signals between objects with known locations and the object with unknown location to develop algorithms that can determine its location from the exchanged signals. The objects with the known location we will refer to as *anchors* and the objects with the unknown locations we call *mobile* nodes. The RF signal sent from an anchor to the mobile node also reflects from surrounding objects creating its replicas that arrive with different powers, time-delays, and angles at the mobile node, similar to echos of our voice that we hear after shouting in a tunnel or a cave. We refer to the signal that propagates directly between an anchor and mobile node as the direct or line-of-sight (LOS) path, while its reflected replicas are called multipaths. This propagation is described in

signal processing using a mathematical model known as the multipath channel model, where characteristics of the paths (e.g., power, time-delays, and angles) are called path parameters. The location of the mobile node is encoded in the parameters of the LOS path, while multipaths encode locations of surrounding reflectors and obfuscate the estimation of the LOS parameters. Therefore, estimation of location is challenging in environments where there is a lot of multipath, such as inside our house, in an airport, or in a big city. Unfortunately, these environments are typically the ones where precise localization is needed the most.

This thesis aims to derive algorithms for high-resolution estimation of the channel parameters and calibration of RF transceivers, and demonstrate the application of these results in practical localization scenarios. We limit ourselves to the estimation of time-delay parameters as it provides an opportunity for high-accuracy localization with simple single antenna RF transceivers. However, the methods introduced in this thesis are general and can be applied to other problems where multipath channels arise (such as radar or ultrasound imaging).

In this chapter, we briefly go through the history of radio localization and illustrate the motivation for precise localization with few examples of emerging applications. We then formulate the problem of multipath channel estimation for localization and elaborate on the main questions that are answered in this thesis. We then provide the scope of research performed in this thesis and the outline of the thesis. Finally, we conclude with our research contributions within fields of signal processing and wireless communications.

1.1. BRIEF HISTORY OF RADIO LOCALIZATION

Localization refers to the process of determining the location of a targeted object in space. This problem has a long history, and it originates from the science of navigation. Navigation is the science that deals with the problems of determining the location and course of an object (e.g., ship, airplane, etc.) and guiding it to a specific destination. The word navigation is derived from the Latin words *navis* ("ship") and *agere* ("to drive"). It is first mentioned in the records left by the Minoan civilization that arose on the island of Crete, flourishing from 3000 to 1100 before the Christian era (BCE). Minoan sailors used celestial objects to navigate trading ships on the Mediterranean sea without any special instruments. Since then, many specialized maps, techniques, and instruments have been developed to support more precise localization, such as the astrolabe, chronometer, sextant, and magnetic compass. However, these techniques strongly depend on the availability of reliable astronomical and meteorological clues when performing navigation. This has motivated the development of navigation systems based on radio frequency (RF) signals, which are resilient to atmospheric effects and can provide ubiquitous localization in any weather conditions, including rain, snow, and fog.

The first radio navigation systems appeared in the early 1900s when the German companies Telefunken and Lorenz started developing a navigation system called "Funkbaken" based on RF beacon signals [1]. Later, in 1928, a low-frequency four-course radio range was introduced as an airplane navigation system. However, these systems had limited coverage and were not globally accessible. The launch of the first satellite, Sputnik

1

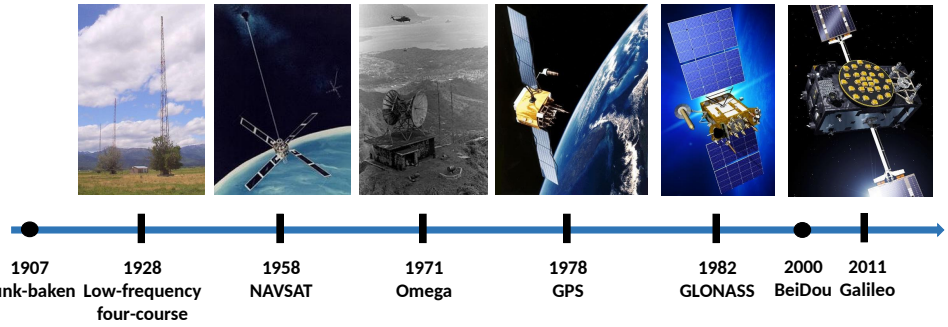

Figure 1.1: The historical evolution of radio navigation systems. (Images courtesy of www.insidegnss.com)

I, by the Soviet Union in 1957 has inspired the development of global navigation satellite systems (GNSSs). In 1958, the United States (US) started developing Transit (or NAVSAT), the first global satellite-based navigation system. This system required a constellation of five satellites to provide global coverage, and during its operation, at least ten satellites were kept in orbit to ensure reliable localization. However, only one satellite was visible from the earth at any moment, meaning that this system could not offer continuous localization. A user needed to wait for 35 to 100 minutes to update location estimates depending on the latitude of its location. The first navigation system with global and continuously present coverage was a terrestrial-based system called Omega [2], developed in 1971 by the United States and six-partner nations. This system was based on a network of 8 fixed terrestrial base stations transmitting very-low-frequency (VLF) radio beacons that were used for two-dimensional (2-D) localization of objects. Omega had an average root-mean-square (RMS) localization accuracy of 2 to 4 km and was shut down in 1997 in favor of the Global Positioning System (GPS).

The development of GPS started in the 1960s as a joint project of the US Navy and US AirForce, and initially the project was named Navigation System with Timing and Ranging (NAVSTAR) [3]. The first GPS satellite was launched in 1978, and the system became operational in 1995. At first, the GPS constellation consisted of 24 satellites in medium earth orbit. This was extended to 27 satellites in 2011.

GPS was first aimed for military purposes, and it was first used during the Persian Gulf war in 1990. Following the Korean Airlines disaster in 1983, the US government announced that GPS will be available for civilian applications [4]. Since then, GPS evolved far beyond its military origin and became the prevalent localization, navigation, and timing technology. The success of GPS in military and civilian applications has driven the development of other GNSSs such as the Russian GLONASS (first launched in 1982), the Chinese BeiDou (2000), and the European Galileo (2011). Thanks to their global coverage, high accuracy, and lack of need for infrastructure for the user on earth, today GNSSs are used as a crucial tool for navigation and timing in many vital industries [5] such as transportation and logistics (fleet management and route navigation) [6], civil engineering (surveying and monitoring of infrastructure) [7] and location-aware and location-based services (Google Maps, Uber, etc.) [8]. These applications have become an in-

evitable part of our modern society, and they have improved the quality of our daily life [9]. However, emerging applications demand even more precise localization and often in scenarios where GNSSs perform poorly, such as in indoor or urban environments. In what follows, we discuss these applications and their localization requirements.

1.2. WHY GNSS LOCALIZATION IS NOT GOOD ENOUGH?

Localization using GNSS is based on time-delay estimation of radio signal propagation between a number of satellites and the GNSS receiver of the mobile node that is to be localized. The GNSS satellites transmit simultaneously and synchronously direct-sequence spread-spectrum (DS-SS) signals where each satellite uses its unique Pseudo-Random Noise (PRN) code for signal spreading [10]. The DS-SS signals enable implementation of a Code Division Multiple Access (CDMA) scheme where orthogonality of the PRN codes is used to distinguish signals coming from different satellites and avoid interference. These signals arrive at the GNSS receiver with unknown time-delays and frequency Doppler shifts. The time-delays encode distances (ranges) between the satellites and the receiver, while Doppler frequency shifts encode relative speed difference between satellites and the receiver. After sampling the received signal, the GNSS receiver does a parallel search for maximum correlations between locally generated PRN codes and the received signals to estimate the time-delays by finding the peaks of these correlations. The ranges between the satellites and the GNSS receiver then directly follow from the estimated time-delays using the fact that radio signals in air and vacuum propagate with the speed of light $c = 3 \cdot 10^8$ m/s. The estimated ranges are then used to localize the receiver, and we refer to this method as code-based GNSS localization. Likewise, the speed of the receiver is estimated from the frequency offset of the received signal introduced by the Doppler effect [11]. After the initial estimation of time-delays and frequency offsets, these parameters are tracked using a delay locked loop (DLL) and phase locked loop (PLL), respectively, to ensure continuous localization. The GNSS-based localization works well in outdoor scenarios with a clear view between the receiver and the satellites. However, RF signals are highly reflective, and the signal sent from a satellite gets reflected by objects close to the GNSS receiver. These signal reflections are called multipath components (MPCs), which get superimposed on the original signal at the GNSS receiver. This physical propagation phenomenon is called the multipath effect, and mathematically, it is described by multipath channel models. The multipath effect severely impairs the performance of GNSS localization in challenging propagation scenarios such as indoor, urban canyons, or tunnels. Furthermore, in these scenarios, GNSS localization is often unavailable due to the high attenuation and blockage of GNSS signals. These signals are also not secure and robust against cyber manipulations. Therefore, the reliability and performance of localization using GNSS are often reduced due to the following main limitations of GNSS signals [12]:

- They have narrow bandwidth and are extremely weak when observed on earth [13]. Considering that the resolution of time-delay estimation using the correlation-based method is inversely proportional to the bandwidth of the GNSS signals, the achievable resolution is poor. This limitation makes accurate and reliable localization using these signals almost impossible in challenging propagation

environments defined by multipath effects.

- Due to their low power, when received on earth, they are not robust to intentional jamming or unexpected interference from terrestrial radio technologies (e.g., communications or radar systems) [14].
- The civilian GNSS signals are not encrypted, making them easily spoofable and vulnerable to cyber-attacks [15].

Correlation-based GNSS time-delay estimation has limited resolution, which results in a ranging accuracy of a few meters on average. This accuracy does not meet localization requirements for many critical applications. Methods for time-delay estimation based on carrier phase measurements of GNSS signals are proposed to further improve ranging accuracy in [16]. The carrier phase of the GNSS signal at the receiver changes in proportion to the time-delay between the receiver and the satellite that sent a signal. Therefore, the carrier phases of the received GNSS signals encode the delays between the satellites and the receiver. In theory, ranging using carrier phase measurements enables sub-centimeter level accuracy. Unfortunately, these measurements are ambiguous because the total integer number of 2π cycles of the carrier phase between a satellite and the receiver is unknown [17]. Several algorithms have been proposed to solve this problem and resolve the unknown integer ambiguity [18, 19]. These algorithms are used in carrier-based GNSS localization methods such as Real-Time Kinematic (RTK) and Precise Point Positioning (PPP). These methods have orders of magnitude higher accuracy than code-based methods. However, the carrier phase of the received signal is severely impaired by multipath effects, which causes these methods to perform poorly in multipath environments. When the GNSS receiver has a clear view of the sky and when multipath effects are negligible, combined code and carrier-phase-based GNSS delay estimation methods result in a ranging accuracy of few tens of centimeters. However, when the GNSS receiver does not have a clear view of the sky, the multipath effects lead to biased delay estimation, which significantly degrades localization.

Due to the discussed limitations, GNSS can not meet the security and accuracy demands of emerging applications such as autonomous navigation [20], intelligent transportation systems [21], internet-of-things (IoT) [22], and assisted living [23]. This is especially the case in urban and indoor scenarios where severe multipath propagation impairs the GNSS signals and performance of localization is poor or impossible due to the high attenuation of GNSS signals [24]. Next, we illustrate the demand for novel and precise localization methods for two specific groups of important emerging applications.

Example 1.1 (Autonomous navigation) Autonomous navigation is becoming increasingly important for civilian and military applications, and it is revolutionizing the automotive [27], aviation [28], and naval industries [29]. One example application of autonomous navigation is self-driving [30]. Self-driving comes with stringent safety and reliability demands. The key enablers to ensure these demands are environmental awareness and accurate localization. Self-driving is relying on a fusion of data from multiple sensors such as radar, lidar, cameras, and GNSS receivers to achieve environmental awareness and accurate localization. However, lidar and cameras perform poorly under adverse weather conditions such as fog, rain, and snow, which impede self-driving in

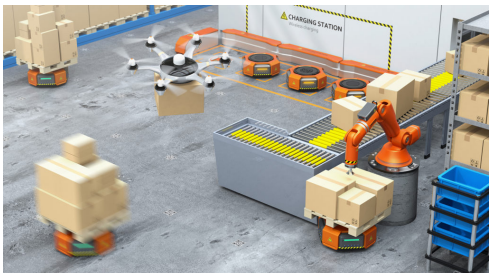

(a) Vision of fulfillment center where autonomous robots and drones are used for payload distribution. (Image courtesy of [25])

(b) Smart farming: autonomous drones are doing crop inspection and chemical treatment. (Image courtesy of [26])

Figure 1.2: Example applications of autonomous navigation.

bad weather conditions [31]. In these conditions, self-driving typically relies on radar and GNSS sensors which are resilient to weather conditions. However, radar sensors can only ensure relative localization, while GNSS performs poorly in environments such as urban canyons and tunnels due to the multipath effects and signal blocking. Therefore, to ensure complete safety under any condition and in any environment, self-driving requires ubiquitous localization with decimeter level (30 cm) accuracy and lane-level vehicle navigation [32]. Similarly, autonomous navigation of robots and drones in smart factories requires centimeter-level (10 cm) localization accuracy in indoor environments [33]. In these environments, GNSS signals are unavailable, and alternative localization approaches are needed. The example applications of autonomous navigation in distribution centers and smart farming are illustrated in Fig. 1.2.

Example 1.2 (Assisted Living) Assisted living (AL) technologies are becoming crucial for ensuring health and safety services in our aging society. The advent of the Internet of Things (IoT) technologies and wearable health monitoring sensors allows the development of many innovative AL applications that will revolutionize current health care systems [34]. Precise positioning has been recently identified as a key enabler for these applications in [35]. Several interesting AL systems based on RF signal analytics and positioning have been illustrated in [23], such as activity recognition, behavior pattern monitoring, and anomaly detection. Some of these systems use RF signals for applications such as emergency (fall) detection of the elderly or individuals with disabilities to alert caretakers and emergency services (cf. Fig. 1.3), navigation for visually impaired individuals, geofencing for people with dementia, and behavior monitoring to assess the physical and mental health of individuals. All these applications require decimeter-level (10cm) positioning accuracy, typically in indoor environments where GNSS is not available or performs poorly [36]. Other examples are applications for contact tracing and human interaction monitoring that recently became crucial for containing the outbreak of the COVID-19 pandemic [37]. Precise RF-based distance measuring proved to be the key component for these applications, and a vital tool to contain the virus [38].

From these examples, we see that new approaches are needed for localization in GNSS denied environments. The major challenge is to design practical localization sys-

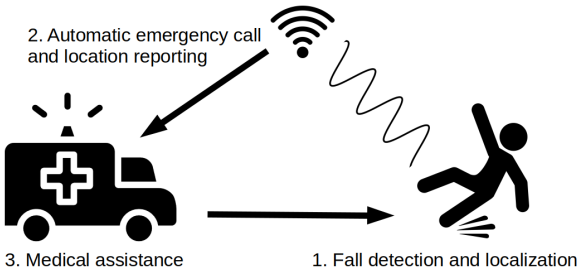

Figure 1.3: Illustration of the system for automatic fall detection and localization using radio signals.

tems and estimation methods that are robust to multipath propagation effects. In the next section, we will do a gentle introduction to the problem of localization in multipath radio channels and the main approaches for location estimation.

1.3. LOCALIZATION IN THE MULTIPATH RADIO CHANNEL

A promising localization approach in GNSS-denied environments is to use the existing wireless communication infrastructure, and ambient RF signals [39]. Localization using these signals starts with probing the multipath channels between the mobile node and multiple anchors. For example, an anchor transmits a known training signal that bounces off surrounding objects and arrives at the mobile node as a superposition of multipath components (MPCs) (cf. Fig. 1.4) that have different powers, directions-of-arrival and time-delays. The propagation of the RF signals between the anchor and the mobile node is mathematically modeled by the continuous-time channel impulse response (CIR). For the multipath channel with K paths the baseband equivalent of CIR is a function that is parameterized by the complex-amplitudes $\alpha_k \in \mathbb{C}$, Doppler frequencies $\eta_k \in \mathbb{R}$, time-delays $\tau_k \in \mathbb{R}_+$, and directions of arrival β_k, $k = 1,\ldots,K$, of MPCs present in the channel. We denote the CIR as $h(t;\boldsymbol{\theta})$, where $\boldsymbol{\theta} = [\boldsymbol{\alpha},\boldsymbol{\eta},\boldsymbol{\tau},\boldsymbol{\beta}]^T$ collects the vectors $\boldsymbol{\alpha},\boldsymbol{\eta},\boldsymbol{\tau}$, and $\boldsymbol{\beta}$ that are collecting the parameters α_k, η_k, τ_k, and β_k, $k = 1,\ldots,K$, respectively. The parameters $\boldsymbol{\alpha},\boldsymbol{\beta}$, and $\boldsymbol{\tau}$ encode the locations of the mobile node and surrounding RF reflectors. In contrast, $\boldsymbol{\eta}$ encodes the relative speeds of RF reflectors compared to the mobile node, and for the static scenario, it is the zero vector [40].

The location of the mobile node is encoded in the parameters of the line-of-sight (LOS) path $\{\alpha_1,\tau_1,\beta_1\}$ while the MPCs obfuscate estimation of these parameters. Therefore, the first step in radio localization is to estimate $h(t;\boldsymbol{\theta})$, detect the LOS path, and obtain its parameters from the signals exchanged between the anchor and the mobile node. We refer to this problem as channel estimation for localization. A slightly different problem is channel estimation for simultaneous localization and mapping (SLAM) using radio signals, which is the problem of simultaneous localization of the mobile node and surrounding reflectors from the estimated multipath channels [41]. In this problem, estimation of both parameters of the LOS path and MPCs is of interest.

To determine the location of the mobile node, typically the multipath channels between the mobile node and multiple anchors must be estimated. The number of chan-

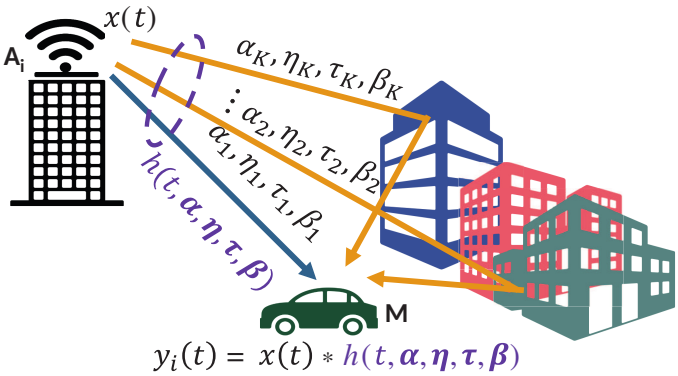

Figure 1.4: Illustration of an RF signal propagating in a multipath channel.

nels that need to be estimated for localization depends on the formulation of the localization problem and this is discussed in Chapter 2. After estimating $h(t;\boldsymbol{\theta})$ for the multiple anchors, the estimation of the location can proceed using (i) two-step or (ii) direct location estimation (DLE) methods. In two-step methods, first the parameters of the LOS paths are estimated, which are then used to estimate the location. In DLE methods, the location is directly estimated from estimates of $h(t;\boldsymbol{\theta})$ for multiple anchors.

In this thesis we are interested in practical approaches for localization and we limit ourselves to the two-step methods. In particular, we focus on localization using time-delay estimation in multipath channels. However, in Chapter 2 we provide a general discussion on the problem of localization and show that measurements of any of the LOS parameters satisfy the general model given by

$$\mathbf{r} = \boldsymbol{f}(\mathbf{p}_0) + \mathbf{n}, \tag{1.1}$$

where $\mathbf{r}$ is the vector collecting the estimates of the selected LOS parameter for multiple anchors, $\boldsymbol{f}(\mathbf{p}_0)$ is a known nonlinear vector-valued function of the unknown mobile node position $\mathbf{p}_0$, and $\mathbf{n}$ is a noise vector. The form of the function $\boldsymbol{f}(\mathbf{p}_0)$ depends on the LOS parameter that is selected for localization. From model (1.1), it follows that any two-step localization can be formulated as a nonlinear least squares optimization problem of the form

$$\hat{\mathbf{p}}_0 = \underset{\mathbf{p}}{\operatorname{argmin}} \ \left\| \mathbf{r} - \boldsymbol{f}(\mathbf{p}) \right\|_2^2, \tag{1.2}$$

where $\mathbf{p}$ is the optimization variable. The solution to this problem will depend on the selected LOS parameter used for localization. The exact forms that the function $\boldsymbol{f}(\mathbf{p}_0)$ can take, and solutions to the resulting problems are discussed in Chapter 2.

1.4. SCOPE AND CONTEXT OF THIS THESIS

In this section, we present the context of this thesis, the main research questions, and objectives. We start by providing a brief overview of the SuperGPS research project that steered the research context in this thesis. Then we introduce the main problem, research questions, and objectives that we aim to solve, answer and achieve, respectively.

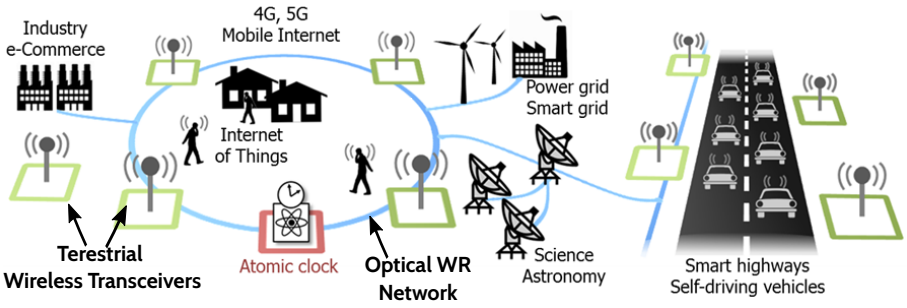

Figure 1.5: High-level architecture of the SuperGPS project.

1.4.1. SUPERGPS

The research in this thesis was supported by KPN and NWO under the SuperGPS project. The objective of the SuperGPS project is to design a system for accurate timing and localization in GNSS-denied environments. The main idea of the project is to combine optical and terrestrial wireless (radio) networks to enable accurate localization and synchronization in challenging radio propagation environments (cf. Fig. 1.5 for an illustration of the SuperGPS architecture). Timing distribution with sub-nanosecond accuracy via the optical network is based on the White Rabbit (WR) system. WR was developed as a collaboration of the European Organization for Nuclear Research (CERN), several universities and companies aiming to provide new technology for synchronized control and data acquisition. In the SuperGPS project, we used these results to synchronize a wireless localization infrastructure, that is, to synchronize the anchors. The wireless infrastructure developed in the SuperGPS project consists of radio transceivers that equip anchors and mobile nodes, which perform signal acquisition and location estimation. The research in this thesis focuses on developing estimation and calibration methods for precise localization that are the key signal processing components of the SuperGPS system.

1.4.2. PROBLEM STATEMENT AND RESEARCH GOALS

In Section 1.3 we discussed the problem of localization using RF signals in multipath propagation environments. We have shown that the first step to localize the mobile node is to estimate the multipath channels between it and multiple anchors. Multipath channel estimation for localization is different from classical channel estimation for communications, where the goal is to estimate the compound effects of propagation and transceivers on signals and maximize energy per symbol to noise power spectral density ratio E_s/N_0. The goal of channel estimation for localization is to detect the LOS path of the multipath channel and estimate its parameters free of any transceiver hardware impairments such as non-ideal frequency response or phase and frequency offsets. In this thesis, we focus on localization using practical single antenna transceivers capable of carrier frequency switching. From signals acquired using these transceivers, we can estimate time-delays and complex amplitudes of the multipath components. However,

the complex amplitudes are highly sensitive to multipath fading, and therefore they are changing abruptly, making accurate localization using these parameters hard to achieve.

In this thesis, we are interested in high accuracy localization, and thus we focus on location estimation from time-delay parameters. The main challenge for achieving precise localization using these parameters is the detection of the LOS path and high-resolution estimation of its time delay. The resolution of time-delay estimation using classical methods such as matched filtering is inversely proportional to the bandwidth of the training signals used for channel probing. Therefore, the high-resolution time-delay estimation using these methods can be achieved when channel measurements are collected over a large bandwidth. This has motivated the use of ultra-wideband (UWB) communication technology for localization in recent years [42]. UWB based localization systems achieve an accuracy of 10 to 20 cm in indoor environments. However, these localization systems require a dedicated UWB infrastructure, and they can only be used for localization in small areas due to the limits set on the transmitted signal power. This limit is defined by radio regulatory bodies, which define the rules for RF spectrum usage and coexistence. As an example of constraints set on signals by radio regulators, we will consider radio regulations set on the popular WiFi technology in Europe. The European radio regulators define three frequency bands on 2.5, 5, and 6 GHz for WiFi communication [43] [1]. Within these bands, several frequency channels with a bandwidth of 20, 40, 80, and 160 MHz are defined for instantaneous usage. The regulations and standardization set on WiFi technology allow usage of multiple of these frequency channels in a non-instantaneous fashion. This leads us to the first question to be answered in this thesis:

Q1 *How can we increase the accuracy of time-delay estimation and localization using practical single-antenna transceivers considering constraints set by radio regulators on the power and the bandwidth of the training signals?*

The indoor multipath channel at 2.4 GHz between the anchor and a pedestrian mobile node moving at a speed of 1 m/s is stationary for approximately 53 ms, and this duration we call the channel coherence time. Considering that the typical WiFi training signal used for channel probing has a duration of 40 μs, which is 1000 times less than the channel coherence time, there is an opportunity to increase the bandwidth of the multipath channel measurements by probing the channel over multiple carrier frequencies during the channel coherence time. We call this approach for acquiring multipath channel measurements the multiband channel probing scheme. Our end goal is to achieve a high-resolution time-delay estimation of MPCs from these measurements. This brings us to the following subquestions of Q1 that we answer in this thesis:

Q1.1 What is a reasonable parametric model for multiband multipath channel measurements?

Q1.2 Is there an efficient and practical estimator that can estimate time-delays and achieve the Cramér Rao Bound (CRB)?

[1] Here, we did not consider the frequency band at 900 MHz defined for usage in long-range WiFi networks specified by the IEEE 802.11ah standard.

Q1.3 Considering the proposed model, what is the theoretical limit on the variation of the time-delay estimates, that is, what is the CRB?

In reality, the RF transceivers used to probe multipath channels and obtain measurements are not ideal, and they introduce various hardware impairments which impact the channel measurements. When these impairments are not calibrated, the estimated time-delays are biased. This motivates the following question:

Q2 *How can we jointly calibrate hardware impairments of RF transceivers and estimate time-delay parameters?*

In particular, the time-delay estimators are sensitive to hardware impairments that directly impair the multipath channel measurements, such as non-ideal frequency response and clock-skew of RF transceiver oscillators. This brings us to the following related subquestions of Q2:

Q2.1 Can we jointly estimate the time-delays and calibrate unknown frequency responses of multiband RF transceivers?

Q2.2 Is there an efficient estimator for joint time-delay and clock-skew estimation of RF transceivers from multiband channel measurements?

While answering questions Q1 and Q2, several modeling assumptions are made, which might not hold for all localization and measurement scenarios. Therefore, it is important to consider modeling errors resulting from approximations of multipath channel propagation done during data modeling when using real channel measurements. In particular, it is hard to model the frequency dependency effects of the MPCs. In this thesis, we choose to avoid these effects by ensuring that the frequency aperture of the multiband channel measurements is not too large. This motivates the following research question:

Q3 *What is the performance of multiband time-delay estimation and localization in real indoor multipath channels?*

In particular, we are interested under which conditions the frequency dependency of multipath components is negligible. This brings us to the subquestion of Q3:

Q3.1 What is the impact of modeling errors caused by frequency dependency of multipath propagation on the performance of time-delay estimation?

In the next sections, we provide a summary of the main parts of this thesis and their respective contributions to the literature.

1.5. OUTLINE

This thesis is organized as follows. We first provide an introduction to principles of radio localization and a general overview of localization approaches in Chapter 2. In Chapter 3, we focus on the problem of multipath channel time-delay estimation for localization and discuss the main signal processing frameworks for solving this problem. Next, we

discuss the signal model for multiband channel measurements and derive an algorithm for time-delay estimation in Chapter 4. The proposed algorithm requires initialization, and to provide initial estimates in Chapter 5 we propose a multiresolution time-delay estimation algorithm that has a close-form solution. Following the development of the algorithms, we assess the performance of the proposed algorithms by comparing them to the CRB and other methods. These chapters address questions Q1.1, Q1.2, and Q1.3. In Chapter 6, we discuss the problem of joint calibration of transceiver impairments and time-delay estimation, where we address question Q2.1. We address question Q2.2 in Chapter 7, where we discuss the problem of joint clock-skew and time-delay estimation using narrowband radios and multiband channel measurements. In Chapter 8, we evaluate the performance of the algorithms using real indoor multiband multipath channel measurements and address question Q3. Finally, we conclude the thesis and provide interesting open problems for future related research in Chapter 9. In what follows, we provide a summary of the main parts of this thesis.

Chapter 2: This chapter introduces principles of radio localization. We start by introducing a general parametric model for multipath radio channels between an anchor and the mobile node. We show that the multipath channel parameters encode the location of the mobile node and discuss the relation between these parameters and the location. Following this discussion, we define the general model for typical measurements obtained from the estimates of multipath channel parameters that are used for localization, such as time of arrival (TOA), time difference of arrival (TDOA), received signal strength (RSS), and direction of arrival (DOA). Using the general data model for these measurements, we show that two-step localization is a nonlinear estimation problem. The exact formulation of this problem depends on the type of measurements selected for localization and the function that relates the measurements to the location of the mobile node. We define these functions for the aforementioned measurements and illustrate the derivations of several location estimators on the example of TOA measurements. Next, we discuss the model for direct location estimation (DLE), where the multipath channel is parameterized by the location and the location is directly estimated from the multipath channel measurements. Finally, we conclude this chapter by comparing the discussed localization methods.

Chapter 3: This chapter discusses the problem of channel estimation for localization and motivates the rest of this thesis. In particular, we focus on the problem of time-delay estimation in multipath channels. We formulate this problem in the frequency domain, define the parametric model for multipath channel measurements and discuss the signal processing frameworks that apply to this problem. The model shows that time-delay estimation in the frequency domain becomes the problem of estimating the parameters of a sum of complex exponentials. This problem has been extensively treated in several signal processing frameworks such as subspace-based estimation, finite rate of innovation (FRI) sampling, and compressive sensing. We then discuss the formulation of the multipath channel delay estimation problem in these frameworks and provide an overview of popular estimators that can be used to obtain a solution to this problem.

Chapter 4: Here, we address question Q1 and its subquestions Q1.1 and Q1.2. In particular, we purpose increasing the resolution of delay estimation by multiband channel probing. The main idea here is to increase the bandwidth, i.e., frequency aperture, of the multipath channel measurements by probing the channel over multiple separate frequency bands during the channel coherence time. This provides an opportunity for high-resolution time-delay estimation, even when using narrowband RF transceivers. We then derive the model for multiband channel measurements considering hardware impairments introduced by the transceivers, such as a non-ideal frequency response and phase offset. Next, we present techniques for mitigation of the unknown phase offset and calibration of the frequency response. We formulate the multiband time-delay estimation as a multidimensional spectral estimation problem and exploit the structure present in the measurements to estimate delays. We then propose an algorithm that estimates the delays by solving a weighted subspace fitting (WSF) problem. We refer to this algorithm as the multiband weighted delay estimation (MBWDE) algorithm. To assess the performance of the MBWDE algorithm, we derive the CRB for the data model of multiband multichannel measurements and perform numerical simulations. We then compare the performance of the MBWDE algorithm against several other methods presented in Chapter 3 and the CRB. From the results, it is seen that MBWDE is statistically efficient and asymptotically meeting the theoretical CRB.

Chapter 5: The algorithm presented in Chapter 4 is based on WSF, which is a nonlinear least-squares problem and requires initialization. In this chapter, we present an algorithm with a closed-form solution that can be used to initialize the MBWDE algorithm. We refer to this algorithm as a multiresolution time-delay (MRTD) estimation algorithm. Similar to the previous chapter, to improve the resolution of time-delay estimation while avoiding arriving at unrealistic sampling rates, we use multiband channel measurements collected over a large frequency aperture. However, now the multiband measurements are collected in two frequency bands and preferably in those that create the largest frequency aperture. The MRTD algorithm exploits the multiple shift-invariance properties of the collected measurements and joint-diagonalization to provide a closed-form solution for the time-delays. In particular, this algorithm uses shift-invariance introduced over a small frequency aperture within the bands to provide low-resolution but unambiguous time-delay estimates and shift-invariance over a large frequency aperture between the bands, to provide high-resolution but ambiguous time-delay estimates. These estimates are then combined and results in high resolution and unambiguous time-delay estimation. Numerical simulations are then used to assess the performance of the proposed algorithm. The performance of the algorithm is compared against several other methods and the CRB. These results show that the algorithm is asymptotically efficient and asymptotically converges to the CRB.

Chapter 6: The MBWDE and MRTD algorithms presented in Chapter 4 are both sensitive to calibration errors of the RF transceivers. There, we assumed that the frequency response of the transceivers is measured and calibrated. However, in practical

scenarios, the frequency response of transceivers might not be known nor calibrated before time-delay estimation. Using the MBWDE and MRTD algorithms to estimate delays from uncalibrated multiband measurements leads to a bias, which degrades the performance of estimation. This chapter discusses this problem and proposes an algorithm for joint calibration of multiband RF transceivers and delay estimation. We show that this problem can be formulated as a particular case of covariance matching. This problem is severely ill-posed, and to find its solution, we use prior information about radio-frequency chain distortions and multipath channel sparsity for regularization. This formulation results in a , which we reformulate to a rank-constrained linear system, and solve by a simple group Lasso algorithm. We use numerical simulations to benchmark the performance of this algorithm against several existing methods for joint calibration and delay estimation. From these results, it is seen that the proposed algorithm outperforms the existing methods.

Chapter 7: In Chapters 4, 5 and 6, we assumed that the local oscillators of the mobile node and anchors are frequency synchronized during channel probing. This frequency synchronization can be achieved using a known preamble at the beginning of every training signal to estimate the frequency offsets. However, in the Internet of Things (IoT) networks, where the mobile nodes are typically cheap battery-powered sensor devices with low-quality clock sources, the process of synchronization needs to be repeated regularly, which increases training overhead. This chapter focuses on the problem of joint delay (range) and clock synchronization using phase difference of arrival (PDoA) measurements of narrowband RF signals. We derive a data model for PDoA measurements that incorporates the unknown clock-skew effects. We then formulate joint estimation of the clock-skew and range as a two-dimensional (2-D) frequency estimation problem. Furthermore, we propose: (i) a two-way communication protocol for collecting PDoA measurements and (ii) a weighted least squares (WLS) estimator for joint estimation of clock-skew and range, leveraging the shift-invariance property of the measurement data. We use numerical simulations to benchmark the performance of the algorithm against the CRB and several other methods. From these results, it is seen that the proposed estimator is efficient and asymptotically meeting the theoretical CRB.

Chapter 8: In chapters 4 and 5, we made sensible modeling assumptions to approximate RF signal propagation and derive data models and estimators for multiband delay estimation. We then used numerical simulations and CRBs to benchmark the performance of the proposed estimators. From these results, it is seen that the proposed estimators are statistically efficient and that they meet the CRBs. However, these results do not say how these estimators perform in practical scenarios when real measurements are used. This chapter evaluates the performance of multiband delay estimation using real indoor multipath channel measurements collected in a hospital and a university building. We select the parameters of the measurements following the definitions given in the emerging IEEE 802.11be standard for WiFi networks. We then estimate the ranges, i.e., time-delays, from collected measurements and use the empirical cumulative distribution function (CDF) of the range estimation errors to illustrate the performance of the MBWDE algorithm and to compare it with several other methods. Next, we

demonstrate the performance of 2-D localization in a hospital environment by using the estimated ranges. The results show that when channel measurements are collected over a large frequency aperture (bandwidth), they exhibit frequency-dependent behavior. The frequency dependency is not captured by the data model that is used to derive the algorithms. Therefore, to avoid modeling errors, the frequency bands where measurements are collected must be selected carefully. Finally, we discuss the implementation of multiband delay estimation and localization systems on practical IEEE 802.11be transceivers.

Chapter 9: In this chapter we provide conclusions driven from the results of this thesis and we outline a number of open questions and possible future research directions.

1.6. LIST OF CONTRIBUTIONS

Finally, we provide an overview of the contributions made to the scientific literature during the work on this Ph.D. thesis. The overview is organized in two parts. The first part, includes peer-reviewed contributions, a patent and a technical report that are directly related to the topic of this thesis, while the second part lists other peer-reviewed contributions made to the general area of wireless communications and signal processing.

1.6.1. THESIS RELATED CONTRIBUTIONS

Journal Papers

J1 **T. Kazaz**, GJM Janssen, J. Romme, and A.J. van der Veen, "Delay Estimation for Ranging and Localization Using Multiband Channel State Information", *IEEE Transactions on Wireless Communications*, vol. 21, no. 4, pp. 2591-2607, April 2022.

J2 C. Diouf, GJM Janssen, H. Dun, **T. Kazaz**, and CJM Tiberius, "A USRP-Based Testbed for Wideband Ranging and Positioning Signal Acquisition", *IEEE Transactions on Instrumentation and Measurement*, vol. 70, 1-15, 2021.

Conference Papers

C1 **T. Kazaz**, G.J.M. Janssen, J. Romme, and A.J. van der Veen, "Analysis of Multipath Channel Delay Estimation Using Subspace Fitting", 54nd Asilomar Conference on Signals, Systems, and Computers, Pacific Grove, USA, Nov. 2020.

C2 C. Diouf, H. Dun, **T. Kazaz**, G.J.M. Janssen, and C.J.M. Tiberius, "Demonstration of a Decimeter-Level Accurate Hybrid Optical-Wireless Terrestrial Positioning System", 33rd International Technical Meeting of the Satellite Division of The Institute of Navigation (ION GNSS+ 2020), pp. 2220-2228, Sep. 2020.

C3 **T. Kazaz**, M. Coutino, G.J.M. Janssen, and A.J. van der Veen, "Joint Blind Calibration and Time-Delay Estimation for Multiband Ranging", IEEE International Con-

ference on Acoustics, Speech, and Signal Processing (ICASSP), Barcelona, Spain, May 2020.

C4 **T. Kazaz**, G.J.M. Janssen, and A.J. van der Veen, "Time Delay Estimation from Multiband Radio Channel Samples in Nonuniform Noise", 53nd Asilomar Conference on Signals, Systems, and Computers, Pacific Grove, USA, Nov. 2019.

C5 C. Diouf, G.J.M. Janssen, **T. Kazaz**, H. Dun, and C.J.M. Tiberius, "A 400 Msps SDR Platform for Prototyping Accurate Wideband Ranging Techniques", 16th Workshop on Positioning, Navigation and Communications (WPNC), Bremen, Germany, Oct. 2019.

C6 **T. Kazaz**, R.T. Rajan, G.J.M. Janssen, and A.J. van der Veen, "Multiresolution Time-of-Arrival Estimation from Multiband Radio Channel Measurements", IEEE International Conference on Acoustics, Speech, and Signal Processing (ICASSP), Brighton, United Kingdom, May 2019.

C7 **T. Kazaz**, Mario Coutino, G. Janssen, G. Leus and A.J. van der Veen, "Joint Ranging and Clock Synchronization for Dense Heterogeneous IoT Networks", 52nd Asilomar Conference on Signals, Systems, and Computers, Pacific Grove, USA, Oct. 2018.

Patents

P1 **T. Kazaz**, M. Coutino, G.J.M. Janssen, G. Leus and A.J. van der Veen, "Phase-based Distance Determination For Wireless Sensor Networks", *Patent, USPTO* 621 81 5,1 64, March 2019.

Technical Reports

R1 **T. Kazaz**, and G.J.M. Janssen, "Software-Defined Radio Platforms and Architectures for Rapid Prototyping of Radio Signal Processing Innovations", August 7, 2018, 20 pages, (available on request.)

1.6.2. OTHER CONTRIBUTIONS

Journal Papers

J3 M. Kulin, **T. Kazaz**, E. de Poorter, and I. Moerman, "A survey on machine learning-based performance improvement of wireless networks: PHY, MAC and network layer", *MDPI Electronics*, 10.3, 2021.

J4 M. Kulin, **T. Kazaz**, I. Moerman, and E. de Poorter, "End-to-End Learning from Spectrum Data: A Deep Learning Approach for Wireless Signal Identification in Spectrum Monitoring Applications", *IEEE Access*, vol. 6, 18484-18501, 2018.

2

PRINCIPLES OF RADIO LOCALIZATION

"A problem well-defined is a problem half-solved."

— Charles Kettering

2.1. INTRODUCTION

IN the first chapter of the thesis, we provided a gentle introduction to localization in multipath radio channels. This chapter goes a step further and discusses the relation of the multipath channel parameters to the location information. We start from the general parametric signal model for the multipath radio channel and then define the relation between its parameters and the location information. This thesis focuses on time-delay estimation for localization methods such as time-of-arrival (TOA) and time-difference-of-arrival (TDOA). However, for the sake of completeness, we provide in this chapter a general overview of localization methods based on multipath channel parameters, which also include direction-of-arrival (DOA) and received signal strength (RSS). We show that under the additive Gaussian noise assumption on the errors of TOA, TDOA, DOA, and RSS measurements, all related localization problems have a common underlying model and can be formulated as non-linear least squares (NLS) problems.

2.2. INFERRING LOCATION FROM MULTIPATH RADIO CHANNELS

We introduced the problem of localization in multipath radio environments in Section 1.3. There, we discussed parametric multipath channel models and the model parameters that encode the locations of the mobile node and RF signal reflectors present in the environment surrounding the mobile node and anchor stations. Therefore, the key idea of localization in these environments is to estimate the location encoding multipath channel parameters from the radio signals exchanged between the mobile node and anchors.

This process starts with probing the channels between the mobile node and multiple anchors. Let us consider a scenario where we have N_{A} anchors, denoted with indexes $i = 1, \ldots, N_{\mathrm{A}}$, and where the mobile node determines its location using signals sent by the anchors. For example, anchor i transmits a known training signal $x(t)$ that bounces off surrounding objects and arrives at the mobile node as a superposition of multipath components (MPCs) (see Fig. 1.4) that have different powers, directions-of-arrival, and time-delays [44]. This propagation phenomenon is mathematically modeled by the baseband equivalent continuous-time channel impulse response (CIR), which including the antenna response, is given as [45]

$$h^{(i)}(t) = \sum_{k=1}^{K^{(i)}} \alpha_k^{(i)} e^{j\beta(\vartheta_k^{(i)})} \delta(t - \tau_k^{(i)}). \tag{2.1}$$

In this model, there are $K^{(i)}$ resolvable MPCs, where the kth MPC is characterized by its parameters: complex path amplitude $\alpha_k^{(i)} \in \mathbb{C}$, direction-of-arrival $\vartheta_k^{(i)} \in \mathbb{R}$, and time-delay $\tau_k^{(i)} \in \mathbb{R}_+$. Here, $\beta(\vartheta_k^{(i)})$ is the phase shift with respect to the reference point and is related to the direction-of-arrival of the signal on the antenna. Typically, antenna arrays are required to resolve the $\vartheta_k^{(i)}$ parameters, and thus they are usually ignored in the single-antenna scenarios and channel models. Exceptions are recently proposed metasurface frequency-diverse antennas that encode and compress spatial information of

RF signals before sampling and support DOA estimation from samples collected using single antenna receivers [46]. The parameters of the MPCs $\{\alpha_k^{(i)}, \tau_k^{(i)}, \vartheta_k^{(i)}\}, k = 1, \ldots, K^{(i)}$ encode the locations of the mobile node and surrounding RF signal reflectors [40]. Note that here we assume that the mobile node has low speed and therefore the Doppler frequency shifts may be ignored.

Taking into account multipath propagation, the signals received at the mobile node are given by

$$y^{(i)}(t) = x(t) * h^{(i)}(t), \quad i = 1, \ldots, N_{\mathrm{A}}, \tag{2.2}$$

where $*$ represents convolution operator. In this model, we ignored hardware effects and frequency and phase offsets between the mobile node and anchors, which deteriorate the channel measurements and performance of localization. We will discuss this in more detail in Chapters 6 and 7.

Now, radio localization can be defined as the problem of estimating the location of the mobile node from the received signals $y^{(i)}(t)$. The location of the mobile node is encoded in the parameters of the line-of-sight (LOS) paths $\{\alpha_1^{(i)}, \tau_1^{(i)}, \beta_1^{(i)}\}$ while the MPCs obfuscate estimation of these parameters. Therefore, the first step in radio localization is to estimate the true $h^{(i)}(t)$, from the received signals $y^{(i)}(t)$, and then detect the LOS path and obtain its parameters. We refer to this process as channel estimation for localization. Important to note is that this is different from channel estimation for communications, where the goal is to equalize the compound effects of hardware and $h^{(i)}(t)$, maximize energy per symbol to noise power spectral density, and estimate $x(t)$ [47].

After estimating $h^{(i)}(t), i = 1, \ldots, N_{\mathrm{A}}$, the estimation of the location can proceed using (i) two-step, or (ii) direct location estimation (DLE) methods. In the two-step methods, first, the parameters of the MPCs are estimated, which are then used to estimate the location. In direct location estimation (DLE) methods, the multipath channel is parameterized by the location parameters, and the location is directly estimated from the multipath channel measurements.

In what follows, we discuss the multipath channel parameters and the measurements used for two-step and direct localization estimation methods. We start by defining a generalized data model for the measurements used in two-step localization methods. We then briefly discuss derivations of two-step localization algorithms for an example of time-delay measurements. These derivations are based on a generalized measurement model, and they can be followed when deriving algorithms for two-step localization based on other multipath channel parameters.

2.3. MEASUREMENTS FOR TWO-STEP LOCALIZATION METHODS

For simplicity of exposition we will discuss measurements for two-step methods on an example of localization in two-dimensional (2-D) space. The derived data models can be easily extended to 3-D localization scenarios. Consider for example localization in 2-D space, where there are N_{A} anchors with known positions $\mathbf{z}_i = [z_x^{(i)}, z_y^{(i)}]^T \in \mathbb{R}^2$, $i = 1, \ldots, N_{\mathrm{A}}$ and the mobile node with unknown position $\mathbf{z}_0 = [z_x^{(0)}, z_y^{(0)}]^T \in \mathbb{R}^2$.

The parameters of the *line-of-sight* (LOS) path $\{\alpha_1^{(i)}, \tau_1^{(i)}, \beta_1^{(i)}\}$ present in the multi-

path channel $h^{(i)}(t)$, between anchor i and the mobile node, are directly linked to the location of the mobile node $\mathbf{z}_0$ [48]. The two-step localization approaches use estimates of LOS parameters $\{\alpha_1^{(i)}, \tau_1^{(i)}, \beta_1^{(i)}\}$, obtained for multiple anchors, to estimate the location $\mathbf{z}_0$ [49]. Depending on the parameter that is selected for localization, these methods can be classified into methods based on time-delays $\tau_1^{(i)}$ [50], received signal powers $|\alpha_1^{(i)}|^2$ [51] [1], and direction-of-arrivals $\beta_1^{(i)}$ [52]. However, the underlying measurement models for the previously mentioned LOS parameters can be written in the general form as

$$\mathbf{r} = \boldsymbol{f}(\mathbf{z}_0) + \mathbf{n}, \tag{2.3}$$

where $\mathbf{r}$ is the vector collecting the estimates of the LOS parameter selected for location estimation, $\boldsymbol{f}(\mathbf{z}_0)$ is a known nonlinear vector-valued function of $\mathbf{z}_0$ and its form depends on the selected LOS parameter, and $\mathbf{n}$ is the error vector. Here, we assume that errors of time-delay estimates are Gaussian distributed, and we model their disturbance on the true time-delays as additive noise. This modeling assumption does not hold in general, and it is valid for scenarios where the variance of the observation errors is small [53]. Likewise, in practice, the estimation errors are not necessarily Gaussian distributed [54]. For example, this can be seen in Chapter 8, where it is shown that time-delay estimates obtained from real channel measurements using a multiband weighted delay estimation algorithm presented in Chapter 4 have errors distributed in accordance with Lévy alpha-stable distribution. There, we show that by ignoring the large outliers in the time-delay estimates, Lévy alpha-stable distribution can be approximated by Gaussian distribution. In practice, determining the exact distribution of the estimation errors caused by the observation noise is often intractable [55]. Therefore, for simplicity of exposition in the remaining of this chapter, we will use an approximate model for the estimation errors of time-delay, direction-of-arrival, and received signal strength parameters and model them as additive Gaussian random variables. This model in the context of time-delay and direction-of-arrival estimates is accurate under the conditions that the variance of the noise is small. In what follows, we discuss the multipath channel parameters and exact formulations of the localization problems. We start by discussing time-delay parameters and localization methods.

2.3.1. TIME-DELAY MEASUREMENTS

The Euclidian distance (range) between anchor i and the mobile node is given by

$$d^{(i)}(\mathbf{z}_0) := \|\mathbf{z}_0 - \mathbf{z}_i\|_2 = \sqrt{(z_x^{(0)} - z_x^{(i)})^2 + (z_y^{(0)} - z_y^{(i)})^2}, \quad i = 1, \ldots, N_\mathrm{A}. \tag{2.4}$$

These distances are directly linked to the delays of the LOS paths $\tau_1^{(i)}$, which is given by

$$d^{(i)} = c\tau_1^{(i)}, \tag{2.5}$$

where $c = 3 \cdot 10^8$ m/s is the speed of radio signals (electromagnetic waves) in the air. However, the true delays $\tau_1^{(i)}$, $i = 1, \ldots, N_\mathrm{A}$ are not known, and they need to be estimated

[1] Note that parameter $|\alpha_1^{(i)}|^2$ is not the overall received signal power, but rather the power of the signal received via the LOS path.

from the signals sent from the anchors and received at the mobile node. In the general scenario, when the clock of an anchor i and the mobile node are not synchronized, the estimated delay of the LOS component is given by

$$\hat{\tau}_1^{(i)} := \tau_1^{(i)} + \Delta\tau^{(i)} + n_\tau^{(i)}, \quad i = 1,\dots,N_\mathrm{A}, \tag{2.6}$$

where $\Delta\tau^{(i)}$ is an unknown offset, and $n_\tau^{(i)}$ is a zero-mean Gaussian random variable representing the error of the time-delay estimates introduced by the presence of noise. Depending on the requirement for clock synchronization between the mobile node and the anchors, time-delay localization methods can be divided into: *(i) time-of-arrival (TOA)* and *(ii) time-difference-of-arrival (TDOA)* [56].

TIME-OF-ARRIVAL (TOA):

In TOA-based localization, it is assumed that the clocks of the anchors and the mobile node are synchronized. As a consequence, there is no offset in (2.6) and the estimated delays between the mobile node and the anchors are given by

$$\hat{\tau}_1^{(i)} := \tau_1^{(i)} + n_\tau^{(i)}, \quad i = 1,\dots,N_\mathrm{A}. \tag{2.7}$$

From (2.5) it follows that we can use the estimated delays $\hat{\tau}_1^{(i)}$ to estimate the ranges as $\hat{d}^{(i)} = c\hat{\tau}_1^{(i)}$. The estimated ranges satisfy the following model

$$\hat{d}^{(i)} := d^{(i)} + n^{(i)}, \quad i = 1,\dots,N_\mathrm{A}, \tag{2.8}$$

where $n^{(i)} = cn_\tau^{(i)}$. The ranges computed from TOA estimates are collected in the vector $\mathbf{r}_\mathrm{TOA} = [\hat{d}^{(1)},\dots,\hat{d}^{(N_\mathrm{A})}]^T$. In the absence of errors in the TOA estimates, each range $d^{(i)}$ defines a circle on which the mobile node must lie in the 2-D space where the center of the circle has the coordinates $\mathbf{z}_i$. This is illustrated in Fig. 2.1a. It is easy to see that geometrically, three or more circles defined from error-free TOAs will result in a unique intersection (cf. Fig. 2.1c), which is the mobile node location $\mathbf{z}_0$. This implies that to estimate the location of the mobile node in 2-D space, the TOA estimates between the mobile node and at least three N_A =3 anchors are required. The green color around the circles indicates the influence of noise on range (delay) estimation and its consequence on localization, and we define it as the 2σ region. The region marked by a darker green color indicates the higher probability that erroneous estimates will lie in it. The darkest green color is around the circles that mark the true range (delay) between the mobile node and the anchors. We can see that due to the influence of noise, the circles defined using TOAs may not intersect or may have multiple intersections, and then the location $\mathbf{z}_0$ can not be directly estimated by looking at the problem from a geometrical perspective. Therefore, in what follows, we formulate the problem of location estimation from TOA estimates mathematically using the model (2.3). This mathematical formulation results in a system of nonlinear equations that can be solved using appropriate optimization methods. The solution to the problem will be the estimated location of the mobile node.

Starting from (2.3) we can write the model for $\mathbf{r}_\mathrm{TOA}$ as

$$\mathbf{r}_\mathrm{TOA} = \boldsymbol{f}_\mathrm{TOA}(\mathbf{z}_0) + \mathbf{n}_\mathrm{TOA}, \tag{2.9}$$

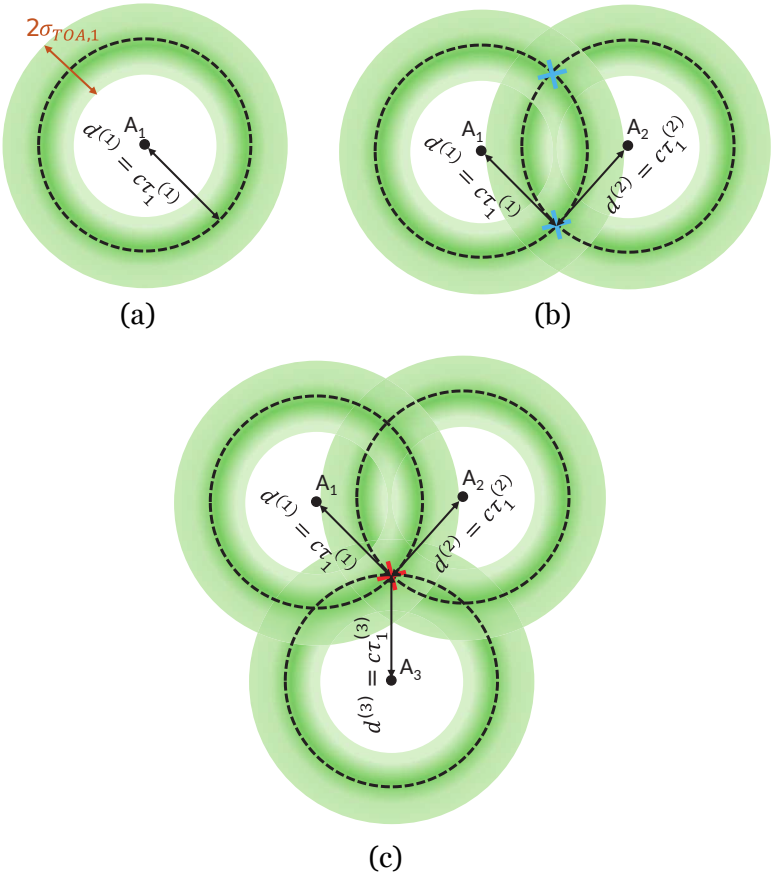

Figure 2.1: Illustration of TOA-based localization: (a) the circle on which the mobile node is lying is denoted by a black dashed line, and it is defined by the range (delay) between the mobile node and the anchor A_1, (b) the two points on which the circles (drawn based on TOA estimates between the mobile node and two anchors) intersect, are marked by blue crosses, and these are equally possible locations of the mobile node, (c) the intersection point of three circles drawn based on TOA estimates between the mobile node and three anchors reveals the location of the mobile node, which is marked by the red cross.

where $\mathbf{n}_{\mathrm{TOA}} = [n^{(1)}, \ldots, n^{(N_\mathrm{A})}]^T$ is the error vector and

$$\boldsymbol{f}_{\mathrm{TOA}}(\mathbf{z}_0) := \begin{bmatrix} d^{(1)}(\mathbf{z}_0) \\ d^{(2)}(\mathbf{z}_0) \\ \vdots \\ d^{(N_\mathrm{A})}(\mathbf{z}_0) \end{bmatrix} = \begin{bmatrix} \|\mathbf{z}_0 - \mathbf{z}_1\|_2 \\ \|\mathbf{z}_0 - \mathbf{z}_2\|_2 \\ \vdots \\ \|\mathbf{z}_0 - \mathbf{z}_{N_\mathrm{A}}\|_2 \end{bmatrix}. \tag{2.10}$$

The function $\boldsymbol{f}_{\mathrm{TOA}}(\mathbf{z}_0)$ is known, and it is parameterized by the unknown position of the mobile node $\mathbf{z}_0$. This function is vector-valued and it collects the error-free ranges defined in (2.4).

The problem of location estimation using TOAs is to estimate $\mathbf{z}_0$ from $\mathbf{r}_{\text{TOA}}$ using the model (2.9). The function $\boldsymbol{f}_{\text{TOA}}(\mathbf{z}_0)$ is nonlinear in the location parameter $\mathbf{z}_0$. Therefore, the estimate of location $\mathbf{z}_0$ can be obtained by solving the system of nonlinear equations (2.10). We first will derive the statistical model for the TOA estimates to support the algorithm development and performance analysis in the coming section.

Assuming that $n^{(i)}, i = 1,\ldots,N_{\text{A}}$ are zero-mean uncorrelated Gaussian random variables, then the vector $\mathbf{n}_{\text{TOA}}$ is also zero-mean Gaussian distributed. Therefore, we can write $\mathbf{n}_{\text{TOA}} \sim \mathcal{N}(\mathbf{0}, \boldsymbol{\Sigma}_{\text{TOA}})$, where $\mathbf{0}$ is the zero vector of length N_{A}, and covariance matrix $\boldsymbol{\Sigma}_{\text{TOA}}$ is given by

$$\boldsymbol{\Sigma}_{\text{TOA}} := \mathbb{E}(\mathbf{n}_{\text{TOA}}\mathbf{n}_{\text{TOA}}^T) = \text{diag}([\sigma^2_{\text{TOA},1},\ldots,\sigma^2_{\text{TOA},N}]), \tag{2.11}$$

where $\sigma^2_{\text{TOA},i}$ are the variances of the estimates (cf. 2.1a) and $\mathbb{E}(\cdot)$ is the statistical expectation operator. From this assumption and the model (2.9) it follows that the estimates collected in $\mathbf{r}_{\text{TOA}}$ are also Gaussian random variables and we can write $\mathbf{r}_{\text{TOA}} \sim \mathcal{N}(\mathbf{d}, \boldsymbol{\Sigma}_{\text{TOA}})$. Here, $\mathbf{d} = \boldsymbol{f}_{\text{TOA}}(\mathbf{z}_0)$ collects error-free ranges where dependency on $\mathbf{c}_0$ is dropped as the position $\mathbf{c}_0$ is fixed during TOA estimation. Therefore, the probability density function (PDF) of the $\mathbf{r}_{\text{TOA}}$, denoted by $p(\mathbf{r}_{\text{TOA}})$ is given by

$$p(\mathbf{r}_{\text{TOA}}) = \frac{1}{(2\pi)^{N_{\text{A}}/2}(\det(\boldsymbol{\Sigma}_{\text{TOA}}))^{1/2}} \exp\left(-\frac{1}{2}(\mathbf{r}_{\text{TOA}} - \mathbf{d})^T \boldsymbol{\Sigma}^{-1}_{\text{TOA}}(\mathbf{r}_{\text{TOA}} - \mathbf{d})\right). \tag{2.12}$$

Using the property that $\boldsymbol{\Sigma}_{\text{TOA}}$ is a diagonal matrix, we can rewrite (2.12) as

$$p(\mathbf{r}_{\text{TOA}}) = \frac{1}{(2\pi)^{N_{\text{A}}/2}\prod_{i=1}^{N_{\text{A}}}\sigma_{\text{TOA},i}} \exp\left(-\frac{1}{2}\sum_{i=1}^{N_{\text{A}}}\frac{\left(\hat{d}^{(i)} - d^{(i)}\right)^2}{\sigma^2_{\text{TOA},i}}\right), \tag{2.13}$$

where $\hat{d}^{(i)}$ and $d^{(i)}$ are the estimated and the true ranges for the fixed position of the mobile node $\mathbf{z}_0$, respectively.

TIME-DIFFERENCE-OF-ARRIVAL (TDOA)

The TDOA methods assume that the clocks of the anchors are synchronized. However, it does not require that the mobile node is synchronized with the anchors [57]. Therefore, there is an unknown offset $\Delta\tau$ in the estimated delays, and their model is given by (2.6). The $\Delta\tau$ can be eliminated by selecting an anchor as a reference node and subtracting the estimated delay corresponding to it from the delays estimated for other anchors [58]. Let us denote the reference anchor node with index j and the estimated delay corresponding to it with $\hat{\tau}_1^{(j)}$. Then the TDOA estimate for an anchor i and reference anchor j is given by

$$\hat{\tau}_{\text{D}}^{(i,j)} := \hat{\tau}_1^{(i)} - \hat{\tau}_1^{(j)} = \tau_1^{(i)} - \tau_1^{(j)} + n_\tau^{(i,j)}, \quad \forall i \mid i \neq j, \tag{2.14}$$

where the difference of errors $n_\tau^{(i,j)} = n_\tau^{(i)} - n_\tau^{(j)}$ has a two times larger variance compared to the variance of $n_\tau^{(i)}$ and $n_\tau^{(j)}$ when their variances are equal. The error-free TDOAs are denoted by $\tau_{\text{D}}^{(i,j)}$ and defined as $\tau_{\text{D}}^{(i,j)} = \tau_1^{(i)} - \tau_1^{(j)}, \forall i \mid i \neq j$. Alternatively, the TDOAs $\hat{\tau}_{\text{D}}^{(i,j)}$ can be directly estimated from the channel measurements (2.1) without first estimating the delays $\hat{\tau}_1^{(i)}$, $i = 1,\ldots,N_{\text{A}}$ and then computing them using (2.14). The direct TDOA

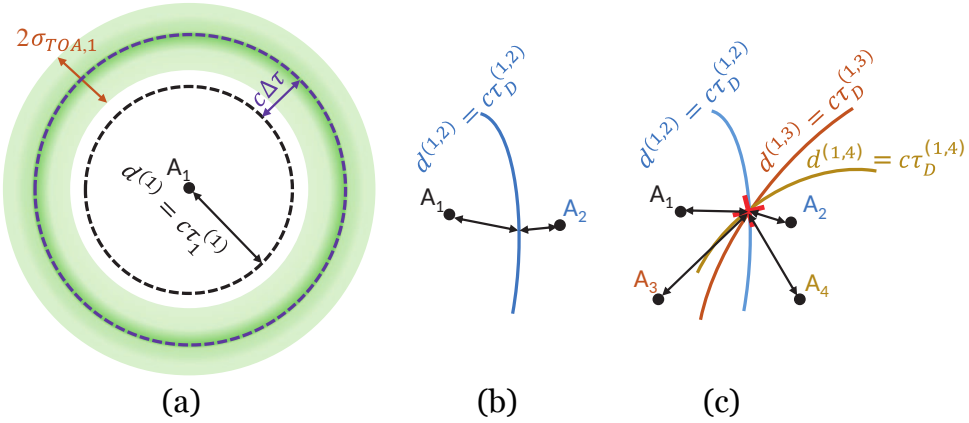

Figure 2.2: Illustration of TDOA-based localization. (a) A black dashed line denotes the circle on which the mobile node is lying, and it is defined by the true range (delay) between the mobile node and the anchor A_1. Due to a clock offset, the estimated ranges (delays) are biased. We illustrate the influence of positive bias by the purple dashed line and influence of the estimation errors by the green colored band. (b) The hyperbola on which the mobile node is lying is defined by the delay (range) differences between the mobile node and the anchors A_1 and A_2. (c) The location of the mobile node is marked by the red cross and it is found as the intersection of three hyperbolas that are defined as the range difference between the mobile node and four anchors, of which anchor A_1 is the reference node.

estimation has better performance compared to two-step delay difference estimation due to lower error variance of the estimates [59, 60].

The difference of ranges that corresponds to reference anchor j and anchors i is denoted by $d^{(i,j)}(\mathbf{z}_0)$ and defined as

$$d^{(i,j)}(\mathbf{z}_0) := d^{(i)}(\mathbf{z}_0) - d^{(j)}(\mathbf{z}_0) = \|\mathbf{z}_0 - \mathbf{z}_i\|_2 - \|\mathbf{z}_0 - \mathbf{z}_j\|_2 , \quad \forall i \mid i \neq j . \tag{2.15}$$

Similar as for TOA estimates, the differences of the ranges $d^{(i,j)}(\mathbf{z}_0)$ are directly proportional to the TDOAs $\tau_{\mathrm{D}}^{(i,j)}$, where the relation is given by

$$d^{(i,j)}(\mathbf{z}_0) := c\tau_{\mathrm{D}}^{(i,j)} , \quad \forall i \mid i \neq j . \tag{2.16}$$

It is easy to see from (2.15) and Fig. 2.2b that each error-free estimate $d^{(i,j)}(\mathbf{z}_0)$ defines a hyperbola in the 2-D space on which the mobile node must lie. Geometrically the position of the mobile node can be determined as the point of intersection of at least three hyperbolas (cf. Fig. 2.2). Therefore, the minimum number of anchors required to determine the position of the mobile node in 2-D space using TDOA estimates is $N_{\mathrm{A}} = 4$. However, in the presence of errors, the hyperbolas do not necessarily need to have an intersection point. This motivates the mathematical formulation of the problem of TDOA-based localization. In what follows, we will show that by using the TDOAs, the location of the mobile node $\mathbf{z}_0$ can be found by solving a set of hyperbolic equations.

Let us consider the most general scenario where the delays $\hat{\tau}_1^{(i)}$ are estimated between the mobile node and every one of the anchors $i = 1, \ldots, N_{\mathrm{A}}$. From these collected

delays we can calculate in total $N_A(N_A-1)/2$ TDOAs $\hat{\tau}_D^{(i,j)}$ if we consider all possible selections of the reference node. However, some of the calculated TDOAs will be redundant, i.e., linear combination of other TDOAs. The number of non-redundant TDOAs is (N_A-1). It is shown in [61] that improved performance of localization can be achieved by first estimating (N_A-1) non-redundant TDOAs from $N_A(N_A-1)/2$ redundant ones using weighted least squares. Then these estimates should be used for location estimation.

Without loss of generality, we will consider anchor j as reference node and denote the estimated non-redundant TDOAs by $\hat{\tau}_D^{(i,j)}$, $\forall i \mid i \neq j$. The difference of ranges are obtained from the TDOA estimates following the relation (2.16) as $\hat{d}^{(i,j)}(\mathbf{z}_0) := c\hat{\tau}_D^{(i,j)}$, $\forall i \mid i \neq j$ and they satisfy the following model

$$\hat{d}^{(i,j)}(\mathbf{z}_0) = d^{(i,j)}(\mathbf{z}_0) + n^{(i,j)}, \quad \forall i \mid i \neq j, \tag{2.17}$$

where $n^{(i,j)} = cn_\tau^{(i,j)}$. These differences of ranges are then collected in the vector $\mathbf{r}_{\text{TDOA}} = [\hat{d}^{(1,j)}, \ldots, \hat{d}^{(N_A,j)}]^T$ of length (N_A-1) that has the following model

$$\mathbf{r}_{\text{TDOA}} = \boldsymbol{f}_{\text{TDOA}}(\mathbf{z}_0) + \mathbf{n}_{\text{TDOA}}, \tag{2.18}$$

where $\mathbf{n}_{\text{TDOA}} = [n^{(1,j)}, \ldots, n^{(N_A,j)}]^T$ is the error vector and

$$\boldsymbol{f}_{\text{TDOA}}(\mathbf{z}_0) := \begin{bmatrix} d^{(1,j)}(\mathbf{z}_0) \\ d^{(2,j)}(\mathbf{z}_0) \\ \vdots \\ d^{(N_A,j)}(\mathbf{z}_0) \end{bmatrix} = \begin{bmatrix} \|\mathbf{z}_0 - \mathbf{z}_1\|_2 - \|\mathbf{z}_0 - \mathbf{z}_j\|_2 \\ \|\mathbf{z}_0 - \mathbf{z}_2\|_2 - \|\mathbf{z}_0 - \mathbf{z}_j\|_2 \\ \vdots \\ \|\mathbf{z}_0 - \mathbf{z}_{N_A}\|_2 - \|\mathbf{z}_0 - \mathbf{z}_j\|_2 \end{bmatrix}. \tag{2.19}$$

Similar to the TOA case, the function $\boldsymbol{f}_{\text{TDOA}}(\mathbf{z}_0)$ is known, and it is parameterized by the unknown position of the mobile node $\mathbf{z}_0$. This is the vector-valued function that collects the error-free differences of ranges given by (2.15).

The problem of location estimation using TDOAs is to estimate $\mathbf{z}_0$ given the $\mathbf{r}_{\text{TDOA}}$ and the model (2.18). The function $\boldsymbol{f}_{\text{TDOA}}(\mathbf{z}_0)$ is nonlinear in the location parameter $\mathbf{z}_0$. Therefore, the estimate of the location $\mathbf{z}_0$ can be obtained by solving the system of nonlinear equations (2.19). To facilitate the algorithm development and performance analysis, we derive the statistical model for the TDOAs.

Assuming that $n^{(i,j)}$ are zero-mean Gaussian random variables, then the vector $\mathbf{n}_{\text{TDOA}}$ is also zero-mean Gaussian distributed. Therefore, we can write $\mathbf{n}_{\text{TDOA}} \sim \mathcal{N}(\mathbf{0}, \boldsymbol{\Sigma}_{\text{TDOA}})$, where $\mathbf{0}$ is the zero vector of length N_A and $\boldsymbol{\Sigma}_{\text{TDOA}}$ is the covariance matrix. Different from the covariance for TOAs, $\boldsymbol{\Sigma}_{\text{TDOA}}$ is not a diagonal matrix as now $\hat{\boldsymbol{\tau}}^{(i,j)}$, $\forall i \mid i \neq j$ are correlated as they are all determined compared to reference node j. Furthermore, the variance of the TDOA $\hat{\boldsymbol{\tau}}^{(i,j)}$ is two times larger compared to the variance of the TOAs from which it is computed when these TOAs have equal variances.

We denote the vector that collects error-free differences of ranges compared to the anchor j by $\mathbf{d}_j$ and it is given as $\mathbf{d}_j = \boldsymbol{f}_{\text{TDOA}}(\mathbf{z}_0)$. Here, the dependency of $\mathbf{d}_j$ on $\mathbf{z}_0$ is dropped as the position $\mathbf{z}_0$ is assumed to be fixed during TDOA estimation. Following from the assumption on the distribution of the error vector $\mathbf{n}_{\text{TDOA}}$, we can write $\mathbf{r}_{\text{TDOA}} \sim$

$\mathcal{N}(\mathbf{d}, \mathbf{\Sigma}_{\text{TDOA}})$. Then, the probability density function (PDF) of the $\mathbf{r}_{\text{TDOA}}$ is given by

$$p(\mathbf{r}_{\text{TDOA}}) = \frac{1}{(2\pi)^{(N_{\text{A}}-1)/2}(\det(\mathbf{\Sigma}_{\text{TDOA}}))^{1/2}} \exp\left(-\frac{1}{2}(\mathbf{r}_{\text{TDOA}} - \mathbf{d}_j)^T \mathbf{\Sigma}_{\text{TDOA}}^{-1}(\mathbf{r}_{\text{TDOA}} - \mathbf{d}_j)\right). \tag{2.20}$$

2

2.3.2. RECEIVED SIGNAL STRENGTH

The received signal strength (RSS) is the power of the received signal at the mobile node. Typically it is assumed that this received power follows an exponentially decaying function, which is parameterized by the power of the signal at the transmitter (anchor node), path loss exponent, and the distance between the mobile and anchor node [62]. This model holds for channels in which multipath effects are small or can be ignored. However, in the presence of multipath effects, the power of the received signal varies significantly with a slight change in position of the mobile node [63]. This phenomenon is known as the multipath channel fading effect, and it is complex to model as a function of the location. Due to these modeling errors, RSS-based localization typically has poor performance. The accuracy of RSS-based methods in multipath channels can be improved by estimating the power of the LOS path instead of the average power of the received signal. However, this requires resolving the LOS path from the MPCs in the time domain. This is the objective of time-delay based localization methods, and generally, these methods outperform RSS-based localization [50]. The advantage of RSS-based localization systems is that compared to TOA and DOA based localization systems, they do not require synchronization or an antenna array, respectively. Therefore, they are simpler to implement.

Let us consider a scenario where the ith anchor sends a signal with power $P_{\text{Tx}}^{(i)}$. This signal propagates through the channel and arrives at the receiver of the mobile node with power $P_0^{(i)}$. Assuming that there is no noise and fading disturbances in the channel, then the influence of the propagation on the received signal power $P_0^{(i)}$ is given by

$$P_0^{(i)} := G^{(i)} P_{\text{Tx}}^{(i)} \left(d^{(i)}(\mathbf{z}_0)\right)^{-\kappa}, \quad i = 1, \ldots, N_{\text{A}}, \tag{2.21}$$

where $G^{(i)}$ captures all the hardware effects on $P_0^{(i)}$, such as antenna heights and gains at the ith anchor and the mobile node, and κ is the path-loss exponent. The path-loss exponent κ depends on the propagation environment, and in general, it takes values from 2 to 5, where $\kappa = 2$ for free-space channels. However, κ does not capture the disturbances in the received signal power $P_0^{(i)}$ that are caused by noise or fading. These disturbances of $P_0^{(i)}$ are known as shadow and multipath fading. Channel measurement campaigns and statistical analysis of acquired measurements have shown that shadow fading on average follows the log-normal distribution [64]. Therefore, the logarithmic model for $P_0^{(i)}$ that takes into account noise and shadowing effects, is given by

$$\log_{10}(P_0^{(i)}) = \log_{10}(G^{(i)}) + \log_{10}(P_{\text{Tx}}^{(i)}) - \kappa \log_{10}\left(d^{(i)}(\mathbf{z}_0)\right) + n_{\text{RSS}}^{(i)}, \quad i = 1, \ldots, N_{\text{A}}. \tag{2.22}$$

where $\log_{10}(\cdot)$ is the logarithm of a variable with base 10 and $n_{\text{RSS}}^{(i)}$ is a Gaussian random variable (in dB) that models shadow fading.

Assuming that the total hardware gains $G^{(i)}$ and the transmitted signal powers $P_{\text{Tx}}^{(i)}, i = 1,\dots,N_{\text{A}}$ are measured in advance and known, we can define the calibrated error-free RSSs as

$$s^{(i)} := \log_{10}(P_0^{(i)}) - \log_{10}(G^{(i)}) - \log_{10}(P_{\text{Tx}}^{(i)}), \quad i = 1,\dots,N_{\text{A}}. \tag{2.23}$$

From (2.22), it follows that the estimated RSSs after calibration of hardware effects satisfy the model given by

$$\hat{s}^{(i)} = -\kappa \log_{10}\left(d^{(i)}(\mathbf{z}_0)\right) + n_{\text{RSS}}^{(i)}, \quad i = 1,\dots,N_{\text{A}}. \tag{2.24}$$

These measurements are collected in the vector $\mathbf{r}_{\text{RSS}} = [\hat{s}^{(1)},\dots,\hat{s}^{(N)}]^T$ that satisfies the following model

$$\mathbf{r}_{\text{RSS}} = \boldsymbol{f}_{\text{RSS}}(\mathbf{z}_0) + \mathbf{n}_{\text{RSS}}, \tag{2.25}$$

where $\mathbf{n}_{\text{RSS}} = [n_{\text{RSS}}^{(1)},\dots,n_{\text{RSS}}^{(N_{\text{A}})}]^T$ and

$$\boldsymbol{f}_{\text{RSS}}(\mathbf{z}_0) := -\kappa \begin{bmatrix} \log_{10}\left(d^{(1)}(\mathbf{z}_0)\right) \\ \log_{10}\left(d^{(2)}(\mathbf{z}_0)\right) \\ \vdots \\ \log_{10}\left(d^{(N_{\text{A}})}(\mathbf{z}_0)\right) \end{bmatrix}. \tag{2.26}$$

The problem of localization using RSSs is to estimate $\mathbf{z}_0$ given the $\mathbf{r}_{\text{RSS}}$ and a known model of the function $\boldsymbol{f}_{\text{RSS}}(\mathbf{z}_0)$. The function $\boldsymbol{f}_{\text{RSS}}(\mathbf{z}_0)$ has a similar form as the function $\boldsymbol{f}_{\text{TOA}}(\mathbf{z}_0)$ in the TOA model as both of them model the relation between the estimates and the ranges. The position $\mathbf{z}_0$ can be obtained by solving a nonlinear system of equations (2.25), and the geometrical interpretation of this problem is the same as shown in Fig. 2.1 for TOA-based localization. The first step to design an algorithm and analyse its efficiency is to statistically model $\boldsymbol{f}_{\text{RSS}}$.

Assuming that $n_{\text{RSS}}^{(i)}$ are zero-mean uncorrelated Gaussian random variables we can write $n_{\text{RSS}}^{(i)} \sim \mathcal{N}(0, \sigma_{\text{RSS},i}^2)$, where $\sigma_{\text{RSS},i}^2$ is the variance of the ith estimate. The vector $\mathbf{n}_{\text{RSS}}$ is then also zero-mean Gaussian distributed, and we can write $\mathbf{n}_{\text{RSS}} \sim \mathcal{N}(\mathbf{0}, \boldsymbol{\Sigma}_{\text{RSS}})$, where $\boldsymbol{\Sigma}_{\text{RSS}}$ is the covariance matrix. The matrix $\boldsymbol{\Sigma}_{\text{RSS}}$ is diagonal, as the estimation errors are assumed to be uncorrelated. Using these assumptions we can derive the distribution for the RSS estimates. Let us first denote the vector that collects error-free RSS estimates with $\mathbf{s} = [s^{(1)},\dots,s^{(N_{\text{A}})}]^T$. This vector satisfies the model $\mathbf{s} = \boldsymbol{f}_{\text{RSS}}(\mathbf{z}_0)$, where we drop its dependency on $\mathbf{z}_0$ as the position of the mobile node is fixed during the collection of the measurements. Using the assumption on $\mathbf{n}_{\text{RSS}}$, we can write $\mathbf{r}_{\text{RSS}} \sim \mathcal{N}(\mathbf{s}, \boldsymbol{\Sigma}_{\text{RSS}})$ and define the probability density function (PDF) of the $\mathbf{r}_{\text{RSS}}$ as

$$\begin{aligned} p(\mathbf{r}_{\text{RSS}}) &= \frac{1}{(2\pi)^{N_{\text{A}}/2}(\det(\boldsymbol{\Sigma}_{\text{RSS}}))^{1/2}} \exp\left(-\frac{1}{2}(\mathbf{r}_{\text{RSS}} - \mathbf{s})^T \boldsymbol{\Sigma}_{\text{RSS}}^{-1}(\mathbf{r}_{\text{RSS}} - \mathbf{s})\right) \\ &= \frac{1}{(2\pi)^{N_{\text{A}}/2}\prod_{i=1}^{N_{\text{A}}}\sigma_{\text{RSS},i}} \exp\left(-\frac{1}{2}\sum_{i=1}^{N_{\text{A}}}\frac{\left(r_{\text{RSS}}^{(i)} + \kappa\log_{10}\left(d^{(i)}(\mathbf{z}_0)\right)\right)^2}{\sigma_{\text{RSS},i}^2}\right), \end{aligned} \tag{2.27}$$

where $\boldsymbol{\Sigma}_{\text{RSS}} = \text{diag}([\sigma_{\text{RSS},1}^2,\dots,\sigma_{\text{RSS},N_{\text{A}}}^2])$.

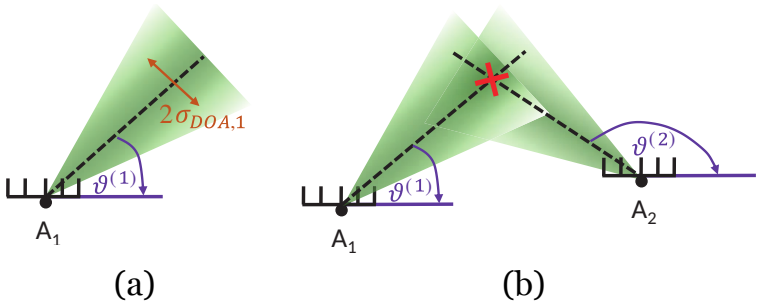

Figure 2.3: Illustration of DOA-based localization. (a) The black dashed line denotes the true direction of arrival of the signal transmitted from the mobile node. The green color indicates the effects of noise in the DOA estimates. (b) The location of the mobile node is marked by the red cross, and it is found as the intersection of the two lines defined by the DOAs estimated for the two anchors.

It is important to note that when the hardware gains $G^{(i)}$ and the powers $P_{\text{Tx}}^{(i)}$ are calibrated at the anchors such that $G^{(i)} = G$ and $P_{\text{Tx}}^{(i)} = P_{\text{Tx}}, \forall i$ but unknown at the mobile node, it is possible to eliminate the unknowns G and P_{Tx} by calculating the received signal strength differences (RSSDs) [65]. The RSSDs are calculated following the same idea used to obtain the TDOAs. The RRSDs are linked to the difference of ranges in the same way as it was the case for TDOAs. The geometrical interpretation for localization using TDOA and RRSD is the same as shown in Fig. 2.2. We will not derive the model for RRSD measurments, as the same steps as used for the TDOA model derivation can be used.

2.3.3. DIRECTION OF ARRIVAL (DOA)

The DOA of a signal is the angle under which that signal arrives at the receiver [66]. Without loss of generality, we will assume that DOAs are collected at a mobile node that is equipped with an antenna array. The location of the mobile node in 2-D space can be determined using DOAs estimated from the signals transmitted by two anchors, as shown in Fig. 2.3. These DOAs can be used to draw direct lines from the anchors to the mobile node. The point of intersection of these lines then represents the location of the mobile node. DOA-based localization does not require clock synchronization between the mobile node and the anchors or between the anchors [67]. This makes DOA localization more attractive for scenarios where synchronization is hard to achieve. However, DOA-based localization requires receivers equipped with antenna arrays that have known orientation. This requirement increases the implementation complexity of DOA-based localization systems. Furthermore, here we assume that mobile nodes are far-field sources, and thus their location can be directly estimated from DOAs. In scenarios where mobile nodes are in the near-field regions of antenna arrays, both DOAs and ranges are necessary to estimate their location, which results in a more complicated problem [68].

Let us consider the scenario of DOA estimation of the signal sent from anchor i to the mobile node. We will consider a scenario of 2-D localization to simplify the relationship between the true DOA $\vartheta^{(i)}$ of this signal and the locations of the anchor $\mathbf{z}_i$ and the mobile

node $\mathbf{z}_0$ as

$$\tan(\vartheta^{(i)}) = \frac{z_y^{(0)} - z_y^{(i)}}{z_x^{(0)} - z_x^{(i)}}, \quad i = 1, \ldots, N_{\mathrm{A}}. \tag{2.28}$$

Geometrically, $\vartheta^{(i)}$ represents the angle between the direction line drawn from anchor i and the mobile node as shown in Fig. 2.3. The estimated DOAs are contaminated by noise and they satisfy the model

$$\hat{\vartheta}^{(i)} := \vartheta^{(i)} + n_{\mathrm{DOA}}^{(i)} = \tan^{-1}\left(\frac{z_y^{(0)} - z_y^{(i)}}{z_x^{(0)} - z_x^{(i)}}\right) + n_{\mathrm{DOA}}^{(i)}, \quad i = 1, \ldots, N_{\mathrm{A}}. \tag{2.29}$$

where $n_{\mathrm{DOA}}^{(i)}$, are zero-mean uncorrelated Gaussian variables with variances $\sigma_{\mathrm{DOA},i}^2$. The DOA estimates are collected in the vector $\mathbf{r}_{\mathrm{DOA}} = [\hat{\vartheta}^{(1)}, \ldots, \hat{\vartheta}^{(N_{\mathrm{A}})}]^T$ that satisfies the following model

$$\mathbf{r}_{\mathrm{DOA}} = \boldsymbol{f}_{\mathrm{DOA}}(\mathbf{z}_0) + \mathbf{n}_{\mathrm{DOA}}, \tag{2.30}$$

where $\mathbf{n}_{\mathrm{DOA}} = [n_{\mathrm{DOA}}^{(1)}, \ldots, n_{\mathrm{DOA}}^{(N_{\mathrm{A}})}]^T$ is the error vector and

$$\boldsymbol{f}_{\mathrm{DOA}}(\mathbf{c}_0) := \begin{bmatrix} \tan^{-1}\left(\frac{z_y^{(0)} - z_y^{(1)}}{z_x^{(0)} - z_x^{(1)}}\right) \\ \tan^{-1}\left(\frac{z_y^{(0)} - z_y^{(2)}}{z_x^{(0)} - z_x^{(2)}}\right) \\ \vdots \\ \tan^{-1}\left(\frac{z_y^{(0)} - z_y^{(N_{\mathrm{A}})}}{z_x^{(0)} - z_x^{(N_{\mathrm{A}})}}\right) \end{bmatrix}. \tag{2.31}$$

The mobile node localization problem using DOA measurements is to estimate $\mathbf{z}_0$ given $\mathbf{r}_{\mathrm{DOA}}$ and the known model for the function $\boldsymbol{f}_{\mathrm{DOA}}(\mathbf{z}_0)$, which is nonlinear in the parameter $\mathbf{z}_0$. We can estimate the location $\mathbf{z}_0$ by solving the nonlinear system of equations (2.30) [69]. However, there are several approaches to arrive at the algorithm and the solution to this problem. The first step to design an algorithm and perform the analysis of its efficiency is to statistically model the estimates $\mathbf{r}_{\mathrm{DOA}}$.

From the assumption that the error vector $n_{\mathrm{DOA}}^{(i)}$ is zero-mean Gaussian distributed, it follows that $\mathbf{n}_{\mathrm{DOA}} \sim \mathcal{N}(\mathbf{0}, \boldsymbol{\Sigma}_{\mathrm{DOA}})$, where $\boldsymbol{\Sigma}_{\mathrm{DOA}}$ is the covariance matrix. As the errors are assumed to be uncorrelated, the matrix $\boldsymbol{\Sigma}_{\mathrm{DOA}}$ is diagonal. Now, using these assumptions, it is straightforward to derive the PDF of the DOA measurements. Let us first denote the vector that collects error-free DOA measurements $\vartheta^{(i)}, i = 1, \ldots, N_{\mathrm{A}}$, as $\boldsymbol{\vartheta} = [\vartheta^{(1)}, \ldots, \vartheta^{(N_{\mathrm{A}})}]^T$. This vector satisfies model $\boldsymbol{\vartheta} = \boldsymbol{f}_{\mathrm{DOA}}(\mathbf{z}_0)$, where we drop its dependency on $\mathbf{z}_0$ as it is fixed during the collection of the measurements. Then, we can write $\mathbf{r}_{\mathrm{DOA}} \sim \mathcal{N}(\boldsymbol{\vartheta}, \boldsymbol{\Sigma}_{\mathrm{DOA}})$ and define the PDF of the $\mathbf{r}_{\mathrm{DOA}}$ as

$$\begin{aligned} p(\mathbf{r}_{\mathrm{DOA}}) &= \frac{1}{(2\pi)^{N_{\mathrm{A}}/2}(\det(\boldsymbol{\Sigma}_{\mathrm{DOA}}))^{1/2}} \exp\left(-\frac{1}{2}(\mathbf{r}_{\mathrm{DOA}} - \boldsymbol{\vartheta})^T \boldsymbol{\Sigma}_{\mathrm{DOA}}^{-1}(\mathbf{r}_{\mathrm{DOA}} - \boldsymbol{\vartheta})\right) \\ &= \frac{1}{(2\pi)^{N_{\mathrm{A}}/2}\prod_{i=1}^{N_{\mathrm{A}}}\sigma_{\mathrm{DOA},i}} \exp\left(-\frac{1}{2}\sum_{i=1}^{N_{\mathrm{A}}}\frac{\left(r_{\mathrm{DOA}}^{(i)} - \vartheta^{(i)}\right)^2}{\sigma_{\mathrm{DOA},i}^2}\right), \end{aligned} \tag{2.32}$$

where $\mathbf{\Sigma}_{\text{DOA}} = \text{diag}([\sigma^2_{\text{DOA},1}, \ldots, \sigma^2_{\text{DOA},N_A}])$.

2.4. ALGORITHMS FOR TWO-STEP LOCALIZATION METHODS

In Section 2.3, we discussed measurements and parameters that can be used as input for two-step localization algorithms, namely we discussed data models for TOA, TDOA, RSS, and DOA measurements. We showed that for all these measurements, their data models can be generalized to $\mathbf{r} = \boldsymbol{f}(\mathbf{z}_0) + \mathbf{n}$ (2.3), where $\mathbf{r}$ is the vector collecting the measurements, $\boldsymbol{f}(\mathbf{z}_0)$ is the vector-valued function of the mobile node position $\mathbf{z}_0$, which is specific for each of the measurements, and $\mathbf{n}$ is the error vector. The exact forms of the vector-valued function $\boldsymbol{f}(\mathbf{z}_0)$ for TOA, TDOA, RSS, and DOA measurements are given in (2.10), (2.19), (2.26), and (2.31), respectively. It can be seen that for all the measurements $\boldsymbol{f}(\mathbf{z}_0)$ is a nonlinear function of the parameter $\mathbf{z}_0$. Therefore, the problem of mobile node location estimation can be formulated as a nonlinear least squares (NLS) or weighted nonlinear least squares (WNLS) optimization problem. These methods use model (2.3) and the known function $\boldsymbol{f}(\mathbf{z}_0)$ to minimize the least squares (LS) or weighted least squares (WLS) cost function constructed from the nonlinear error function given by

$$\mathbf{e}_{\text{nlin}}(\mathbf{z}) = \mathbf{r} - \boldsymbol{f}(\mathbf{z}), \tag{2.33}$$

where $\mathbf{z} = [z_x \;\; z_y]^T$ is the optimization variable.

These nonlinear optimization problems may not have a global solution, and their computational complexity is higher than the complexity of linear least squares (LLS) problems. Another approach to solve problems described by the model (2.3) is to transform the model such that that a nonlinear function $\boldsymbol{f}(\mathbf{z}_0)$ in $\mathbf{z}_0$ is approximated by a linear function in $\mathbf{z}_0$. This process is called linearization of the model (2.3), and the result is the linear model in $\mathbf{z}_0$ given by

$$\mathbf{m} = \mathbf{A}\mathbf{z}_0 + \mathbf{q}, \tag{2.34}$$

where $\mathbf{m}$ and $\mathbf{A}$ are a vector of the measurements after transformation and the known design matrix, respectively, and $\mathbf{q}$ is the transformed error vector. The linear error function for this model is then given by

$$\mathbf{e}_{\text{lin}}(\mathbf{z}) = \mathbf{m} - \mathbf{A}\mathbf{z}. \tag{2.35}$$

Minimizing the LS or WLS cost function of the linear error function $\mathbf{e}_{\text{lin}}(\mathbf{z})$ results in linear least squares (LLS) and weighted linear least squares (WLLS) estimators. Minimizing a linear error function $\mathbf{e}_{\text{lin}}(\mathbf{z})$ in LS or WLS sense has a unique solution, and solving it is less computationally complex compared to nonlinear methods. However, nonlinear estimators outperform linear estimators, especially in the sense of root mean square error (RMSE) for low signal-to-noise (SNR) scenarios.

In what follows, we will illustrate derivations of localization algorithms based on nonlinear and linear cost functions. In this thesis, we focus on time-delay estimation of multipath channel parameters for localization. Therefore, we select to illustrate derivations of the algorithms for localization using the example of TOA measurements. However, we already showed that all the other measurements that we have discussed before, such as TDOA, RSS, DOA, share the same underlying data model (2.3) as TOA measure-

ments. Therefore, this derivation can be used as a guideline to derive the algorithms for localization based on these measurements.

2.4.1. NONLINEAR ESTIMATION

We saw that nonlinear algorithms obtain the location by solving NLS or WNLS optimization problems, which results in NLS or Maximum Likelihood (ML) estimators, respectively. The cost functions used in these optimization problems are multi-modal, and therefore, the convergence to the global solution is not guaranteed. The NLS estimator is simpler than the ML estimator, and it does not require information about noise statistics. However, the ML estimator has better performance in terms of RMSE as it takes into account the differences in the measurement errors by applying weights to the errors according to the noise statistics. The ML estimator is optimal in the sense that it is unbiased, and it asymptotically achieves the lower bound on the RMSE of the estimated parameter, i.e., the Cramér Rao Bound (CRB), when the number of measurements is increasing.

NONLINEAR LEAST SQUARES (NLS) ESTIMATION:

The NLS algorithms estimate the location by finding the minimum of the LS cost function constructed from the error function (2.33), where the function $\boldsymbol{f}(\mathbf{z})$ is selected depending on the measurements that are used as input to the algorithm. We will illustrate the NLS algorithm using TOA measurements as example.

NLS TOA Localization: Using the error function (2.33) and the function (2.10) that relates TOA measurements to the position, we can define the NLS cost function $J_{\text{NLS,TOA}}(\mathbf{z})$ as

$$\begin{aligned} J_{\text{NLS,TOA}}(\mathbf{z}) &:= \left(\mathbf{r}_{\text{TOA}} - \boldsymbol{f}_{\text{TOA}}(\mathbf{z})\right)^T \left(\mathbf{r}_{\text{TOA}} - \boldsymbol{f}_{\text{TOA}}(\mathbf{z})\right) \\ &= \sum_{i=1}^{N} \left(\hat{d}^{(i)} - d^{(i)}(\mathbf{z})\right)^2 . \end{aligned} \tag{2.36}$$

The location estimate is obtained by finding $\mathbf{z}$ that minimizes the cost function $J_{\text{NLS,TOA}}(\mathbf{z})$, that is by solving the following optimization problem

$$\hat{\mathbf{z}}_0 = \underset{\mathbf{z}}{\operatorname{argmin}} \; J_{\text{NLS,TOA}}(\mathbf{z}) . \tag{2.37}$$

Solving this optimization problem is possible by using iterative optimization methods such as Gauss-Newton, Levenberg-Marquardt, and steepest descent. All of these methods require as input an initial estimate of the location $\hat{\mathbf{z}}_0^{(0)}$ and then they perform a search for the local minimum close to the initial estimate. If the initial estimate is close to the true solution $\mathbf{z}_0$, then these methods will converge to it. Otherwise, they will converge to $\hat{\mathbf{z}}_0$ that corresponds to the local minimum of the cost function. Other approaches for solving the problem (2.37) are based on a search for the global minimum using a grid search or random search techniques such as genetic algorithms [70] or particle swarm optimization [71].

MAXIMUM LIKELIHOOD (ML) ESTIMATION:

When deriving the ML algorithm, it is assumed that the probability distribution of the errors in the measurements is known. Then the objective of the ML algorithms is to find $\mathbf{z}$ that maximizes the likelihood functions of the TOA (2.12), TDOA (2.20), RSS (2.27), and DOA (2.32) measurements, respectively. Therefore, we can define the ML estimator as

$$\hat{\mathbf{z}} = \underset{\mathbf{z}}{\operatorname{argmax}} \; p(\mathbf{r}; \mathbf{z}), \tag{2.38}$$

where $p(\mathbf{r};\mathbf{z})$ denotes the PDF of measurements. Typically, we consider that errors are zero-mean Gaussian distributed, and therefore the PDFs have exponential models. Finding the maximum of a PDF requires computing its gradient, and this can be complicated if computed directly from the PDF with exponential form. We use the fact that the logarithm is monotonically increasing on $\mathbb{R}_+$ and redefine the ML estimator as

$$\hat{\mathbf{z}} = \underset{\mathbf{z}}{\operatorname{argmax}} \; \ln p(\mathbf{r}; \mathbf{z}). \tag{2.39}$$

This formulation is equivalent to the one in (2.38), as the location of the extremes of the function will not change. When the noise is assumed to be zero-mean Gaussian distributed, the resulting estimator is the weighted version of the previously discussed NLS estimator. Next, we will illustrate the derivation of the ML estimator for location estimation from the TOA measurements. This procedure is general, and the same steps can be followed to derive estimators for other discussed types of measurements.

ML TOA Localization: We apply the logarithm operation to the PDF for the TOA measurements (2.12) and write the result as [72]

$$\ln p(\mathbf{r}_{\text{TOA}}; \mathbf{z}) = \ln \frac{1}{(2\pi)^{N/2}(\det(\boldsymbol{\Sigma}_{\text{TOA}}))^{1/2}} - \frac{1}{2}\left(\mathbf{r}_{\text{TOA}} - \boldsymbol{f}(\mathbf{z})\right)^T \boldsymbol{\Sigma}_{\text{TOA}}^{-1}\left(\mathbf{r}_{\text{TOA}} - \boldsymbol{f}(\mathbf{z})\right). \tag{2.40}$$

We can see that only the second term in this expression depends on $\mathbf{z}$. Therefore, maximizing $\ln p(\mathbf{r}_{\text{TOA}}; \mathbf{z})$ with respect to $\mathbf{z}$ is equivalent to minimizing the second term in (2.40). We use this to define the ML location estimator as

$$\hat{\mathbf{z}}_0 = \underset{\mathbf{z}}{\operatorname{argmin}} \; \left(\mathbf{r}_{\text{TOA}} - \boldsymbol{f}(\mathbf{z})\right)^T \boldsymbol{\Sigma}_{\text{TOA}}^{-1}\left(\mathbf{r}_{\text{TOA}} - \boldsymbol{f}(\mathbf{z})\right). \tag{2.41}$$

Using the cost function we can define the ML estimator as

$$\hat{\mathbf{z}}_0 = \underset{\mathbf{z}}{\operatorname{argmin}} \; J_{\text{ML,TOA}}(\mathbf{z}). \tag{2.42}$$

From (2.41) the ML cost function immediately follows and it is given as

$$\begin{aligned} J_{\text{ML,TOA}}(\mathbf{z}) &= \left(\mathbf{r}_{\text{TOA}} - \boldsymbol{f}(\mathbf{z})\right)^T \boldsymbol{\Sigma}_{\text{TOA}}^{-1}\left(\mathbf{r}_{\text{TOA}} - \boldsymbol{f}(\mathbf{z})\right) \\ &= \sum_{i=1}^{N} \frac{\left(\hat{d}^{(i)} - d^{(i)}\right)^2}{\sigma_{\text{TOA},i}^2}. \end{aligned} \tag{2.43}$$

Comparing the cost functions $J_{\text{ML,TOA}}(\mathbf{z})$ (2.43) and $J_{\text{NLS,TOA}}(\mathbf{z})$ (2.36), we observe that for the zero-mean Gaussian assumption on the distribution of the measurements

$\mathbf{r}_{\text{TOA}}$, $J_{\text{ML,TOA}}(\mathbf{z})$ is the weighted version of the $J_{\text{NLS,TOA}}(\mathbf{z})$ (2.36). Therefore, we can conclude that the ML estimator is a generalized version of the NLS estimator. The ML estimator is equivalent to the NLS estimator when the noise covariance matrix $\mathbf{\Sigma}_{\text{TOA}}$ is proportional to the identity matrix, that is when the variance of the noise in the TOA measurements is equal for all anchors. The same optimization methods for solving NLS problems can be used to solve the WNLS problem given in (2.42). However, now the noise covariance matrix $\mathbf{\Sigma}_{\text{TOA}}$ is assumed to be known or estimated prior to ML location estimation.

2.4.2. LINEAR ESTIMATION METHODS

We already mentioned that the basic idea behind linear location estimation methods is to linearize the nonlinear model of the measurements given in (2.9), (2.18), (2.25), and (2.30) [48]. Then the LS and WLS cost functions constructed from the linear error function (2.35) are unimodal, and it is guaranteed that optimization methods will find their global minimum. The resulting estimator will depend on the selected cost function used in the optimization. Minimizing the LS cost function of the errors will result in the LLS location estimator while minimizing the WLS cost function of the error will lead to the WLLS location estimator. Another approach to estimate the location from the linearized model of the measurements is to use subspace techniques to solve for the unknown parameter $\mathbf{z}$ from the set of linear measurement equations. However, we will not discuss these methods in this thesis. In what follows, we will illustrate derivations of LLS and WLLS location estimators.

LINEAR LEAST SQUARES (LLS) ESTIMATION:

To derive the LLS estimators, we need to linearize the functions that are given in the measurement models (2.9), (2.18), (2.25) and (2.30), with respect to the unknown parameter $\mathbf{z}$. Then the location $\mathbf{z}$ can be estimated using the ordinary LS method. We will illustrate the derivation of the LLS location estimator using the example of TOA measurements.

LLS TOA Localization: To linearize the model for the TOA measurements, we first define the squared range estimates using the model given in (2.8) as

$$\left(\hat{d}^{(i)}\right)^2 = \left(d^{(i)}(\mathbf{z}_0)\right)^2 + \left(n^{(i)}\right)^2 + 2d^{(i)}n^{(i)}, \quad i = 1,\ldots,N_{\text{A}}. \tag{2.44}$$

Using the definition of the Euclidian distance (2.4) we can express the squared ranges as a function of the unknown coordinates $\mathbf{z}_0 = [z_x^{(0)}, z_y^{(0)}]^T$ of the mobile node as

$$\left(\hat{d}^{(i)}\right)^2 = (z_x^{(0)} - z_x^{(i)})^2 + (z_y^{(0)} - z_y^{(i)})^2 + q^{(i)}, \quad i = 1,\ldots,N_{\text{A}}, \tag{2.45}$$

where $q^{(i)} = \left(n^{(i)}\right)^2 + 2d^{(i)}n^{(i)}$. Next, we rearrange the terms in (2.45) to separate the unknowns from the knowns as

$$\left(\hat{d}^{(i)}\right)^2 - \left(z_x^{(i)}\right)^2 - \left(z_y^{(i)}\right)^2 = -2z_x^{(i)}z_x^{(0)} - 2z_y^{(i)}z_y^{(0)} + \left(z_x^{(0)}\right)^2 + \left(z_y^{(0)}\right)^2 + q^{(i)}, \quad i = 1,\ldots,N_{\text{A}}. \tag{2.46}$$

There are two approaches on how to write a linear model for these equations. One approach is to select one of these equations and subtract it from the others to cancel the

term $\left(z_x^{(0)}\right)^2+\left(z_y^{(0)}\right)^2$. However, the better approach that will be illustrated here is to define $\left(z_x^{(0)}\right)^2+\left(z_y^{(0)}\right)^2$ as a new unknown variable γ and estimate it together with $z_x^{(0)}$ and $z_y^{(0)}$. Then the set of the equations (2.46) can be rewritten as

$$\left(\hat{d}^{(i)}\right)^2-\left(z_x^{(i)}\right)^2-\left(z_y^{(i)}\right)^2=-2z_x^{(i)}z_x^{(0)}-2z_y^{(i)}z_y^{(0)}+\gamma+q^{(i)},\quad i=1,\ldots,N_{\mathrm{A}}. \tag{2.47}$$

Now, we can write the model for these equations as

$$\mathbf{m}:=\mathbf{A}\mathbf{b}+\mathbf{q}, \tag{2.48}$$

where

$$\mathbf{m}=\begin{bmatrix}\left(\hat{d}^{(1)}\right)^2-\left(z_x^{(1)}\right)^2-\left(z_y^{(1)}\right)^2\\ \left(\hat{d}^{(2)}\right)^2-\left(z_x^{(2)}\right)^2-\left(z_y^{(2)}\right)^2\\ \vdots\\ \left(\hat{d}^{(N_A)}\right)^2-\left(z_x^{(N_A)}\right)^2-\left(z_y^{(N_A)}\right)^2\end{bmatrix},\qquad \mathbf{q}=\begin{bmatrix}q^{(1)}\\ q^{(2)}\\ \vdots\\ q^{(N_A)}\end{bmatrix}$$

$$\mathbf{A}=\begin{bmatrix}-2z_x^{(1)} & -2z_y^{(1)} & 1\\ -2z_x^{(2)} & -2z_y^{(2)} & 1\\ \vdots & \vdots & \vdots\\ -2z_x^{(N_A)} & -2z_y^{(N_A)} & 1\end{bmatrix},\quad \text{and}\qquad \mathbf{b}=\begin{bmatrix}z_x^{(0)}\\ z_y^{(0)}\\ \gamma\end{bmatrix}.$$

Assuming that $n^{(i)}, i=1,\ldots,N_{\mathrm{A}}$, are zero-mean Gaussian distributed random variables with relatively small variances such that $\mathbb{E}(\mathbf{q})\approx\mathbf{0}$, we can approximate (2.48) as

$$\mathbf{m}\approx\mathbf{A}\mathbf{b}. \tag{2.49}$$

Using this approximation, we can define the LS cost function for the linearized model of TOA measurements as

$$J_{\mathrm{LLS,TOA}}(\mathbf{b})=(\mathbf{A}\mathbf{b}-\mathbf{m})^T(\mathbf{A}\mathbf{b}-\mathbf{m}). \tag{2.50}$$

The LS estimator of vector $\mathbf{b}$ is then given by

$$\hat{\mathbf{b}}=\underset{\mathbf{b}}{\operatorname{argmin}}\ J_{\mathrm{LLS,TOA}}(\mathbf{b}). \tag{2.51}$$

The cost function $J_{\mathrm{LLS,TOA}}(\mathbf{b})$ is unimodal and therefore this optimization problem has a unique solution which is easy to compute. In fact this problem has the closed form solution given by

$$\hat{\mathbf{b}}=\left(\mathbf{A}^T\mathbf{A}\right)^{-1}\mathbf{A}^T\mathbf{m}. \tag{2.52}$$

Finally, the LS location estimate $\hat{\mathbf{z}}_0$ is obtained by selecting the first and second entries of $\hat{\mathbf{b}}$ as $\hat{z}_x^{(0)}$ and $\hat{z}_y^{(0)}$, respectively.

WEIGHTED LINEAR LEAST SQUARES (WLLS) ESTIMATION:

The LLS estimator given in (2.52) is not statistically efficient when errors in the measurements (2.48) are not independent and identically distributed. The performance of estimation can be improved by constructing the weighted least squares cost function from the linear error function. We will illustrate the derivations of the WLLS estimation for the example of TOA measurements.

WLLS TOA Localization: We start from the LLS cost function (2.50) and define the WLLS cost function by including the weighting matrix $\mathbf{W}$ in it as

$$J_{\text{WLLS,TOA}}(\mathbf{b}) = (\mathbf{Ab}-\mathbf{m})^T \mathbf{W} (\mathbf{Ab}-\mathbf{m}) \,. \tag{2.53}$$

The matrix $\mathbf{W}$ is typically symmetric and its choice will influence the statistical performance of the estimator. The WLLS location estimator is then given by

$$\hat{\mathbf{b}} = \underset{\mathbf{b}}{\operatorname{argmin}} \; J_{\text{WLLS,TOA}}(\mathbf{b}) \,. \tag{2.54}$$

This optimization problem has a closed form solution given by

$$\hat{\mathbf{b}} = \left(\mathbf{A}^T \mathbf{W} \mathbf{A}\right)^{-1} \mathbf{A}^T \mathbf{W} \mathbf{m} \,. \tag{2.55}$$

Computing the weighting matrix from the noise covariance matrix as $\mathbf{W} = \mathbf{\Sigma}_{\mathbf{q}}^{-1}$, where $\mathbf{\Sigma}_{\mathbf{q}} = \mathbb{E}(\mathbf{q}\mathbf{q}^T)$, results in the best linear unbiased estimator (BLUE) [72]. The BLUE estimator is unbiased and has the smallest variance of the estimation error of all the linear estimators. Likewise, as for LLS estimator, $\hat{z}_x^{(0)}$ and $\hat{z}_y^{(0)}$ directly follow from $\hat{\mathbf{b}}$.

2.4.3. DIRECT LOCATION ESTIMATION (DLE)

The direct location estimation (DLE) methods treat the location estimation from the received signals differently than the two-step methods. These methods estimate the location $\mathbf{z}_0$ directly from the measurements of the received signals $y_i(t), i = 1,...,N_{\text{A}}$, without the intermediate step of first estimating specific parameters of the LOS path [73]. The DLE methods start from the parametric model for the received signals where the received signals are expressed as a nonlinear function of the position $\mathbf{z}_0$ [74]. We will illustrate DLE for the simplified example of localization using single antenna narrowband transceivers. Due to the narrowband assumption, we model radio signal propagation with a single path LOS channel model. Therefore, the signals from the anchors as received at the mobile node are given by

$$y_i(t) := \alpha^{(i)} x(t-\tau^{(i)}) + n^{(i)}, \quad i = 1,\ldots,N_A \,, \tag{2.56}$$

where $n^{(i)}$ are zero-mean uncorrelated Gaussian distributed random variables with variances $\sigma_i^2, i = 1,\ldots,N_{\text{A}}$. We can write the delays of the LOS paths as $\tau^{(i)} = \|\mathbf{z}_0 - \mathbf{z}_i\|_2 / c$. Then the model for the received signal can be written as

$$y_i(t;\mathbf{z}_0) := \alpha^{(i)} x\left(t - \frac{\|\mathbf{z}_0 - \mathbf{z}_i\|_2}{c}\right) + n^{(i)}, \quad i = 1,\ldots,N_A \,. \tag{2.57}$$

Assuming that for each received anchor signal $y_i(t;\mathbf{z}_0)$, N samples are collected in the vector $\mathbf{y}^{(i)} = [y^{(i)}[0], y^{(i)}[1], \ldots, y^{(i)}[N-1]]^T$ and using the assumption made for the distribution of the noise, the PDFs for the received signals are given by

$$p(\mathbf{y}^{(i)};\, \mathbf{z}_0) = \frac{1}{\left(2\pi\sigma_i^2\right)^{N/2}} \exp\left(-\frac{1}{2} \sum_{i=1}^{N} \frac{\left(y^{(i)}[n] - \alpha^{(i)} x\left(nT_s - \frac{\|\mathbf{z}_0 - \mathbf{z}_i\|_2}{c} \right) \right)^2}{\sigma_i^2} \right), \tag{2.58}$$

where T_s is the sampling interval. When the signals $\mathbf{y}^{(i)}, i = 1, \ldots, N_A$, are independent and identically distributed (i.i.d), then their join PDF is

$$p\left(\mathbf{y}^{(1)}, \mathbf{y}^{(2)}, \ldots, \mathbf{y}^{(N_A)};\, \mathbf{z}_0\right) = \prod_{i=1}^{N_A} p(\mathbf{y}^{(i)}; \mathbf{z}_0)\,. \tag{2.59}$$

The ML estimator for DLE now becomes

$$\hat{\mathbf{z}}_0 = \underset{\mathbf{z}}{\operatorname{argmin}}\ \ p\left(\mathbf{y}^{(1)}, \mathbf{y}^{(2)}, \ldots, \mathbf{y}^{(N_A)}; \mathbf{z}\right). \tag{2.60}$$

where $\mathbf{z}$ is the optimization variable. By estimating location directly from signals received from all anchors, the DLE methods introduce an additional constraint in the location estimation problem that all the measurements of the received signals must be a function of the unknown location [73]. This constraint is not present in two-step localization methods since measurements such as TOA, TDOA, or DOA are obtained for each anchor separately. Then afterward, these measurements are used to estimate the unknown location. This is the reason why the DLE methods outperform the two-step localization methods. However, using the raw signal measurements from all anchors to estimate unknown locations in the single-step results in a complex optimization problem whose complexity increases significantly with an increase of the number of multipath components in the channel [75]. Therefore, these methods are typically applied for localization using narrowband signals or scenarios where multipath propagation can be ignored [76].

2.5. CONCLUSIONS

In this section, we discussed methods for location estimation using radio signals. We showed that multipath channel parameters encode the location information. We then presented two-step and direct location estimation methods in Sections 2.3 and 2.4.3, respectively.

In the two-step localization approaches, first, a parameter of the LOS path is estimated from the received signal measurements $y_i(t), i = 1, \ldots, N_A$ (2.2). Then the relation between the estimated parameter $\mathbf{r}$ and the mobile node location $\mathbf{z}_0$ is used to define a nonlinear system of equations (2.3). At last, the location $\mathbf{z}_0$ is estimated by finding the solution to this nonlinear system of equations. We did not discuss two-step approaches where multiple location parameters are used to estimate the location. For example, these methods combine TOA and DOA [77, 78, 79], TDOA and DOA [80] or RSS and DOA [81] measurements to estimate the location. These methods improve the accuracy of

localization compared to single parameter localization methods. However, at the same time, they result in a more complex nonlinear optimization problem.

In direct location estimation methods, the received signal measurements $y_i(t)$ or estimated multipath channel response $h^{(i)}(t), i = 1,\ldots,N_A$, are directly parametrized by the location parameter $\mathbf{z}$. The location is directly estimated from the collected measurements, without the intermediate step of first estimating a specific parameter and then estimating the location based on this parameter. These methods have a large computational complexity and are typically not practical for localization in multipath environments.

3

MULTIPATH TIME-DELAY ESTIMATION AND SUPER-RESOLUTION PROBLEMS

"Mathematics is the language in which God has written the universe."

— Galileo Galilei

3.1. INTRODUCTION

THIS chapter introduces the problem of multipath channel time-delay estimation for localization and provides necessary theoretical preliminaries and terminology used throughout the thesis. First, we discuss the signal model for multipath channel measurements and formulate the problem of time-delay estimation for localization. We start from the general parametric multipath channel model (2.1) given in Chapter 2 and tailor it to the problem of time-delay estimation with single antenna wireless transceivers. The resulting model is known from spectral estimation and appears in several other popular applications such as underwater communications, radar, and ultrasound imaging, to name a few. The parameter estimation for this model is well studied in the past using popular signal processing frameworks related to spectral estimation such as maximum likelihood [72], subspace-based [82], and compressive sensing-based [83] estimation. We provide an introduction to these signal processing frameworks and discuss how they can be applied of our problem. In particular, we focus on methods for parametric time-delay estimation and provide an overview of previous works related to this thesis.

3.2. TIME-DELAY ESTIMATION FOR LOCALIZATION

In Chapter 2, we introduced a general parametric signal model for multipath channel measurements (2.1) and discussed the parameters that encode the location information. We saw that the time-delays $\tau_k^{(i)}$, complex path amplitudes $\alpha_k^{(i)}$, and directions of arrival $\vartheta_k^{(i)}$, $k = 1,\ldots,K$, of the MPCs present in the channel between anchor i and the mobile node encodes the mobile node's location and those of the surrounding RF reflectors. To estimate the location of the mobile node using two-step localization approaches, we first need to estimate the parameters of the multipath channels between the mobile node and several anchors. The number of multipath channels whose parameters need to be estimated depends on the formulation of the localization problem, and this has been discussed in the previous chapter. This thesis focuses on the problem of time-delay estimation for TOA and TDOA based localization using single antenna RF transceivers. In particular, we focus on the estimation of the time-delay of the LOS path $\tau_1^{(i)}$ which, up to a possible bias, directly relates to the range between the mobile node and anchor i. The causes of a bias can be imperfect calibration of the RF transceivers [84] or failure to resolve all the MPCs present in the channel [85]. Therefore, to accurately estimate the time-delay of the LOS path, MPCs present in the channel must be resolved and their time-delays estimated as well. The accuracy of time-delay estimation depends on the bandwidth of the training signals used for the channel probing and the signal-to-noise ratio (SNR) at the receiver. High accuracy estimation can be achieved if multipath channel measurements are collected with large bandwidth training signals. However, most practical RF transceivers do not have large instantaneous frequency bandwidth, making high-resolution time-delay estimation challenging. In this thesis, we propose multipath channel acquisition methods and algorithms that can solve this problem.

We start from the general multipath channel model (2.1) and tailor it to the problem of time-delay estimation using single antenna RF transceivers. To simplify notation in the rest of this thesis, we drop the dependency of the channel parameters on index i. We

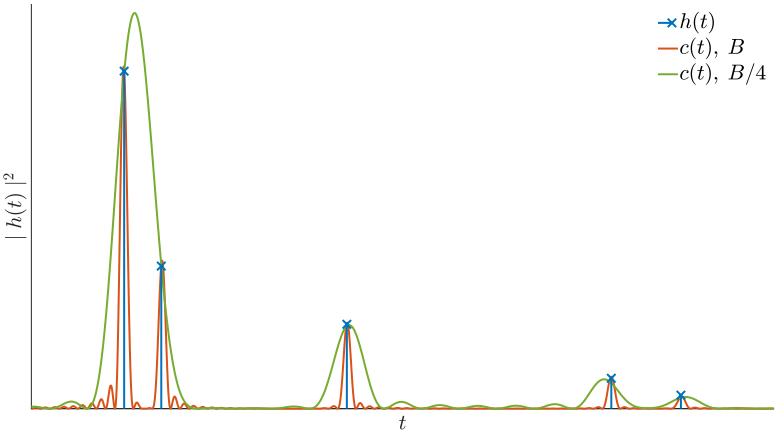

Figure 3.1: The true multipath channel impulse response $h(t)$ and the compound impulse response $c(t)$ after filtering by the low-pass filter. The compound impulse response is generated for two different bandwidths of the low-pass filter.

will implicitly assume that we estimate time-delays between the mobile node and multiple anchors when discussing location estimation. The signal model (2.1), after tailoring to our problem and notation simplification, is given by

$$h(t) = \sum_{k=1}^{K} \alpha_k \delta(t - \tau_k), \tag{3.1}$$

where $\tau_k \in \mathbb{R}_+$ is the time-delay of the kth resolvable multipath component and $\alpha_k \in \mathbb{C}$ is its complex path amplitude. In practice, when we estimate time-delays, we do not have direct access to the samples of $h(t)$. We first need to probe the channel with the training signal and then estimate $h(t)$ from the discrete samples of the noise corrupted received signal $y(t)$. In the acquisition process, the bandwidth of the training signals is limited due to the limited bandwidth of the transceiver's RF front-end and sampling rates. We model these effects of bandwidth limitation using an ideal low-pass filter $g(t)$ that has continuous-time Fourier transform (CTFT) $G(\omega)$ limited to the interval $[-\pi B, \pi B]$, where B is the bandwidth. We can write $G(\omega)$ as

$$G(\omega) = \begin{cases} 1, & \omega \in [-\pi B, \pi B] \\ 0, & \text{otherwise}. \end{cases} \tag{3.2}$$

The received signal before sampling is then given by

$$y(t) = x(t) * c(t) + q(t), \tag{3.3}$$

where $c(t) = g(t) * h(t)$ is the compound impulse response of the multipath channel and low-pass filter, and $q(t)$ represents a zero-mean Gaussian noise process. Considering the assumption on $g(t)$, we can write the compound impulse response $c(t)$ as

$$c(t) = \sum_{k=1}^{K} \alpha_k \cdot B\text{sinc}\left[B(t - \tau_k)\right]. \tag{3.4}$$

Therefore, the time-delay parameters are estimated from the samples of $y(t)$, where the multipath channel is represented by its low-pass approximation $c(t)$ that has bandwidth limited to $[-B/2, B/2]$. Figure 3.1 shows the multipath channel impulse response $h(t)$ and the compound impulse responses $c(t)$ for two different bandwidths of the low-pass filter $g(t)$ when there are $K = 5$ paths in the channel. We can see that after low-pass filtering, the MPCs are smoothed by the sinc kernel of the filter. When MPCs are sufficiently separated in the time domain compared to the bandwidth of the low-pass filter, we can resolve them from the compound response $c(t)$ and accurately determine their time-delays. This scenario is represented by the orange color in Fig. 3.1. However, if we decrease the bandwidth of the filter, the width of the sinc kernel increases, and MPCs that arrive close by are superimposed over each other and form a single MPC. This scenario is represented by the green color in Fig. 3.1, and we can see that the first two paths are now represented as a single path. Therefore, these two paths are not directly resolvable from Fig. 3.1. On the other hand, in this scenario, the last two paths are resolvable, but they interfere with each other, and the maxima of their powers do not correspond to the true time-delays.

From this example, it is obvious that the ability to detect a number of MPCs present in the channel and estimate their time-delays depends on the separation of their delays and the bandwidth of the channel measurements. The minimum time-delay between two MPCs that is resolvable by an algorithm will be called the resolution of the algorithm. In this example, we did not consider the influence of noise in the measurements, which makes time-delay estimation even more challenging. The influence of noise on the estimation will be illustrated in the next section. In this thesis, we are interested in practical approaches for acquiring multipath channel measurements using off-the-shelf RF transceivers and algorithms that support high-resolution time-delay estimation from these measurements.

Using the property of the time-frequency duality, we can equivalently formulate the problem of the time-delay estimation in the frequency domain. The continuous-time Fourier transform (CTFT) of $h(t)$ is given by

$$H(\omega) = \sum_{k=1}^{K} \alpha_k e^{-j\omega\tau_k}, \tag{3.5}$$

where ω represents angular frequency. The channel frequency response $H(\omega)$ resembles the model whose parameter estimation has been treated extensively in spectral estimation [82]. The multipath channel frequency response (3.5) is modeled as a sum of complex exponentials, and the objective of spectral estimation is to estimate the powers $|\alpha_k|^2$ and their corresponding frequencies. The estimated frequencies are directly related to the time-delays of the MPCs $\tau_k, k = 1, \ldots, K$. Therefore, the problem of detecting the frequencies with the highest power from the samples of $H(\omega)$ coincides with the problem of detecting MPCs and estimating their time-delays. This means that the objective of time-delay estimation in the frequency domain and the objective of spectral estimation are the same. This is an important signal processing problem and has been studied in several signal processing frameworks such as subspace and sparsity-based estimation.

In the next section, we connect our problem to similar problems in other useful ap-

plications such as optics, radar, or ultrasound imaging. We then use the example from single-molecule microscopy [86] to illustrate the challenges set by noise and limited resolution of the measurement devices on the accurate estimation of the parameters.

3.3. SUPER-RESOLUTION PROBLEMS

The problem of super-resolution parameter estimation arises in many signal processing applications that share the goal of overcoming the sensors' resolution limit in order to increase the resolution of parameter estimation. Therefore, this problem is important for applications such as radar [87, 88, 89], microscopy, ultrasound imaging [90, 91], wireless [92, 93, 94] and underwater communications [95], to name a few. In these applications, sensors typically limit the temporal or spatial resolution of the acquired signal due to various limitations introduced by physics or hardware, such as the numerical aperture of a microscope, the wavelength of the electromagnetic waves, or the sampling rate of the analog-to-digital converter [96]. Although the physical phenomena of interest in these applications are different, the acquired signal is typically modeled as a linear superposition of translated and modulated versions of some template function (e.g., a sinc or a point spread function). The challenge to increase the resolution of estimation of the translation (e.g., delay or location) or modulation (e.g., frequency offset or Doppler) parameters is known as the super-resolution problem.

Next, We will shortly detour from our original problem to illustrate the super-resolution problem and the impact of noise and limited resolution on it using an example of the recovery of the point sources in single-molecule microscopy [97]. This example is more intuitive for illustration as we can use images to illustrate the effects of noise and limited resolution. At the same time, it is an extension of our problem to two-dimensional (2D) parameter estimation.

In single-molecule microscopy, the goal is to estimate the location of small fluorescing molecules, i.e., point sources, from the optical signals observed by a microscope. This is a challenging problem as the molecules are typically closely spaced while the resolution of the microscope is limited by the inverse of the wavelength of the optical signal that is observed. The limited resolution of the microscope is due to the diffraction limit of light, which causes blurring effects in the observed image. This effect is similar to the effect of limited time-delay resolution of a receiver on RF signals.

To illustrate these effects, we perform an experiment where we generate a 300×300 samples image as shown in Fig. 3.2a. This image has four quarters with different point source densities where: (i) the top-left quarter has 4, (ii) the top-right quarter has 12, (iii) the bottom-left has 16, and (iv) the bottom-right has 20 sources. Figures 3.2b and 3.2c illustrate the effects of limited resolution of the microscope on the observed sources, where in Fig. 3.2c more blurring is introduced. We introduce blurring by convolving the ground truth image shown in Fig. 3.2a with Gaussian kernels to generate images shown in Figures 3.2b and 3.2c. By comparing the ground truth with Figures 3.2b and 3.2c we can notice that due to the limited resolution and blurring we are unable to resolve closely spaced source by the bare eye in Fig. 3.2c. To illustrate the effect of noise we generate Fig. 3.2d by adding Gaussian noise to Fig. 3.2a. We then introduce blurring on Fig. 3.2d to generate Fig. 3.2e. To illustrate the joint effects of a limited resolution

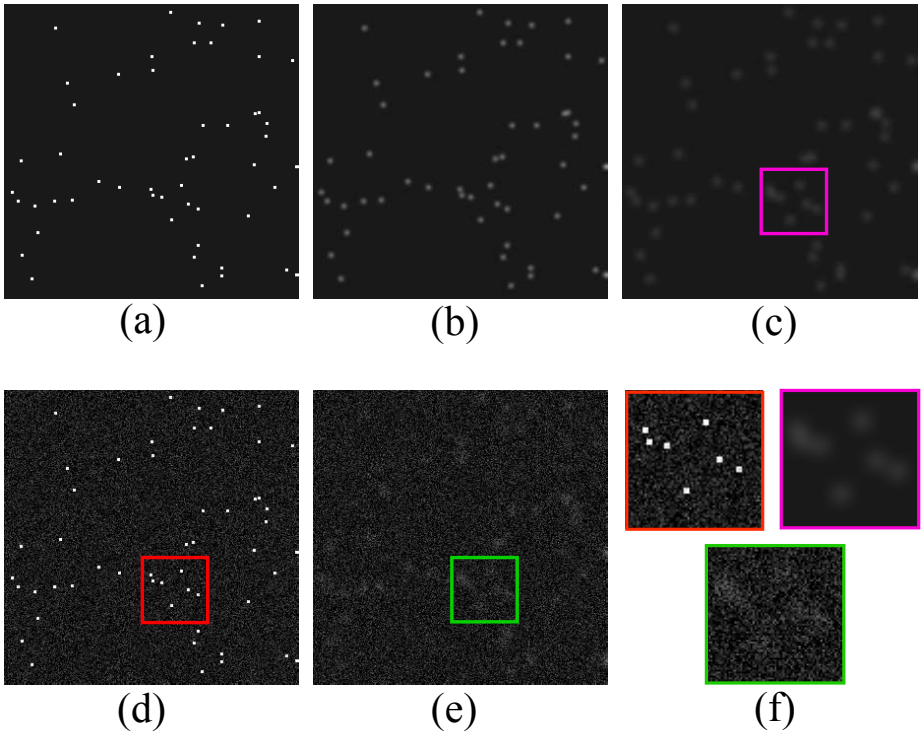

Figure 3.2: (a) Ground truth image of point sources, and images with introduced (b) small blurring, (c) severe blurring, (d) noise, (e) noise and severe blurring. (f) Magnified segments of images (c), (d) and (e).

and noise we zoom in on three identical segments of the Figures 3.2c, 3.2d, and 3.2e, which are marked by purple, red, and green colors, in Fig. 3.2f, respectively. From the red segment we see that effect of moderate level of noise is not severe for the source separation. However, in the purple segment, due to blurring, we are not able to distinguish three closely spaced sources in the top-left corner. When the effects of noise and blurring are combined the problem of detecting and resolving sources becomes even more challenging as illustrated by the green segment in the Fig. 3.2f.

The solutions to super-resolution estimation problems are typically found by making the assumptions that we know the signal model for the physical phenomenon that we observe and that we have some prior knowledge of its structure. For example from Figures 3.1 and 3.2 we can observe that sources are sparse in the time-domain and have 2-D coordinates, respectively. Therefore, collecting samples of the multipath channel response in the time domain, in which it is compact, is not a good idea as there is a high probability that we will miss sparse MPCs. For this reason, typically, alternative sampling schemes are designed that allow recovering the signals Fourier coefficients from low rate samples of the signal [98, 99]. In this thesis, we use a practical approach to increase the bandwidth of the multipath channel measurements by sampling the channel frequency

response over multiple bands. We then use signal processing frameworks known from spectral estimation to develop super-resolution time-delay estimation algorithms.

In the next section, we discuss the discrete data model for multipath channel measurements and signal processing frameworks that can be used to design algorithms for super-resolution time-delay estimation.

3.4. SUPER-RESOLUTION SPECTRAL ESTIMATION

We begin the overview of spectral estimation methods by introducing the discrete frequency domain data model for multipath channel measurements. We then show that this model has the same form as the general model used in 1-D spectral estimation. Finally, we introduce the main super-resolution spectral estimation methods that apply to our problem. This includes *(i) maximum likelihood methods* and methods based on *(ii) subspace*, and *(iii) sparsity estimation*.

3.4.1. DISCRETE DATA MODEL

We start the derivation of our discrete model for multipath channel measurements by writing the CTFT of the received signal $y(t)$ (3.3) as

$$Y(\omega) = X(\omega) \cdot C(\omega) + Q(\omega), \tag{3.6}$$

where $C(\omega) = H(\omega) \cdot G(\omega)$ is the compound channel frequency response (CFR), $G(\omega)$ is the CTFT of the low-pass filter (3.2), and $X(\omega)$ and $Q(\omega)$ are the CTFTs of the training signal $x(t)$ and noise $q(t)$. Considering the CTFT $G(\omega)$ of the low-pass filter we can write the CTFT for the received signals as

$$Y(\omega) = \begin{cases} X(\omega) \cdot H(\omega) + Q(\omega), & \omega \in [-\pi B, \pi B] \\ 0, & \text{otherwise}. \end{cases} \tag{3.7}$$

The receiver samples the signal $y(t)$ with sampling period $T_s = 1/B$, and during the period of one training symbol $T_{sym} = NT_s$ it collects N complex samples. Next, an N-point DFT is applied on the collected samples, the output of which is stacked in increasing order of DFT frequencies in $\mathbf{y} \in \mathbb{C}^N$. The discrete-time data model for the received signal (3.7) can now be written as

$$\mathbf{y} = \text{diag}(\mathbf{x})\mathbf{h} + \mathbf{q}, \tag{3.8}$$

where $\mathbf{x}$ collects N samples of $X(\omega)$, $\mathbf{q} \sim \mathcal{CN}(\mathbf{0}, \mathbf{\Sigma}_q)$ is zero-mean circularly-symmetric Gaussian noise with covariance $\mathbf{\Sigma}_q = \sigma_q^2 \mathbf{I}_N$, and σ_q^2 is its variance. Likewise, $\mathbf{h}$ collects N samples of $H(\omega), \omega \in [-\pi B, \pi B]$, and its entries are given by

$$[\mathbf{h}]_n = \int_0^{T_{sym}} h(t) e^{-j\Delta\omega n t} dt, \quad n = -\frac{N}{2}, \ldots, \frac{N}{2} - 1, \tag{3.9}$$

where $\Delta\omega = \frac{2\pi}{NT_s}$, and we assume that N is an even number. The entries of $\mathbf{h}$ are then given by

$$H[n] = H(n\Delta\omega), \quad n = -\frac{N}{2}, \ldots, \frac{N}{2} - 1. \tag{3.10}$$

Inserting the channel model (3.5) into (3.10) gives

$$H[n] = \sum_{k=1}^{K} \alpha_k e^{-jn\Delta\omega\tau_k}. \tag{3.11}$$

We use this result to write $\mathbf{h}$ in a more compact form as

$$\mathbf{h} = \mathbf{M}(\boldsymbol{\phi})\boldsymbol{\alpha}, \tag{3.12}$$

where $\mathbf{M}(\boldsymbol{\phi}) = [\mathbf{m}(\phi_1)\ \mathbf{m}(\phi_2)\ \ldots\ \mathbf{m}(\phi_K)] \in \mathbb{C}^{N\times K}$ is a Vandermonde matrix, given by

$$\mathbf{M}(\boldsymbol{\phi}) = \begin{bmatrix} 1 & 1 & \cdots & 1 \\ \phi_1 & \phi_2 & \cdots & \phi_K \\ \vdots & \vdots & \ddots & \vdots \\ \phi_1^{N-1} & \phi_2^{N-1} & \cdots & \phi_K^{N-1} \end{bmatrix}, \tag{3.13}$$

$\phi_k = e^{-j\phi_k}$, $\phi_k = \Delta\omega\tau_k$ is the phase shift introduced by the delay of kth MPC τ_k, and $\boldsymbol{\phi} = [\phi_1,\ldots,\phi_K]^T \in \mathbb{C}^K$ collects the phase shifts for all the MPCs. Likewise, with a slight abuse of notation $\boldsymbol{\alpha} = [\alpha_1,\ldots,\alpha_K]^T \in \mathbb{C}^K$ collects the complex amplitudes of the MPCs where each α_k captures the normalizing phase shift factor $\phi_k^{-N/2}$.

We assume that the training signal $\mathbf{x}$ is known and that none of its samples are zero or close to zero, so we can estimate $\mathbf{h}$ from $\mathbf{y}$ in (3.8) by applying deconvolution as $\mathbf{h} = \text{diag}^{-1}(\mathbf{x})\mathbf{y}$. The resulting data after deconvolution with a slight abuse of notation satisfies the model

$$\mathbf{h} = \mathbf{M}(\boldsymbol{\phi})\boldsymbol{\alpha} + \mathbf{q}. \tag{3.14}$$

Here, we assume that the transceivers are phase synchronized during the channel probing, and therefore there is no additional phase offset introduced in the measurements. We will discuss the data model for the channel measurements collected using unsynchronized transceivers and techniques to eliminate the unknown phase offset in Section 4.2.3. We also assume that samples of the training symbols $\mathbf{x}$ have a constant magnitude ensuring that $\mathbf{q}$ has the same statistics after deconvolution and the noise remains white.

The multipath channel is typically probed multiple times during its channel coherence time. We assume that the delays $\boldsymbol{\tau}$, i.e., phase shifts $\boldsymbol{\phi}$, stay constant during this period while the complex amplitudes $\boldsymbol{\alpha}$ and noise $\mathbf{q}$ may vary. Therefore, usually multiple observations (let us say M) of (3.14) are available. These observations satisfy the following model

$$\mathbf{h}^{(m)} = \mathbf{M}(\boldsymbol{\phi})\boldsymbol{\alpha}^{(m)} + \mathbf{q}^{(m)}, \quad m = 1,\ldots,M. \tag{3.15}$$

where $\boldsymbol{\alpha}^{(m)}$ and $\mathbf{q}^{(m)}$ collect the complex amplitudes of the MPCs and the noise samples for the mth observation, respectively.

The objective of multipath channel time-delay estimation from the (3.14) or (3.15) is to estimate the phase shifts $\boldsymbol{\phi}$ introduced by the time-delays $\boldsymbol{\tau}$ of MPCs. From the estimated $\boldsymbol{\phi}$, $\boldsymbol{\tau}$ immediately follows. Therefore, in the rest of this section, we will focus on the estimation of the phase shifts $\boldsymbol{\phi}$. The models (3.14) and (3.15) are often indicated as single measurement vector (SMV) and multiple measurement vector (MMV) models, respectively [100]. These models appear in many signal processing applications and they

are well known from array signal processing [101], spectral analysis [82], and compressive sensing [102]. Therefore, many super-resolution algorithms for estimation of these models have been already proposed for various popular signal processing applications related to radars [103, 89], ultrasound imaging [90, 91], and wireless communications [87, 88], to name a few. In what follows, we provide an overview of the most important methods and super-resolution frameworks that can be used for super-resolution time-delay estimation of MPCs.

3.4.2. MAXIMUM LIKELIHOOD ESTIMATION

In Chapter 2, we showed an example of TOA based localization to illustrate principles of maximum likelihood (ML) estimation [72]. The key idea is to define the likelihood function of the measurements parameterized by the unknown parameter that we aim to estimate. Then the ML estimator is found by finding the value of the parameter that maximizes the likelihood function. The problem of ML estimation can be formulated in two ways which are known as *deterministic* and *stochastic* ML estimation [101]. The difference in these two formulations comes from the different assumptions made on the statistical properties of the measurements when deriving ML estimators.

To derive the deterministic ML delay estimator, we model noise $\mathbf{q}$ in (3.14) as a zero-mean circularly-symmetric Gaussian noise with covariance $\mathbf{\Sigma}_{\mathrm{q}}$, and we assume that the complex path amplitudes $\boldsymbol{\alpha}$ are unknown but deterministic parameters. Under these assumptions, the likelihood function of the multipath channel measurements is given by

$$p(\mathbf{h};\,\boldsymbol{\phi},\boldsymbol{\alpha}) = \frac{1}{(2\pi)^{N/2}(\det(\mathbf{\Sigma_q}))^{1/2}}\exp\left(-\frac{1}{2}(\mathbf{h}-\mathbf{M}(\boldsymbol{\phi})\boldsymbol{\alpha})^{H}\mathbf{\Sigma}_{\mathbf{q}}^{-1}(\mathbf{h}-\mathbf{M}(\boldsymbol{\phi})\boldsymbol{\alpha})\right), \tag{3.16}$$

where $\mathbf{M}(\boldsymbol{\phi})\boldsymbol{\alpha}$ and $\mathbf{\Sigma}_{\mathrm{q}}$ are the mean and covariance of the PDF, respectively. As already discussed in Section 2.4.1, finding the parameter $\boldsymbol{\phi}$ that maximizes the likelihood function $p(\mathbf{h};\,\boldsymbol{\phi},\boldsymbol{\alpha})$ is equivalent to finding the parameter that maximizes the log-likelihood function $\ln\big(p(\mathbf{h};\,\boldsymbol{\phi},\boldsymbol{\alpha})\big)$. In the case of exponential distributions, such as the Gaussian distribution, the second approach is more convenient. Therefore, we define the ML estimator as

$$\hat{\boldsymbol{\phi}} = \underset{\boldsymbol{\phi},\boldsymbol{\alpha}}{\operatorname{argmax}}\ \ln\big(p(\mathbf{h};\ \boldsymbol{\phi},\boldsymbol{\alpha})\big)\,. \tag{3.17}$$

Assuming that the covariance matrix of the noise satisfies $\mathbf{\Sigma_q} = \sigma_{\mathrm{q}}^2\mathbf{I}_N$, the ML estimator is given by

$$\hat{\boldsymbol{\phi}} = \underset{\boldsymbol{\phi},\boldsymbol{\alpha}}{\operatorname{argmin}}\ \|\mathbf{h}-\mathbf{M}(\boldsymbol{\phi})\boldsymbol{\alpha}\|_2^2\,. \tag{3.18}$$

The deterministic ML formulation of the estimation problem results in a non-linear least squares (NLS) problem. Therefore, the parameters $\boldsymbol{\phi}$ and $\boldsymbol{\alpha}$ can be estimated by solving the NLS problem given in (3.18).

In the stochastic formulation of the ML estimation problem, we consider that not only the noise $\mathbf{q}$ but also the complex path amplitudes $\boldsymbol{\alpha}$ are assumed to be independent random variables. The procedure for deriving a stochastic ML estimator is similar to the one shown for the deterministic formulation, and we will not elaborate on it in

this thesis. The readers interested in stochastic estimators for estimation of multipath channel parameters we refer to [104, 105].

We discussed ML estimation by using the SMV model (3.14) as an example. The extensions of these results to the MMV model (3.15) is straightforward to do and this is described in [106]. Next, we discuss the major properties of the ML estimators.

The ML estimators have the asymptotic properties of being unbiased, efficient, and achieving the CRB as N tends to infinity [72]. These estimators are also robust to violations of statistical assumptions on the data model, such as assumptions on noise and statistical correlation between the complex amplitudes $\boldsymbol{\alpha}$ [107, 108]. This means that in these cases, the performance of ML estimators is not severely degraded. However, the deterministic ML estimators do not stay asymptotically efficient for the MMV models, i.e., when $M > 1$, which is the consequence of the increase in the number of complex amplitude parameters that need to be estimated for these models [106]. On the other hand, the stochastic ML estimator remains consistent and asymptotically efficient as M tends to infinity.

The main disadvantage of ML estimators is that they are usually not practical for implementation. For example, the objective function of the NLS problem given in (3.18) is highly multimodal with many local minima [109]. As already discussed in Chapter 2, the typical approach to finding the solution to NLS problems is to use iterative optimization methods such as Gauss-Newton, Levenberg-Marquardt, or steepest descent [110, 111, 112]. However, all of these methods require initialization by the solution of some suboptimal estimator. If the initial estimate of a suboptimal estimator is close to the global minimum of the cost function, then these methods will converge to the optimal solution [113]. Otherwise, however, they will converge to a local minimum and not the optimal solution. Therefore, the performance of these methods strongly depends on the accuracy of the initialization. Another disadvantage is that ML estimators assume prior knowledge of the model order in (3.14) or (3.15) [72]. For our problem, the order of the model is proportional to the number of the MPCs K and can be estimated before parameter estimation by using methods given in [114, 115, 116].

3.4.3. SUBSPACE BASED ESTIMATION

The subspace-based super-resolution methods use analysis of signal and noise subspaces for the estimation of parameters. These methods can be classified according to their numerical procedure [117, 118] into

- extrema-searching techniques such as MUSIC [119] and RARE [120] algorithms,
- polynomial-rooting techniques such as Pisarenko's harmonic decomposition [121], root-MUSIC [122] and MODE [123] algorithms, and
- matrix-shifting techniques such as ESPRIT [124], matrix pencil methods [125, 126], optimally weighted ESPRIT [127], and Unitary ESPRIT [128].

All of these methods, as a first step, perform subspace decomposition on the covariance matrix of the data $\boldsymbol{\Sigma}_{\mathbf{h}}$ or on the Hankel matrix constructed from the data $\mathbf{h}^{(m)}$, $m = 1, \ldots, M$. The subspace decomposition of these matrices can be done by using eigenvalue

decomposition (EVD) [118] or singular value decomposition (SVD) [129]. In this thesis, we choose to estimate the signal and noise subspaces by constructing a Hankel matrix and applying SVD.

From the channel measurements $\mathbf{h}$, we can construct a Hankel matrix of size $P \times Q$ as follows

$$\mathbf{H} := \begin{bmatrix} H[0] & H[1] & \cdots & H[Q] \\ H[1] & H[2] & \cdots & H[Q+1] \\ \vdots & \vdots & \ddots & \vdots \\ H[P-1] & H[P] & \cdots & H[N-1] \end{bmatrix}, \tag{3.19}$$

where P is a design parameter and $Q = N-P+1$. The constructed Hankel matrix satisfies the model

$$\mathbf{H} = \mathbf{M}'(\boldsymbol{\phi})\mathbf{X} + \mathbf{Q}, \tag{3.20}$$

where $\mathbf{M}'(\boldsymbol{\phi})$ is $P \times K$ submatrix of $\mathbf{M}$,

$$\mathbf{X} := [\boldsymbol{\alpha} \quad \boldsymbol{\Phi}\boldsymbol{\alpha} \quad \boldsymbol{\Phi}^2\boldsymbol{\alpha} \cdots \boldsymbol{\Phi}^{Q-1}\boldsymbol{\alpha}],$$

$\mathbf{Q}$ is a noise matrix and $\boldsymbol{\Phi} = \text{diag}(\boldsymbol{\phi})$. When matrix $\mathbf{H}$ is designed such that it is full rank, i.e., $\text{rank}(\mathbf{H}) = K$, then its SVD is given by

$$\mathbf{H} := \mathbf{U}\boldsymbol{\Lambda}\mathbf{V}^H = \begin{bmatrix} \mathbf{U}_\text{s} & \mathbf{U}_\text{n} \end{bmatrix} \boldsymbol{\Lambda} \begin{bmatrix} \mathbf{V}_\text{s}^H \\ \mathbf{V}_\text{n}^H \end{bmatrix}, \tag{3.21}$$

where $\boldsymbol{\Lambda}$ is a $P \times Q$ diagonal matrix containing the singular values. These singular values are ordered such that

$$\lambda_1 \geq \lambda_2 \geq \cdots \geq \lambda_K > \lambda_{K+1} \approx \cdots \approx \lambda_P \approx \sigma,$$

where σ^2 is the noise power. The first K singular values are associated to the columns of $\mathbf{U}_\text{s} = [\mathbf{u}_1 \ \ldots \ \mathbf{u}_K]$. The remaining $P-K$ smaller singular values are associated to the columns of $\mathbf{U}_\text{n} = [\mathbf{u}_{K+1} \ \ldots \ \mathbf{u}_N]$. The columns of $\mathbf{U}_\text{s}$ and $\mathbf{U}_\text{n}$ are called signal and noise singular vectors, respectively. The signal singular vectors span the signal subspace, the same subspace that is spanned by steering matrix $\mathbf{M}(\boldsymbol{\phi})$. On the other hand, the noise singular vectors span the noise subspace, that is, the same subspace that is orthogonal to the signal subspace. We can write this more compactly as

$$\text{range}(\mathbf{U}_\text{s}) = \text{range}(\mathbf{M}(\boldsymbol{\phi})), \qquad \text{range}(\mathbf{U}_\text{n}) \perp \text{range}(\mathbf{M}(\boldsymbol{\phi})). \tag{3.22}$$

The subspace-based algorithms exploit properties and structures present in the signal and noise subspaces to estimate unknown parameters. We will illustrate time-delay estimation using subspace-based methods in examples of MUSIC and ESPRIT algorithms.

MULTIPLE SIGNAL CLASSIFICATION (MUSIC)

The MUSIC algorithm uses the property that when matrix $\mathbf{H}$ is full rank, the subspaces spanned by $\mathbf{M}'(\boldsymbol{\phi})$ and $\mathbf{U}_\text{n}$ are orthogonal. From this, it follows that

$$\mathbf{m}^H(\phi)\mathbf{U}_\text{n} = \mathbf{0} \qquad \text{if } \phi \text{ is an entry in } \boldsymbol{\phi}, \tag{3.23}$$

Algorithm 1: Standard MUSIC

Input: $N, P, K, \mathbf{h}$
Output: $\hat{\boldsymbol{\phi}}$
$Q \leftarrow N - P + 1$;
$\mathbf{H} \leftarrow \texttt{hankel}(\mathbf{h}, P, Q)$; (3.19)
$\hat{\mathbf{U}} \leftarrow \texttt{SVD}(\mathbf{H})$; (3.21)
$\hat{\mathbf{U}}_{\mathrm{n}} \leftarrow \hat{\mathbf{U}}[:, K+1:Q]$;
$P_{\mathrm{music}}(\phi) \leftarrow \texttt{calPseudoSpectrum}(\hat{\mathbf{U}}_{\mathrm{n}}, \phi), \forall \phi \in [0, 2\pi)$; (3.24)
$\hat{\boldsymbol{\phi}} \leftarrow \texttt{searchPeaks}(P_{\mathrm{music}}(\phi), K)$;

where $\mathbf{0}$ is the null vector. It is shown in [82] that this condition is both necessary and sufficient for ϕ to be an entry in $\boldsymbol{\phi}$. Therefore, if we know the number of MPCs K the phase shifts introduced by their time-delays can be found as K peaks of the MUSIC pseudo spectrum

$$P_{\mathrm{music}}(\phi) = \frac{1}{\|\hat{\mathbf{U}}_{\mathrm{n}}^H \mathbf{m}(\phi)\|_2^2}, \qquad \phi \in [0, 2\pi). \tag{3.24}$$

A summary of the MUSIC algorithm is shown as Algorithm 1. The abstract routine `calPseudoSpectrum`$(\cdot)$ points to the calculation of the MUSIC pseudospectrum (3.24) from $\hat{\mathbf{U}}_{\mathrm{n}}$ and $\forall \phi \in [0, 2\pi)$. The routine `searchPeaks`$(\cdot, K)$ searches for K peaks of the pseudospectrum and returns its corresponding phases. `SVD`$(\cdot)$ refers to the SVD of a matrix. After applying SVD from the estimated column space, we select singular vectors corresponding to the noise singular values, i.e., $\hat{\mathbf{U}}[:, K+1:Q]$. The remaining parts of the summary are self-explanatory.

ESTIMATION OF SIGNAL PARAMETERS VIA ROTATIONAL INVARIANCE (ESPRIT)

The ESPRIT algorithm uses the property (3.22) which says that the columns of $\mathbf{U}_{\mathrm{s}}$ form a K-dimensional basis for the column space of $\mathbf{H}$. Therefore, $\mathbf{U}_{\mathrm{s}}$ and $\mathbf{M}'(\boldsymbol{\phi})$ span the same column space and from $\mathbf{H}$ we can estimate $\mathbf{M}'(\boldsymbol{\phi})$ up to a $K \times K$ non-singular matrix $\mathbf{T}$. This means that we can write $\mathbf{M}'(\boldsymbol{\phi}) = \mathbf{U}_{\mathrm{s}}\mathbf{T}^{-1}$ and that a shift invariance structure present in $\mathbf{M}'(\boldsymbol{\phi})$ is also present in $\mathbf{U}_{\mathrm{s}}$.

Let us define the selection matrices

$$\mathbf{J}_1 = [\mathbf{I}_{P-1} \quad \mathbf{0}_{P-1}], \qquad \mathbf{J}_2 = [\mathbf{0}_{P-1} \quad \mathbf{I}_{P-1}], \tag{3.25}$$

where $\mathbf{I}_{P-1}$ is the identity matrix of size $(P-1) \times (P-1)$ and $\mathbf{0}_{P-1}$ is a null vector of length $(P-1)$. The submatrices $\mathbf{M}_1 = \mathbf{J}_1\mathbf{M}'(\boldsymbol{\phi}) \in \mathbb{C}^{(P-1)\times K}$ and $\mathbf{M}_2 = \mathbf{J}_2\mathbf{M}'(\boldsymbol{\phi}) \in \mathbb{C}^{(P-1)\times K}$ are obtained by dropping the first and last row of $\mathbf{M}'(\boldsymbol{\phi})$, respectively. In view of the shift invariance structure of $\mathbf{M}'(\boldsymbol{\phi})$, we have

$$\mathbf{M}_2 = \mathbf{M}_1\boldsymbol{\Phi}. \tag{3.26}$$

Likewise, we can define submatrices of $\mathbf{U}_{\mathrm{s}}$ as

$$\mathbf{U}_1 = \mathbf{J}_1\mathbf{U}_{\mathrm{s}}, \qquad \mathbf{U}_2 = \mathbf{J}_2\mathbf{U}_{\mathrm{s}}, \tag{3.27}$$

Algorithm 2: Standard ESPRIT

Input: $N, P, K, \mathbf{h}$
Output: $\hat{\boldsymbol{\phi}}$
$Q \leftarrow N - P + 1$;
$\mathbf{H} \leftarrow \texttt{hankel}(\mathbf{h}, P, Q)$; (3.19)
$\hat{\mathbf{U}}_s \leftarrow \texttt{TSVD}(\mathbf{H}, K)$;
$\hat{\mathbf{U}}_1 \leftarrow \mathbf{J}_1 \hat{\mathbf{U}}_s$; (3.27)
$\hat{\mathbf{U}}_2 \leftarrow \mathbf{J}_2 \hat{\mathbf{U}}_s$; (3.27)
$\boldsymbol{\Psi} \leftarrow \hat{\mathbf{U}}_1^{\dagger} \hat{\mathbf{U}}_2$; (3.29)
$\boldsymbol{\Phi} \leftarrow \texttt{EVD}(\boldsymbol{\Psi})$;
$\hat{\tau}_k = \arg\{\hat{\phi}_k\}/(2\pi\Delta\omega), \quad k = 1, \ldots K$

that satisfy the following models

$$\mathbf{U}_1 = \mathbf{M}_1 \mathbf{T}, \qquad \mathbf{U}_2 = \mathbf{M}_2 \mathbf{T}. \tag{3.28}$$

Now, from (3.26) and (3.28) it follows that the matrix $\boldsymbol{\Psi} = \mathbf{U}_1^{\dagger}\mathbf{U}_2$ satisfies the model

$$\boldsymbol{\Psi} = \mathbf{T}\boldsymbol{\Phi}\mathbf{T}^{-1}. \tag{3.29}$$

The diagonal matrix $\boldsymbol{\Phi}$ that collects the phase shifts $\boldsymbol{\phi} = [\hat{\phi}_1 \ldots \hat{\phi}_K]$ on its diagonal can be estimated from $\boldsymbol{\Psi}$ by taking its EVD. In other words, let $\hat{\phi}_k$ be an estimate of the kth eigenvalue of $\boldsymbol{\Psi}$, then the corresponding time delay estimate is $\hat{\tau}_k = \arg\{\hat{\phi}_k\}/(2\pi\Delta\omega)$.

A summary of the ESPRIT algorithm is shown as Algorithm 2. The abstract routine $\texttt{TSVD}(\cdot, K)$ refers to the truncated SVD of a matrix (truncating at rank K). Likewise, $\texttt{EVD}(\cdot)$ refers to EVD of a matrix returning the diagonal matrix that collects its eigenvalues $\hat{\phi}_k, k = 1, \ldots, K$. The remaining parts of the summary are self-explanatory.

The performance of both MUSIC and ESPRIT algorithms can be further improved by using smoothing and forward-backward averaging techniques [130, 128]. Furthermore, both of these algorithms are easily extendable for MMV models. For a more detailed overview and discussion on subspace-based methods, we refer the interested reader to [108].

Subspace-based algorithms, in general, have good performance and are widely used in practice. These methods can resolve sources spaced much below the natural resolution limits, and their estimation performance is close to the CRB. However, there are several disadvantages to these methods. The performance of subspace-based methods degrades if the assumption on white noise and statistical independence of the complex amplitudes $\alpha_k, k = 1, \ldots, K$ are violated [82]. Furthermore, these algorithms assume that MPCs are specular with distinct values of their parameters and that the number of MPCs K present in the channel is known. However, this is usually not the case in practice, as rough surfaces produce diffuse scattering of RF signals. In the presence of diffuse scattering, except for the LOS path, each MPC is often a cluster of paths with similar time-delays and direction-of-arrivals [131]. Therefore in the presence of diffuse scattering, detection of the number of MPCs is a difficult problem, and often methods that are used

for detection such [114, 132, 133, 116] fail in these scenarios. Misdetection of the number of MPCs deteriorates the performance of the subspace-based methods as their performance inherently depends on the accuracy of the estimated subspaces. Furthermore, if the number of available snapshots M is low, the estimated subspaces will be perturbed by noise which limits the accuracy of these methods [134].

3.4.4. SPARSE ESTIMATION METHODS

The previously presented MLE and subspace-based methods require knowledge of the number of MPCs present in the channel before channel estimation. When using these methods, we assume that the number of MPCs is estimated, before time-delay estimation, by methods for model order selection [114, 135]. This two-step approach to channel estimation is usually not favorable. The wrong estimate of the model order leads to modeling errors that significantly deteriorate the performance of time-delay estimation. The sparse estimation methods proposed in [136, 137, 138, 139, 140] alleviate these issues. In this section, we introduce methods for sparse estimation and key related works to this thesis.

The common sparse estimation frameworks are focused on estimating parameters of discrete linear models [83]. This is different from model (3.14) where multipath channel measurements are a nonlinear function of continuous time-delay parameters. Depending on the modeling assumptions, we can classify the sparse estimation methods into the following three main categories, *(i) on-grid*, *(ii) off-grid*, and *(iii) gridless* methods. The on-grid sparse estimation methods assume that unknown parameters take values on a discrete grid of points. This assumption introduces modeling errors when estimating continuous-valued parameters resulting in poor estimation performance. The off-grid sparse estimation methods reduce these errors by introducing a first-order Taylor expansion of the dictionary to estimate off-grid parameters. However, these methods still rely on a discrete grid, and modeling errors are reduced but still present when estimating off-grid parameters. Recently, gridless sparse estimation methods are proposed that do not require discrete dictionaries and can directly estimate continuous-valued parameters.

The sparse estimation methods can also be categorized based on the problem formulation into: *(i) deterministic* and *(ii) Bayesian* sparse estimation methods. In deterministic sparse estimation, we do not make any statistical assumptions on the signal. Instead, we assume that signal parameters are deterministic but unknown variables. The parameters are then estimated as those that result in the sparsest signal candidate by some sparse metric. On the other hand, we make statistical assumptions on the data model and the distribution of unknown parameters in the Bayesian framework. Therefore, in the Bayesian framework, the unknown parameters are treated as random variables, and we assume that we know the probability density distribution that describes them. In particular, to achieve sparsity, a prior distribution that promotes sparsity is assumed for the sparse parameters, and we refer to it as a sparse prior.

In what follows, we present sparsity-based time-delay estimation in examples of on-grid estimation methods. We will formulate the problem of sparse estimation in both deterministic and Bayesian frameworks. Finally, we will provide a brief overview of key results related to off-grid and gridless sparse estimation methods.

ON-GRID SPARSE ESTIMATION

We first discuss the problem of sparse-based multipath channel estimation in a deterministic framework, and later we introduce the Bayesian formulation of the same problem.

Deterministic Sparse Time-Delay Estimation: The sparse model for multipath channel measurements is given by

$$\mathbf{h} = \mathbf{M}(\tilde{\boldsymbol{\phi}})\tilde{\boldsymbol{\alpha}} + \mathbf{q}, \tag{3.30}$$

where $\mathbf{M}(\tilde{\boldsymbol{\phi}}) = [\mathbf{m}(\tilde{\phi}_1) \ \ldots \ \mathbf{m}(\tilde{\phi}_{\tilde{K}})] \in \mathbb{C}^{N\times\tilde{K}}$ is a Vandermonde matrix of the form (3.13), with $N \ll \tilde{K}$, where $\tilde{\boldsymbol{\alpha}} \in \mathbb{C}^{\tilde{K}}$ is a sparse coefficient vector and $\mathbf{q}$ accounts for the noise in the measurements. We refer to $\mathbf{M}(\tilde{\boldsymbol{\phi}})$ as the dictionary and its columns are called atoms. This model is sparse in the sense that only a few entries, i.e., $K \ll \tilde{K}$, of $\tilde{\boldsymbol{\alpha}}$ are of nonzero magnitude and the rest are zero or close to zero. Assuming that there are K MPCs present in the channel with time-delays laying on the grid defined by the dictionary $\mathbf{M}(\tilde{\boldsymbol{\phi}})$, the measurements $\mathbf{h}$ can be well approximated by the model (3.30) as a linear combination of K atoms in $\mathbf{M}(\tilde{\boldsymbol{\phi}})$. Given the measurements $\mathbf{h}$, the problem of sparse multipath channel estimation is to find the sparse vector $\tilde{\boldsymbol{\alpha}}$ that well approximates measurements according to the selected data consistency metric. Therefore, the solution to the sparse multipath channel estimation can be found by solving the following optimization problem

$$\hat{\boldsymbol{\alpha}} = \underset{\tilde{\boldsymbol{\alpha}}}{\operatorname{argmin}} \ \lambda\|\tilde{\boldsymbol{\alpha}}\|_1 + \|\mathbf{h} - \mathbf{M}(\tilde{\boldsymbol{\phi}})\tilde{\boldsymbol{\alpha}}\|_2^2, \tag{3.31}$$

where $\|\tilde{\boldsymbol{\alpha}}\|_1$ promotes the sparse solution to the optimization problem and it is known as the sparsity term, while $\|\mathbf{h} - \mathbf{M}(\tilde{\boldsymbol{\phi}})\tilde{\boldsymbol{\alpha}}\|_2^2$ is the data fidelity term that promotes smaller error between the measurements $\mathbf{h}$ and the model $\mathbf{M}(\tilde{\boldsymbol{\phi}})\tilde{\boldsymbol{\alpha}}$. The regularization parameter $\lambda > 0$ is a design parameter that weights the relative importance of sparsity and data fidelity terms, and it is often selected to be equal to the variance of the noise σ_{q}^2. Therefore, from a practical perspective, this parameter has a similar role as model order selection in subspace-based estimation methods. The optimization problem given in (3.31) is also known as the least absolute shrinkage and selection operator (LASSO) [141]. Alternatively, this optimization problem can be formulated as the basis pursuit de-noising (BPDN) problem as presented in [142]. In general, these problems are known as ℓ_1 optimization problems.

The LASSO and BPDN are convex optimization problems [143] and as such there is guarantee that they can be solved in a polynomial time [144]. However, when the problem dimension is high it is hard to find an efficient solution to this problem since the sparsity term in (3.31) is not a smooth function. In the last decade, several algorithms are proposed to accelerate finding the solution to ℓ_1 optimization problems such as the ℓ_1-magic [145], the conjugate gradient method [146], the Nesterov's smoothing technique with continuation (NESTA) [147, 148], the alternating direction method of multipliers (ADMM) [149] and SPGL1 [150, 151], to name a few.

Sparse estimation methods can be easily extended to the MMV model (3.15) when multiple channel measurements are available. For MMV models, we assume that vectors $\mathbf{h}^{(m)}, m = 1,\ldots,M$, are jointly sparse, and they satisfy the model

$$\mathbf{h}^{(m)} = \mathbf{M}(\tilde{\boldsymbol{\phi}})\tilde{\boldsymbol{\alpha}}^{(m)} + \mathbf{q}^{(m)}, \tag{3.32}$$

where $\tilde{\boldsymbol{\alpha}}^{(m)}$ are jointly sparse vectors. This is typically satisfied if the channel measurements are collected during the channel coherence time. Therefore, the matrix formed by stacking collected measurement as its columns $\boldsymbol{\mathcal{H}} = [\mathbf{h}^{(1)} \ \dots \ \mathbf{h}^{(M)}] \in \mathbb{C}^{N\times M}$ satisfies the following model

$$\boldsymbol{\mathcal{H}} = \mathbf{M}(\tilde{\boldsymbol{\phi}})\boldsymbol{\mathcal{X}} + \boldsymbol{\mathcal{Q}}, \tag{3.33}$$

where $\boldsymbol{\mathcal{X}} = [\tilde{\boldsymbol{\alpha}}^{(1)} \ \dots \ \tilde{\boldsymbol{\alpha}}^{(M)}] \in \mathbf{C}^{\tilde{K}\times M}$ is row sparse matrix with only a few, i.e., K, non-zero rows and $\boldsymbol{\mathcal{Q}} = [\mathbf{q}^{(1)} \ \dots \ \mathbf{q}^{(M)}]$. Now, the sparse solution to multipath channel estimation for the MMV model (3.15) is found by solving the following optimization problem

$$\hat{\boldsymbol{\mathcal{X}}} = \underset{\boldsymbol{\mathcal{X}}}{\operatorname{argmin}} \ \lambda\|\boldsymbol{\mathcal{X}}\|_{2,1} + \|\boldsymbol{\mathcal{H}} - \mathbf{M}(\tilde{\boldsymbol{\phi}})\boldsymbol{\mathcal{X}}\|_F^2, \tag{3.34}$$

where $\|[\mathbf{a}_1 \ \dots \ \mathbf{a}_N]\|_{2,1} := \sum_{i=1}^{N}\|\mathbf{a}_i\|_2$ is the $\ell_{2,1}$-norm of a matrix $\mathbf{A}$ which is known to promote column sparsity. Likewise, $\|\mathbf{A}\|_{\mathrm{F}} = \sqrt{\mathrm{Tr}(\mathbf{A}\mathbf{A}^H)}$ is the Forbenius norm of a matrix and has the role of data fidelity metric. The regularization parameter $\lambda > 0$ weights the relative importance of sparsity and data fidelity terms. It is important to notice that time-delays of MPCs are not directly estimated by solving problems (3.31) and (3.34). Instead, they are found by decoding the indexes of non-zero entries in the vector $\hat{\boldsymbol{\alpha}}$ or non-zero rows in $\hat{\boldsymbol{\mathcal{X}}}$ using the phase grid of the dictionary $\mathbf{M}(\tilde{\boldsymbol{\phi}})$. When the number of snapshots M is too large, the optimization problem (3.34) becomes too computationally expensive. In this case, it is more practical to apply dimensionality reduction on the measurements before sparse estimation. This method for sparse estimation of MMV models is known as $\ell_{2,1}$-SVD [152].

Multipath channel estimation using deterministic sparsity-based methods has been studied in [87, 153, 154]. In these works, it is assumed that the multipath channel has a few specular MPCs with time-delays that lay exactly on the discrete grid defined by the dictionary. This means that the multipath channel is sparse in the time domain and it can be well represented by the sparse model (3.30). However, in reality, time-delays often lay off the grid, which causes a basis mismatch [155, 156], leading to overall estimation performance degradation. Consequently, CS methods cannot achieve super-resolution even in noiseless scenarios.

Bayesian Sparse Time-Delay Estimation: The alternative approach to sparse estimation is by using the Bayesian framework. Bayesian sparse estimation methods are based on statistical assumptions on the data model and solution to promote the desired sparse estimate. In the Bayesian framework, both the noise term $\mathbf{q}$ and amplitudes of MPCs $\boldsymbol{\alpha}$ are assumed to be random variables, where certain prior distribution $p(\boldsymbol{\alpha})$ is assumed on $\boldsymbol{\alpha}$ that promotes a sparse solution [137, 157]. The estimation then proceeds by formulating the estimation problem in Maximum A Posteriori (MAP), or a hierarchical Bayesian framework [158, 159]. We will illustrate the key idea of sparse Bayesian estimation by deriving the MAP estimation for channel estimation using the complex Gaussian scale mixture (GSM) model to model the distribution of the elements in $\boldsymbol{\alpha}$.

The MAP estimator is defined as [157]

$$\begin{aligned}\hat{\boldsymbol{\alpha}} &= \underset{\boldsymbol{\alpha}}{\operatorname{argmax}} \ p(\boldsymbol{\alpha}\mid\mathbf{h}) = \frac{p(\mathbf{h}\mid\boldsymbol{\alpha})p(\boldsymbol{\alpha})}{\int p(\mathbf{h}\mid\boldsymbol{\alpha})p(\boldsymbol{\alpha})d\boldsymbol{\alpha}} \\ &= \underset{\boldsymbol{\alpha}}{\operatorname{argmax}} \ p(\mathbf{h}\mid\boldsymbol{\alpha})p(\boldsymbol{\alpha}),\end{aligned} \tag{3.35}$$

where $p(\boldsymbol{\alpha} \mid \mathbf{h})$ is the posterior distribution of $\boldsymbol{\alpha}$ given the measurements $\mathbf{h}$, $p(\mathbf{h} \mid \boldsymbol{\alpha})$ is the posterior distribution of $\mathbf{h}$ given $\boldsymbol{\alpha}$, and $p(\boldsymbol{\alpha})$ is the prior distribution of $\boldsymbol{\alpha}$. When α is real, it is well known that assuming the Laplace distribution on its elements leads to the ℓ_1 regularized least squares MAP estimator. However, in our case, α_k are complex random variables, and we can not directly use the Laplace distribution to model them. Instead, these variables are first modeled using the complex GSM model with a gamma mixing density (see [160] for details). These modeling assumptions result in the so-called Laplace distribution for complex variables. Now, assuming that $\alpha_k, k = 1, \ldots, K$, are Laplace i.i.d complex distributed random variables their joint prior distribution is given by [160]

$$p(\boldsymbol{\alpha}) = \prod_{k=1}^{K} \text{Lap}(\alpha_k; 0, 1/\lambda) \propto \prod_{k=1}^{K} \exp(-\lambda \mid \alpha_k \mid), \tag{3.36}$$

where $\propto$ denotes proportionality. Assuming that measurements follow model (3.30) and that the noise is Gaussian distributed the posterior distribution $p(\mathbf{h} \mid \boldsymbol{\alpha})$ is given by

$$p(\mathbf{h} \mid \boldsymbol{\alpha}) \propto \exp\left[-(\mathbf{h} - \mathbf{M}(\boldsymbol{\phi})\boldsymbol{\alpha})^H \boldsymbol{\Sigma}_{\text{q}}^{-1} (\mathbf{h} - \mathbf{M}(\boldsymbol{\phi})\boldsymbol{\alpha})\right]. \tag{3.37}$$

Substituting (3.36) and (3.37) in (3.35) we can write the log likelihood posterior distribution as

$$\ln p(\boldsymbol{\alpha} \mid \mathbf{h}) \propto -(\mathbf{h} - \mathbf{M}(\boldsymbol{\phi})\boldsymbol{\alpha})^H \boldsymbol{\Sigma}_{\text{q}}^{-1} (\mathbf{h} - \mathbf{M}(\boldsymbol{\phi})\boldsymbol{\alpha}) - \lambda \sum_{k=1}^{K} \mid \alpha_k \mid . \tag{3.38}$$

We now assume that $\boldsymbol{\Sigma}_{\text{q}} = \sigma^2 \mathbf{I}$ and write $p(\boldsymbol{\alpha} \mid \mathbf{h})$ in a more compact form as

$$\ln p(\boldsymbol{\alpha} \mid \mathbf{h}) \propto -\|\mathbf{h} - \mathbf{M}(\boldsymbol{\phi})\boldsymbol{\alpha}\|_2^2 - \lambda \|\boldsymbol{\alpha}\|_1 . \tag{3.39}$$

Finally, the MAP estimator is given by

$$\hat{\boldsymbol{\alpha}} = \underset{\boldsymbol{\alpha}}{\text{argmin}} \ \lambda \|\boldsymbol{\alpha}\|_1 + \|\mathbf{h} - \mathbf{M}(\boldsymbol{\phi})\boldsymbol{\alpha}\|_2^2 . \tag{3.40}$$

The obtained MAP estimator is equivalent to the estimator given in (3.31). However, we arrived at this result differently by using the Bayesian framework and making the statistical assumption that the complex amplitudes are distributed according to the Laplace distribution. The Laplace distribution has heavy tails, different from the Gaussian distribution which has very light tails. This means that the probability that an observation of a Gaussian random variable can take values far from its mean decreases very fast. In other words, if we provide a Gaussian prior, the predictions far away from the mean are heavily penalized. By selecting a heavy-tail prior distribution with zero mean, we expect that most of the estimates will be around zero, but we allow for a few of them to be large, resulting in a sparse $\boldsymbol{\alpha}$. Therefore, the sparse Bayesian estimation becomes synonymous with imposing heavy-tail priors [159].

Our example does not illustrate the full potential of sparse estimation using the Bayesian framework. Instead, our aim is to illustrate the key idea behind sparse Bayesian estimation. The estimator given in (3.40) is the same as the one given for deterministic sparse estimation (3.31). Therefore, one may wonder what the benefits of formulating sparse estimation in the Bayesian framework are. The Bayesian framework provides us

the flexibility to select the prior distribution that promotes sparsity, and different choices will favor different levels of sparsity [140]. Furthermore, selecting the regularization parameter λ in (3.31) is data-dependent and requires cross-validation. For example, multipath channels in different scattering environments will have different numbers of MPCs, and therefore the optimal selection of parameter λ is data-dependent. The Bayesian framework and hierarchical models enable us to automatically select the regularization parameter and inherently estimate the number of MPCs in the channel [161, 162]. A non-exhaustive list of prior work-related on-grid sparse Bayesian methods for multipath channel estimation is [163, 164, 165, 160]. The off-grid and gridless sparse estimation problems can also be formulated in the Bayesian framework, and in the next sections we will provide a list of related work.

OFF-GRID SPARSE ESTIMATION

In the previous section, we discussed on-grid sparse estimation methods. These methods suffer from basis mismatch when the parameters to be estimated do not lie on the grid defined by the dictionary [155]. The time-delays of the MPCs are continuous parameters, and therefore when using on-grid sparse estimation methods, errors introduced by the basis mismatch are inevitable [166]. Off-grid and gridless sparse estimation methods are proposed in [167] and [168], respectively, to alleviate the basis mismatch problem.

The key idea in off-grid sparse estimation methods is to approximate the model for the dictionary (3.31) to enable estimation of parameters that do not exactly lie on the grid [144]. Let us assume that the phase shift ϕ_k, introduced by the time-delay of the kth MPC, does not lie on the grid defined by the dictionary $\mathbf{M}(\tilde{\boldsymbol{\phi}})$. Then we can approximate its steering vector, i.e., atom, using a first-order Taylor expansion as

$$\mathbf{m}(\phi_k) \approx \mathbf{m}(\tilde{\phi}_{n_k}) + \mathbf{d}(\tilde{\phi}_{n_{\tilde{k}}})(\phi_k - \tilde{\phi}_{n_{\tilde{k}}}), \tag{3.41}$$

where $\mathbf{d}(\tilde{\phi}_{n_{\tilde{k}}}) = \frac{\partial \mathbf{m}(\phi)}{\partial \phi}\Big|_{\phi=\tilde{\phi}_{n_{\tilde{k}}}}$, $\tilde{\phi}_{n_{\tilde{k}}}$ is the nearest grid point to ϕ_k with $|\phi_k - \tilde{\phi}_{n_{\tilde{k}}}| \leq \frac{\Delta}{2}$ and $\Delta = \tilde{\phi}_{\tilde{k}} - \tilde{\phi}_{\tilde{k}-1}, \tilde{k} = 2, \ldots, \tilde{K}$, is the grid interval. Now, the off-grid sparse data model can be written as

$$\mathbf{h} = \left[\mathbf{M}(\tilde{\boldsymbol{\phi}}) + \mathbf{D}(\tilde{\boldsymbol{\phi}})\mathrm{diag}(\Delta\boldsymbol{\phi})\right]\tilde{\boldsymbol{\alpha}} + \mathbf{q}, \tag{3.42}$$

where $\mathbf{M}(\tilde{\boldsymbol{\phi}})$ is defined in (3.30), $\mathbf{D}(\tilde{\boldsymbol{\phi}}) = [\mathbf{d}(\tilde{\phi}_{\tilde{1}}) \ \ldots \ \mathbf{d}(\tilde{\phi}_{\tilde{K}})]$, and $\Delta\boldsymbol{\phi}$ is the vector collecting the grid offsets. Here, $\tilde{\boldsymbol{\alpha}}$ is a sparse vector and the grid offsets $\boldsymbol{\phi} = [\Delta\phi_1 \ \ldots \ \Delta\phi_{\tilde{K}}] \in \left[-\frac{\Delta}{2}, \frac{\Delta}{2}\right]^{\tilde{K}}$, are given by

$$\Delta\phi_{\tilde{k}} = \begin{cases} \phi_k - \tilde{\phi}_{n_{\tilde{k}}}, & \text{if } \tilde{\phi}_{\tilde{k}} = \tilde{\phi}_{n_{\tilde{k}}} \\ 0, & \text{otherwise}. \end{cases} \tag{3.43}$$

Now, the problem of sparse estimation becomes to estimate the parameters $\Delta\boldsymbol{\phi}$ and $\tilde{\boldsymbol{\alpha}}$ from the measurements $\mathbf{h}$ using model (3.42). This problem can be formulated as a sparse total least squares (STLS), BPDN, or sparse Bayesian learning problem as shown in [167], [169], and [170], respectively. Here, we will discuss only the BPDN formulation of the off-grid sparse estimation problem, and for details on other methods, we refer

the reader to previously mentioned references. For the single snapshot case, the sparse off-grid estimation can be formulated as the following BPDN problem

$$\begin{aligned}\hat{\boldsymbol{\alpha}}, \Delta\hat{\boldsymbol{\phi}} = \quad & \underset{\tilde{\boldsymbol{\alpha}}, \Delta\boldsymbol{\phi} \in \left[-\frac{\Delta}{2}, \frac{\Delta}{2}\right]^{\tilde{K}}}{\operatorname{argmin}} \quad \|\tilde{\boldsymbol{\alpha}}\|_1 \,, \\ & \text{subject to } \left\|\mathbf{h} - \left[\mathbf{M}(\tilde{\boldsymbol{\phi}}) + \mathbf{D}(\tilde{\boldsymbol{\phi}})\operatorname{diag}(\Delta\boldsymbol{\phi})\right]\tilde{\boldsymbol{\alpha}}\right\|_2^2 \leq \eta \,,\end{aligned} \tag{3.44}$$

where η should be set according to the expected noise and modeling error levels. This optimization problem is nonconvex, and an alternating algorithm is proposed in [167], that alliteratively solves for $\boldsymbol{\alpha}$ and $\Delta\boldsymbol{\phi}$. However, the difficulty in this algorithm is to select η as it requires prior estimation of noise level and modeling errors, which is often challenging. This issue is solved by formulating off-grid sparse estimation in a Bayesian framework as shown in [170, 171, 172] where the parameter η is automatically selected during the estimation.

To summarize, here we have provided an introduction to off-grid sparse estimation methods. We presented an off-grid sparse estimation method that relies on the fixed grid approach and approximates the dictionary for off-grid phase shifts using the first-order Taylor approximation (3.42). In this method, we needed to jointly estimate the sparse signal $\tilde{\boldsymbol{\alpha}}$ and the grid offset $\Delta\hat{\boldsymbol{\phi}}$ by solving a BPDN-like optimization problem (3.44). Another approach to off-grid sparse estimation is to use a dynamic grid and jointly estimate the sparse vector $\tilde{\boldsymbol{\alpha}}$ and dictionary grid $\tilde{\boldsymbol{\phi}}$ [161, 173, 174]. The off-grid sparse estimation methods overcome the issue of basis mismatch. However, these methods introduce additional unknown parameters that need to be estimated, complicating the algorithm design and implementation. Most of the presented algorithms involve solving nonconvex optimization problems. Therefore, only convergence to the local optimum can be guaranteed. This problem is solved by gridless sparse estimation methods that are presented in the next section.

GRIDLESS SPARSE ESTIMATION

In this section, we provide a brief overview of gridless sparse estimation methods. These methods do not require gridding of the dictionary parameters, i.e., gridding of the phase shifts introduced by time delays of MPCs [144]. Different than on-grid and off-grid sparse estimation methods, these methods work directly in the continuous domain, which solves any issues that arise from grid-based dictionary approximations such as basis mismatch [175, 96]. Furthermore, these methods involve solving convex optimization problems that can be solved in a polynomial-time [176, 177]. Similar to the previous methods, gridless sparse estimation can be formulated in deterministic [176, 177, 178, 179], and Bayesian frameworks [180, 181, 182, 183].

Many gridless sparse estimation methods rely on Vandermonde decomposition of Toeplitz covariance matrices. In particular, these methods transform the frequency estimation problem into the estimation of a positive semidefinite (PSD) Toeplitz matrix from available measurements. The estimated PSD Toeplitz matrix encodes the unknown frequencies, which can be estimated from its Vandermonde decomposition [178, 179]. This is different from classical subspace-based estimation algorithms, where frequencies are estimated from sample covariance matrices that are computed directly from the

available measurements. In stead, the gridless methods use optimization methods to estimate the data covariance matrix from the available measurements by enforcing special structures on it such that it is a PSD Toeplitz matrix with low-rank properties [168]. In general, these methods show better performance than classical subspace-based estimation methods. However, they often require solving computationally unattractive semidefinite programming problems (SDP).

In the context of multipath channel time-delay estimation, the covariance matrix will have a Toeplitz structure only when the measurements are collected in consecutive frequency bands. Therefore many of these methods can not be used for estimation in scenarios where channel measurements are collected in multiple separated frequency bands. The Bayesian view on the problem of gridless sparse estimation of complex exponentials is taken in [180, 183]. In these works, the stochastic ML model regularized by a sparsity promoting prior on the coefficients of the exponentials is used to describe the measurements. These algorithms, in general, have a high estimation accuracy and inherently estimate the number of MPCs present in the channel. In particular, the VALSE algorithm allows gridless estimation of complex exponentials with automatic estimation of the number of MPCs from incomplete but single snapshot measurements [180]. However, this is an iterative algorithm with a high computational complexity due to the variational estimation of the posterior on the frequencies. Its per-iteration complexity is cubic in the number of exponentials, and therefore, its complexity increases rapidly with the number of MPCs.

3.5. CONCLUSIONS

This section introduces the problem of multipath channel time-delay estimation and signal model for multipath channel measurements. We showed that transforming the presented signal model to the frequency domain results in a model that is well known in super-resolution spectral estimation. Subsequently, we described the main challenges of super-resolution problems and introduced several popular signal processing frameworks that can be applied to these problems, such as ML, subspace-based, and compressive sensing-based estimation. We saw that ML algorithms provide unbiased and statistically efficient solutions, yet they are often impractical for implementation. On the other hand, subspace-based approaches have lower computational complexity while performing similarly to ML algorithms. However, the performance of the subspace-based methods inherently depends on the accuracy of the estimated subspaces. Lastly, we discussed sparse estimation methods, including both their deterministic and Bayesian formulation. The main challenges related to these methods are basis mismatch and regularization parameter selection for on-grid sparse estimation methods and computational complexity for gridless sparse estimation methods.

In the rest of this thesis, we will use several of the algorithms presented in this chapter to evaluate the performance of the proposed algorithms that are presented later. In particular, in Chapter 4, we will use ML, MUSIC, ESPRIT and L1 algorithms discussed in Sections 3.4.2, 3.4.3, 3.4.3 and 3.4.4 respectively, for estimation of multipath channel time-delays. Likewise, in Chapters 5 and 7, we will use subspace-based algorithms presented in Section 3.4.3 to estimate multipath channel time-delays and clock-skew of the

wireless nodes. Finally, in Chapter 7, $\ell_{2,1}$-norm based sparse estimation algorithm presented in Section 3.4.4 will be used to jointly estimate multipath channel time-delays and the frequency response of RF transcivers.

4

MULTIBAND TIME-DELAY ESTIMATION FOR RANGING AND LOCALIZATION

"All models are wrong, but some are useful."
— George Box

Part of this chapter is published as: T. Kazaz, GJM Janssen, J. Romme, and A.J. van der Veen, "Delay Estimation for Ranging and Localization Using Multiband Channel State Information", *IEEE Transactions on Wireless Communications*, 2021.

4.1. INTRODUCTION

IN the previous chapters, we presented the idea of utilizing radio frequency (RF) signals [39] to enable precise localization in GPS-denied environments. Localization using these signals starts with the estimation of the multipath channels between the mobile node and multiple anchors [40]. In chapters 2 and 3 we discussed the parametric multipath channel model and the relation of its parameters to the location. In particular, we showed that the time-delay of the line-of-sight (LOS) path is directly linked to the range (distance) of the mobile node to the anchor, and forms the input for range-based localization methods based on time-of-arrival (TOA) and time-difference-of-arrival (TDOA). The localization performance of these methods primarily depends on channel estimation and the ability to resolve MPCs, estimate their parameters, and detect the LOS path. Therefore, to improve the accuracy of localization, it is crucial to increase the resolution of multipath channel time-delay estimation.

In this chapter, we focus on high-resolution estimation of multipath channel time-delays. Channel estimation is fundamental to wireless communications, but there this information is primarily used for equalization [153, 154, 184, 185], where the precise knowledge of multipath parameters is not really important. Classically, time-delay estimation is based on searching for the first dominant peak in the correlation between the received signal and the known training signal [50]. In Chapter 3, we saw that the resolution of such methods is limited by the inverse of the bandwidth of the training signal. Typical training signals used in wireless networks have a fairly low bandwidth due to RF spectrum regulations and hardware constraints. The insufficient resolution prevents separation of the LOS path from closely arriving MPCs, leading to biased range estimates and degraded localization performance [186]. Therefore, the main challenge is the design of *(i)* a practical approach for measuring the channel, and *(ii)* high-resolution time-delay estimation algorithms in the presence of close-in multipath.

The early multipath channel estimation methods were based on maximum likelihood (ML) estimation [72]. It is known that ML estimators are asymptotically consistent and statistically efficient when the number of measurements increases to infinity [72]. However, these methods are often not practical for implementation as they involve minimizing highly multimodal objective functions with many local minima. Many of the super-resolution estimation methods that are presented in Chapter 3 have been applied to the problem of multipath channel time-delay estimation. The methods proposed in the previous works can be classified into those based on *(i) subspace estimation* [92, 187, 188], *(ii) compressive sensing* (CS) [87, 89], and *(iii) finite-rate-of-innovation* (FRI) sampling [189, 99, 190]. However, most of these works consider multipath parameter estimation from channel measurements collected in a single frequency band, limiting the resolution of time-delay estimation.

The route to improve the resolution of time-delay estimation is to increase the bandwidth of the training signals. Practical approaches to achieve this are based on multiband channel probing [191, 192, 193, 194] (see Fig. 4.2). Here, multiple frequency bands are probed during the channel coherence time to increase the frequency aperture of the CSI measurements, thereby increasing the resolution of time-delay estimation. Calibration is needed to undo the effects of transceiver impairments such as frequency and

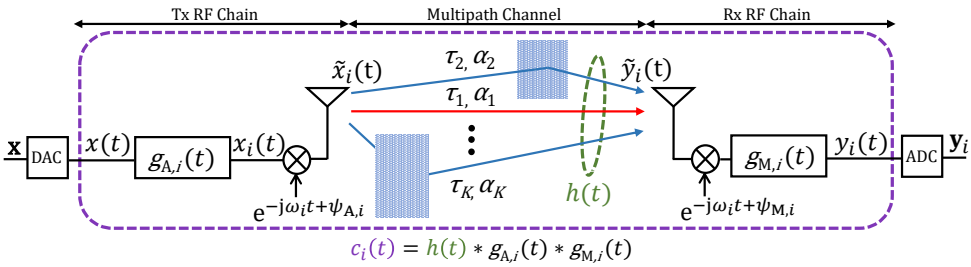

Figure 4.1: The multipath propagation environment between a mobile node and an anchor, described by K MPCs, where the red color denotes the LOS path. Each MPC is characterized by its complex gain α_k and time-delay τ_k. The equivalent baseband channel (including the effects of the RF chains) is $c_i(t)$, where index i refers to the ith band in a multiband system.

phase offsets that affect each band differently [47]. In [47], MUSIC is used for time-delay estimation. However, this approach does not exploit all structures present in the multiband CSI, which results in statistically inefficient estimation. In [192, 194], compressed sensing algorithms based on $\ell 1$-norm regularized least squares (CS(L1)) are proposed. However, these algorithms consider the collection of CSI in consecutive bands and have limited resolution due to basis mismatch.

On the other hand, the classical gridless sparse estimation methods require that multiband channel measurements are collected in consecutive bands to ensure a Toeplitz structure of the covariance matrix of the measurements. This constraint is alleviated by formulating the problem of multiband time-delay estimation in a sparse Bayesian framework. In particular, the VALSE algorithm [180] discussed in Section 3.4.4 can be applied to the problem of multiband time-delay estimation. However, this algorithm has a high numerical complexity that increases rapidly with the number of MPCs present in the channel.

In this chapter, we present a method that exploits the multiband and carrier frequency switching capabilities of modern wireless transceivers, and we propose to acquire the CSI on multiple bands spread over a large frequency aperture to increase time-delay resolution. We start by deriving the data model for multiband CSI considering orthogonal frequency-division multiplexing (OFDM) training signals as used in WiFi, LTE, and DVB networks, but we do not require the collection of CSI in consecutive bands. After stacking the multiband CSI into Hankel matrices, the data model shows a multiple shift-invariance structure. The same structure appears in DOA estimation [195], and related multidimensional spectral estimation algorithms are applicable to this problem [196]. We use these properties to develop a weighted subspace fitting algorithm for time-delay estimation that exploits a multiple shift-invariance structure present in the multiband CSI. We present the optimal weighting and introduce several data extension techniques that further improve the performance of the algorithm. After time-delay estimation, the complex amplitudes of MPCs are estimated by solving a linear least-squares (LS) problem. Then, we derive the Gaussian Cramér-Rao Bound (CRB) [55] for the multiband CSI data model and analyze the effects of wireless system parameters, e.g., bandwidth, number of CSI measurements, and band selection on the CRB. Finally, we demon-

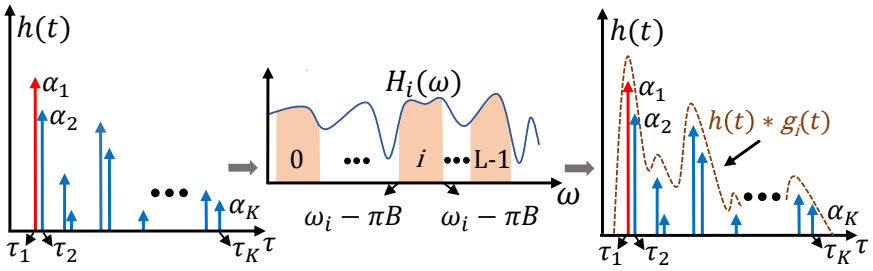

Figure 4.2: Multiband channel probing and effects of the limited transceivers' bandwidth on the time-delay resolution of multipath components.

4

strate the applicability of the proposed algorithm to the problem of time-delay estimation in the future WiFi-7 network defined by the IEEE 802.11be standard [197]. This standard will support multiband operation in 2.4, 5, and 6 GHz bands, which makes this application an interesting showcase for the proposed algorithm. Various scenarios are simulated to show the influence of wireless system parameters on the algorithm's performance.

4.2. DATA MODEL

In this section, we introduce the ranging scenario and derive the corresponding data model. We start derivations from the discrete model for multipath channel measurements presented in Chapter 3 and extend it to the model for multiband channel measurements. While doing derivations, we repeat some of the results presented in Chapter 3. However, to be relevant to current WiFi standards, the model and derivations are now tailored to the scenario of multiband channel ranging using OFDM training signals. In particular, we consider a localization system that uses OFDM training signals exchanged at multiple bands, i.e., frequency channels, to obtain multiband CSI measurements. We will refer to WiFi frequency channels as frequency bands. We first define continuous-time signal models for training signals and the multipath channel. We then derive the data model for multiband CSI, which reveals the multiple-shift invariance structure of the measurements. Finally, we briefly discuss synchronization impairments between transceivers and the impact of phase offset on the measurements.

4.2.1. SYSTEM MODEL

Consider a localization system that uses OFDM training signals to estimate ranges between the mobile node and at least three (four) anchors for localization in 2-D (3-D) space. This process starts with the exchange of a known training signal $x(t)$ between an anchor and the mobile node (or vice versa), and estimation of the corresponding multipath channel (cf. Fig. 4.1). Assume that the training signal has N orthogonal subcarriers in a single OFDM symbol where the symbol duration is T_{sym} and the frequency spacing of adjacent subcarriers is $\omega_{\text{sc}} = 2\pi / T_{\text{sym}}$. The duration of each OFDM symbol is periodically extended with the cyclic prefix of duration T_{cp} to ensure cyclic convolution with

the channel, which results in the total duration of a transmission block $T = T_{\text{sym}} + T_{\text{cp}}$. The baseband model for the training signal in a single transmission block can be written as

$$x(t) = \left[\sum_{n=0}^{N-1} s[n] e^{j\omega_{\text{sc}} nt} \right] p(t-T), \tag{4.1}$$

where $\mathbf{s} = [s[0], \ldots, s[N-1]]^T \in \mathbb{C}^N$ are the known training symbols, and

$$p(t) = \begin{cases} 1, & t \in [-T_{\text{cp}}, T_{\text{sym}}], \\ 0, & \text{otherwise}. \end{cases}$$

This training signal is upconverted to the carrier frequency ω_i and transmitted as

$$\tilde{x}_i(t) = \text{Re}\left\{ x(t) e^{j(\omega_i t + \psi_{\text{A},i})} \right\}, \tag{4.2}$$

where $\psi_{\text{A},i}$ is an unknown phase of the local oscillator at the anchor node. Here we assumed, without loss of generality, that all frequency channels use the same training signal, as is often done in practice. We further consider that the anchor and mobile node are frequency synchronized during channel probing. This is typically the case in practical OFDM systems, where before channel estimation a frequency offset is estimated and compensated using known training signals such as legacy short and long training fields (L-STF and L-LTF) in IEEE 802.11be [197].

4.2.2. MULTIBAND CHANNEL PROBING

To probe the multipath channel, the training signal $x(t)$ is transmitted at L separate frequency bands, $\mathcal{W}_i = [\omega_i - \pi B, \omega_i + \pi B]$, where B is the bandwidth and ω_i is the central angular frequency of the ith band (cf. Fig. 4.2). We consider that the multipath channel is probed over a large frequency aperture. Therefore, it is suitable to use the UWB channel model presented in Chapter 3 to model the propagation between the anchor and the mobile node. For this channel, the continuous-time channel impulse response (CIR) $h(t)$ is given by (3.1). We assume that there are K resolvable MPCs in the channel where their time-delays are sorted in increasing order, i.e., $\tau_{k-1} < \tau_k$, $k = 2, \ldots, K$, and τ_1 is considered to be the time-delay of the LOS path. The complex path amplitudes are assumed to be wide-sense stationary and mutually uncorrelated Gaussian random variables with PDF given by $\alpha_k \sim \mathcal{CN}(0, \sigma^2_{\alpha,k})$, $k = 1, \ldots, K$, where $\sigma^2_{\alpha,k}$ is their average power.

Practical wideband antennas and RF chains have a frequency-dependent response [198]. We model the compound frequency response of the RF chains including antennas at the ith probed band as an equivalent linear and time-invariant baseband filter with impulse response $g_i(t) = g_{\text{A},i}(t) * g_{\text{M},i}(t)$ (cf. Fig. 4.1). Here, $g_{\text{A},i}(t)$ and $g_{\text{M},i}(t)$ are the impulse responses of the RF chains at the transmitter and receiver, respectively. The filter $g_i(t)$ has frequency response $G_i(\omega)$ with passband $\omega \in [-\pi B, \pi B]$. Then, the compound impulse response of the multipath channel and RF chains at the ith band is given by

$$c_i(t) = h(t) * g_i(t). \tag{4.3}$$

We assume that the $c_i(t)$, $i = 0, \ldots, L-1$, are time-limited to the duration of the OFDM symbol's cyclic prefix, i.e., $c_i(t) = 0$ for $t \notin [0, T_{\text{cp}}]$. Therefore, there is no inter-symbol interference, allowing us to consider the signal model for a single OFDM symbol.

Now, using the results of Section 3.4.1, the frequency domain baseband model for the signal received at the ith frequency band is given by

$$Y_i(\omega) = \begin{cases} X(\omega)C_i(\omega) + Q_i(\omega), & \omega \in [-\pi B, \pi B] \\ 0, & \text{otherwise}, \end{cases} \tag{4.4}$$

where $C_i(\omega)$ is the compound Channel Frequency Response (CFR), and $X(\omega)$ and $Q_i(\omega)$ are the CTFTs of the training signal $x(t)$ and low-pass filtered Gaussian noise $q_i(t)$, respectively. Further, with a slight abuse of notation, $C_i(\omega) = G_i(\omega)H_i(\omega)$, where in using subscript i in $H_i(\omega)$ we implicitly take into account the bandwidth limitation effect of $G_i(\omega)$ on the CTFT of $h(t)$, and write $H_i(\omega)$ as

$$H_i(\omega) = \sum_{k=1}^{K} \alpha_k e^{-j(\omega_i+\omega)\tau_k}, \quad \omega \in [-\pi B, \pi B]. \tag{4.5}$$

Here, we assumed that the mobile node and anchor are phase synchronized (cf. the remark at the end of this section for the signal model in the presence of the phase offset).

4.2.3. DISCRETE DATA MODEL

The receiver samples signal $y_i(t)$ with period $T_s = 1/B$, performs packet detection, symbol synchronization, and removes the cyclic prefix. During the period of a single OFDM symbol, N complex samples are collected, where N is equal to the number of subcarriers and $T_{\text{sym}} = NT_s$. Next, an N-point DFT is applied on the collected samples, and they are stacked in increasing order of DFT frequencies in $\mathbf{y}_i \in \mathbb{C}^N$. The discrete-time data model of the received signal (4.4) can be written as

$$\mathbf{y}_i = \text{diag}(\mathbf{s})\mathbf{c}_i + \mathbf{q}_i, \tag{4.6}$$

where $\mathbf{q}_i \sim \mathcal{CN}(\mathbf{0}_N, \sigma^2_{q_i}\mathbf{I}_N)$ represents a complex Gaussian normal distributed noise vector with mean $\mathbf{0}_N$ and covariance matrix $\sigma^2_{q_i}\mathbf{I}_N$. The vector $\mathbf{c}_i$ collects N samples of the compound CFR at the subcarrier frequencies, and its entries are

$$[\mathbf{c}_i]_n = \int_0^{T_{sym}} c_i(t)e^{-j\omega_{sc}nt}dt, \quad n = -\frac{N}{2}, \ldots, \frac{N}{2} - 1, \tag{4.7}$$

where $\omega_{sc} = \frac{2\pi}{NT_s}$, and we assume that N is an even number. Similarly, from (4.3) we obtain (see [199] for details)

$$\mathbf{c}_i = \text{diag}(\mathbf{g}_i)\mathbf{h}_i, \tag{4.8}$$

where $\mathbf{g}_i$ and $\mathbf{h}_i$ collect samples of $G_i(\omega)$ and $H_i(\omega)$ at the subcarrier frequencies, respectively. We further refer to $\mathbf{h}_i$ as the CSI vector and its entries are given as

$$H_i[n] = H_i(n\omega_{\text{sc}}), \quad n = -\frac{N}{2}, \ldots, \frac{N}{2} - 1. \tag{4.9}$$

We consider that the bands $\{\mathcal{W}_i\}_{i=0}^{L-1}$ lie on a discrete frequency grid, i.e., $\omega_i = \omega_0 + n_i\omega_{sc}, i = 1, \ldots, L-1$, where $n_i \in \mathbb{N}$. This is always the case in the WiFi standards [197].

Inserting the channel model (4.5) into (4.9) gives

$$H_i[n] = \sum_{k=1}^{K} \alpha_k e^{-jn_i\omega_{\text{sc}}\tau_k} e^{-jn\omega_{\text{sc}}\tau_k}, \tag{4.10}$$

where $e^{-j\omega_0\tau_k}$ and the normalizing phase shift factor $\phi_k^{-N/2}$ are absorbed in $\alpha_k \,\forall\, k$. Then, $\mathbf{h}_i$ can be written in a more compact form as

$$\mathbf{h}_i = \mathbf{M}\boldsymbol{\Theta}_i\boldsymbol{\alpha}, \tag{4.11}$$

where $\mathbf{M} \in \mathbb{C}^{N\times K}$ is a Vandermonde matrix, given by (3.13). However, now $\phi_k = \omega_{\text{sc}}\tau_k$ is the phase shift introduced by the kth MPC over the subcarriers. Likewise, $\boldsymbol{\Theta}_i$ is a diagonal matrix that collects the band dependent phase shifts introduced by the time-delays $\{\tau_k\}_{k=1}^K$ and the complex path amplitudes are collected in $\boldsymbol{\alpha} = [\alpha_1,\ldots,\alpha_K]^T \in \mathbb{C}^K$. In view of the band positions on the frequency grid, we can write $\boldsymbol{\Theta}_i = \boldsymbol{\Phi}^{n_i}$, where $\boldsymbol{\Phi} = \text{diag}([\phi_1 \cdots \phi_K])$.

We assume that none of the entries of $\mathbf{s}$ or $\mathbf{g}_i$ are zero or close to zero, so we can estimate the CSI from the data vector $\mathbf{y}_i$ using classical channel estimation in the frequency domain as $\mathbf{h}_i = \text{diag}^{-1}(\mathbf{s}\odot\mathbf{g}_i)\mathbf{y}_i$ [200]. Then, from models (4.6) and (4.8), with a slight abuse of notation considering $\mathbf{q}_i$, it follows that $\mathbf{h}_i$ satisfies the model

$$\mathbf{h}_i = \mathbf{M}\boldsymbol{\Phi}^{n_i}\boldsymbol{\alpha} + \mathbf{q}_i. \tag{4.12}$$

Here, we assume that the frequency response $\mathbf{g}_i$ of the RF chains is calibrated and known. An algorithm for joint calibration and time-delay estimation is presented in Chapter 6 and [84]. The training symbols $\mathbf{s}$ typically have a constant magnitude by design, and we assume that the frequency responses of the receiver chains $\mathbf{g}_i$ can be assumed almost flat for a single frequency band. Therefore $\mathbf{q}_i$ is zero-mean white Gaussian distributed noise with covariance $\mathbf{R}_{\text{q}_i} = \sigma^2_{\text{q}_i}\mathbf{I}_N$. When the frequency responses of the RF chains are not flat, $\mathbf{q}_i$ will be colored noise. However, its coloring is known and can be taken into account. We conclude this section with a remark on the influence of phase offset on the estimated channel model (4.12).

Remark. If the mobile node and anchor are not phase synchronized, i.e., $\psi_{\text{M},i} \not\approx \psi_{\text{A},i}$, the data model for the CSI collected at a mobile node becomes

$$\mathbf{h}_{\text{M},i} = \boldsymbol{\Psi}_i\mathbf{h}_i, \tag{4.13}$$

where $\boldsymbol{\Psi}_i = e^{-j\psi_i}\mathbf{I}_N$ and $\psi_i = \psi_{\text{M},i} - \psi_{\text{A},i}$ is the unknown phase offset at the ith carrier frequency. The phase offset changes whenever the carrier frequency of the transceivers is changed. However, assuming that the transceiver is capable of Tx/Rx switching while keeping the phase lock loop (PLL) in-lock, ψ_i stays the same for a fixed carrier frequency and has the opposite sign when estimated at the mobile node compared to the anchor. Using this property and assuming that the channel is reciprocal, we can write the model for the CSI collected at the anchor as $\mathbf{h}_{\text{A},i} = \boldsymbol{\Psi}_i^*\mathbf{h}_i$. Now, the phase offset can be eliminated by taking the square-root of the point-wise product between collected CSIs as $\mathbf{h}_{\text{D},i} = (\mathbf{h}_{\text{M},i}\odot\mathbf{h}_{\text{A},i})^{1/2} = \pm\mathbf{h}_i$, where the exponent is applied element-wise. Here, the square-root is used to avoid generation of additional unknown time-delays which are the result of inter-products between $\{\phi_k\}_{k=1}^K$. The resulting measurements satisfy the model $\mathbf{h}_{\text{D},i} = \pm\mathbf{M}\boldsymbol{\Theta}_i\boldsymbol{\alpha}$, where the ambiguity can be resolved by tracking the phase difference between multiple bands [201].

4.3. MULTIBAND TIME-DELAY ESTIMATION

Given the CSI estimates $\mathbf{h}_i$, $i = 0,\dots,L-1$, the problem of ranging is to detect the LOS MPC and estimate its time-delay τ_1. Then the range between the mobile node and an anchor is given by $d = \tau_1 c$, where c denotes the speed of light. To do this accurately, all MPCs present in the channel need to be resolved and accordingly their time-delay and amplitude parameters $\{\tau_k, \alpha_k\}_{k=1}^K$ must be estimated. We start by stacking the CSI estimates $\mathbf{h}_i$, $i = 0,\dots,L-1$, into a multiband CSI vector $\mathbf{h} = [\mathbf{h}_0^T,\dots,\mathbf{h}_{L-1}^T]^T \in \mathbb{C}^{NL\times 1}$. Using the model (4.12), it follows that $\mathbf{h}$ satisfies

$$\mathbf{h} = \mathbf{A}\boldsymbol{\alpha} + \mathbf{q} := \begin{bmatrix} \mathbf{M} \\ \mathbf{M}\boldsymbol{\Phi}^{n_1} \\ \vdots \\ \mathbf{M}\boldsymbol{\Phi}^{n_{L-1}} \end{bmatrix} \boldsymbol{\alpha} + \begin{bmatrix} \mathbf{q}_0 \\ \mathbf{q}_1 \\ \vdots \\ \mathbf{q}_{L-1} \end{bmatrix}. \tag{4.14}$$

If the band center frequencies ω_i are uniformly spaced, then matrix $\mathbf{A}$ has a multiple shift-invariance structure and resembles the data model of Multiple Invariance ESPRIT [195], which was exploited in our initial works [202] and [203]. The results of the latter work are presented in Chapter 5. In the more general case, the overall structure present in (4.14) can be exploited to estimate the time-delay parameters $\{\tau_k\}_{k=1}^K$ from the phase shifts $\boldsymbol{\phi} = [\phi_1 \cdots \phi_K]$. These phase shifts are introduced over both subcarrier and band frequency apertures. The small aperture of the subcarriers promotes poor resolution but unambiguous estimation, while the very large aperture of the bands favors high resolution but results in ambiguous estimation of the time-delay parameters. We aim at an algorithm that will provide both high resolution and unambiguous time-delay estimates. To utilize all the structure present in the measurements, we formulate the multiband time-delay estimation as a multidimensional spectral estimation problem. We then propose an algorithm that estimates the time-delays $\{\tau_k\}_{k=1}^K$ by solving a weighted subspace fitting problem. After estimating the time-delays, the amplitudes $\{\alpha_k\}_{k=1}^K$ are estimated by solving a linear LS problem.

4.3.1. ALGORITHM OUTLINE

We first outline the key idea and the procedure for the estimation, and then introduce improvements to arrive at the final algorithm.

In subspace fitting methods, we would like to estimate the column span of $\mathbf{A}$ in (4.14). However, this "signal subspace" cannot be directly estimated from a single snapshot of the multiband CSI $\mathbf{h}$. To restore the rank, we construct Hankel matrices $\mathbf{H}_i$ of size $P \times Q$ from the vectors $\mathbf{h}_i$, $i = 0,\cdots,L-1$, as

$$\mathbf{H}_i := \begin{bmatrix} H_i[0] & H_i[1] & \cdots & H_i[Q-1] \\ H_i[1] & H_i[2] & \cdots & H_i[Q] \\ \vdots & \vdots & \ddots & \vdots \\ H_i[P-1] & H_i[P] & \cdots & H_i[N-1] \end{bmatrix}, \tag{4.15}$$

where P is a design parameter, and $Q = N - P + 1$. From (4.12) and the shift-invariance

structure present in $\mathbf{M}$, the constructed Hankel matrices have the factorization

$$\mathbf{H}_i = \mathbf{M}'\mathbf{\Phi}^{n_i}\mathbf{X} + \mathbf{Q}'_i, \tag{4.16}$$

where $\mathbf{M}'$ is an $P \times K$ submatrix of $\mathbf{M}$,

$$\mathbf{X} := [\boldsymbol{\alpha} \quad \mathbf{\Phi}\boldsymbol{\alpha} \quad \mathbf{\Phi}^2\boldsymbol{\alpha} \cdots \mathbf{\Phi}^{Q-1}\boldsymbol{\alpha}],$$

and $\mathbf{Q}'_i$ is a noise matrix with covariance $\mathbf{R}_{\mathrm{q}'_i} = \sigma^2_{\mathrm{q}'_i}\mathbf{I}_P$. Then we construct a block-row matrix $\mathbf{H}$ of size $LP \times Q$ by stacking matrices $\mathbf{H}_i$, $i = 0, \ldots, L-1$, as

$$\mathbf{H} := \begin{bmatrix} \mathbf{H}_0 \\ \mathbf{H}_1 \\ \vdots \\ \mathbf{H}_{L-1} \end{bmatrix}. \tag{4.17}$$

The matrix $\mathbf{H}$ preserves the shift-invariance properties of $\mathbf{h}$ and has a factorization

$$\mathbf{H} = \mathbf{A}'(\boldsymbol{\phi})\mathbf{X} + \mathbf{Q}' := \begin{bmatrix} \mathbf{M}' \\ \mathbf{M}'\mathbf{\Phi}^{n_1} \\ \vdots \\ \mathbf{M}'\mathbf{\Phi}^{n_{L-1}} \end{bmatrix} \mathbf{X} + \begin{bmatrix} \mathbf{Q}'_0 \\ \mathbf{Q}'_1 \\ \vdots \\ \mathbf{Q}'_{L-1} \end{bmatrix}. \tag{4.18}$$

Therefore, if we can choose the design parameter P such that both $LP \geq K$ and $Q \geq K$ and if all factors in (4.16) are full rank, then $\mathbf{H}$ has rank K, the number of MPCs present in the channel. This means that from the column span of $\mathbf{H}$ we can estimate matrix $\mathbf{A}'$ up to a $K \times K$ non-singular matrix $\mathbf{T}$. In other words, we can write $\mathbf{A}' = \mathbf{U}\mathbf{T}^{-1}$, where the columns of $\mathbf{U}$ form a K-dimensional basis of the column space of $\mathbf{H}$.

The matrix $\mathbf{U}$ can of course be estimated using a singular value decomposition (SVD) of $\mathbf{H}$, and selecting the left singular vectors corresponding to the K largest singular values $\{\lambda_j\}_{j=1}^K$. If the noise levels $\sigma^2_{\mathrm{q}'_i}$, $i = 1, \ldots, L-1$, are known and unequal, the blocks $\mathbf{H}_i$ can be prewhitened prior to taking the SVD of $\mathbf{H}$. The dimension K can be estimated from the singular values using information-theoretic criteria [204]. In particular, in Chapter 8 we find K as the value $k \in \{0, 1, \ldots, Q-1\}$ that minimizes the modified minimum description length (MDL) criteria [205] given by

$$\begin{aligned} \mathrm{MDL}(k) = &-(D-k)D \cdot \log \frac{\prod_{j=k+1}^{D} \lambda_j^{1/(D-k)}}{\frac{1}{D-k}\sum_{j=k+1}^{D} \lambda_j} \\ &+ k(2D-k) \cdot \log(D)/4 + k, \end{aligned} \tag{4.19}$$

where $D = Q - 1$.

The estimation of $\boldsymbol{\phi}$ from $\mathbf{H}$ is based on exploiting the shift invariance structure present in $\mathbf{A}'$ and $\mathbf{U}$. Accounting for the errors introduced during estimation of $\mathbf{U}$, we can write $\mathbf{A}'(\boldsymbol{\phi}) \approx \hat{\mathbf{U}}\mathbf{T}^{-1}$. Now, to estimate $\boldsymbol{\phi}$, we formulate the subspace fitting problem

$$\hat{\boldsymbol{\phi}}, \hat{\mathbf{T}} = \underset{\boldsymbol{\phi}, \mathbf{T}}{\operatorname{argmin}} \left\| \hat{\mathbf{U}} - \mathbf{A}'(\boldsymbol{\phi})\mathbf{T} \right\|_F^2. \tag{4.20}$$

The problem of minimizing the cost function in (4.20) is a nonlinear least-squares (NLS) problem. It is easy to see that for the optimal $\boldsymbol{\phi}$, the optimal $\mathbf{T}$ must satisfy $\mathbf{T} = \mathbf{A}'^{\dagger}(\boldsymbol{\phi})\hat{\mathbf{U}}$. Therefore, this problem can be further recast into a separable nonlinear least-squares (SNLS) problem [112],

$$\begin{aligned} \hat{\boldsymbol{\phi}} &= \underset{\boldsymbol{\phi}}{\operatorname{argmin}}\ J(\boldsymbol{\phi}), \\ J(\boldsymbol{\phi}) &= \operatorname{Tr}\left(\mathbf{P}^{\perp}_{\mathbf{A}'}(\boldsymbol{\phi})\hat{\mathbf{U}}\hat{\mathbf{U}}^{H}\right), \end{aligned} \tag{4.21}$$

where $\mathbf{P}^{\perp}_{\mathbf{A}'}(\boldsymbol{\phi}) = \mathbf{I} - \mathbf{P}_{\mathbf{A}'}$ and $\mathbf{P}_{\mathbf{A}'} = \mathbf{A}'\mathbf{A}'^{\dagger}$ is a projection onto the column span of $\mathbf{A}'$. This reformulation reduces the dimension of the parameter space and also results in a better-conditioned problem, which can be efficiently solved using iterative optimization methods such as variable projection or the Levenberg-Marquardt (LM) [112]. We use the LM method, where good initialization of the algorithm is obtained by the multiresolution time-delay (MRTD) estimation algorithm [203]. With this initialization, the LM method converges very fast, typically within five steps for moderate signal-to-noise ratios (SNRs) as shown in Section 4.5.

4

4.3.2. WEIGHTING

The dominant sources of estimation errors in (4.20) are caused by perturbations of the subspace estimates. The estimated singular vectors in $\hat{\mathbf{U}}$ are each perturbed differently. Thus, the estimator based on unweighted subspace fitting is not statistically efficient, and it is sensitive to noise. These errors can be reduced by introducing an appropriate column weighting in the cost function (4.21), [206]. Therefore, to improve estimation and to penalize subspace perturbation errors, we estimate $\boldsymbol{\phi}$ by solving the following weighted subspace fitting problem [196]

$$\hat{\boldsymbol{\phi}}, \hat{\mathbf{T}} = \underset{\boldsymbol{\phi},\mathbf{T}}{\operatorname{argmin}}\ \left\|\hat{\mathbf{U}}\mathbf{W}^{1/2} - \mathbf{A}'(\boldsymbol{\phi})\mathbf{T}\right\|_F^2, \tag{4.22}$$

where $\mathbf{W}$ is a $K \times K$ matrix. Similar as in (4.21), this problem can be recast to the SNLS problem with a cost function $J(\boldsymbol{\phi}) = \operatorname{Tr}(\mathbf{P}^{\perp}_{\mathbf{A}'}(\boldsymbol{\phi})\hat{\mathbf{U}}\mathbf{W}\hat{\mathbf{U}}^{H})$, and the same initialization and optimization methods can be applied to find the solution. The matrix $\mathbf{W}$ is assumed to be positive definite and Hermitian, and its role is to whiten perturbations of the singular vectors in $\hat{\mathbf{U}}$. A good choice for $\mathbf{W}$ is given in [206] as

$$\mathbf{W} = \hat{\boldsymbol{\Lambda}}_{\mathrm{s}} - \hat{\sigma}^2\mathbf{I}_K, \tag{4.23}$$

where $\hat{\boldsymbol{\Lambda}}_{\mathrm{s}}$ is a diagonal matrix that collects the K largest squared singular values of $\mathbf{H}$ and $\hat{\sigma}^2$ is the estimated noise power. The noise power $\hat{\sigma}^2$ follows from the noise levels $\sigma^2_{\mathrm{q}'_i}$, $i = 1, \ldots, L-1$. If these are unequal, we would prewhiten the blocks $\mathbf{H}_i$ prior to taking the SVD of $\mathbf{H}$.

4.3.3. DATA EXTENSIONS

In this section, we discuss techniques for extending the data matrix $\mathbf{H}$ if multiple channel measurements are available or if subcarrier frequencies of a multiband training signal satisfy a centro-symmetric configuration.

MULTIPLE SNAPSHOTS

So far, we have assumed that the CSI is collected only once during the channel coherence time. However, the coherence time of common multipath radio channels is much longer than the duration of training signals. For example, the indoor radio channel that characterizes propagation of WiFi signals in the 2.4 GHz frequency band between anchors and pedestrians with a velocity of 1 m/s, has a coherence time of approximately 53 ms. Now, assuming that a WiFi training signal with a duration of 40 μs is used to estimate the CSI, then at least 50 snapshots of CSI can be collected during the coherence time.

Let us assume that M snapshots of multiband CSI (4.14) are collected during the coherence time. These measurements satisfy the model

$$\mathbf{h}^{(m)} = \mathbf{A}\boldsymbol{\alpha}^{(m)} + \mathbf{q}^{(m)}, \quad m = 1, \ldots, M. \tag{4.24}$$

where $\boldsymbol{\alpha}^{(m)}$ collects the complex amplitudes of the MPCs. Similar as in the single snapshot case, from every snapshot $\mathbf{h}^{(m)}$ a block Hankel matrix $\mathbf{H}^{(m)}$ is formed as shown in Section 4.3.1. We assume that the time-delays $\{\tau_k^{(m)}\}_{k=1}^K$ of the MPCs stay the same during the coherence time. On the other hand, we assume that the amplitudes $\alpha^{(m)}$ are complex Gaussian random variables that can vary with time while their mean magnitudes stay constant during the coherence time. Similar as in (4.18), the matrix $\mathbf{H}^{(m)}$ satisfies the model $\mathbf{H}^{(m)} := \mathbf{A}'\mathbf{X}^{(m)} + \mathbf{Q}'^{(m)}$, where now $\mathbf{X}^{(m)} := [\boldsymbol{\alpha}^{(m)} \quad \boldsymbol{\Phi}\boldsymbol{\alpha}^{(m)} \cdots \boldsymbol{\Phi}^{Q-1}\boldsymbol{\alpha}^{(m)}]$, and $\mathbf{Q}'^{(m)}$ represents the noise matrix of the mth snapshot. The matrices $\mathbf{H}^{(m)}$, $m = 1, \ldots, M$, have the same column subspace and from them an extended $LP \times QM$ data matrix is constructed as

$$\boldsymbol{\mathcal{H}} := [\mathbf{H}^{(1)} \quad \mathbf{H}^{(2)} \cdots \mathbf{H}^{(M)}]. \tag{4.25}$$

The matrix $\boldsymbol{\mathcal{H}}$ has a factorisation

$$\boldsymbol{\mathcal{H}} = \mathbf{A}'\boldsymbol{\mathcal{X}} + \boldsymbol{\mathcal{Q}}, \tag{4.26}$$

where $\boldsymbol{\mathcal{X}} := [\mathbf{X}^{(1)} \cdots \mathbf{X}^{(M)}]$ and $\boldsymbol{\mathcal{Q}} := [\mathbf{Q}'^{(1)} \cdots \mathbf{Q}'^{(M)}]$. The estimation of $\boldsymbol{\phi}$ from $\boldsymbol{\mathcal{H}}$ proceeds as described in Section 4.3.2. However, the number of columns in the data matrix is now increased, which provides improvement of estimation accuracy in terms of noise. Multiple snapshots also enable the opportunity to increase the number of rows in $\mathbf{H}^{(m)}$ as now the number of columns Q, necessary to restore the dimension of the signal subspace, can be smaller: $Q \geq \max(1, K + 1 - M)$. Increasing the number of rows in $\mathbf{H}^{(m)}$ increases the frequency aperture and leads to improved time-delay resolution.

FORWARD-BACKWARD AVERAGING

Another technique to extend the data matrix is known as forward-backward (FB) averaging [130]. This technique can only be applied when multiband CSI is collected on a *centro-symmetric* set of frequencies. Let the central frequency of the set of probed frequencies $\mathcal{W}_i$, $i = 0, \ldots, L-1$, be defined as $\omega_c = (\omega_{L-1} + \omega_0)/2$. A set of frequencies is centro-symmetric if for any frequency in the set there is a corresponding frequency located in the opposite direction and equidistant with respect to the central frequency of the set. If these constraints are satisfied, then FB averaging can be applied by exploiting the structure of $\mathbf{A}$ in (4.14) and the fact that the $\{\phi_k\}_{k=1}^K$ are on the unit circle. Let $\boldsymbol{\Pi}$ denote the $LP \times LP$ exchange matrix that reverses the ordering of the rows, then it is seen

that $\mathbf{\Pi A}^* = \mathbf{A\Upsilon}$, for some unitary diagonal matrix $\mathbf{\Upsilon}$ related to $\mathbf{\Phi}$. In particular, $\mathbf{A}$ and $\mathbf{\Pi A}^*$ have the same column span.

Thus, we can construct the forward-backward averaged multiple snapshot data matrix as

$$\mathcal{H}_{\mathrm{e}} := [\mathcal{H} \quad \mathbf{\Pi}\mathcal{H}^*], \tag{4.27}$$

of size $LP \times 2QM$. Then, $\mathcal{H}_e$ has a factorisation

$$\mathcal{H}_{\mathrm{e}} = \mathbf{A}'\mathcal{X}_{\mathrm{e}} + \mathcal{Q}_{\mathrm{e}} := \mathbf{A}'[\mathcal{X} \quad \mathbf{\Upsilon}\mathcal{X}^*] + [\mathcal{Q} \quad \mathbf{\Pi}\mathcal{Q}^*]. \tag{4.28}$$

Thus, the FB averaging doubles the number of columns of the data matrix, which leads to improved accuracy. It also provides the opportunity to increase the number of rows in $\mathbf{H}^{(m)}$, as now the number of columns Q, necessary to restore the dimension of the signal subspace, is half of what it used to be. The estimation of $\boldsymbol{\tau}$ from the extended data matrix proceeds as described in Section 4.3.2.

4

4.3.4. NOISE REDUCTION

The Hankel matrices $\mathbf{H}_i$, $i = 0, \ldots, L-1$, stacked in $\mathbf{H}$, all have the same K-dimensional basis for their column spaces, i.e., the column span of $\mathbf{M}'$. Instead of stacking the $\mathbf{H}_i$ vertically into $\mathbf{H}$, we can stack them horizontally. This allows us to obtain a good estimate of that basis.

Here, we consider the general case, but first we exploit the structure of $\mathbf{M}$ in (3.13), to apply FB averaging on each of $\mathbf{H}_i$. The FB averaged multiple snapshot data matrix for the ith band is defined as $\mathcal{H}_{\mathrm{e},i} := [\mathcal{H}_i \quad \mathbf{\Pi}'\mathcal{H}_i^*]$, where

$$\mathcal{H}_i := [\mathbf{H}_i^{(1)} \ldots \mathbf{H}_i^{(M)}], \tag{4.29}$$

$\mathbf{H}_i^{(m)}$ is a Hankel matrix formed from CSI collected in the ith band at the mth snapshot, and $\mathbf{\Pi}$ is the $P \times P$ exchange matrix. To estimate the basis, we construct

$$\mathcal{H}_{\mathrm{r}} := [\mathcal{H}_{\mathrm{e},0} \quad \mathcal{H}_{\mathrm{e},1} \cdots \mathcal{H}_{\mathrm{e},L-1}], \tag{4.30}$$

which has a factorisation

$$\begin{aligned} \mathcal{H}_{\mathrm{r}} &= \mathbf{M}\mathcal{X}_{\mathrm{r}} + \mathcal{Q}_{\mathrm{r}} \\ &:= \mathbf{M}[\mathcal{X}_{\mathrm{e},0} \cdots \mathbf{\Theta}_{L-1}\mathcal{X}_{\mathrm{e},L-1}] + [\mathcal{Q}_{\mathrm{e},0} \cdots \mathcal{Q}_{\mathrm{e},L-1}]. \end{aligned} \tag{4.31}$$

After computing the SVD of $\mathcal{H}_{\mathrm{r}}$, let matrix $\hat{\mathbf{U}}_r$ contain the K dominant left singular vectors, i.e., the estimated basis for the column span of $\mathbf{M}'$.

Moving back to the vertically stacked data matrix $\mathcal{H}_{\mathrm{e}}$, the noise in this matrix can be reduced by projecting each of its blocks onto the low dimensional column span of $\hat{\mathbf{U}}_r$:

$$\mathcal{H}_{\mathrm{p}} = \left(\mathbf{I}_L \otimes \mathbf{P}_{\mathbf{U}_r}\right)\mathcal{H}_{\mathrm{e}},$$

where $\mathbf{P}_{\mathbf{U}_{\mathrm{r}}} = \hat{\mathbf{U}}_{\mathrm{r}}\hat{\mathbf{U}}_{\mathrm{r}}^H$. The projected data matrix $\mathcal{H}_{\mathrm{p}}$ has a factorisation

$$\mathcal{H}_{\mathrm{p}} = \mathbf{A}'\mathcal{X}_{\mathrm{e}} + \mathcal{Q}_{\mathrm{p}} := \begin{bmatrix} \mathbf{M}' \\ \mathbf{M}'\mathbf{\Phi}^{n_1} \\ \vdots \\ \mathbf{M}'\mathbf{\Phi}^{n_{L-1}} \end{bmatrix} \mathcal{X}_{\mathrm{e}} + \begin{bmatrix} \mathbf{P}_{\mathbf{U}_{\mathrm{r}}}\mathcal{Q}_{\mathrm{e},0} \\ \mathbf{P}_{\mathbf{U}_{\mathrm{r}}}\mathcal{Q}_{\mathrm{e},1} \\ \vdots \\ \mathbf{P}_{\mathbf{U}_{\mathrm{r}}}\mathcal{Q}_{\mathrm{e},L-1} \end{bmatrix}. \tag{4.32}$$

The column space of matrix $\mathcal{H}_\mathrm{p}$ has the same structure as the column space of $\mathcal{H}_\mathrm{e}$. However, the noise matrices $\mathcal{Q}_{\mathrm{e},i}$, $i = 0,\ldots,L-1$, are projected onto the lower dimensional subspace, which improves accuracy. The estimation of $\boldsymbol{\tau}$ from $\mathcal{H}_\mathrm{p}$ proceeds as described in Section 4.3.2.

4.3.5. ESTIMATION OF AMPLITUDES AND ALGORITHM SUMMARY

After estimation of the time-delays $\boldsymbol{\tau}$, the amplitudes $\boldsymbol{\alpha}^{(m)}$ (if they are of interest) can be found as the least-squares solution to (4.24), that is

$$\hat{\boldsymbol{\alpha}}^{(m)} = \hat{\mathbf{A}}^{\dagger}\mathbf{h}^{(m)}, \quad m = 1,\ldots,M, \tag{4.33}$$

where $\hat{\mathbf{A}}$ is constructed based on model (4.14) using $\hat{\boldsymbol{\tau}}$.

A summary of the resulting Multiband Weighted Delay Estimation (MBWDE) algorithm is shown as Algorithm 3. With the input $\hat{\boldsymbol{\tau}}_\mathrm{MRTD}$ we denote an initial estimate of $\boldsymbol{\tau}$ obtained using the related multiresolution delay estimation algorithm [203]. The abstract routine `construct`$(\cdot)$ points to the construction of $\mathbf{A}$ or $\mathbf{A}'$ from $\boldsymbol{\tau}$ (via $\boldsymbol{\Phi}$) in (4.14) or (4.18), respectively. `TSVD` refers to the truncated SVD (truncating at rank K). The remaining parts of the summary are self-explanatory.

4.4. GAUSSIAN CRAMÉR-RAO BOUND

In this section, we derive the Gaussian CRB for the model (4.24), which sets a lower bound on the error covariance matrix of any unbiased estimator [72]. This bound is accurate under the assumption that the noise present in multiband channel estimates is Gaussian and white distributed, which holds for the case of the training signals with equal power over subcarriers [200]. In the remainder of this thesis, we refer to Gaussian CRB as CRB. After deriving the CRB, we analyze the effects of wireless system parameters, namely the bandwidth, number of CSI measurements and band selection, on it.

The mean square error (MSE) of the estimated time-delays, when only errors due to the variance of the estimator are present [72], is defined as

$$\mathrm{MSE}(\hat{\boldsymbol{\tau}}) := \mathbb{E}\{(\hat{\boldsymbol{\tau}} - \boldsymbol{\tau})^2\} = \mathrm{var}(\hat{\boldsymbol{\tau}}), \tag{4.34}$$

where $\mathrm{var}(\hat{\boldsymbol{\tau}})$ is the variance of the estimates.

Let us assume that all MPCs are resolved and that the bias can be ignored, then the covariance matrix of the time-delay estimation errors and its lower bound are defined as

$$\mathbf{C}_{\hat{\boldsymbol{\tau}}} := \mathbb{E}\{(\hat{\boldsymbol{\tau}} - \boldsymbol{\tau})(\hat{\boldsymbol{\tau}} - \boldsymbol{\tau})^T\} \succcurlyeq \mathrm{CRB}(\boldsymbol{\tau}), \tag{4.35}$$

$$\mathrm{CRB}(\boldsymbol{\tau}) := \mathbf{F}^{-1}, \tag{4.36}$$

where $\hat{\boldsymbol{\tau}}$ are estimated time-delays and $\mathbf{F}$ is the Fisher's Information Matrix (FIM). The entries on the diagonal of $\mathbf{C}_{\hat{\boldsymbol{\tau}}}$ are equal to the variances of the estimated time-delays $\mathrm{var}(\hat{\boldsymbol{\tau}})$.

The data model (4.24) is familiar from array signal processing, and the FIM and the Gaussian CRB for DOA estimation are derived in [207]. We can readily adapt these results to the problem of delay estimation by making the following assumptions:

Algorithm 3: Multiband Weighted Delay Estimation

Input: $\hat{\boldsymbol{\tau}}_{\text{MRTD}}, N, P, K, \{\mathbf{h}_i^{(m)} : m = 1,\dots,M\}_{i=0}^{L-1}$
Output: $\hat{\boldsymbol{\tau}}, \hat{\boldsymbol{\alpha}}^{(m)}$
$Q \leftarrow N - P + 1$;
$\mathbf{H}_i^{(m)} \leftarrow \texttt{hankel}(\mathbf{h}_i^{(m)}, P, Q), \forall i, m$; (4.15)
$\boldsymbol{\mathcal{H}} \leftarrow [\mathbf{H}^{(1)} \dots \mathbf{H}^{(M)}], \forall i$; (4.25)
$\boldsymbol{\mathcal{H}}_{\text{e}} \leftarrow \boldsymbol{\mathcal{H}}$;
if *ForwardBackward* **then**
  $\boldsymbol{\mathcal{H}}_{\text{e}} \leftarrow [\boldsymbol{\mathcal{H}} \quad \boldsymbol{\Pi}\boldsymbol{\mathcal{H}}^*]$; (4.27)
end
if *NoiseReduction* **then**
  $\boldsymbol{\mathcal{H}}_i \leftarrow [\mathbf{H}_i^{(1)} \dots \mathbf{H}_i^{(M)}], \forall i$; (4.29)
  $\boldsymbol{\mathcal{H}}_{\text{e},i} \leftarrow [\boldsymbol{\mathcal{H}}_i \quad \boldsymbol{\Pi}'\boldsymbol{\mathcal{H}}_i^*]$;
  $\boldsymbol{\mathcal{H}}_{\text{r}} \leftarrow [\boldsymbol{\mathcal{H}}_{\text{e},0} \quad \boldsymbol{\mathcal{H}}_{\text{e},1} \cdots \boldsymbol{\mathcal{H}}_{\text{e},L-1}]$; (4.30)
  $\hat{\mathbf{U}}_{\text{r}} \leftarrow \texttt{TSVD}(\boldsymbol{\mathcal{H}}_{\text{r}}, K)$;
  $\mathbf{P}_{\mathbf{U}_{\text{r}}} \leftarrow \hat{\mathbf{U}}_{\text{r}}\hat{\mathbf{U}}_{\text{r}}^H$;
  $\boldsymbol{\mathcal{H}}_{\text{e}} \leftarrow \left(\mathbf{I}_L \otimes \mathbf{P}_{\mathbf{U}_{\text{r}}}\right)\boldsymbol{\mathcal{H}}_{\text{e}}$;
end
$\{\hat{\mathbf{U}}, \hat{\boldsymbol{\Lambda}}_{\text{s}}, \hat{\sigma}^2\} \leftarrow \texttt{TSVD}(\boldsymbol{\mathcal{H}}_{\text{e}}, K)$;
$\mathbf{W} \leftarrow \hat{\boldsymbol{\Lambda}}_{\text{s}} - \hat{\sigma}^2\mathbf{I}_K$; (4.23)
$\hat{\mathbf{A}}'_{\text{MRTD}} \leftarrow \texttt{construct}(\hat{\boldsymbol{\tau}}_{\text{MRTD}})$; (4.14)
$\hat{\boldsymbol{\tau}} \leftarrow \texttt{solNLS}(\hat{\mathbf{A}}'_{\text{MRTD}}, \hat{\mathbf{U}}, \mathbf{W})$; (4.22)
$\mathbf{h}^{(m)} \leftarrow [\mathbf{h}_1^{(m)T} \dots \mathbf{h}_{L-1}^{(m)T}]^T, \forall m$;
$\hat{\mathbf{A}} \leftarrow \texttt{construct}(\hat{\boldsymbol{\tau}})$; (4.14)
$\hat{\boldsymbol{\alpha}}^{(m)} \leftarrow \texttt{solLS}(\hat{\mathbf{A}}, \mathbf{h}^{(m)}), \forall m$; (4.33)

(**A1**) The noise $\mathbf{q}^{(m)}$ in the model (4.24) is zero-mean circularly-symmetric Gaussian with covariance $\mathbf{R}_{\text{q}} = \sigma_{\text{q}}^2\mathbf{I}_{LN}$. This assumption is satisfied when the transceivers have equal gain in all bands and the training symbols $\mathbf{s}$ have a constant magnitude.

(**A2**) The amplitudes of the MPCs are assumed to be circularly symmetric complex Gaussian random variables, i.e., $\alpha_k \sim \mathcal{CN}(0, \sigma_{\alpha,k}^2)$, $k = 1,\dots,K$, with covariance matrix $\mathbf{R}_\alpha$. Thus, the magnitudes of the MPCs are Rayleigh distributed, and we assume that they have an exponentially decaying power-delay profile. This is different from the assumption made in Section 3.4.4, where to promote a sparse solution for $\boldsymbol{\alpha}$ we used the complex Gaussian scale mixture model with a gamma mixing density to model the PDF of $\alpha_k, k = 1,\dots,K$.

(**A3**) The FIM matrix given in (4.37) is non-singular and the CRB can be computed by taking its inverse. The validity of this assumption depends on the delay separation between MPCs with respect to the system bandwidth [208]. As a rule of thumb, we say that matrix $\mathbf{F}$ will become rank deficient if the delay separation of two MPCs

is much smaller than the inverse of the total bandwidth, i.e., much smaller than $1/(LB)$. In numerical experiments presented in Section 4.5 we see that for $LB = 80$ MHz, this assumption is satisfied even if the delay separation of MPCs is 125 times smaller than $1/(LB)$.

(**A4**) The MPCs and noise are temporally uncorrelated.

Based on the above assumptions, the FIM for the time-delay parameters, conditioned on the path amplitudes, is given as

$$\mathbf{F} = \frac{2M}{\sigma_q^2} \mathrm{Re}\left\{ \mathbf{D}^H \mathbf{P}_{\mathbf{A}}^{\perp} \mathbf{D} \odot \mathbf{R}_{\alpha} \right\}, \tag{4.37}$$

where

$$\mathbf{D} = \left[\frac{\partial \mathbf{a}(\tau_1)}{\partial \tau_1}, \ldots, \frac{\partial \mathbf{a}(\tau_K)}{\partial \tau_K} \right], \tag{4.38}$$

$\mathbf{a}(\tau_k)$ is the kth column of $\mathbf{A}$, $\mathbf{P}_{\mathbf{A}}^{\perp} = \mathbf{I}_{LN} - \mathbf{P}_{\mathbf{A}}$, $\mathbf{P}_{\mathbf{A}} = \mathbf{A}\mathbf{A}^{\dagger}$. To gain further insights in the CRB we partition the FIM in terms associated to the time-delays of MPCs and their coupling with other multipath parameters, and write it in the following explicit form as

$$\mathbf{F} = \frac{2M}{\sigma_q^2} \mathrm{Re}\{ \underbrace{\mathbf{D}^H \mathbf{D} \odot \mathbf{R}_{\alpha}}_{\substack{\text{Partition of FIM} \\ \text{of delay parameters}}} - \underbrace{\mathbf{D}^H \mathbf{P}_{\mathbf{A}} \mathbf{D} \odot \mathbf{R}_{\alpha}}_{\substack{\text{Partition of FIM} \\ \text{of coupled parameters}}} \}. \tag{4.39}$$

We can make the following observations.

- The CRB depends on the time-delays $\boldsymbol{\tau}$, frequency band selection $\{\mathcal{W}_i\}_{i=0}^{L-1}$ through $\mathbf{A}$ and $\mathbf{D}$, and correlation between amplitudes $\boldsymbol{\alpha}$ through $\mathbf{R}_{\alpha}$.
- The first term in the FIM represents the effects of the time-delays $\boldsymbol{\tau}$ on the estimation error, and is equivalent to the FIM for time-delay estimation in the additive white Gaussian noise channel when there is no multipath propagation.
- The second term represents the effects of coupling between parameters $\boldsymbol{\tau}$ and $\boldsymbol{\alpha}$ on the estimation error of time-delays $\boldsymbol{\tau}$. This term is always non-negative, and it will increase the CRB except when the parameters are decoupled. An increase of the CRB due to coupling of the parameters depends on the conditioning of matrix $\mathbf{A}^H\mathbf{A}$, and it will be low when this matrix is well-conditioned.

Unfortunately, these observations do not intuitively interpret the impact of band selection $\{\mathcal{W}_i\}_{i=0}^{L-1}$ on the CRB. To arrive at a more interpritable expression for the CRB, we will make the additional assumption that matrix $\mathbf{R}_{\alpha} = \mathrm{diag}[\sigma_{\alpha,k}^2, k = 1 \ldots K]$ is diagonal, which holds for *wide sense stationary uncorrelated scattering* (WSSUS) channels [209]. Then using (4.37), we can write the closed-form expression for the CRB on the time-delay estimates of the kth MPC as

$$\mathrm{CRB}(\hat{\tau}_k) = \frac{1}{2M \cdot \mathrm{SNR}_k} b^{-1}(\tau_k), \tag{4.40}$$

where $\text{SNR}_k = \sigma^2_{\alpha,k}/\sigma^2_{\text{q}}$, $b(\tau_k) = \mathbf{d}^H(\tau_k)(\mathbf{I}_{LN} - \mathbf{P}_\mathbf{A})\mathbf{d}(\tau_k)$ and $\mathbf{d}(\tau_k)$ is the kth column of $\mathbf{D}$. This expression shows that the CRB is inversely proportional to the number of snapshots M, SNR_k and the scalar $b(\tau_k)$, where $b(\tau_k)$ depends on the coupling between the parameters. If we ignore the effects of coupling, then $\mathbf{d}^H(\tau_k)\mathbf{P}_\mathbf{A}\mathbf{d}(\tau_k) = 0$, and (4.40) reduces to the CRB for time-delay estimation in AWGN channels [210]. The scalar $b(\tau_k)$ then can be written as $b(\tau_k) = \sum_{n\in\mathcal{S}}(\omega_{sc}n)^2$, where $\mathcal{S}$ is the index set of all used subcarriers of all frequency bands. It is defined as $\mathcal{S} = \bigcup_{i=0}^{L-1}\mathcal{S}_i$, where $\mathcal{S}_i = \{n \in \mathbb{Z} \mid n_{c,i} - \frac{N}{2} \le n < n_{c,i} + \frac{N}{2}\}$, $n_{c,i} = n_i - \frac{n_{L-1}-n_0}{2}$, and $n_i = \frac{\omega_i - \omega_0}{\omega_{sc}}$, $i = 0,\ldots,L-1$. Now, it is easy to see that the CRB (4.40) can be reduced by collecting the CSI over a large frequency aperture. However, the results of real data experiments show that a large frequency aperture introduces modeling errors caused by frequency dependency of multipath channels [211]. Therefore the bands need to be selected carefully, and this is further discussed in Chapter 8.

4.5. NUMERICAL EXPERIMENTS

This section presents numerical results that illustrate the performance of the MBWDE algorithm. We first describe the simulation setup and then compare different variants of the algorithm and study how the trade-offs among design and system parameters impact the performance. Lastly, we compare the performance of the algorithm against several other algorithms. The results show that the algorithm is asymptotically efficient, achieves the CRB, and improves the resolution of time-delay estimation with respect to the bandwidth of the training signals.

In the simulations, we consider time-delay estimation using IEEE 802.11be transceivers. Although the IEEE 802.11be standard is in a preliminary phase, its main candidate features are already known [197]. In particular of interest to us is that it will enable multiband operation at 2.4, 5, and 6 GHz. At 6 GHz, the RF spectrum from 5.925 to 7.125 GHz will be allocated for primary 20, 40, 80, and 160 MHz channels and their contiguous and non-contiguous combinations. The large bandwidth allocated at the 6 GHz band offers a great opportunity for localization.

In the default setup, we consider that CSIs are collected using OFDM training signals with subcarrier spacing $\omega_{sc} = 78.125$ kHz and a bandwidth of $B = 20$ MHz at $L = 4$ bands with central frequencies $\{6, 6.120, 6.320, 6.440\}$ GHz. This corresponds to probing the channel using the 20 MHz wide extremely high throughput long training fields (EHT-LTF) described in the standard. We consider that $M = 12$ CSI snapshots are collected within the channel's coherence time and assume that the multipath channel has $K = 7$ MPCs with Rayleigh distributed magnitudes. The time-delays of MPCs are set to $\{3, 5, 10, 16, 22, 28, 33\}$ ns and their average powers are set to $\{0, -3, -5, -4, -6, -5.5, -7\}$ dB. The number of iterations allowed for convergence of the SNLS problem (4.21) is set to 10. To assess the performance of the algorithm, we compute the root mean square error (RMSE) of the LOS time-delay estimate using 10^4 Monte Carlo trials and compare it to the CRB derived in Section 4.4. The RMSE is defined as $\text{RMSE}(\hat{\boldsymbol{\tau}}) := \sqrt{\text{MSE}(\hat{\boldsymbol{\tau}})}$, where the MSE is given by (4.34). In the subsequent simulations, some of these parameters are varied.

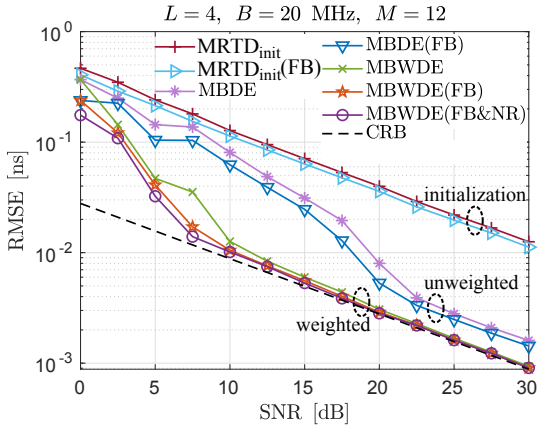

Figure 4.3: RMSE of LOS time-delay estimation for different variants of the MBDE and MBWDE algorithms.

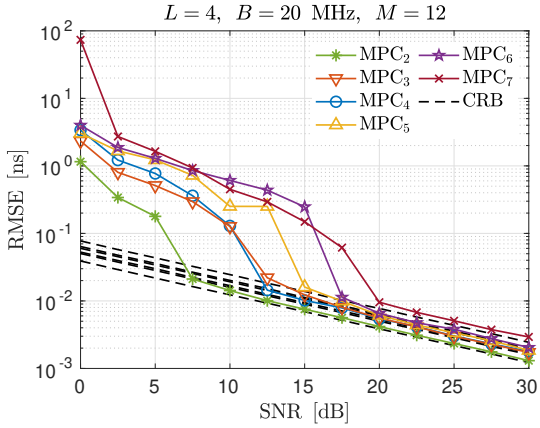

Figure 4.4: RMSE of time-delay estimation using the MBWDE(FB&NR) algorithm for the MPCs in the channel.

PERFORMANCE OF MBWDE

Fig. 4.3 shows the RMSE of time-delay estimation for different variants of the MBWDE algorithm and its initialization is obtained using MRTD estimation as a function of SNR. The unweighted variant of the algorithm is indicated with MBDE, and the variants that include FB averaging and noise reduction or both have extensions (FB), (NR), and (FB&NR), respectively. All simulation parameters are set as listed previously. It is seen that the MBWDE algorithm asymptotically achieves the CRB as the SNR increases. The results also show that FB averaging and NR techniques provide approximately 2.5 dB of SNR gain. The MBWDE(FB&NR) variant of the algorithm performs best, and in the following, we will mostly focus on it.

In this thesis, we aim at time-delay estimation for ranging, where the primary interest

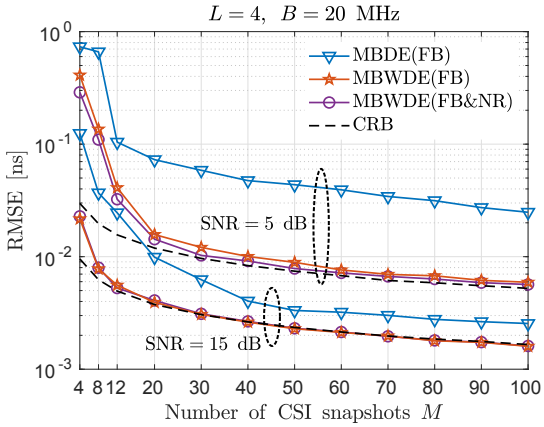

Figure 4.5: Influence of the number of CSI snapshots M on the performance of time-delay estimation.

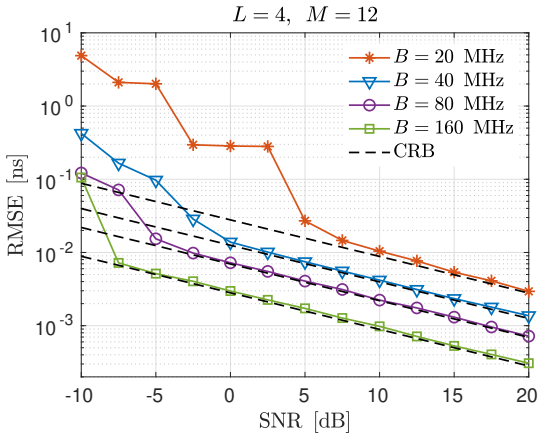

Figure 4.6: Impact of the bandwidth B of training signals on the RMSE.

is to estimate the delay of the line-of-sight (LOS) path. However, we also evaluated the performance of time-delay estimation using the MBWDE(FB&NR) algorithm for later arriving MPCs. Here, we present the Root Mean Square Error (RMSE) of delay estimation for the MPCs $k = 2,3,4,5,6$. We used the same simulation setup as in the previous scenario to generate these results.

From Fig. 4.4, we see that the algorithm converges to the CRB for all MPCs. However, the SNR level for which the algorithm starts to converge to the CRB is different for each MPC. These levels depend on the mean magnitudes of the MPCs, and in general, the algorithm will converge sooner to the CRB for the MPCs with a higher magnitude. This is the consequence of the differences in the levels of the subspace perturbations.

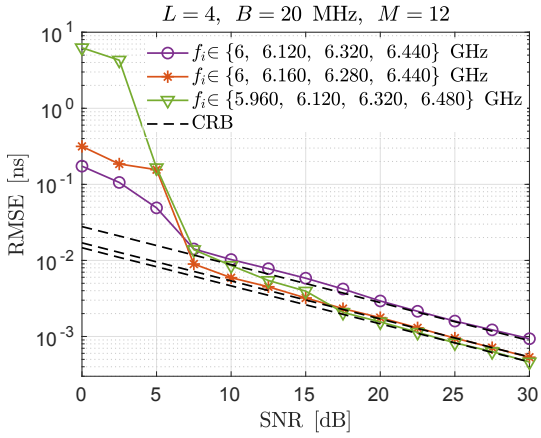

Figure 4.7: Impact of the choice of carrier frequencies of the bands on the RMSE.

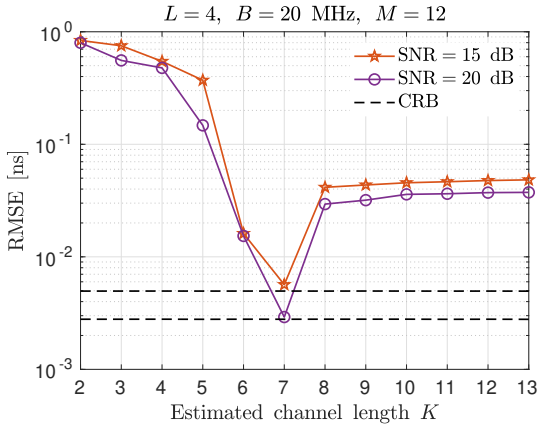

Figure 4.8: Impact of MPC misdetection on the performance of MBWDE (FB&NR)

INFLUENCE OF SYSTEM PARAMETERS M, B AND $\{f_{c,i}\}_{i=1}^{L}$

We first study the scenario where all parameters are set as in the default setup, except that now we vary the number of CSI snapshots. We repeat these simulations for SNR = 5 and 15 dB and compare the performance of MBDE(FB), MBWDE(FB), and MBWDE(FB&NR). From Fig. 4.5, it is seen that the performances of all algorithms improve when the number of CSI snapshots is increased. However, MBDE(FB) never achieves the CRB and stays biased, even for high SNR, due to the lack of weighting of the subspace perturbations. On the other hand, 12 snapshots are enough for the MBWDE(FB) and MBWDE(FB&NR) algorithms to attain the CRB for high SNR (15 dB), while for low SNR (5 dB), these algorithms attain the bound for 30 snapshots and more.

Next, we simulate the scenario where the bandwidth of the training signals is varied. We set the bandwidth parameter B to $\{20, 40, 80, 160\}$ MHz. The other parameters are set

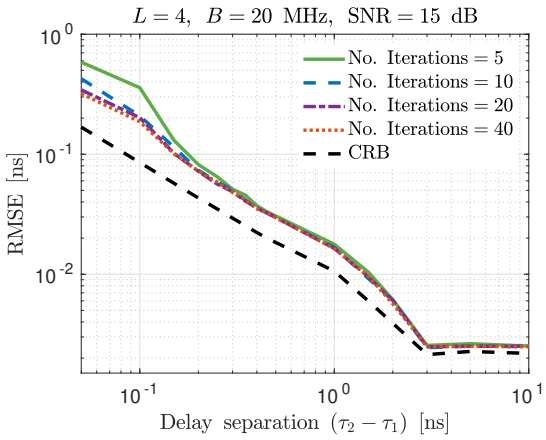

Figure 4.9: RMSE of estimation for MBWDE(FB&NR) considering time-delay separation between the LOS path and the closest MPC.

as in the default simulation setup. Fig. 4.6 shows the RMSE of the time-delay estimation for the MBWDE(FB&NR) algorithm. As expected, it is seen that by increasing the bandwidth, the resolution increases. A gain of approximately 10 dB in SNR is achieved when the bandwidth B is doubled.

We have shown in Section 4.4 that by increasing the frequency aperture of the CSI measurements, the CRB decreases. Now, we simulate scenarios where the carrier frequencies of the bands are set to the following sets: $\{6, 6.120, 6.320, 6.440\}$, $\{6, 6.160, 6.320, 6.440\}$ and $\{5.960, 6.120, 6.320, 6.480\}$ GHz. Fig. 4.7 shows that the resolution of estimation increases for larger frequency apertures. However, it is also seen that for low SNR, the RMSE increases for a larger aperture. This confirms the results of Section 4.4, and we can conclude that the band selection is a trade-off between resolution and robustness to noise. Later, in Chapter 8 we will see that real multipath channels are frequency-dependent, which sets a limit on the size of frequency aperture that can be selected without introducing modeling errors in (4.14).

INFLUENCE OF MPC DETECTION

Fig. 4.8 shows the RMSE of the MBWDE algorithm when the number of MPCs in the channel K is wrongly detected. We consider two scenarios where the value of SNR is set to 15 and 20 dB. The true number of MPCs K is 7. It is seen that when K is correctly detected, the algorithm attains the CRB. Its performance sharply deteriorates when K is wrongly detected. The underestimation of K introduces modeling error, and it is more severe compared to overestimation.

RESOLUTION AND CONVERGENCE OF MBWDE

We assess the resolution of the MBWDE(FB&NR) algorithm by varying the time-delay separation between LOS and the closest MPC, i.e., $\Delta\tau_{2,1} = \tau_2 - \tau_1$, in the range from 0.01 to 10 ns, while keeping the SNR fixed at 15 dB. We repeat this simulation scenario

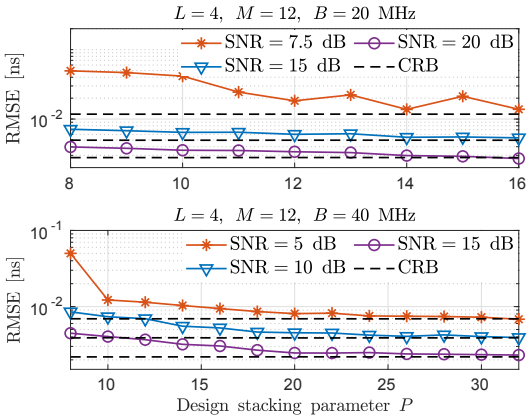

Figure 4.10: Influence of stacking design parameter P on the RMSE.

while setting the number of iterations allowed for convergence of the SNLS problem to $\{5, 10, 20, 40\}$. Fig. 4.9 shows the RMSE for this scenario, and it can be seen that the algorithm converges to the CRB for a time-delay separation larger than 2 ns. It is also seen, that for "well-separated" paths ($\Delta\tau_{2,1} \geq 2$ ns), 5 iterations are sufficient for the algorithm (4.21) to converge. For critical scenarios, when paths are closely spaced ($\Delta\tau_{2,1} \leq 0.2$ ns), there is a slight improvement when 10 or more iterations are allowed for convergence. However, allowing more than 10 iterations does not result in substantially better performance. This experiment illustrated the impact of the first MPC on the delay estimation of the LOS path. In [212], we analyzed the impact of other MPCs of delay estimation of the LOS path using the MBWDE(FB&NR) algorithm. There we used the idea of the first contiguous cluster [213] and showed that all the MPCs that are within this cluster, i.e., that are separated less than $1/(BL)$ from the LOS path, introduce a bias in the delay estimation of the LOS path. This bias depends on the relative powers of the MPCs compared to the LOS path and their delay separation from the LOS.

INFLUENCE OF DESIGN PARAMETER P

In Section 4.3.1, we have introduced the design parameter P, which controls the dimensions of the Hankel matrices (4.15). We use the default simulation setup to evaluate the influence of parameter P on the RMSE of the algorithm. From Fig. 4.10 it is seen that for high SNR, the performance improves when P is increased. This result is intuitive as an increased number of rows in the Hankel matrices increases the frequency aperture. Furthermore, the matrix $\mathbf{A}'$ (4.18) becomes taller and the mutual linear independence of its columns increases.

COMPARISON TO OTHER ALGORITHMS

Finally, we compare MBWDE to DML [113] and SML [105] methods, algorithms proposed in [47] (MUSIC), [192, 194] (CS(L1)), and DOA estimation algorithms ESPRIT [124] and MI-MUSIC [214], that are tailored to the problem of delay estimation. We provide

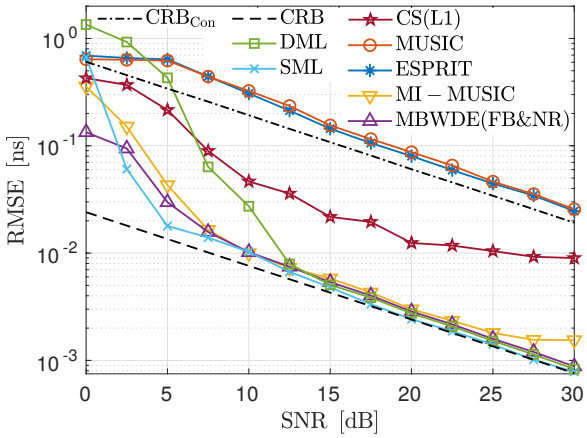

Figure 4.11: Performance comparison of MBWDE(FB&NR) with ESPRIT, MUSIC, DML, SML, MI-MUSIC and CS(L1).

CSI with a contiguous bandwidth of B = 80 MHz to MUSIC and ESPRIT. For all other algorithms, we provide multiband CSI collected in L = 4 bands with B = 20 MHz. The CRB is computed for both contiguous and non-contiguous band allocations. We use delay estimates obtained using the MR algorithm [203] to initialize DML, SML, and MBWDE(FB&NR). Fig. 4.11 shows that algorithms that utilize contiguous bands have a more than 10 times higher RMSE compared to algorithms that use multiband CSI. The best performance is shown by SML, which is asymptotically consistent and statistically efficient as M and B tend to infinity. However, it has a higher complexity than MBWDE(FB&NR) as it minimizes a complex multimodal cost function for the delays, complex amplitudes, and noise. The performance of MBWDE(FB&NR) is close to SML. It is also seen in Fig. 4.11 that the consistency and efficiency properties do not hold for DML in multiple snapshot scenarios. The results show that CS(L1) never attains the CRB due to basis mismatch and that MI-MUSIC diverges from it for high SNR (>23 dB) where grid mismatch errors dominate noise errors. These errors are caused by the discretization of the delay grid, where we set the grid step to 0.005 ns. For lower SNR, the performance of MBWDE(FB&NR) and MI-MUSIC are almost the same. However, MI-MUSIC has a much higher computational complexity due to an exhaustive grid search.

4.6. CONCLUSIONS

This chapter considered the problem of high-resolution time-delay estimation for range-based localization using multiband CSI measurements. We derived a data model for multiband CSI and showed that it has multiple shift-invariance structures. We designed the Multiband Weighted Delay Estimation (MBWDE) algorithm that exploits this structure to estimate time-delay parameters. This algorithm requires initialization, and we used a MRTD estimation algorithm [203] to find a good initial estimate of the time-delays. This algorithm and its performance will be presented in Chapter 5. We presented several data extension and preprocessing techniques that further improve the perfor-

mance of MBWDE. To assess the performance of MBWDE and several other algorithms, we derived the CRB on the RMSE of time-delay estimates considering a multiband CSI model. We used parameters of the emerging IEEE 802.11be standard to define simulation scenarios that illustrate the performance of MBWDE. The results of simulations showed that MBWDE almost attains the CRB when MPCs, present in the channel, are resolved and outperforms other multiband estimation algorithms such as CS(L1) and MI-MUSIC. However, the results of numerical simulations are not a sufficient indicator of the performance of algorithms in real scenarios. For this reason, we present additional experiments with real channel measurements in Chapter 8, to verify the modeling assumptions and illustrate the performance of the MBWDE algorithm in practical localization scenarios.

5

MULTIRESOLUTION TIME-DELAY ESTIMATION

"The beginning is the most important part of the work."

— Plato

Part of this chapter is published as: T. Kazaz, R.T. Rajan, G.J.M. Janssen, and A.J. van der Veen, "Multiresolution Time-of-Arrival Estimation from Multiband Radio Channel Measurements", IEEE International Conference on Acoustics, Speech, and Signal Processing (ICASSP), Brighton, United Kingdom, May 2019.

5.1. INTRODUCTION

In the previous chapter, we presented multiband time-delay estimation algorithms referred to as MBDE and MBWDE. These algorithms are based on subspace fitting, and they estimate time-delays by finding solutions to the separable nonlinear least-squares (SNLS) problems given in (4.20) and (4.22). The optimization problems that are solved in these algorithms have a highly multimodal objective function with many local minimums. The solution to these optimization problems can be found using iterative optimization methods such as variable projection [112], Gauss-Newton [111], Levenberg-Marquardt [215], and steepest descent [216]. However, all of these optimization methods require initialization, and then they perform a search for the local minimum that is close to the initial estimate. These methods will converge to a true solution when the initial estimate is close to it. Otherwise, they might converge to any other local minimum of the objective functions given in (4.20) and (4.22). Therefore, to improve the performance of time-delay estimation using the MBDE and MBWDE algorithms, it is crucial to find accurate estimates to initialize optimization of SNLS problems.

In this chapter, we present a multiresolution time-delay (MRTD) estimation algorithm. Similar to the MBDE and MBWDE algorithms, to improve resolution while avoiding arriving at unrealistic sampling rates, we use multiband sampling to acquire channel measurements [91, 102]. We showed in Chapter 4 that after stacking these measurements into Hankel matrices, the resulting data model has a multiple shift-invariance structure (4.18). The same structure appears in Multiple Invariance ESPRIT [195] and the related algorithms are applicable to our problem, in particular the Multiresolution ESPRIT algorithm [217], which was aimed at carrier frequency estimation.

Similar to [217], we propose an algorithm where the invariance structure of a single band will provide coarse parameter estimates, while the invariance structure of the lowest against the highest frequency band will provide high-resolution but phase wrapped estimates. The wrapping is resolved using the coarse estimates.

The proposed algorithm improves resolution compared to single band estimation methods, such as classical ESPRIT [124] and MUSIC [119], presented in Chapter 2. This algorithm allows time-delay estimation from channel measurements collected in two separate frequency bands, which provides the opportunity to increase the resolution of time-delay estimation by selecting frequency bands that form a large frequency aperture. At the same time, it does not require solving an NLS and has a closed-form solution based on joint-diagonalization [218].

To derive the algorithm, we first revisit the data model (4.18) for multiband channel measurements, as presented in Chapter 4. We then discuss derivations of the algorithm and present the results of numerical simulations. To evaluate the performance of MRTD estimation algorithm, we compare the the root mean square error (RMSE) of its time-delay estimates against the CRB given in Section 4.4. The results show that the algorithm is asymptotically consistent and efficient when the number of measurements increases to infinity, and it converges to the CRB.

5.2. DATA MODEL

In Section 4.3, we showed that multipath channel measurments $\mathbf{h}_i$, $i = 1,\ldots,L-1$, satisfy the following data model

$$\mathbf{h}_i = \mathbf{M}\boldsymbol{\Theta}_i\boldsymbol{\alpha} + \mathbf{q}_i\,, \tag{5.1}$$

where $\mathbf{M}$ is a Vandermonde matrix given in (3.13) and $\boldsymbol{\Theta}_i = \boldsymbol{\Phi}^{n_i}$, $\boldsymbol{\Phi} = \mathrm{diag}([\phi_1 \cdots \phi_K])$ is collecting the subcarrier dependent phase shifts $\phi_k = e^{-j\phi_k}$, $k = 1,\ldots,K$, where $\phi_k = \omega_{\mathrm{sc}}\tau_k$ with ω_{sc} is subcarrier spacing, and $\boldsymbol{\alpha} = [\alpha_1,\ldots,\alpha_K]^T \in \mathbb{C}^K$ collects the complex-amplitudes of the MPCs.

5.3. MULTIRESOLUTION TIME-DELAY ESTIMATION

Our next objective is to estimate the time-delays $\{\tau_k\}_{k=1}^K$. We begin with an algorithm for estimating the time-delays using a single frequency band, which is later extended to two bands. The single-band algorithm is in fact a classical array signal processing algorithm (cf. [124, 219, 220]).

5.3.1. SINGLEBAND TIME-DELAY ESTIMATION ALGORITHM

Following the structure for the Hankel matrix, as given in Section 4.3.1, from $\mathbf{h}_i$, $i = 1,\ldots,L-1$, we form the Hankel matrices $\mathbf{H}_i$, $i = 1,\ldots,L-1$, that satisfy the following model

$$\mathbf{H}_i = \mathbf{M}'\boldsymbol{\Phi}^{n_i}\mathbf{X} + \mathbf{Q}_i'\,, \tag{5.2}$$

where $\mathbf{M}'$ is an $P \times K$ submatrix of $\mathbf{M}$,

$$\mathbf{X} := [\boldsymbol{\alpha} \quad \boldsymbol{\Phi}\boldsymbol{\alpha} \quad \boldsymbol{\Phi}^2\boldsymbol{\alpha} \cdots \boldsymbol{\Phi}^{Q-1}\boldsymbol{\alpha}],$$

and $\mathbf{Q}_i'$ is a noise matrix.

Since (5.2) resembles the data model of the classical ESPRIT algorithm, $\boldsymbol{\Phi}$ can be estimated by exploiting the shift-invariance properties of the Hankel matrices $\mathbf{H}_i$, $i = 1,\ldots,L-1$. For the single band time-delay estimation algorithm we select a band i and estimate $\boldsymbol{\Phi}$ from the low-rank approximation of $\mathbf{H}_i$. Then from the estimated $\boldsymbol{\Phi}$, the parameters τ_k immediately follow.

In particular, let $\mathbf{U}$ be a K-dimensional orthonormal basis for the column span of $\mathbf{H}_i$, obtained using the singular value decomposition, then we can write $\mathbf{M}' = \mathbf{U}\mathbf{T}$, where $\mathbf{T}$ is a $K \times K$ nonsingular matrix. Next, let us define the selection matrices

$$\mathbf{J}_1^{(r)} = [\mathbf{I}_{P-r} \quad \mathbf{0}_{P-r,r}], \qquad \mathbf{J}_2^{(r)} = [\mathbf{0}_{P-r,r} \quad \mathbf{I}_{P-r}]\,. \tag{5.3}$$

For $r = 1$, $\mathbf{U}_1 = \mathbf{J}_1^{(1)}\mathbf{U}$ and $\mathbf{U}_2 = \mathbf{J}_2^{(1)}\mathbf{U}$ are submatrices of $\mathbf{U}$ obtained by dropping its first and last row, respectively. In view of the shift-invariance structure of $\mathbf{M}'$, we have

$$\mathbf{U}_1 = \mathbf{M}_1'\mathbf{T}^{-1}\,, \qquad \mathbf{U}_2 = \mathbf{M}_1'\boldsymbol{\Phi}\mathbf{T}^{-1}, \tag{5.4}$$

where $\mathbf{M}_1' = \mathbf{J}_1^{(1)}\mathbf{M}'$. Finally, we compute the matrix $\boldsymbol{\Psi} = \mathbf{U}_1^{\dagger}\mathbf{U}_2$. Now, $\boldsymbol{\Phi}$ can then be estimated directly from the eigenvalue decomposition of $\boldsymbol{\Psi}$, as it satisfies the model

$$\boldsymbol{\Psi} = \mathbf{T}\boldsymbol{\Phi}\mathbf{T}^{-1}\,. \tag{5.5}$$

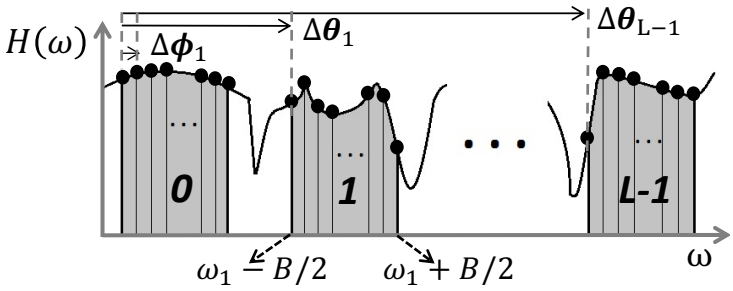

Figure 5.1: Multiband channel frequency response with phase shifts introduced over the subcarriers and carrier frequency defined apertures denoted by $\Delta\phi_i$ and $\Delta\theta_i$. The channel frequency responses from the 0th and $L-1$th bands are used for multiresolution time-delay estimation.

In other words, $\hat{\lambda}_k$ is equivalent to the estimate of the phase shift ϕ_k introduced by the time-delay τ_k of the kth multipath component. Therefore, τ_k can be estimated from $\hat{\lambda}_k$ as $\tau_k = \arg\{\lambda_k\}/\omega_{sc}$. Since $\omega_{sc}\tau_k < 2\pi$ because $\tau_k < T_{sym}$, there is no phase wrapping issue here. Note that for time-delay estimation, we are mostly interested in retrieving the smallest τ_k as it belongs to the LOS propagation, i.e. due to the true distance between the transmitter and the receiver.

5.3.2. MULTIRESOLUTION TIME-DELAY ESTIMATION ALGORITHM

The aforementioned algorithm uses data from a single frequency band and has a limited time resolution, since it is based on the shift of one row in the Hankel matrix $\mathbf{H}_i$, which results in only a small phase shift $\omega_{sc}\tau_k$. Note that the sampling rate does not play a role in $\omega_{sc} = \frac{2\pi}{T_{sym}}$, only the total signal duration $T_{sym} = NT_s$. Thus, increasing the sampling rate without increasing the bandwidth of the training signal would, until a certain level, increase the signal-to-noise ratio (SNR) but not the temporal resolution.

The matrix $\mathbf{M}$ is also invariant for shifts over multiple rows, and therefore, if N is sufficiently large, we can increase the resolution by considering shifts of multiple rows of $\mathbf{H}_i$. Indeed, a shift of r rows using shift matrices $\mathbf{J}_1^{(r)}$ and $\mathbf{J}_2^{(r)}$ (or by interleaving rows of $\mathbf{H}_i$ [221]) leads to an estimate of $\mathbf{\Phi}^r$. Unfortunately, phase shifts have an ambiguity of multiples of 2π, so these approaches for increasing the resolution introduce ambiguity in the estimates of $\tau_k, k = 1,\ldots,K$. If T_{sym} is not very large, the improvement in resolution with this approach is limited.

In Chapter 4, we introduced algorithms that use channel measurements collected in all L bands, however, these algorithms involved solving SNLLS optimization problems presented in Section 4.3.1, that require initialization. Here, we are interested in an algorithm for high resolution and unambiguous estimation of τ_k from multiband channel measurements with a closed-form solution. This algorithm is aimed to provide initialization for the algorithms proposed in Chapter 4. To avoid arriving at the NLLS optimization problem, we focus on time-delay estimation from only two frequency bands. In particular, to increase the temporal resolution, we estimate time-delays from channel measurements collected in two frequency bands that give the largest frequency aperture, i.e., from the two frequency bands that are furthest apart. However, this algorithm

is general and can be applied to time-delay estimation from any two frequency bands. We will denote these bands with indexes $i = 0$ and $i = L-1$, and their central frequencies are ω_0 and $\omega_{L-1} = \omega_0 + n_{L-1}\omega_{sc}$, where $n_{L-1} \in \mathbb{N}$ is a positive integer number that relates ω_0 and ω_{L-1}. Following the procedure described in Section 5.3.1, we form the Hankel matrices $\mathbf{H}_0$ and $\mathbf{H}_{L-1}$, following the structure given in (4.15), and stack them in a block matrix

$$\mathbf{H} = \begin{bmatrix} \mathbf{H}_1 \\ \mathbf{H}_{L-1} \end{bmatrix}. \tag{5.6}$$

The matrix $\mathbf{H}$ has the model

$$\mathbf{H} := \mathbf{A}\mathbf{X} + \mathbf{Q} = \begin{bmatrix} \mathbf{M}' \\ \mathbf{M}'\mathbf{\Theta} \end{bmatrix} \mathbf{X} + \mathbf{Q}, \tag{5.7}$$

where $\mathbf{X} = [\boldsymbol{\alpha} \quad \mathbf{\Phi}\boldsymbol{\alpha} \quad \mathbf{\Phi}^2\boldsymbol{\alpha} \cdots \mathbf{\Phi}^{Q-1}\boldsymbol{\alpha}]$, $\mathbf{Q}$ is formed by stacking $\mathbf{Q}'_1$ on top of $\mathbf{Q}'_2$, $\mathbf{\Theta} = \text{diag}([\theta_1 \cdots \theta_K])$ is a diagonal matrix collecting the band dependent phase shifts $\theta_k = e^{-j\theta_k}$, $k = 1, \ldots, K$, on its diagonal. Here, $\theta_k = n_{L-1}\omega_{\text{sc}}\tau_k$, and we can write $\mathbf{\Theta} = \mathbf{\Phi}^{n_{L-1}}$. Note that $\mathbf{H}$ has a double shift-invariance structure introduced by the time-delays $\tau_k, k = 1, \ldots, K$, over (i) the subcarrier spacing within a single band, i.e., $\phi_k = \omega_{sc}\tau_k$, and over (ii) the carrier frequency difference between two bands, i.e., $\theta_k = n_{L-1}\phi_k$, as shown in Fig. 5.1. In general, the carrier frequency difference is much higher than the subcarrier spacing, and therefore, $\theta_k \gg \phi_k$ for $k = 1, \cdots, K$. The estimation of $\tau_k, k = 1, \ldots, K$, from $\mathbf{\Theta}$ will result in high resolution but ambiguous estimates due to unknown multiples of 2π in the phases. However, we can use the idea of multiresolution (MR) parameter estimation [217] to develop the algorithm for high resolution estimation of τ_k without ambiguity by combining coarse and fine estimates obtained from $\mathbf{\Phi}$ and $\mathbf{\Theta}$, respectively.

We follow a similar approach as in the previous section. Let $\mathbf{U}$ be an orthonormal basis for the column span of $\mathbf{H}$, obtained using a truncated SVD. Let us, define the selection matrices

$$\begin{aligned} \mathbf{J}^{(r)}_{\Phi,1} &= \mathbf{I}_2 \otimes [\mathbf{I}_{P-r} \quad \mathbf{0}_{P-r,r}], \qquad & \mathbf{J}_{\Theta,1} &= [1 \quad 0] \otimes \mathbf{I}_P, \\ \mathbf{J}^{(r)}_{\Phi,2} &= \mathbf{I}_2 \otimes [\mathbf{0}_{P-r,r} \quad \mathbf{I}_{P-r}], \qquad & \mathbf{J}_{\Theta,2} &= [0 \quad 1] \otimes \mathbf{I}_P. \end{aligned} \tag{5.8}$$

To estimate $\mathbf{\Phi}$, we set $r = 1$ and take submatrices consisting of the first and the last row of each block matrix stacked in $\mathbf{U}$, respectively, that is $\mathbf{U}_{\Phi,1} = \mathbf{J}^{(1)}_{\Phi,1}\mathbf{U}$ and $\mathbf{U}_{\Phi,2} = \mathbf{J}^{(1)}_{\Phi,2}\mathbf{U}$. The estimation of $\mathbf{\Theta}$ is based on the first and the second block matrix present in $\mathbf{U}$, respectively, that is $\mathbf{U}_{\Theta,1} = \mathbf{J}_{\Theta,1}\mathbf{U}$ and $\mathbf{U}_{\Theta,2} = \mathbf{J}_{\Theta,2}\mathbf{U}$. The selected matrices have the following models:

$$\begin{aligned} \mathbf{U}_{\Phi,1} &= \begin{bmatrix} \mathbf{M}'' \\ \mathbf{M}''\mathbf{\Theta} \end{bmatrix} \mathbf{T}^{-1}, \qquad & \mathbf{U}_{\Theta,1} &= \mathbf{M}'\mathbf{T}^{-1}, \\ \mathbf{U}_{\Phi,2} &= \begin{bmatrix} \mathbf{M}'' \\ \mathbf{M}''\mathbf{\Theta} \end{bmatrix} \mathbf{\Phi}\mathbf{T}^{-1}, \qquad & \mathbf{U}_{\Theta,2} &= \mathbf{M}'\mathbf{\Theta}\mathbf{T}^{-1}, \end{aligned} \tag{5.9}$$

where $\mathbf{M}'' = \mathbf{J}^{(1)}_1\mathbf{M}'$ and $\mathbf{J}^{(1)}_1$ is given in (5.3). The Least Squares approximate solutions to the set of equations in (5.9) satisfy a model of the form

$$\begin{aligned} \mathbf{\Psi} &:= \mathbf{U}^{\dagger}_{\Phi,1}\mathbf{U}_{\Phi,2} = \mathbf{T}\mathbf{\Phi}\mathbf{T}^{-1}, \\ \mathbf{\Upsilon} &:= \mathbf{U}^{\dagger}_{\Theta,1}\mathbf{U}_{\Theta,2} = \mathbf{T}\mathbf{\Theta}\mathbf{T}^{-1}. \end{aligned} \tag{5.10}$$

5

Observe that $\boldsymbol{\Psi}$ and $\boldsymbol{\Upsilon}$ are jointly diagonalizable by the same matrix $\mathbf{T}$. If each submatrix in (5.9) has at least K rows, the joint diagonalization can be computed by means of QZ iterations or Jacobi iterations [222, 223]. After $\mathbf{T}$ has been determined, the parameters ϕ_k and θ_k for $k = 1, \cdots, K$, are estimated.

Based on the phase estimates, coarse and fine time-delay estimates are computed as

$$\tau_k = \omega_{sc}^{-1}\phi_k = (n_{L-1}\omega_{sc})^{-1}(\theta_k + 2\pi m_k). \tag{5.11}$$

The unknown number of cycles m_k is determined as the best fitting integer that satisfies (5.11), that is,

$$m_k = \text{round}\left\{\frac{1}{2\pi}\left(n_{L-1}\phi_k - \theta_k\right)\right\}. \tag{5.12}$$

If the estimation errors of the ϕ_k and the θ_k are comparable, then the τ_k estimate based on θ_k is n_{L-1} times more accurate and less affected by noise compared to the one based on ϕ_k. Therefore, the final estimate of ϕ_k is obtained based on θ_k, or by optimal combining of coarse and fine estimates [217].

5

5.3.3. DATA EXTENSIONS

So far, we have discussed MRTD estimation considering single snapshot multipath channel measurements. Similar as in Section 4.3.3, MRTD estimation can be used to estimate time-delay from multiple snapshot measurements. Furthermore, data matrix $\mathbf{H}$ can be extended using the forward-backward (FB) averaging technique [130]. Next, we discuss these extensions of the basic MRTD estimation algorithm.

MULTIPLE SNAPSHOTS

Let us assume that M snapshots of channel measurements $\mathbf{h}_i^{(m)}, \quad m = 1, \ldots, M$ (5.1) are collected during the coherence time for the bands $i = 1, L-1$. Then, similar as in the single snapshot case, from measurements collected in every snapshot $\mathbf{h}_i^{(m)}$, $i = 1, L-1$, we can construct a block Hankel matrix $\mathbf{H}^{(m)}$

$$\mathbf{H}^{(m)} = \begin{bmatrix} \mathbf{H}_1^{(m)} \\ \mathbf{H}_{L-1}^{(m)} \end{bmatrix}, \tag{5.13}$$

where $\mathbf{H}_i^{(m)}$ is a Hankel matrix (4.15) constructed from $\mathbf{h}_i^{(m)}$. The block Hankel matrix $\mathbf{H}^{(m)}$ satisfies the following model

$$\mathbf{H}^{(m)} = \mathbf{A}\mathbf{X}^{(m)} + \mathbf{Q}^{(m)}, \tag{5.14}$$

where now $\mathbf{X}^{(m)} := [\boldsymbol{\alpha}^{(m)} \quad \boldsymbol{\Phi}\boldsymbol{\alpha}^{(m)} \cdots \boldsymbol{\Phi}^{Q-1}\boldsymbol{\alpha}^{(m)}]$, and $\mathbf{Q}^{(m)}$ represents the noise matrix of the mth snapshot. Here, we assumed that the time-delays $\{\tau_k^{(m)}\}_{k=1}^K$, $m = 1, \ldots, M$, of the MPCs stay the same during the coherence time. From (5.14), it is easy to see that the matrices $\mathbf{H}^{(m)}$, $m = 1, \ldots, M$, have the same column subspace. We use this property to increase the dimension of the data matrix by constructing the following extended data matrix

$$\boldsymbol{\mathcal{H}} := [\mathbf{H}^{(1)} \quad \mathbf{H}^{(2)} \cdots \mathbf{H}^{(M)}], \tag{5.15}$$

which has factorization $\boldsymbol{\mathcal{H}} = \mathbf{A}\boldsymbol{\mathcal{X}} + \boldsymbol{\mathcal{Q}}$,. Here, $\boldsymbol{\mathcal{X}} := [\mathbf{X}^{(1)} \cdots \mathbf{X}^{(M)}]$ and $\boldsymbol{\mathcal{Q}} := [\mathbf{Q}'^{(1)} \cdots \mathbf{Q}'^{(M)}]$. The estimation of $\boldsymbol{\tau}$ from $\boldsymbol{\mathcal{H}}$ proceeds as described in Section 5.3.2. Now the number of columns in the data matrix is increased, which reduces errors when estimating the signal subspace and it improves time-delay estimation accuracy due to noise.

FORWARD-BACKWARD AVERAGING

The multiband channel measurements collected for any two frequency bands of equal size are taken *centro-symmetric* [130]. Therefore we can apply the forward-backward (FB) averaging technique presented in Section 4.3.3 to double the number of columns in the data matrix $\boldsymbol{\mathcal{H}}$. The forward-backward averaged multiple snapshot data matrix $\boldsymbol{\mathcal{H}}_{\mathrm{e}}$ is constructed as

$$\boldsymbol{\mathcal{H}}_{\mathrm{e}} := [\boldsymbol{\mathcal{H}} \quad \boldsymbol{\Pi}\boldsymbol{\mathcal{H}}^*], \tag{5.16}$$

where $\boldsymbol{\Pi}$ denote the $2P \times 2P$ exchange matrix that reverses the ordering of the rows, and $(\cdot)^*$ denotes the complex conjugate of the elements of a matrix. The column space of the matrix $\boldsymbol{\mathcal{H}}_e$ is spanned by the same basis $\boldsymbol{\mathcal{H}}$ and all shift-invariance properties stay preserved after FB averaging. However, the number of columns in $\boldsymbol{\mathcal{H}}_{\mathrm{e}}$ is twice the number of columns in $\boldsymbol{\mathcal{H}}$, which leads to improved accuracy when estimating the signal subspace and time-delays. The estimation of $\boldsymbol{\tau}$ from $\boldsymbol{\mathcal{H}}_{\mathrm{e}}$ proceeds as described in Section 5.3.2.

5.3.4. ALGORITHM SUMMARY

A summary of MRTD estimation algorithm is given as Algorithm 4. The routine `JDIAG`$(\cdot,\cdot)$ refers to joint diagonalization of matrices [222, 223]. The remaining parts of the summary are self-explanatory.

5.4. NUMERICAL EXPERIMENTS

In this section, we present numerical results that illustrate the performance of MRTD algorithm. We first describe the general simulation setup, and later we introduce several specific scenarios that are considered in the experiments. We consider a scenario where the multipath channel has eight dominant MPCs, i.e., $K = 8$, with the gains distributed according to the Rayleigh distribution. The time-delays of MPCs are set to $\{1, 7, 14, 21, 27, 31, 35, 40\}$ ns, and their relative average powers are set to $\{0, -4, -5, -4, -6, -5.5, -8, -7\}$ dB. In the simulations, we consider that the multipath channel is probed using OFDM training signals with a subcarrier spacing of $\omega_{sc} = 78.125$ kHz. These training signals are used to probe multiple frequency bands and obtain multiband channel measurements, which are then used as input to the algorithms for time-delay estimation. In particular, we compare the performance of multiresolution time-delay (MRTD) estimation to the following: single band time delay estimation algorithm ESPRIT [124], multiband time-delay estimation algorithms MBWDE [224], and finally MI-MUSIC [214], which are previously discussed in Chapter 4. We use RMSE as the metric to compare the performance of the time-delay estimation for the algorithms mentioned before. The RMSEs are obtained over 10^4 independent Monte Carlo runs

Algorithm 4: Multiresolution (MR) Time-Delay Estimation

Input: $N, P, K, r, \{\mathbf{h}_i^{(m)} : m = 1, \ldots, M\}_{i=0,L-1}$
Output: $\hat{\boldsymbol{\tau}}$
$Q \leftarrow N - P + 1$;
$\mathbf{H}_i^{(m)} \leftarrow \texttt{hankel}(\mathbf{h}_i^{(m)}, P, Q), \forall i, m$; (4.15)
$\boldsymbol{\mathcal{H}} \leftarrow [\mathbf{H}^{(1)} \ldots \mathbf{H}^{(M)}], \forall i$; (5.15)
$\boldsymbol{\mathcal{H}}_{\mathrm{e}} \leftarrow \boldsymbol{\mathcal{H}}$;
if *ForwardBackward* **then**
  $\boldsymbol{\mathcal{H}}_{\mathrm{e}} \leftarrow [\boldsymbol{\mathcal{H}} \quad \boldsymbol{\Pi}\boldsymbol{\mathcal{H}}^*]$; (5.16)
end
$\{\mathbf{U}, \sim, \sim\} \leftarrow \texttt{TSVD}(\boldsymbol{\mathcal{H}}_{\mathrm{e}}, K)$;
$\mathbf{J}_{\Phi 1}^{(r)} \leftarrow \mathbf{I}_2 \otimes [\mathbf{I}_{P-r} \quad \mathbf{0}_{P-r,r}]$; (5.8)
$\mathbf{J}_{\Phi 2}^{(r)} \leftarrow \mathbf{I}_2 \otimes [\mathbf{0}_{P-r,r} \quad \mathbf{I}_{P-r}]$; (5.8)
$\mathbf{J}_{\Theta 1} \leftarrow [1 \quad 0] \otimes \mathbf{I}_P$; (5.8)
$\mathbf{J}_{\Theta 2} \leftarrow [0 \quad 1] \otimes \mathbf{I}_P$; (5.8)
$\mathbf{U}_{\Phi 1} \leftarrow \mathbf{J}_{\Phi 1}^{(1)} \mathbf{U}$; (5.9)
$\mathbf{U}_{\Phi 2} \leftarrow \mathbf{J}_{\Phi 2}^{(1)} \mathbf{U}$; (5.9)
$\mathbf{U}_{\Theta 1} \leftarrow \mathbf{J}_{\Theta 1} \mathbf{U}$; (5.9)
$\mathbf{U}_{\Theta 2} \leftarrow \mathbf{J}_{\Theta 2} \mathbf{U}$; (5.9)
$\boldsymbol{\Psi} \leftarrow \mathbf{U}_{\Phi 1}^{\dagger} \mathbf{U}_{\Phi 2} = \mathbf{T}\boldsymbol{\Phi}\mathbf{T}^{-1}$; (5.10)
$\boldsymbol{\Upsilon} \leftarrow \mathbf{U}_{\Theta 1}^{\dagger} \mathbf{U}_{\Theta 2} = \mathbf{T}\boldsymbol{\Theta}\mathbf{T}^{-1}$; (5.10)
$\mathbf{T} \leftarrow \texttt{JDIAG}(\boldsymbol{\Psi}, \boldsymbol{\Upsilon})$;
$\boldsymbol{\Phi} \leftarrow \mathbf{T}^{-1}\boldsymbol{\Psi}\mathbf{T}$;
$\boldsymbol{\Theta} \leftarrow \mathbf{T}^{-1}\boldsymbol{\Upsilon}\mathbf{T}$;
$m_k \leftarrow \text{round}\left\{\frac{1}{2\pi}\left(n_{L-1}\phi_k - \theta_k\right)\right\}, k = 1, \ldots, K$; (5.12)
$\tau_k \leftarrow (n_{L-1}\omega_{sc})^{-1}(\theta_k + 2\pi m_k), k = 1, \ldots, K$; (5.11)

and they are compared against the CRB for the multiband channel data model derived in Section 4.35.

We first evaluate the influence of the bandwidth of the training signals on the performance of MRTD algorithm. We simulate scenarios where the bandwidth B of the training signals is set to $\{20, 40, 80\}$ MHz. The channel is probed in $L = 2$ frequency bands with carrier frequencies set to $\{6, 6.120\}$ GHz and $M = 10$ snapshots are collected during the channel coherence time. Fig. 5.2 presents the RMSEs of the estimated time-delay (τ_1) for the LOS path plotted against the SNR for the scenarios where training signals have varying bandwidths. From the figure, it can be seen that the proposed algorithm asymptotically achieves the CRB for increasing SNR. Furthermore, as expected, for larger bandwidths, the proposed algorithm is more robust to noise and offers higher resolution.

In the second experiment, we evaluate the influence of carrier frequency selection of the probed bands on the performance of MRTD estimation. In these scenarios, we keep the bandwidth of the training signals and the number of snapshots fixed to $B = 20$ MHz

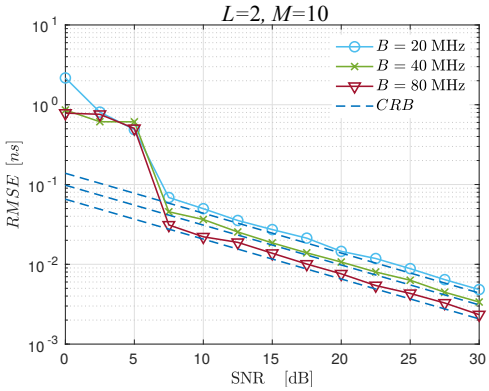

Figure 5.2: Root Mean Square Error (RMSE) of time-delay estimates (τ_1) for varying bandwidths of the measurements. The results show that the algorithm asymptotically achieves the CRB for increasing SNR and that for larger bandwidths of the measurements, it is more robust to noise and offers higher resolution.

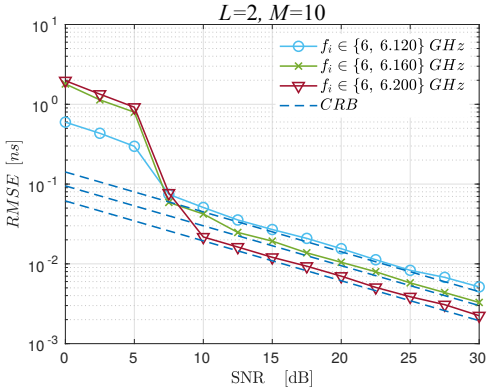

Figure 5.3: Root Mean Square Error (RMSE) of time-delay estimates (τ_1) for varying band positions. The results show that by separating the two bands further apart, i.e., by increasing the frequency aperture, the resolution of the multiresolution time-delay estimation increases.

and $M = 10$, respectively, while the carrier frequencies of the probed frequency bands are set to $\{6, 6.120\}$, $\{6, 6.160\}$, and $\{6, 6.200\}$ GHz respectively. Fig. 5.3 shows the RMSEs of the estimated time-delays (τ_1) for the LOS path. It can be seen that by separating the two bands further apart, i.e., by increasing the frequency aperture, the resolution of MRTD estimation increases. However, for low SNR, MRTD estimator has slightly better performance in scenarios where the frequency aperture is lower due to decreased ambiguity and lower error for fine time-delay estimation.

Fig. 5.4 shows the performance of the MRTD, MBWDE, ESPRIT and MI-MUSIC algorithms as a function of SNR. MRTD supports time-delay estimation from channel measurements collected in two separate frequency bands, i.e., $L = 2$. The performance of this algorithm is evaluated using the measurements collected from the training signals that

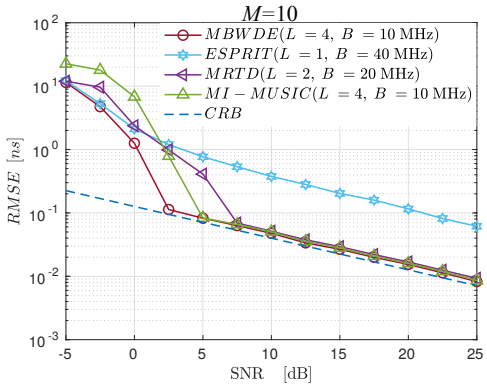

Figure 5.4: Performance comparison of multiresolution time-delay (MRTD) estimation with ESPRIT, MBWDE, and MI-MUSIC. The results show that from algorithms that have a closed-form solution, i.e., ESPRIT and MRTD, MRTD algorithm has better performance, and it converges to the CRB with the increase of SNR.

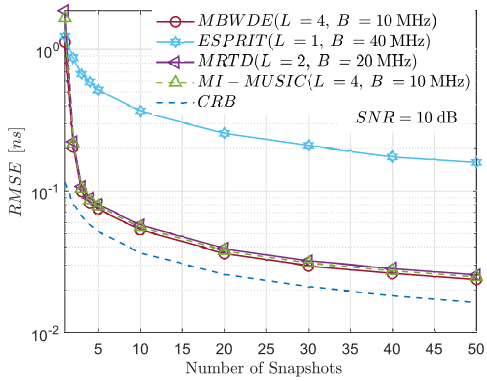

Figure 5.5: Influence of the number of multiband channel snapshots M on the performance of multiresolution time-delay (MRTD) estimation. The results show that the RMSE of time-delay estimation decreases with the number of snapshots.

have a bandwidth of B = 20 MHz, where their carrier frequency parameters are set to $\{6, 6.120\}$ GHz. To compare the performance of MRTD against single band time-delay estimation algorithms, we use ESPRIT [124], to which we provide multipath channel measurements collected in a single band. However, to have a fair comparison, the measurements provided to ESPRIT are collected using a training signal whose bandwidth is twice the bandwidth of the signals used for MRTD, i.e., B = 40 MHz. Meanwhile, the carrier frequency of the training signal is set to 6 GHz. Lastly, we compare the performance of MRTD against MBWDE [224] and MI-MUSIC [214]. For these algorithms, we provide multiband channel measurements collected in L = 4 frequency bands, where each band has a bandwidth that is half the bandwidth used for MRTD, i.e., B = 10 MHz,

and their carrier frequencies are set to $\{6, 6.04, 6.08, 6.120\}$, the frequency aperture remains the same. Fig. 5.4 shows that MBWDE has the best performance as it is the first one to converge to CRB. MRTD shows worse performance than MI-MUSIC, but it outperforms classical ESPRIT. More specifically, due to the small frequency aperture of the channel measurements used for time-delay estimation with ESPRIT, it never converges to the CRB derived for the multiband channel model. These results are in accordance with those presented in Fig. 4.11, where it can be seen that single band time-delay algorithms have worse performance than multiband time-delay estimation algorithms and that the CRB for single-band channel measurements is above the CRB for multiband measurements.

In the last experiment, we fixed the signal-to-noise ratio to $SNR = 10$ dB, while other parameters were kept as in the previous experiment. We then evaluate the performance of the algorithms listed in the previous experiment for different numbers of snapshots M. From Fig. 5.5, it is seen that the RMSE of time-delay estimation decreases with the number of snapshots. It can be observed that the number of snapshots needs to be sufficiently high, i.e., equal to or higher than 3, for the algorithms to perform well, which comes as a consequence of subspace estimation errors. The minimum number of snapshots required for MRTD to converge to CRB increases as the SNR decreases.

5.5. CONCLUSIONS

In this chapter, we introduced the MRTD estimation algorithm, which has a closed-form solution and supports time-delay estimation from channel measurements collected in two frequency bands. From numerical results, we observed that this algorithm converges to the CRB derived for multiband channel measurements. The results also showed that the time-delay resolution of the algorithm can be improved by increasing the frequency aperture over which multiband channel measurements are collected. The performance of MRTD is compared against ESPRIT, which supports time-delay estimation from single-band channel measurements. As expected, MRTD outperforms ESPRIT due to the lower frequency aperture of the measurements provided to the ESPRIT algorithm. Likewise, the performance of MRTD is compared against MBWDE and MI-MUSIC, which are more general multiband time-delay estimation algorithms that support time-delay estimation from multiband channel measurements collected in an arbitrary number of bands. These algorithms converge to the CRB at a lower SNR compared to MRTD. However, MBWDE does not have a closed-form solution, and it requires a good initial estimate of the time-delays, while MI-MUSIC demands an exhaustive search. At the same time, MRTD has a performance close to those of MBWDE and MI-MUSIC while having a closed-form solution, being asymptotically efficient and converging to the CRB. Therefore, MRTD can provide good initial estimates for solving the optimization problems described in (4.20) and (4.22).

6

JOINT RF CHAIN CALIBRATION AND TIME-DELAY ESTIMATION

"Any measurement that you make without the knowledge of its uncertainty is completely meaningless."

— Walter Lewin

Part of this chapter is published as: T. Kazaz, M. Coutino, G.J.M. Janssen, and A.J. van der Veen, "Joint Blind Calibration and Time-Delay Estimation for Multiband Ranging", IEEE International Conference on Acoustics, Speech, and Signal Processing (ICASSP), Barcelona, Spain, May 2020.

6.1. INTRODUCTION

So far, we have assumed that multiband channel measurements are collected using ideal RF transceivers. In particular, we considered that the frequency response of transceivers' RF chains is measured and calibrated before the acquisition of the channel measurements. However, in practical scenarios, the frequency response of transceivers might not be known nor calibrated. When this is the case, the nonideal response of RF chains will introduce modeling errors in the data models that are used for the development of MBWDE and MRTD algorithms in Chapters 4 and 5, respectively. For this reason, these algorithms are sensitive to RF chain calibration errors and will result in biased time-delay estimation from uncalibrated multiband measurements.

As a large frequency band (aperture) must be covered during channel probing to increase the resolution of time-delay estimates [225], nodes are required to have integrated wideband RF chains. These often introduce frequency-dependent gain and phase distortions in the training signals due to the used amplifiers and anti-aliasing filters [226]. For instance, consider multiband acquisition of multipath signals [227, 228, 102]. Due to the large frequency aperture required during channel probing [203], channel measurements are affected by distortions introduced in the RF chains. As these effects can significantly deteriorate range estimation, they need to be estimated and corrected in a *calibration* process. In channel sounding experiments, distortions of RF chains are usually manually calibrated [229]. Unfortunately, calibration in localization scenarios is challenging as the mobile and anchor nodes are diverse, and manual calibration of each node is not practical.

Calibration is of interest for many applications such as communications [230, 231, 232], radio astronomy [233, 234, 235], and medical imaging [236]. Therefore, many signal processing algorithms have already been proposed for calibration in these applications. While some of these algorithms assume prior knowledge of the measurement matrix, e.g., the array response or the second-order statistics of the calibration parameters, others rely on the Toeplitz structure of the covariance matrix related to the underlying sensor array.

In this chapter, our goal is to design an algorithm that jointly calibrates the RF chains and estimates parameters of the multipath components. Differently from previous works, we exploit the properties of the communication channel and formulate the joint calibration and time-delay estimation as a special case of a covariance matching problem [237]. Even though this formulation leads to an ill-posed problem, using prior information about the distortions of RF chains and the sparse property of multipath channels, the problem can be regularized. Here, we consider that gain distortions of RF chains are slowly varying with frequency, while phase distortions are negligible [238]. This assumption allows us to approximate the distortions of the RF chains with a set of known basis functions, leading to a biconvex problem in the calibration and time-delay parameters. Although biconvex optimization algorithms are applicable, e.g., [239, 240], the approach in [239] does not consider multiple measurement scenarios, and the algorithm in [240] has high complexity and no convergence guarantees. Therefore, we propose to re-cast the biconvex optimization problem as a rank-1 constrained linear system using the *lifting* technique [241, 242, 243], which can be solved efficiently as a group

Lasso problem.

The performance of the proposed algorithm is evaluated through simulations by comparing it with algorithms presented in [240, 244]. The results show that the proposed algorithm provides better calibration performance and a higher resolution for time-delay estimation.

6.2. PROBLEM FORMULATION AND DATA MODEL

In this chapter, we are interested in estimating time-delays $\boldsymbol{\tau}$ and calibrating the multiband frequency response of RF transceivers $\mathbf{g}_i, i = 0,\dots,L-1$. This problem is similar to the one presented in Chapter 4. However, now we assume that the frequency responses of the RF chains at the mobile and anchor nodes are not calibrated in advance, and they are to be estimated together with parameters $\boldsymbol{\alpha}$ and $\boldsymbol{\tau}$ from the multiband channel measurements. We assume that the multiband channel measurements are collected by probing the channel using a known wideband OFDM training signal $x(t)$ transmitted over $i = 0,\dots,L-1$, frequency bands $\mathcal{W}_i = [\omega_i - \pi B, \omega_i + \pi B]$, where B is the bandwidth, and ω_i is the central angular frequency of the ith band. The channel probing is performed M times during the channel coherence time. We consider that transceivers with unknown frequency responses of their RF chains are used during the channel probing, and our objective is to perform calibration of their frequency responses and estimate $\boldsymbol{\tau}$ and $\boldsymbol{\alpha}$ from the collected measurements.

We consider a baseband signal model presented in Section 4.2.2 and assume ideal conversion to and from the passband. The unknown responses of the RF chains at the ith frequency band are modeled using equivalent linear and time-invariant low-pass filters $g_i(t) = g_{\mathrm{A},i}(t) * g_{\mathrm{M},i}(t)$, where the corresponding CTFT $G_i(\omega) = G_{\mathrm{A},i}(\omega)G_{\mathrm{M},i}(\omega)$ has passband $[-\pi B, \pi B]$. The compound impulse response of the RF chains and the channel is $c_i(t) = g_i(t) * h(t)$, where $h(t)$ is the baseband equivalent channel impulse response given in (3.1), and its CTFT is given in (4.5). Now, using the results of Section 4.2.2, we can write the frequency domain continuous-time model for the signal received in the ith band as

$$Y_i(\omega) = \begin{cases} X(\omega)C_i(\omega) + Q_i(\omega), & \omega \in [-\pi B, \pi B] \\ 0, & \text{otherwise}, \end{cases} \tag{6.1}$$

where $C_i(\omega) = G_i(\omega)H_i(\omega)$ is the compound CFR and $H_i(\omega)$ is given by (4.5). Likewise, $X(\omega)$ and $Q_i(\omega)$ are the CTFTs of training signal $x(t)$ and the low-pass filtered zero-mean Gaussian noise $q_i(t)$, respectively.

6.2.1. DISCRETE-TIME SIGNAL MODEL

The continuous-time data model is the similar to the one presented in Chapter 4. The difference now is that we assume that the multiband frequency responses of the RF chains $G_i(\omega)$, $i = 0,\dots,L-1$, are unknown while in Chapter 4 we assumed them as known. Therefore, we can directly use the derivations given in Section 4.2.3 and write the discrete data model for the signals (cf. (4.6) for details) received during M probing intervals as

$$\mathbf{y}_i^{(m)} = \mathrm{diag}(\mathbf{s})\mathbf{c}_i^{(m)} + \mathbf{q}_i^{(m)}, \quad m = 1,\dots,M, \tag{6.2}$$

where $\mathbf{c}_i^{(m)} = \text{diag}(\mathbf{g}_i)\mathbf{h}_i^{(m)}$, $\mathbf{s}$ collects the pilot symbols, and $\mathbf{q}_i^{(m)} \in \mathbb{C}^N$ is zero-mean white Gaussian distributed noise. The samples of $G_i(\omega)$ at the subcarrier frequencies are collected in $\mathbf{g}_i = [g_{i,0}, \ldots, g_{i,N-1}]^T \in \mathbb{C}^N$, where $g_{i,n} = \rho_{i,n} e^{j\psi_{i,n}}$ with $\rho_{i,n}$ and $\psi_{i,n}$ denoting the unknown gain and phase introduced by the nonideal frequency response of the RF chains, respectively. Likewise, $\mathbf{h}_i^{(m)} \in \mathbb{C}^N$ collects the samples of $H_i(\omega)$ in increasing order of frequencies and its model is given by (cf. (4.11) for details)

$$\mathbf{h}_i^{(m)} = \mathbf{M}\boldsymbol{\Theta}_i \boldsymbol{\alpha}^{(m)}, \tag{6.3}$$

where $\mathbf{M}$ is a Vandermonde matrix given by (3.13) and $\boldsymbol{\Theta}_i = \boldsymbol{\Phi}^{n_i}$ is a diagonal matrix collecting band dependent phase shifts introduced by the time-delays of the MPCs.

6.2.2. DATA MODEL

From $\mathbf{y}_i^{(m)}$, the compound responses $\mathbf{c}_i^{(m)}$ are estimated by deconvolution of (6.2) as

$$\mathbf{c}_i^{(m)} = \text{diag}^{-1}(\mathbf{s})\mathbf{y}_i^{(m)}.$$

The deconvolved measurements satisfy the model

$$\mathbf{c}_i^{(m)} = \text{diag}(\mathbf{g}_i)\mathbf{M}\boldsymbol{\Theta}_i \boldsymbol{\alpha}^{(m)} + \mathbf{q}_i'^{(m)}, \tag{6.4}$$

where the pilot symbols have a constant magnitude and $\mathbf{q}_i'^{(m)} = \text{diag}^{-1}(\mathbf{s})\mathbf{q}_i^{(m)}$ is zero-mean white Gaussian distributed noise.

The estimates of the compound frequency response, $\mathbf{c}_i^{(m)}$, are stacked in $\mathbf{c}^{(m)} = [(\mathbf{c}_0^{(m)})^T, \ldots, (\mathbf{c}_{L-1}^{(m)})^T]^T \in \mathbb{C}^{NL}$. From (6.4), the model for $\mathbf{c}_i^{(m)}$ is

$$\mathbf{c}^{(m)} = \text{diag}(\mathbf{g})\mathbf{A}(\boldsymbol{\tau})\boldsymbol{\alpha}^{(m)} + \mathbf{q}^{(m)}, \tag{6.5}$$

where $\mathbf{A}(\boldsymbol{\tau}) = [\mathbf{a}(\tau_1), \ldots, \mathbf{a}(\tau_K)] \in \mathbb{C}^{NL\times K}$ has the multiple shift-invariance structure

$$\mathbf{A}(\boldsymbol{\tau}) = \begin{bmatrix} \mathbf{M} \\ \mathbf{M}\boldsymbol{\Theta}_1 \\ \vdots \\ \mathbf{M}\boldsymbol{\Theta}_{L-1} \end{bmatrix}, \qquad \mathbf{g} = \begin{bmatrix} \mathbf{g}_1 \\ \mathbf{g}_2 \\ \vdots \\ \mathbf{g}_L \end{bmatrix},$$

and likewise, $\mathbf{q}^{(m)} \in \mathbb{C}^{NL}$ collects $\mathbf{q}_i'^{(m)}$, $i = 0, \ldots, L-1$.

Stacking all the estimates of the compound frequency responses, collected during M probing intervals in $\mathbf{C} = [\mathbf{c}(1), \ldots, \mathbf{c}(M)] \in \mathbb{C}^{NL\times M}$, leads to the model given by (6.5)

$$\mathbf{C} = \text{diag}(\mathbf{g})\mathbf{A}(\boldsymbol{\tau})\mathbf{X} + \mathbf{Q}, \tag{6.6}$$

where $\mathbf{X} = \left[\boldsymbol{\alpha}^{(1)}, \ldots, \boldsymbol{\alpha}^{(M)}\right] \in \mathbb{C}^{K\times M}$, and $\mathbf{Q}$ collects $\mathbf{q}^{(m)}$ $\forall$ M.

6.3. JOINT CALIBRATION AND TIME-DELAY ESTIMATION

Our objective is to estimate the unknown responses of the RF chains, $\mathbf{g}$, and time-delays, $\boldsymbol{\tau}$, of the MPCs from the measurement matrix $\mathbf{C}$. We first introduce a general problem

formulation for joint calibration and time-delay estimation and then propose an efficient algorithm for solving it. Joint calibration and time-delay estimation can be formulated as the following optimization problem

$$\hat{\mathbf{g}}, \hat{\boldsymbol{\tau}}, \hat{\mathbf{X}} = \underset{\mathbf{g},\boldsymbol{\tau},\mathbf{X}}{\operatorname{argmin}} \ \|\mathbf{C} - \operatorname{diag}(\mathbf{g})\mathbf{A}(\boldsymbol{\tau})\mathbf{X}\|_F^2 . \tag{6.7}$$

This problem is clearly ill-posed and nonlinear, making it difficult to solve without further assumptions or prior information. Therefore, we use prior knowledge about the frequency response of RF chains and the sparsity of the multipath channels to reformulate the problem.

6.3.1. ASSUMPTIONS

We assume that the response of the RF chains is gradually varying with respect to frequencies within a single frequency band [238]. Therefore, the entries of $\mathbf{g}_i$, $i = 0, \dots, L-1$ are slowly changing, and $\mathbf{g}_i$ can be approximated as $\mathbf{g}_i = \mathbf{B}_i\mathbf{p}$, where the columns of $\mathbf{B}_i \in \mathbb{C}^{NL\times R}$ are given by R known basis functions whose choice depends on the calibration scenario, and $\mathbf{p}$ are the unknown calibration parameters. For example, $\mathbf{B}_i$ can be a matrix constructed from the first R columns of the DFT (Discrete Fourier Transform) matrix [239] or the first R Chebyshev polynomials of the first kind [245]. In this paper, we aim at a near minimax polynomial approximation of $\mathbf{g}_i$, and we select the columns of $\mathbf{B}_i$ to be the first R Chebyshev polynomials of the first kind [245]. The columns of $\mathbf{B}_i$ are constructed from the polynomials evaluated at the normalized frequencies corresponding to $\mathbf{g}_i$ to capture changes in the response between the frequency bands, i.e., between the vectors $\mathbf{g}_i, i = 0, \dots, L-1$. Therefore, to approximate the overall frequency response of all bands, the matrix $\mathbf{B}$ that collects basis vectors is constructed as $\mathbf{B} = [\mathbf{B}_0^T, \dots, \mathbf{B}_{L-1}^T]^T$. Now, the overall frequency response $\mathbf{g}$ can be approximated as $\mathbf{g} = \mathbf{B}\mathbf{p}$.

Let the maximum expected time-delay to be estimated in the ranging scenario be $\tau_{\max} = \frac{d_{\max}}{c} + \tau_{\text{tot}}$, where $d_{\max}$ is the maximum distance, c is the speed of light, and τ_{tot} is the maximum delay spread of the channel. Assuming that the unknown time-delays lie on a uniform grid of $V \gg NL$ delays, i.e., $\tau_k \in \mathcal{T} = \{0, \frac{\tau_{\max}}{V}, \dots, \frac{\tau_{\max}(V-1)}{V}\}$, the following optimization problem can be formulated to solve the joint blind calibration and time-delay estimation

$$\hat{\mathbf{p}}, \hat{\mathbf{X}}_s = \underset{\mathbf{p},\mathbf{X}_s}{\operatorname{argmin}} \ \|\mathbf{C} - \operatorname{diag}(\mathbf{B}\mathbf{p})\mathbf{A}_D\mathbf{X}_s\|_F^2 + \lambda\|\mathbf{X}_s^T\|_{2,1} , \tag{6.8}$$

where $\mathbf{A}_D = [\mathbf{a}(t_0), \dots, \mathbf{a}(t_{V-1})] \in \mathbb{C}^{NL\times V}$ is a dictionary matrix with column vector defined in (6.5), $t_v = \frac{v}{V}\tau_{\max}$ and $\mathbf{X}_s \in \mathbb{C}^{V\times M}$ is a *row sparse matrix*. The regularization parameter $\lambda > 0$ determines the sparsity, i.e., the number of non-zero rows in $\mathbf{X}_s$, and $\|[\mathbf{a}_1, \dots, \mathbf{a}_n]\|_{2,1} := \sum_{i=1}^n \|\mathbf{a}_i\|_2$ is the $\ell_{2,1}$-norm of a matrix which is known to promote column sparsity.

The optimization problem in (6.8) is biconvex, i.e., it is convex in $\mathbf{p}$ for fixed $\mathbf{X}_s$ and convex in $\mathbf{X}_s$ for fixed $\mathbf{p}$, and alternating minimization can be used to estimate both $\mathbf{X}_s$ and $\mathbf{p}$. However, this optimization problem has no convergence guarantees, and it has high computational complexity when multiple snapshots are used for estimation,

which makes the problem formulation given in (6.8) unpractical. Therefore, we propose a method that offers a better solution using the ideas of covariance matching.

Let us assume that the multipath channel is a wide-sense stationary and uncorrelated scattering (WSSUS) fading channel. Therefore, $\boldsymbol{\alpha}^{(m)}$ and $\mathbf{q}^{(m)}$ are statistically independent and mutually uncorrelated variables with covariance matrices $\boldsymbol{\Sigma}_\alpha = \text{diag}(\boldsymbol{\sigma}_\alpha)$, with $\boldsymbol{\sigma}_\alpha = [\sigma^2_{\alpha,1},\ldots,\sigma^2_{\alpha,K}]^T$ and $\boldsymbol{\Sigma}_q = \sigma^2_q \mathbf{I}_{NL}$ [209]. With this assumption, we can write the covariance matrix of $\mathbf{c}^{(m)}$ as

$$\begin{aligned}\mathbf{R}_c &:= \mathbb{E}\left\{\mathbf{c}^{(m)}\left(\mathbf{c}^{(m)}\right)^H\right\} \in \mathbb{C}^{NL\times NL},\\ &= \text{diag}(\mathbf{g})\mathbf{A}(\boldsymbol{\tau})\boldsymbol{\Sigma}_\alpha\mathbf{A}^H(\boldsymbol{\tau})\text{diag}(\bar{\mathbf{g}}) + \sigma^2_q\mathbf{I}_{NL}.\end{aligned} \tag{6.9}$$

To obtain a linear measurement model, we vectorize (6.9) and write it as

$$\mathbf{r}_c = \text{diag}(\mathbf{g}^*\otimes\mathbf{g})\mathbf{K}(\boldsymbol{\tau})\boldsymbol{\sigma}_\alpha + \mathbf{r}_q, \tag{6.10}$$

where $\mathbf{K}(\boldsymbol{\tau}) = \mathbf{A}^*(\boldsymbol{\tau})\circ\mathbf{A}(\boldsymbol{\tau}) \in \mathbb{C}^{(NL)^2\times K}$ and $\mathbf{r}_q = \sigma^2_q\text{vec}(\mathbf{I}_{NL})$.

6.3.2. ALGORITHM

The covariance matrix can be estimated from the measurements as $\hat{\mathbf{R}}_c = \frac{1}{M}\mathbf{C}\mathbf{C}^H$, where its vectorized form is $\hat{\mathbf{r}}_c = \text{vec}(\hat{\mathbf{R}}_c)$. Here, we assume *a priori* knowledge of the noise power σ^2_q, and we define $\tilde{\mathbf{r}}_c = \hat{\mathbf{r}}_c - \mathbf{r}_q$. For the case with unknown σ^2_q, we can first estimate it according to [246]. Considering the modelling assumption on $\mathbf{g}$ and multipath channel sparsity, and using the properties of the Kronecker product, we can rewrite (6.10) as

$$\mathbf{r}_c = \text{diag}(\mathbf{D}\mathbf{z})\mathbf{K}_D\mathbf{r}_\alpha + \mathbf{r}_q, \tag{6.11}$$

where $\mathbf{D} = \mathbf{B}^*\otimes\mathbf{B}$ has size $(NL)^2\times R^2$, $\mathbf{z} = \mathbf{p}^*\otimes\mathbf{p} \in \mathbb{C}^{R^2}$, $\mathbf{K}_D = \mathbf{A}^*_D\circ\mathbf{A}_D \in \mathbb{C}^{(NL)^2\times V}$ is a dictionary matrix and $\mathbf{r}_\alpha \in \mathbb{R}^V$ is a K sparse vector that collects the entries of $\boldsymbol{\sigma}_\alpha$, i.e., that collects the powers of the MPCs. The unknown parameters in the data model are the calibration parameters $\mathbf{z}$ and the powers of the MPCs $\mathbf{r}_\alpha$. Note that finding the columns of $\mathbf{K}_D$ that correspond to the non-zero elements of $\mathbf{r}_\alpha$ is equivalent to estimating $\boldsymbol{\tau}$. To estimate these parameters, we formulate the following sparse covariance matching optimization problem

$$\hat{\mathbf{z}},\hat{\mathbf{r}}_\alpha = \underset{\mathbf{z},\mathbf{r}_\alpha}{\text{argmin}}\ \|\tilde{\mathbf{r}}_c - \text{diag}(\mathbf{D}\mathbf{z})\mathbf{K}_D\mathbf{r}_\alpha\|_2^2 + \lambda\|\mathbf{r}_\alpha\|_1, \tag{6.12}$$

where $\lambda > 0$ controls the level of sparsity of $\mathbf{r}_\alpha$.

Similar to (6.8), the objective function of this optimization problem is biconvex in the unknown parameters $\mathbf{z}$ and $\mathbf{r}_\alpha$. To alleviate difficulties arising from the biconvexity of the objective function, we reformulate (6.12) as a problem involving solving a linear system whose solution obeys a rank-1 constraint by *lifting* the unknown variables. The elements of $\mathbf{r}_c$ can be written as

$$[\mathbf{r}_c]_n = [\mathbf{D}\mathbf{z}]_n\mathbf{k}_n^T\mathbf{r}_\alpha + [\mathbf{r}_q]_n = \mathbf{d}_n^T\mathbf{z}\mathbf{r}_\alpha^T\mathbf{k}_n + [\mathbf{r}_q]_n,\ \forall\, n, \tag{6.13}$$

Algorithm 5: Joint Blind Calibration and Time-Delay Estimation

Input: $\{\mathcal{T}, \mathbf{B}, \mathbf{\Gamma}, \tilde{\mathbf{r}}_c, \lambda\}$

$\hat{\mathbf{e}} \leftarrow \underset{\mathbf{e}}{\text{argmin}} \ \|\tilde{\mathbf{r}}_c - \mathbf{\Gamma}\text{vec}(\mathbf{E})\|_2^2 + \lambda\|\mathbf{E}\|_{2,1}$;

$\hat{\mathbf{E}} \leftarrow \texttt{unvec}(\hat{\mathbf{e}})$;

$\{\hat{\mathbf{z}}, \sim, \hat{\mathbf{r}}_\alpha\} \leftarrow \texttt{TSVD}(\mathbf{E}, 1)$;

$\mathbf{Z} \leftarrow \texttt{unvec}(\hat{\mathbf{z}})$;

$\{\sim, \sim, \hat{\mathbf{p}}\} \leftarrow \texttt{TSVD}(\mathbf{Z}, 1)$;

$\hat{\mathbf{g}} \leftarrow \mathbf{B}\hat{\mathbf{p}}$;

$\{\hat{\boldsymbol{\sigma}}_{\boldsymbol{\alpha}}, \text{indxSet}\} \leftarrow \texttt{find}\ (\hat{\mathbf{r}}_\alpha \sim= 0)$;

$\hat{\boldsymbol{\tau}} \leftarrow \mathcal{T}(\text{indxSet})$;

Output: $\{\hat{\mathbf{p}}, \hat{\mathbf{g}}, \hat{\boldsymbol{\sigma}}_{\boldsymbol{\alpha}}, \hat{\boldsymbol{\tau}}\}$

where $\mathbf{d}_n^T$ and $\mathbf{k}_n^T$ denote the nth row of $\mathbf{D}$ and $\mathbf{K}_D$, respectively. Let us define the rank-1 matrix $\mathbf{E} := \mathbf{z}\mathbf{r}_\alpha^T$ and the linear operator $\mathcal{A} : \mathbb{C}^{R^2 \times V} \rightarrow \mathbb{C}^{NL}$ as

$$\mathbf{r}_c = \mathcal{A}(\mathbf{E}) + \mathbf{r}_q := \text{vec}(\{\mathbf{d}_n^T \mathbf{E} \mathbf{k}_n\}_{n=1}^{NL}) + \mathbf{r}_q \,. \tag{6.14}$$

Given that $\mathbf{d}_n^T \mathbf{E} \mathbf{k}_n = (\mathbf{k}_n \otimes \mathbf{d}_n)^T \text{vec}(\mathbf{E}) \ \forall \ n$, (6.14) becomes

$$\mathbf{r}_c = \mathbf{\Gamma}\mathbf{e} + \mathbf{r}_q \,, \tag{6.15}$$

where the nth row of $\mathbf{\Gamma} \in \mathbb{C}^{NL \times R^2 V}$ (the matrix representation of the operator $\mathcal{A}$) is $\boldsymbol{\gamma}_n^T = (\mathbf{k}_n \otimes \mathbf{d}_n)^T$, and $\mathbf{e} = \text{vec}(\mathbf{E})$.

The problem of estimating $\mathbf{z}$ and $\mathbf{r}_\alpha$ then reduces to finding a rank-1 matrix $\mathbf{E}$ satisfying the set of linear constrains (6.15). The find solution that promotes the rank-1 properties of $\mathbf{E}$, we can solve the following relaxed problem

$$\hat{\mathbf{E}} = \underset{\mathbf{E}}{\text{argmin}} \ \|\tilde{\mathbf{r}}_c - \mathbf{\Gamma}\text{vec}(\mathbf{E})\|_2^2 + \lambda\|\mathbf{E}\|_* \,, \tag{6.16}$$

where $\|\cdot\|_*$ denotes the nuclear norm of a matrix which promotes low rank solutions. To further simplify the problem, we use the sparsity of $\mathbf{E}$. Due to $\mathbf{r}_\alpha$, the matrix $\mathbf{E}$ is not only rank-1 but also column sparse. Since for any matrix $\mathbf{L}$, $\|\mathbf{L}\|_{2,1} > \|\mathbf{L}\|_*$ holds, we can use the $\|\cdot\|_{2,1}$-norm to regularize (6.16) instead of $\|\cdot\|_*$ following [239] and obtain a simpler formulation. Therefore, to estimate $\mathbf{z}$ and $\mathbf{r}_\alpha$ it is sufficient to solve

$$\hat{\mathbf{e}} = \underset{\mathbf{e}}{\text{argmin}} \ \|\tilde{\mathbf{r}}_c - \mathbf{\Gamma}\text{vec}(\mathbf{E})\|_2^2 + \lambda\|\mathbf{E}\|_{2,1} \,, \tag{6.17}$$

where the regularization parameter $\lambda > 0$ is set to be proportional to the noise power σ_q^2. This problem, besides of being convex, can be identified as a *group Lasso* problem, which can be solved efficiently. Here, we use the spectral gradient-projection method [150, 247].

To estimate $\mathbf{z}$ and $\mathbf{r}_\alpha$ after solving (6.17), first $\mathbf{E}$ is reconstructed from $\mathbf{e}$, and then the singular value decomposition is used to find the best rank-1 approximation of $\mathbf{E}$ in the

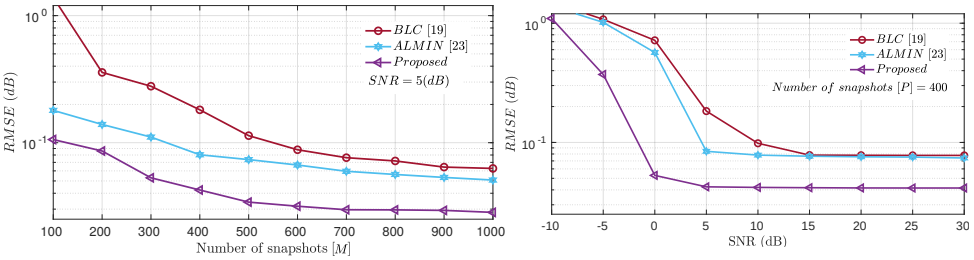

Figure 6.1: RMSE for estimated calibration parameters with respect to the number of snapshots (M) (a) and signal-to-noise ratio (SNR) (b).

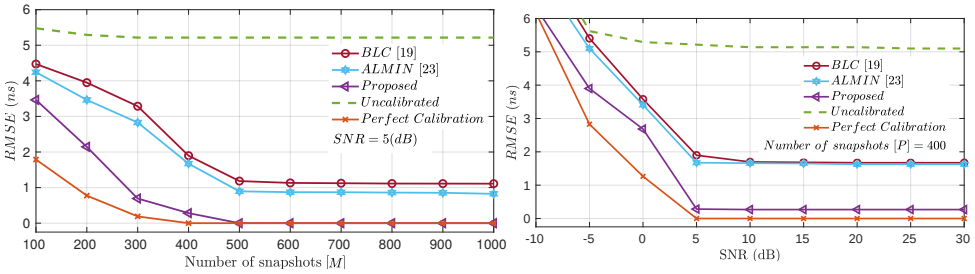

Figure 6.2: RMSE for the estimated time-delay parameter with respect to the number of snapshots (M) (a) and signal-to-noise ratio (SNR) (b).

ℓ_2-sense [129]. Then, $\mathbf{z}$ and $\mathbf{r}_\alpha$ are found as the left and right principal singular vectors, respectively. Similarly, to estimate the calibration parameters $\mathbf{p}$, first matrix $\mathbf{Z} \in \mathbb{C}^{R\times R}$ is constructed from $\mathbf{z}$, and then $\mathbf{p}$ is proportional, up to a complex scaling factor, to the right principal singular vector of $\mathbf{Z}$. As this scaling ambiguity does not influence performance of the time-delay estimation, it can be ignored. The estimates for parameters $\mathbf{g}$, $\boldsymbol{\tau}$ and $\boldsymbol{\sigma}_{\boldsymbol{\alpha}}$, then directly follow.

A summary of the resulting algorithm is shown as Algorithm 5. The abstract routine `unvec`$(\cdot)$ points to the construction of a matrix by splitting a vector into equal subvectors and stacking them one after another as columns of the matrix. `TSVD`$(\cdot, n)$ refers to the truncated SVD (truncation at rank n). `find`$(\cdot,$condition$)$ points to the routine for searching values and indices of the elements in an vector that satisfy a given condition. The remaining parts of the summary are self-explanatory.

As the resolution of the $\boldsymbol{\tau}$ estimates from (6.17) is restricted by the resolution of the chosen grid $\mathcal{T}$, in case that the TDs $\boldsymbol{\tau}$ do not lie exactly on the grid $\mathcal{T}$, this algorithm can be extended with grid-less estimation methods such as multiple invariance ESPRIT [202, 195].

6.4. NUMERICAL EXPERIMENTS

This section evaluates the performance of the proposed algorithm via numerical simulations. We consider a scenario where the multipath channel has eight dominant MPCs, i.e., $K = 8$, with gains distributed according to a Rayleigh distribution. The continuous-time channel is modeled using a 2 GHz grid, with channel tap delays spaced at 500 ps. We consider that the receiver estimates the channel frequency response in four frequency bands, i.e., $L = 4$, using a probing signals with $N = 64$ subcarriers and a bandwidth of $B = 20$ MHz. The center frequencies of the bands are $\{10, 70, 130, 280\}$ MHz, respectively. The gain errors, i.e., the elements of $\mathbf{g}$, are taking values from the interval of $[-3, 3]$ dB, while the gain variations are smooth over subcarriers. During the simulations, $\mathbf{g}$ is kept fixed. To evaluate the performance for time-delay estimation, we use the root mean square error (RMSE) of the time-delay estimation of the line-of-sight (LOS) path. Likewise, to assess the performance of the calibration, we use the average RMSE of the gain estimates over all the subcarriers and bands. The RMSE is computed using 10^3 independent Monte-Carlo trials and compared with the RMSEs of the algorithms proposed in [240, 244] which we refer to as ALMIN and BLC, respectively.

The original formulation of the BLC algorithm does not require knowledge of the noise covariance $\mathbf{\Sigma}_q$, as the authors in [244] assume that the non ideal response of the sensor array is affecting both signal and noise. While this is typically the case for acoustic sensor vectors, this assumption does not hold for calibrating RF chains. Therefore, we provide a good initial estimate of $\mathbf{\Sigma}_q$ to the BLC algorithm. Likewise, the ALMIN algorithm is initialized with a good initial guess on $\mathbf{g}$, and to limit its computational complexity the maximum number of iterations is set to eight.

Fig. 6.1a shows the calibration performance of the proposed, ALMIN and BLC algorithms with respect to the number of snapshots M. The signal-to-noise ratio (SNR) is set to 5 dB and kept fixed during the trials. From Fig. 6.1a, we observe that the calibration RMSE decreases as the number of snapshots increases for all three algorithms due to better estimation of the covariance matrix, $\hat{\mathbf{R}}_c$, and a better model matching (cf. (6.17)).

In the second scenario, we fixed the number of snapshots to $M = 400$, and evaluated the methods performance as a function of SNR. From Fig. 6.1b, it is seen that the calibration RMSE decreases with SNR. However, for SNR > 5 dB, for the proposed and ALMIN algorithm, or a SNR > 15 dB, for the BLC algorithm, the RMSE saturates, due to model mismatch related to the limited number of snapshots.

The same simulation scenarios are repeated for the time-delay estimation, and the corresponding RMSEs are shown in Fig. 6.2a and Fig. 6.2b. In addition to the algorithms mentioned above, the RMSEs of the estimates obtained using the ℓ_1 based algorithm, with perfectly calibrated and uncalibrated RF chains, are shown. From Fig. 6.2a, we observe that for a sufficient number of snapshots, the proposed algorithm is able to perfectly estimate the time-delay of the LOS path. However, the BLC and ALMIN algorithm are biased due to the model mismatch and the limited number of iterations allowed for convergence, respectively. In Fig. 6.2b, the RMSEs are shown for $M = 400$ snapshots and different SNR levels. It is seen that in the case of a limited number of snapshots, the RMSEs of all the algorithms saturate for SNR > 5 dB. Therefore, all the algorithms are biased compared to the ℓ_1 based time-delay estimation with perfect calibration. This is a con-

sequence of errors in the estimation of the covariance matrix from the limited number of snapshots.

6.5. CONCLUSIONS

In this chapter, we presented an algorithm for joint blind calibration and time-delay estimation for multiband ranging by formulating this problem as a particular case of covariance matching. Although this problem is severely ill-posed, prior information about RF chain distortions and multipath channel sparsity was used to regularize it. The resulting optimization problem, though biconvex, can be recast as a rank-1 constrained linear system of equations by using the *lifting* technique, which can be solved efficiently using a group Lasso algorithm. We have performed a numerical simulation to evaluate the performance of calibration and time-delay estimation. The simulation results have shown that errors in the compound channel covariance matrix estimation highly deteriorate the performance of calibration. Therefore, to reduce the calibration errors, it is crucial to have a sufficient number, i.e., $M > 300$, of snapshots of the compound channel frequency response. These results have also demonstrated that the limited number of snapshots has a milder impact on the proposed algorithm's calibration performance than to the ALMIN and BLC methods. In addition, the simulations reveal that time-delay estimation becomes highly biased when the frequency responses of RF chains are not calibrated. However, it is observed that for a sufficient number of snapshots, i.e., $M > 400$, the performance of the time-delay estimation of the proposed algorithm for joint calibration and time-delay estimation matches up to the performance of the ℓ_1 based algorithm that estimates time-delays from perfectly calibrated measurements.

7

JOINT RANGING AND SYNCHRONIZATION FOR NARROWBAND TRANSCEIVERS

"Time is an illusion."

— Albert Einstein

Part of this chapter is published as: T. Kazaz, M. Coutino, G. Janssen, G. Leus and A.J. van der Veen, "Joint Ranging and Clock Synchronization for Dense Heterogeneous IoT Networks", 52nd Asilomar Conference on Signals, Systems, and Computers, Pacific Grove, USA, Oct. 2018.

7.1. INTRODUCTION

In previous chapters, we considered the problem of time-delay estimation, i.e., ranging, using wideband radios. We assumed that the clocks of the anchors and the mobile node are synchronized during time-delay estimation, or that clock impairments are eliminated from the measurements using frequency and phase offset estimation or two-way ranging techniques such as time-difference-of-arrival (TDOA). However, in Internet-of-Things (IoT) and sensor networks, wireless nodes are low-power devices equipped with poor reference clock sources, making their accurate synchronization challenging. The individual clocks, i.e., local oscillators, drift from each other during the collection of measurements due to clock imperfections caused by environmental and voltage variations. These clock drifts directly impact the channel measurements and introduce a bias in the range estimation. This bias deteriorates the performance of synchronization and localization in IoT networks. However, accurate synchronization and localization are crucial for many IoT applications such as distributed sensing, data aggregation, and processing, and other tasks which benefit from node location information and network-wide synchronization [248, 249]. Therefore, to support these applications, it is essential to design methods that will support accurate clock synchronization and range estimation.

The problems of synchronization and localization in IoT networks have received considerable attention in the past. Many research efforts have approached these problems as either separate or joint estimation problems [250, 251, 252, 57, 253, 254, 255]. Existing methods can be classified into (i) time-stamping methods based on ultra-wideband (UWB) signals [250, 251, 252, 57], and (ii) phase-based methods that utilize carrier phase measurements of narrowband signals [253, 254, 255]. Methods falling in the first category offer high temporal resolution, and a plethora of protocols and algorithms for joint ranging and clock synchronization have been proposed [251, 252, 57]. However, in general, these methods are not applicable to IoT networks due to the narrowband constraints of the nodes. On the other hand, the methods based on phase-based ranging, i.e., the phase difference of arrival (PDoA), use frequency hopping (i.e., carrier switching) capabilities of narrowband radios to increase the frequency aperture of the collected measurements and improve the resolution of time-delay estimation [201]. However, the traditional PDoA data models typically ignore the impact of unknown clock-skew on these measurements, which results in a biased range estimation in the presence of clock-skew.

In this chapter, we study the problem of clock-skew and range estimation from PDoA measurements. We derive a precise data model that captures the clock-skew and channel effects on the PDoA measurements. Following the model, we propose a two-way communication protocol for collecting PDoA measurements over a two-dimensional (2-D) set of time epochs and carrier frequencies. The proposed protocol is practical and can be easily implemented as an adaptation of existing medium access control (MAC) protocols which are based on channel frequency switching such as time-slotted channel hopping (TSCH), or WirelessHART [256]. The structures present in the collected measurements allow for joint clock-skew and range estimation. To exploit these structures, we construct a data matrix whose rows collect measurements acquired on the same car-

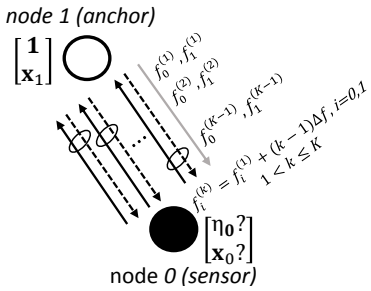

Figure 7.1: Illustration of the nodes in the IoT network, with known and unknown parameters, two-way carrier messages and a data message.

rier frequencies but at different time epochs. The data matrix has a structure that allows us to apply 2-D subspace estimation techniques to jointly estimate clock-skew and range. In particular, we show that for the radio channels with dominant LOS path, the data matrix has rank one and that its principal singular vectors have shift-invariance properties that can be used to estimate clock-skew and range.

We propose an estimator for joint clock-skew and range estimation, based on a weighted least squares (WLS) algorithm for 2-D frequency estimation [257, 258, 259]. This algorithm exploits the shift-invariance structure present in the data matrix to estimate unknown clock-skew and range. In particular, the shift-invariance of the left singular vector encodes the range, while the shift-invariance of the right singular vector encodes the clock-skew. Finally, the performance of the proposed protocol and estimator is compared against the Gaussian Cramér Rao Bound (CRB), using numerical simulations, demonstrating that the proposed estimator is asymptotically efficient and converges to the CRB as the signal-to-noise ratio (SNR) increases.

7.2. PROBLEM FORMULATION AND SIGNAL MODEL

Without loss of generality, we will consider a scenario with a single sensor (*node 0*) and anchor node (*node 1*) in a fully asynchronous wireless IoT network, as shown in Fig. 7.1. Lets assume that the anchor node has a relatively stable clock oscillator and known position, while the sensor node has an unknown position and a non-ideal oscillator with frequency drift. The clock behavior of the sensor node is considered to be characterized by the first-order affine clock model [260]

$$\nu_0 = \nu_1(1+\eta_o), \tag{7.1}$$

where η_o is the relative clock-skew of the sensor node, which it is typically very small, and therefore measured in parts per million (ppm) [261]. However, in the above equation, we have assumed implicit conversion from ppm to a number, hence the relative clock-skew is given as this number. Likewise, ν_0 and ν_1 are the frequencies of the oscillator signals at the sensor and anchor node, respectively.

We assume that the nodes are equipped with narrowband radio transceivers allowing two-way communication. In addition, the radio transceivers support estimation of the phase difference between the carrier frequency of the received signal and its own local oscillator frequency.

For simplicity, consider that the nodes are distributed over a two-dimensional space, and let the vectors $\mathbf{x}_i \in \mathbb{R}^{2\times 1}$, $i = 0,1$ collect the coordinates of the nodes, where the coordinates of the sensor node $\mathbf{x}_0$ are unknown. The range between the anchor and sensor nodes is defined as $d_{01} = d_{10} = \|\mathbf{x}_1 - \mathbf{x}_0\|_2$, where $\|\cdot\|_2$ denotes the Euclidean norm.

7.2.1. FREQUENCY SYNTHESIZER MODEL

Each radio transceiver generates a carrier signal using a frequency synthesizer driven by the clock signal of the local oscillator to transmit a signal at the desired carrier frequency. Modern radio transceivers support communication on a number of carrier frequencies which can be selected by changing the gain of the divider in the frequency synthesizer. The key idea of PDoA measurements is to exploit these carrier frequency switching capabilities of narrowband radio devices to sequentially hop over a large bandwidth and increase the frequency aperture of the measurements. In the following, we assume that all the nodes have the same frequency synthesizer with a set of K equispaced gains defined as $G^{(k)} = G^{(1)} + (k-1)\Delta G$, $k = 1,\ldots,K$, where $G^{(k)} \in \mathbb{Q}$ is the kth gain and ΔG is the step of the frequency divider. The carrier frequency generated at the output of the frequency synthesizer for the kth gain is given by $f_i^{(k)} = G^{(k)}\nu_i$, $i = 0,1$, where i denotes the node index [262]. The set of all equispaced carrier frequencies supported by the frequency synthesizer can now be written as

$$\mathscr{F}_i = \left\{ f_i^{(k)} = f_i^{(1)} + (k-1)\Delta f_i : \{f_i^{(1)}, \Delta f_i\} \in \mathbb{R} \right\}_{k=1}^{K}, \tag{7.2}$$

where $\Delta f_i = \Delta G \nu_i$ is the step size of the frequency synthesizer, and it depends on the clock oscillator frequency as given in (7.1).

7.2.2. SIGNAL MODEL

In this section, we will derive the signal model that captures propagation and clock-skew effects on the radio signal. We start from the narrowband signal model that is adapted to carrier frequency switching scenarios. The resulting signal model is used in the next section to derive a data model for PDoA measurements. Consider that the sensor node transmits a single tone unmodulated carrier signal at the kth carrier frequency

$$s_0^{(k)}(t) = \mathrm{Re}\left\{ \underline{s}_0 e^{j\left(2\pi f_0^{(k)} t + \varphi_0^{(k)}\right)} \right\}, \tag{7.3}$$

where $\underline{s}_0 \in \mathbb{R}$ is the amplitude of the complex envelope of $s_0^{(k)}(t)$ and $\varphi_0^{(k)}$ is the unknown phase offset introduced by the frequency synthesizer during the process of carrier frequency switching [263].

The transmitted signal $s_0^{(k)}(t)$ is narrowband, and therefore, it is reasonable to consider a flat-fading channel model. Therefore, the signal received at the anchor node after propagation through the channel and down-conversion by $f_1^{(k)}$ is given by

$$r_{01}^{(k)}(t) = \beta_{01}^{(k)} \underline{s}_0 e^{j\left(2\pi \mu_{01}^{(k)} t + \delta_{01}^{(k)}\right)} + n_1^{(k)}(t), \tag{7.4}$$

where $\beta_{01}^{(k)} \in \mathbb{C}$ is the complex path attenuation of the channel at $f_0^{(k)}$, and $n_1^{(k)}(t) \backsim \mathcal{CN}(0,\sigma_1^2)$ denotes the zero-mean complex Gaussian noise present at the anchor node.

The complex path attenuation $\beta_{01}^{(k)}$ is given by

$$\beta_{01}^{(k)} = \alpha_{01}^{(k)} e^{-j2\pi f_0^{(k)} \tau_{01}},$$

where $\alpha_{01}^{(k)} \in \mathbb{R}_+$ is the channel attenuation, $\tau_{01} = d_{01}/c = d_{10}/c$ is the unknown propagation delay between two nodes and c is the speed of radio signal propagation. Likewise, $\mu_{01}^{(k)}$ and $\delta_{01}^{(k)}$ denote the unknown frequency and phase offsets at kth carrier frequency, respectively, and they are given by

$$\begin{aligned} \mu_{01}^{(k)} &= f_0^{(k)} - f_1^{(k)}, \quad \text{and} \\ \delta_{01}^{(k)} &= \varphi_0^{(k)} - \varphi_1^{(k)}. \end{aligned}$$

Now, from the frequency synthesizer (7.2) and clock (7.1) models, it follows that the carrier frequency offset can be written as

$$\mu_{01}^{(k)} = \mu_{01}^{(1)} + (k-1)\Delta\mu_{01}, \tag{7.5}$$

where $\Delta\mu_{01} = \Delta f_1 \eta_o$.

7.3. COMMUNICATION PROTOCOL AND DATA MODEL

Our objective is to estimate the unknown parameters η_o and d_{01} given the PDoA measurements collected by the radio transceivers. In the following section, we first derive a detailed data model for PDoA measurements considering a classical two-way protocol for ranging. Then, based on the derived model we propose a novel 2-D PDoA protocol for joint ranging and clock-skew estimation.

7.3.1. CLASSICAL PDOA RANGING PROTOCOL

In the classical two-way PDoA protocol (cf. Fig. 7.2a), the sensor node initiates the communication and sends a message using the signal $s_0^{(k)}(t)$, i.e., using carrier frequency $f_0^{(k)}$, to the anchor node. When the anchor node receives the message as the signal $r_{01}^{(k)}(t)$, it replies back to the sensor node by sending a message using signal $s_1^{(k)}(t)$, i.e., using carrier frequency $f_1^{(k)}$. After the exchange, both nodes change their carrier frequencies to $f_i^{(k+1)} = f_i^{(k)} + \Delta f_i$, $i = 0, 1$, and the same two-way message exchange pattern is repeated. The phase difference of the carrier signals, $\psi_0^{(k)}$ and $\psi_1^{(k)}$, using the kth carrier frequency are measured at both sensor and anchor nodes, respectively.

Now, considering the noiseless case and assuming that the channel reciprocity[1] conditions hold, using (7.4) $\psi_0^{(k)}$ and $\psi_1^{(k)}$ are given by

$$\begin{aligned} \psi_0^{(k)} &= -2\pi\mu_{01}^{(k)}\Delta t - 2\pi f_1^{(k)}\tau_{01} - \delta_{01}^{(k)} \\ \psi_1^{(k)} &= -2\pi f_0^{(k)}\tau_{01} + \delta_{01}^{(k)}, \end{aligned} \tag{7.6}$$

where Δt is the deterministic time epoch between the measurements collected at anchor and sensor nodes, while all other nondeterministic timing differences between the

[1] The received signals at anchor and sensor nodes differ only in the signs of the phases and the frequency offset.

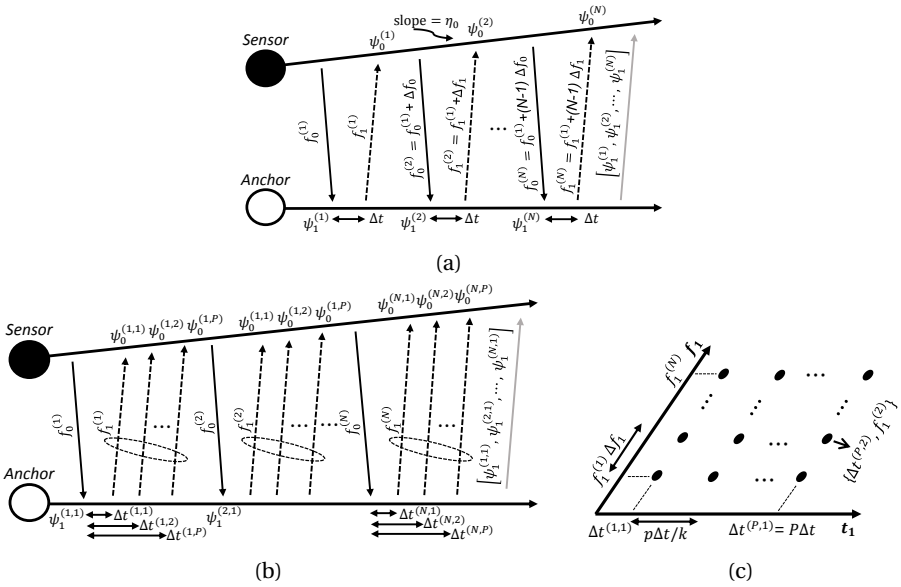

Figure 7.2: (a) Classical PDoA two-way ranging protocol, (b) 2-D PDoA protocol for ranging and synchronization, and (c) 2-D equispaced time-frequency grid at anchor node.

nodes are absorbed in $\delta_{01}^{(k)}$. In general, the time epoch Δt is controllable by the anchor node and it has values in the order of tens of microseconds. However, in the classical PDoA protocol, it is assumed that Δt is fixed during the collection of measurements.

In this paper, we focus on indoor localization scenarios where the channel coherence time is typically of the order of several hundreds of milliseconds [264]. Hence, we can assume that $N \leq K$ two-way messages can be exchanged according to the PDoA protocol within the channel coherence time. For the sake of simplicity, the N phase difference measurements recorded at the sensor and anchor nodes are transformed to their negative complex exponential form and collected in the vectors

$$\begin{aligned} \mathbf{b}_0 &= \left[e^{-j\psi_0^{(1)}}, \ldots, e^{-j\psi_0^{(N)}} \right]^T \in \mathbb{C}^{N\times 1}, \\ \mathbf{b}_1 &= \left[e^{-j\psi_1^{(1)}}, \ldots, e^{-j\psi_1^{(N)}} \right]^T \in \mathbb{C}^{N\times 1}. \end{aligned} \tag{7.7}$$

For ranging purposes, the phase offset represents a nuisance parameter which can be eliminated from the acquired measurements by considering $\mathbf{a} = \mathbf{b}_0 \odot \mathbf{b}_1$ instead. The argument of the kth element in $\mathbf{a}$ is given by

$$\arg\{a_k\} = 2\pi\mu_{01}^{(k)}\Delta t + 2\pi(f_1^{(k)} + f_0^{(k)})\tau_{01}. \tag{7.8}$$

Using the frequency synthesizer model and (7.6), we can write

$$\begin{aligned} \mu_{01}^{(k)} &= G^{(1)}\nu_1\eta_0 + (k-1)\eta_0\Delta f_1, \\ f_1^{(k)} + f_0^{(k)} &= (2+\eta_0)(G^{(1)}\nu_1 + (k-1)\Delta f_1). \end{aligned} \tag{7.9}$$

Therefore, the vector $\mathbf{a}$ has the following structure:

$$\mathbf{a}(\tau_\eta) = a(\tau_\eta)\left[1, e^{j2\pi\Delta f_1\tau_\eta}, \ldots, e^{j2\pi(N-1)\Delta f_1\tau_\eta}\right]^T, \tag{7.10}$$

where $a(\tau_\eta) = e^{j2\pi G^{(1)}\nu_1\tau_\eta}$ is the the first element of $\mathbf{a}(\tau_\eta)$ and $\tau_\eta = \eta_o\Delta t + (2+\eta_o)\tau_{01}$. Note that $\mathbf{a}(\tau_\eta)$ has a shift invariance structure. This structure is identical to that of the uniform linear array (ULA) response vector in array processing [101]. However, in this case the phase shift of the elements in $\mathbf{a}(\tau_\eta)$ is caused by equispaced carrier frequency switching, i.e., a special form of frequency hopping [253].

7.3.2. 2-D PDoA RANGING AND SYNCHRONIZATION PROTOCOL

The shift invariance of $\mathbf{a}(\tau_\eta)$ only allows for the estimation of a single parameter τ_η. Therefore, η_o and τ_{01}, i.e., d_{01}, cannot be uniquely determined from $\mathbf{a}(\tau_\eta)$. For example, estimation of τ_{01} from $\mathbf{a}(\tau_\eta)$ results in an estimate that is biased by the clock-skew. To alleviate this, we propose the protocol for collecting measurements that allows joint clock-skew and range estimation.

In the classical PDoA protocol, measurements are collected over the set of equispaced carrier frequencies, while the time epoch Δt is fixed during the message exchange period. In the 2-D PDoA protocol, we propose to collect the measurements over a 2-D set of time epochs and carrier frequencies (cf. Figs. 7.2b and 7.2c). In this case, the sensor node transmits a single message per two-way exchange, while the anchor node transmits P messages based on the set of time epochs. The set of time epochs for the kth carrier frequency is given by $\Delta t^{(k,p)} = p\Delta t/k$, where $k = 1,\ldots,N$ and $p = 1,\ldots,P$. Note that these time epochs depend on the index of the carrier frequency, i.e., k.

The P phase difference measurements recorded at the sensor node for the kth carrier frequency are transformed in their negative complex exponential form and collected in the vector $\mathbf{b}_k \in \mathbb{C}^{P\times 1}$. As before, we follow a similar approach for nuisance parameters elimination. The vector that collects noiseless PDoA measurements recorded at the kth carrier frequency is written as $\mathbf{a}_k = e^{-j\psi_1^{(k)}}\mathbf{b}_k \in \mathbb{C}^{P\times 1}$ which satisfies the model

$$\mathbf{a}_k(\eta_o,\tau_{01}) = a(\tau_\eta)\gamma^{k-1}[1,\phi,\ldots,\phi^{P-1}]^T, \tag{7.11}$$

where $a(\tau_\eta)$ is defined in (7.10), $\gamma = e^{j2\pi\Delta f_1(2+\eta_o)\tau_{01}}$ and $\phi = e^{j2\pi\Delta f_1\eta_o\Delta t}$.

Remark on practical implementation: The 2-D PDoA protocol requires that during a single two-way message exchange no carrier frequency switching occurs. This constraint ensures that the phase offset between two nodes remains constant during time hopping. However, there is no constraint on the frequency hopping sequence. This makes the proposed protocol attractive for implementation as an extension of existing MAC protocols such as time-slotted channel hopping (TSCH) [265] or WirelessHART [266].

7.4. JOINT CLOCK-SKEW AND RANGE ESTIMATION

In the following, we show how to jointly estimate clock-skew η_o and time delay τ_{01}, i.e., range, from collected measurements.

The noise-corrupted version of $\mathbf{a}_k$ is given by $\mathbf{m}_k = \mathbf{a}_k + \mathbf{n}_k$, where $\mathbf{n}_k$ is a zero-mean complex Gaussian distributed noise vector[2]. From a set of N noisy 2-D PDoA measurements, we construct a measurement matrix of size $P \times N$ as

$$\mathbf{M} = [\mathbf{m}_1, \ldots, \mathbf{m}_N]. \tag{7.12}$$

The measurement matrix satisfies the model

$$\mathbf{M} = \mathbf{A} + \mathbf{N}, \tag{7.13}$$

where $\mathbf{A} = [\mathbf{a}_1, \ldots, \mathbf{a}_N]$ and $\mathbf{N} \in \mathbb{C}^{P \times N}$ is the noise matrix. Using (7.11), it is straightforward to show that $\mathbf{A}$ can be modeled as

$$\mathbf{A} = \mathbf{q}(\eta_0, \tau_{01})\mathbf{h}^T(\eta_0, \tau_{01}), \tag{7.14}$$

where

$$\begin{aligned} \mathbf{q} &= a(\tau_\eta)[1, \phi, \ldots, \phi^{P-1}]^T \\ \mathbf{h} &= [1, \gamma, \ldots, \gamma^{N-1}]^T. \end{aligned} \tag{7.15}$$

Model (7.13), after replacing $\mathbf{A}$ with (7.14), resembles the signal model for 2-D frequency estimation of a single complex sinusoid in white Gaussian noise. This is a classical signal processing problem for which numerous methods have been proposed [268, 257, 258, 259]. Although the maximum likelihood estimator proposed in [268] can attain optimum performance, it has high computational requirements due to the multidimensional search. Here, we are interested in computationally more attractive methods that have close to optimal performance.

To develop an estimator for joint clock-skew and range estimation, we start from the results of [259]. We can observe from (7.14) that $\mathbf{A}$ has rank one and that the vectors $\mathbf{q}$ and $\mathbf{h}$ span its column and row space, respectively. Since $\mathbf{q}$ and $\mathbf{h}$ exhibit shift invariance, it is possible to estimate γ and ϕ from the low-rank approximation of $\mathbf{M}$. Then, from ϕ and γ, the parameters η_o and τ_{01}, i.e., d_{01}, immediately follow.

In particular, let $\mathbf{u}_1$ and $\mathbf{v}_1$ be the principal orthonormal basis vectors for the column and row span of the rank-one approximation of $\mathbf{M}$, respectively. These vectors can be obtained using the singular value decomposition (SVD) of $\mathbf{M}$ and can be expressed as

$$\mathbf{u}_1 = 1/\rho_q \mathbf{q}, \qquad \mathbf{v}_1 = 1/\rho_h \mathbf{h}^*, \tag{7.16}$$

where ρ_q and ρ_h are unknown complex constants. Now, let us define the selection matrices:

$$\begin{aligned} \mathbf{J}_{\phi 1} &= [\mathbf{I}_{P-1} \quad \mathbf{0}_{P-1}], & \mathbf{J}_{\gamma 1} &= [\mathbf{I}_{N-1} \quad \mathbf{0}_{N-1}], \\ \mathbf{J}_{\phi 2} &= [\mathbf{0}_{P-1} \quad \mathbf{I}_{P-1}], & \mathbf{J}_{\gamma 2} &= [\mathbf{0}_{N-1} \quad \mathbf{I}_{N-1}]. \end{aligned} \tag{7.17}$$

To estimate ϕ, we take subvectors consisting of the first and the last $P-1$ elements of $\mathbf{u}_1$. That is, we consider $\mathbf{u}_{\phi 1} = \mathbf{J}_{\phi 1}\mathbf{u}_1$ and $\mathbf{u}_{\phi 2} = \mathbf{J}_{\phi 2}\mathbf{u}_1$, respectively. We follow the same

[2] The phase estimation errors in PLLs are von Mises distributed [267]. However, for large signal to noise ratio, the von Mises distribution can be approximated by a Gaussian distribution.

process for the estimation of γ, i.e., we take subvectors $\mathbf{v}_{\gamma 1} = \mathbf{J}_{\gamma 1}\mathbf{v}_1$ and $\mathbf{v}_{\gamma 2} = \mathbf{J}_{\gamma 2}\mathbf{v}_1$, respectively. From the shift invariance property of $\mathbf{u}_1$ and $\mathbf{v}_1$ we have that

$$\mathbf{u}_{\phi 2} \approx \mathbf{u}_{\phi 1}\phi \quad \text{and} \quad \mathbf{v}_{\gamma 2} \approx \mathbf{v}_{\gamma 1}\gamma^*. \tag{7.18}$$

In the case of white noise, the approximate solutions to the relations in (7.18) can be found using least squares (LS). However, here we adopt the weighted least squares (WLS) approach [258] and formulate problem (7.18) as

$$\begin{aligned} \widehat{\phi} &= \underset{\phi}{\operatorname{argmin}} \ \|\mathbf{C}_{\phi}^{-1/2}(\mathbf{u}_{\phi 1}\phi - \mathbf{u}_{\phi 2})\|_2^2 \\ \widehat{\gamma} &= \underset{\gamma}{\operatorname{argmin}} \ \|\mathbf{C}_{\gamma}^{-1/2}(\mathbf{v}_{\gamma 1}\gamma^* - \mathbf{v}_{\gamma 2})\|_2^2, \end{aligned} \tag{7.19}$$

where $\mathbf{C}_{\phi} = \mathbb{E}(\mathbf{r}_{\phi}\mathbf{r}_{\phi}^H)$ and $\mathbf{C}_{\gamma} = \mathbb{E}(\mathbf{r}_{\gamma}\mathbf{r}_{\gamma}^H)$ are the covariance matrices of the residuals $\mathbf{r}_{\phi} = \mathbf{u}_{\phi 1}\phi - \mathbf{u}_{\phi 2}$ and $\mathbf{r}_{\gamma} = \mathbf{v}_{\gamma 1}\gamma^* - \mathbf{v}_{\gamma 2}$, respectively. Therefore, the weighting matrices are the inverse of the covariance of the residuals, i.e., $\mathbf{W}_{\phi} = \mathbf{C}_{\phi}^{-1}$ and $\mathbf{W}_{\gamma} = \mathbf{C}_{\gamma}^{-1}$, respectively. The optimal $\mathbf{W}_{\phi}$ and $\mathbf{W}_{\gamma}$ for the considered problem are given in closed-form by [269]

$$\begin{aligned} \mathbf{W}_{\phi}[p,n] &= (P\min(p,n) - pn)\phi^{(p-n)}/P \\ \mathbf{W}_{\gamma}[p,n] &= (N\min(p,n) - pn)\gamma^{(n-p)}/N, \end{aligned} \tag{7.20}$$

where $p = 1,\ldots,P$ and $n = 1,\ldots,N$. Note that $\mathbf{W}_{\phi}$ and $\mathbf{W}_{\gamma}$ depend on the unknown parameters ϕ and γ. Therefore, first we estimate ϕ and γ using LS and then these estimates are used for the construction of $\mathbf{W}_{\phi}$ and $\mathbf{W}_{\gamma}$. Finally, the WLS is used to obtain $\hat{\phi}$ and $\hat{\gamma}$. Based on the WLS estimates of ϕ and γ the unknown parameters are computed as

$$\begin{aligned} \widehat{\eta}_o &= (2\pi\Delta f_1 \Delta t)^{-1}\arg(\hat{\phi}) \\ \widehat{d}_{01} &= c(2\pi\Delta f_1 \Delta t(2+\hat{\eta}_o))^{-1}\arg(\hat{\gamma}). \end{aligned} \tag{7.21}$$

Note that first the clock-skew is estimated and later this estimate is used for estimating the range.

7.5. GAUSSIAN CRAMÉR RAO BOUND

The errors on PDoA measurements are typically modeled as circular random variables. Previously we mentioned that the central limit theorem over circular domains shows that the most entropic model for circular variables with known mean and variance is the von Mises distribution [255]. For a large SNR, the von Mises distribution can be approximated by a Gaussian distribution. Therefore, to assess the performance of the proposed estimators (7.19) we derive the Gaussian CRB for joint clock-skew and range estimation using model (7.13), which is accurate for large SNR scenarios. In the remainder of this chapter, we refer to Gaussian CRB as CRB.

For an unbiased estimator $\widehat{\boldsymbol{\theta}}$, the CRB is the lower bound on the error variance, that is

$$\operatorname{var}(\widehat{\boldsymbol{\theta}}) \geq \mathbf{F}^{-1} \tag{7.22}$$

where $\text{var}(\widehat{\boldsymbol{\theta}}) = \mathbb{E}((\widehat{\boldsymbol{\theta}} - \boldsymbol{\theta})(\widehat{\boldsymbol{\theta}} - \boldsymbol{\theta})^T)$ and $\mathbf{F}$ is the Fisher information matrix. We assume that the proposed estimators (7.19) are approximately unbiased for sufficiently large SNR and well designed measurement matrix $\mathbf{M}$ [270].

In the case of 2-D frequency estimation of a sum of sinusoids, the Fisher information matrix is given by [126]

$$\mathbf{F}_{p,k} = 2\boldsymbol{\sigma}^{-2}\Re\left[\frac{\partial \mathbf{a}^H}{\partial \theta_p}\frac{\partial \mathbf{a}}{\partial \theta_k}\right] \in \mathbb{R}^{2\times 2} \tag{7.23}$$

where $\mathbf{F}_{p,k}$ is the (p, k)th element of $\mathbf{F}$, σ^2 is the variance of the noise, $\partial/\partial\theta_p$ is the partial derivative with respect to the pth element of $\boldsymbol{\theta}$, $\mathbf{a} = \text{vec}(\mathbf{A}) \in \mathbb{C}^{PN\times 1}$ is the vector formed by stacking the columns of $\mathbf{A}$. The resulting Fisher information matrix is invertible, so closed-form expressions for the CRBs are given by

$$\begin{aligned}\text{var}(\widehat{\eta}_0) &\geq \frac{6}{SNR(2\pi\Delta f_1 \Delta t)^2 PN(P^2-1)},\\ \text{var}(\widehat{d}_{01}) &\geq \frac{6c^2}{SNR(4\pi\Delta f_1)^2 PN(N^2-1)}.\end{aligned} \tag{7.24}$$

where $SNR = \sigma^{-2}$.

7.6. NUMERICAL EXPERIMENTS

In the following, simulations are used to compare the performance of the proposed estimator against state-of-the-art estimators for the same problem. In particular, to benchmark the performance of the proposed estimator, we use estimators based on approximate iterative quadratic maximum-likelihood (AIQML) [269], weighted linear predictor (WLP) [271] and ESPRIT [257] algorithms. In the simulations, we consider two nodes, i.e., an anchor and a sensor node, which are deployed randomly within a range of 140 m. The carrier frequency step Δf_i, $i = 0, 1$ and time epoch Δt are set to 0.5 MHz and 80 μs, respectively. The clock-skew of the sensor node η_o is set to 80 ppm. The phase difference of arrival measurements are corrupted with zero-mean Gaussian noise and all root mean square errors (RMSEs) of the estimates are averaged over 10^3 independent Monte Carlo runs.

Figs. 7.3a and 7.4a show the RMSEs of the clock-skew and range estimates vs SNR for the previously mentioned estimators, respectively. In these simulation scenarios, the number of time and frequency hops is equal to 10. All the estimators are independently applied to the same set of PDoA measurements. As shown in the figures, the proposed estimator outperforms the estimators based on AIQML, WLP, and ESPRIT algorithms. Furthermore, for sufficiently high SNR the proposed estimator is asymptotically efficient and approaches the CRB.

Fig. 7.3b and 7.4b show the RMSE of clock-skew and range estimates vs the SNR for a varying number of PDoA measurements collected over P time epochs and a varying number of carrier frequency hops N. It is shown that by increasing the number of time epochs, the accuracy of the clock-skew estimates increases whereas the accuracy of the range estimates increases with the number of frequencies, i.e., the covered bandwidth of PDoA measurements.

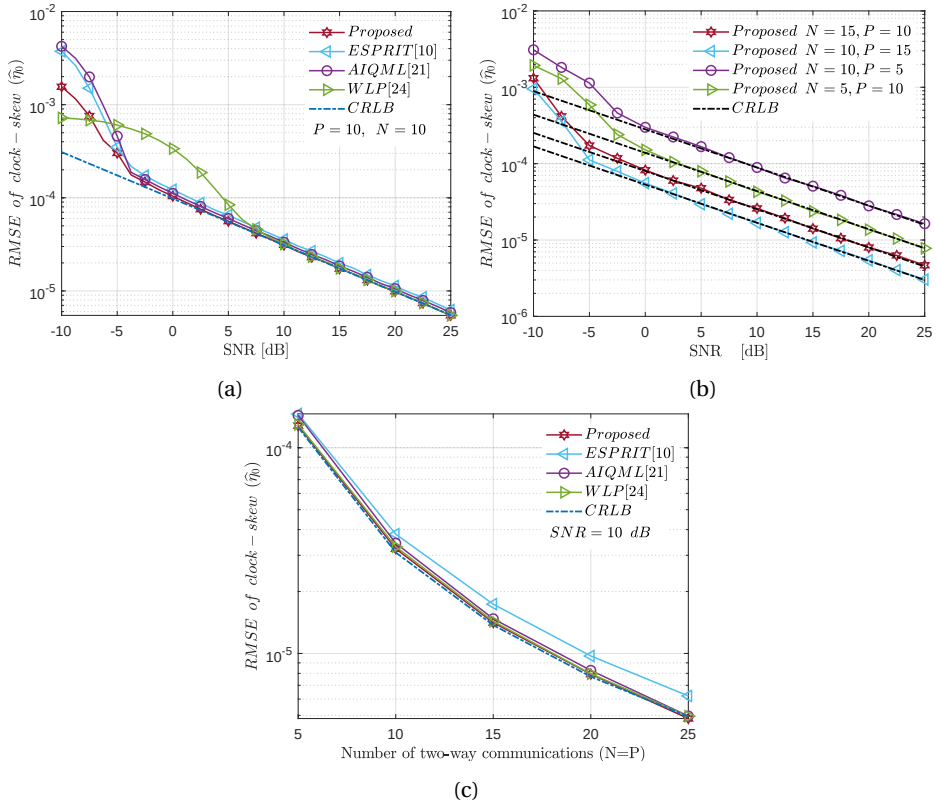

Figure 7.3: (a) RMSE of the clock-skew estimates, $\hat{\eta}_0$, vs signal-to-noise ratio (SNR) for the proposed estimator, approximate iterative quadratic maximum-likelihood (AIQML), weighted linear predictor (WLP), and ESPRIT. The results show that the proposed estimator outperforms other methods and converges to the CRB with increasing SNR. (b) RMSE of the estimated clock-skew vs SNR for varying number of PDoA measurements collected over P time epochs and a varying number of carrier frequency hops N. The results show that the accuracy of clock-skew estimation increases with P. (c) RMSE of the estimated clock-skew for fixed SNR = 10 dB and a jointly varying number of P and N. The results show that the proposed estimator outperforms other methods and achieves the CRB.

Fig. 7.3c and 7.4c show the RMSE of clock-skew and range against the number of PDoA measurements, with the SNR set to 10 dB. In these scenarios, the number of time and frequency hops is equal. Similar as in the previous scenarios, the proposed estimator outperforms AIQML, WLP and ESPRIT. In addition, it can be seen that the proposed estimator achieves the CRB.

7.7. CONCLUSIONS

In this chapter, we investigated the problem of joint ranging and clock-skew estimation using PDoA measurements. A novel and precise data model for PDoA measurements is derived. The derived model shows that it is possible to jointly estimate clock-skew

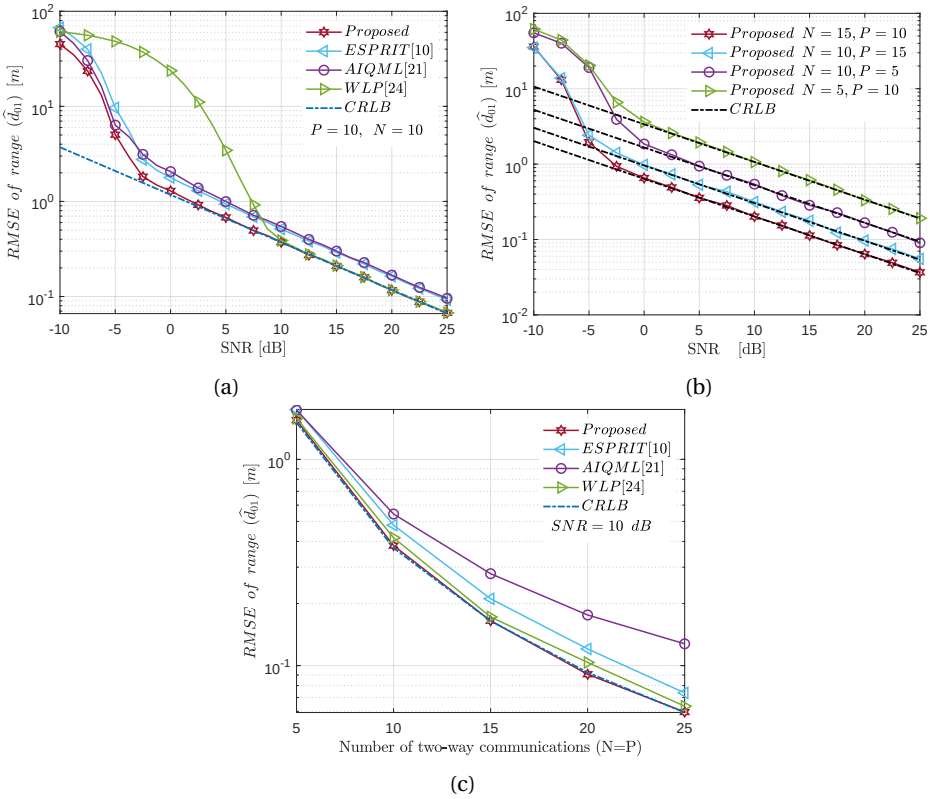

Figure 7.4: (a) RMSE of the range estimates, $\hat{d}_{01}$, vs signal-to-noise ratio (SNR) for the proposed estimator, approximate iterative quadratic maximum-likelihood (AIQML), weighted linear predictor (WLP), and ESPRIT. The results show that the proposed estimator outperforms other methods and converges to the CRB with increasing SNR. (b) RMSE of the estimated range vs SNR for varying number of PDoA measurements collected over P time epochs and a varying number of carrier frequency hops N. The results show that the accuracy of range estimation increases with N. (c) RMSE of the estimated range for fixed SNR = 10 dB and a jointly varying number of P and N. The results show that the proposed estimator outperforms other methods and achieves the CRB.

and range by collecting PDoA measurements over a 2-D time-frequency grid. Starting from this data model, we have proposed a novel protocol for collecting PDoA measurements and an estimator based on WLS for joint estimation of clock-skew and range. The presented algorithm leverages shift-invariance properties of the principal singular vectors of the collected measurements. To benchmark the performance of the proposed estimator, we have performed numerical simulations and calculated RMSEs of clock-skew and range estimation for the proposed estimator and other estimators based on AIQML, WLP and ESPRIT. The simulations show that the proposed estimator outperforms AIQML, WLP and ESPRIT estimators. Furthermore, these results show that the proposed estimator is asymptotically efficient and reaches the CRB for sufficiently high SNR values.

8

MULTIBAND TIME-DELAY ESTIMATION AND LOCALIZATION EXPERIMENTS

"Today's scientists have substituted mathematics for experiments, and they wander off through equation after equation, and eventually build a structure which has no relation to reality."

— Nikola Tesla

Part of this chapter is published as: T. Kazaz, GJM Janssen, J. Romme, and A.J. van der Veen, "Delay Estimation for Ranging and Localization Using Multiband Channel State Information", *IEEE Transactions on Wireless Communications*, 2021.

8.1. INTRODUCTION

THe algorithms presented in Chapters 4 and 5 assumed that multipath radio propagation is described by the model given in 3.1. The numerical experiments that we have performed in these chapters evaluated the performance of the algorithms on synthetic multiband channel datasets. These datasets were generated using the multiband channel model, and therefore these experiments did not validate the modeling assumptions made in these chapters. In this chapter, we perform experiments with real channel measurements to validate the modeling assumptions and evaluate the performance of multiband time-delay estimation algorithms presented in chapters 4 and 5. Furthermore, we demonstrate the applicability of the proposed algorithms in practical localization scenarios. In particular, we consider localization in future WiFi-7 wireless networks [272] defined by the emerging IEEE 802.11be standard [197]. This standard will support multichannel and multiband operation in the 2.4, 5, and 6 GHz bands (cf. Fig. 8.1), which makes localization in these networks an interesting showcase for the proposed algorithms. We perform several experiments to show the influence of IEEE 802.11be system parameters on time-delay estimation and localization performance. For the experiments, we use two multipath channel frequency response (CFR) datasets collected using a vector network analyzer (VNA) in a hospital [273], and a university building environment [274]. The results of these experiments are mostly following the results of the numerical simulations, however, it is seen that if multiband channel measurements are collected over a frequency aperture that is larger than approximately 20% of the carrier frequency of the band, frequency dependency effects of multipath radio propagation [275] introduce modeling errors. Reducing these modeling errors is important for achieving high-resolution time-delay estimation with multiband delay estimation algorithms, and we discuss how to achieve this in Section 8.4.

This chapter is organized as follows. The IEEE 802.11be standard and channel estimation using its training signals are discussed in Section 8.2. The measurement campaigns and the obtained datasets, used in the experiments, are presented in Section 8.3. Lastly, in Section 8.4 we present the experimental results and draw conclusions.

8.2. OVERVIEW OF IEEE 802.11BE TRAINING SIGNALS AND CHANNEL ESTIMATION

In the experiments, we consider time-delay estimation using IEEE 802.11be transceivers. The IEEE 802.11be standard is in a preliminary phase. However, its main candidate features are already defined [197]. Of particular interest to us is that it will allow multiple frequency channel aggregation and multiband operation at 2.4, 5, and 6 GHz, as shown in Fig. 8.1. At 6 GHz, the RF spectrum from 5.925 to 7.125 GHz will be allocated for primary frequency channels with a bandwidth of 20, 40, 80, and 160 MHz and their contiguous and non-contiguous combinations. The large bandwidth available in the 6 GHz band offers a great opportunity for localization and is an interesting use case for our multiband time-delay estimation. Therefore, we will focus our experiments on time-delay estimation in the 6 GHz band to avoid frequency dependency effects.

Next, we will introduce the system parameters of IEEE 802.11be and explain the

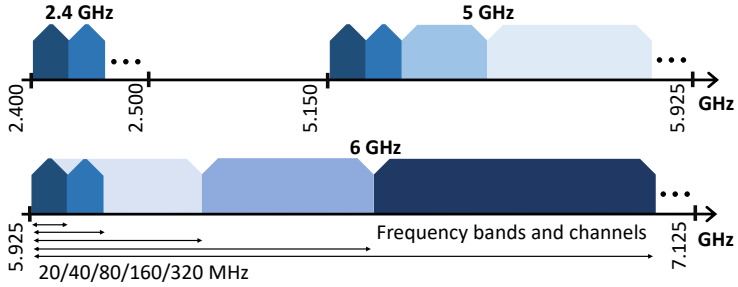

Figure 8.1: Example of a multiband system: Frequency bands defined for use in the IEEE 802.11be standard at 2.4, 5, and 6 GHz, with bandwidths of 20, 40, 80, and 160 MHz.

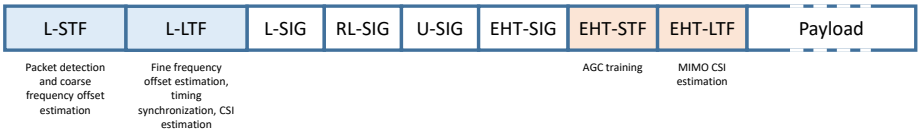

Figure 8.2: The physical protocol data unit (PPDU) consisting of legacy and EHT training signals. The legacy training signals are used for packet detection, frequency offset, timing, and channel state information (CSI) estimation, while EHT signals are used for AGC training and MIMO CSI estimation.

training signals and channel frequency response (CFR) estimation process. The CFR is called channel state information (CSI) in IEEE 802.11be terminology. Therefore, in the remainder of this chapter, we will refer to multiband CFR measurements as multiband CSI. There are several orthogonal frequency division multiplexing (OFDM) training signals, which are specifically designed for synchronization and channel estimation in IEEE 802.11be transceivers. These training signals are organized in a data frame known as the physical protocol data unit (PPDU) presented in Fig. 8.2. From this figure we see that a PPDU consists of legacy training signals and signal fields, and extremely high-throughput (EHT) training signals and signal fields. The legacy training signals are known as Legacy Short Training Field (L-STF) and Legacy Long Training Field (L-LTF). Likewise, EHT training signals are known as EHT Short Training Field (EHT-STF) and EHT Long Training Field (EHT-LTF). The signal fields are known as legacy SIG field (L-SIG), repeat legacy signal field (RL-SIG), a universal SIG (U-SIG) field, and EHT-SIG field. The training signals are important for estimation of CSI, and in what follows, we will summarize how they are used for synchronization and channel estimation.

In the receiver, the first frame is detected and a coarse frequency offset is estimated using the L-STF training signals. The coarse frequency offset is then compensated and the remaining frequency offset is estimated using the L-LTF training signals [200]. After compensation for the fine frequency offset, these signals are then used for time synchronization and in older versions of WiFi receivers for channel estimation. The signal fields, i.e., L-SIG, RL-SIG, U-SIG, and EHT-SIG, carry information necessary for further signal processing in the receiver, such as information about modulation and coding schemes, frame length, uplink and downlink flag, to name a few. Finally, EHT-STF and EHT-LTF are used for automatic gain control (AGC) training and fine MIMO CSI estimation, respec-

tively. The CSI estimate is the collection of channel frequency responses at the subcarrier frequencies of the EHT-LTF training signals. The estimated CSI is then used to equalize the effects introduced by multipath propagation. The CSI is directly related to the channel frequency response in which the location information is encoded. The multiband CSI is a collection of the CSI estimates obtained at several frequency channels, and in the following, we use it for location estimation.

8.3. DATASETS

The main goal of the measurement campaigns described here, is to assess the performance of indoor localization in realistic scenarios. For this reason, the measurements are performed along predefined trajectories between a mobile node and multiple anchors. The measurements consist of channel frequency response (CFR) measurements collected between a mobile node and anchors at each trajectory point. The CFRs are determined by measuring the complex gains of a discrete set of equispaced frequencies, which is similar to CSI estimation on OFDM subcarrier frequencies by using training signals such as EHT-LTF in IEEE 802.11be. The measurements are carried out in two different indoor environments, namely in a hospital [273], and a university building environment [274]. Next, we discuss the details of the datasets collected in these measurement campaigns.

DATASET COLLECTED IN THE UNIVERSITY BUILDING

In this measurement campaign, CFR measurements are collected between two anchors and a mobile node in the hallway of a university building, where the mobile node is moving in an area of 1 m^2 [274] on a 22x22 grid, i.e. the distance between neighboring measurement points is 5 cm, as shown in Fig. 8.3. In total, 484 CFRs are collected for different positions of the mobile node. The CFR is measured over 7501 discrete and equispaced frequencies with a spacing of 1 MHz, starting from 3.1 to 10.6 GHz. This frequency spacing is 12.8 times larger than the subcarrier spacing of 78.125 kHz used in EHT-LTF. The smaller frequency spacing, i.e., a larger number of CFR samples, would allow for a larger unambiguous range and would improve the RMSE of range estimates with respect to the noise. However, it will not impact time-delay resolution as the bandwidth of the measurements is the same as in the IEEE 802.11be standard. The transmit power of the training signal is set to +15 dBm. We use this dataset for experiments that illustrate the effects of band and bandwidth selection on the RMSE of the range estimates.

DATASET COLLECTED IN THE HOSPITAL

The performance of 2-D positioning is assessed by using the CFR dataset collected in an indoor hospital environment. These measurements are collected between 7 anchors and a mobile node for 150 points on a trajectory shown in Fig. 8.4. The CFR is measured over a set of 4096 equispaced frequency points, covering the frequency range of 5 to 10 GHz, with a link budget of 110 dB [273]. This is equivalent to a subcarrier spacing of 1.22 MHz, which is 15.6 times larger than the IEEE 802.11be configuration. The same conclusions related to resolution and noise performance as for the previous dataset hold. To estimate the number of multipath components K in these experiments, we use the MDL criteria

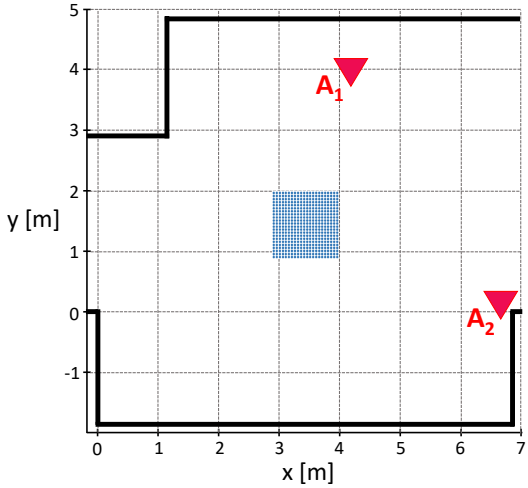

Figure 8.3: Measurement scenario in the university building with a 22 x 22 trajectory grid of 484 measurement points with 5 cm spacing. The measurements are collected between the mobile node moving on the grid (shown in blue) and two anchors, A1 and A2.

described in Chapter 4. The estimated K takes values between 12 and 21 MPCs for the trajectory shown in Fig. 8.4.

When collected with off-the-shelf transceivers, the CSI measurements might get affected by various hardware impairments. A detailed discussion on these effects is provided in [47, 198]. In Chapter 4, we discussed how to calibrate some of these effects, such as nonideal frequency response, phase, and frequency offsets of the RF chains. The CFR measurements that we consider in this chapter are calibrated up to the effects of the antennas. However, the connections of the antennas and their phase center offsets will introduce an unknown bias in the range estimates. We compute this bias as the median error of the range estimates compared to the ground truth and eliminate it from the estimates. Another approach would be to directly estimate the bias from the range estimates using the known positions of the anchors and multidimensional scaling algorithms [276]. The two datasets that we consider are collected using different antennas. Therefore, the calculated biases are different, and they are equal to 5 cm for the hospital dataset and 4.3 cm for the university building dataset. However, the biases remain constant for all the anchors in a single dataset, as they use the same type of antenna.

8.4. EXPERIMENTS

To evaluate the performance of the methods presented in previous chapters, we conducted several experiments with the datasets described in the previous section. We first use the dataset collected in the university building to illustrate the effects of frequency band $\{f_{c,i}\}_{i=1}^{L}$ and bandwidth B selection on the performance of ranging with the Multiband Weighted Delay Estimation (MBWDE) algorithm presented in Chapter 4. These results are compared with those obtained with the Multiband Delay Estimation (MBDE) algorithm and the Multiresolution Time-Delay (MRTD) estimation algorithm presented

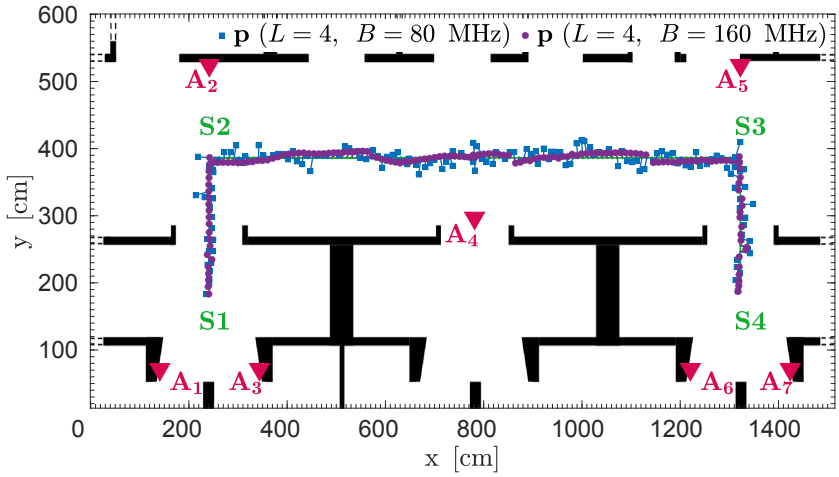

Figure 8.4: Anchors {A1, ... ,A7} and trajectory of the mobile node with 2-D position estimates in a hospital building, for bandwidths $B \in \{80, 160\}$MHz.

in Chapter 5.

We then use the dataset collected in the hospital environment to evaluate the performance of ranging and 2-D positioning with the MBWDE algorithm on the trajectory shown in Fig. 8.4. In these experiments, we vary the bandwidth of the multiband CSI measurements to illustrate its influence on the performance of ranging and positioning. The performance of the MBWDE algorithm is compared with the MI-MUSIC, CS(L1), MUSIC, and ESPRIT algorithms, that are presented in chapters 3 and 4.

8.4.1. INFLUENCE OF SYSTEM PARAMETERS $\{f_{c,i}\}_{i=1}^{L}$ AND B

We first illustrate the impact of bandwidth B selection on the reconstructed channel impulse response (CIR). We control the bandwidth by varying the number of discrete frequency points, i.e., subcarriers, at which the CFR is estimated. The effects of bandwidth selection on the CIR are shown in Fig. 8.5. Here, the CIRs are computed using the CFRs with bandwidths of 1920 and 320 MHz for one of the mobile node positions. The figure also shows the estimated MPCs obtained using the MR, MBDE, and MBWDE algorithms.The number of bands for the MR algorithm is set to $L = 2$ where their central frequencies are set to $f_i \in \{5.990, 6.230\}$ and the bandwidth to $B = 80$ MHz. Similarly, for the MBDE and MBWDE algorithms, the number of bands is set to $L = 4$ bands, where their central frequencies are set to $f_i \in \{5.990, 6.030, 6.070, 6.110\}$ and their bandwidth stays the same as for the MR algorithm. The CIR for the bandwidth $B = 320$ MHz shows that the LOS path and the first two MPCs are not resolved, which would result in a biased delay estimation with traditional methods. On the other hand, it is seen that the MBWDE algorithm almost perfectly estimates the delay of the LOS path for the same total bandwidth.

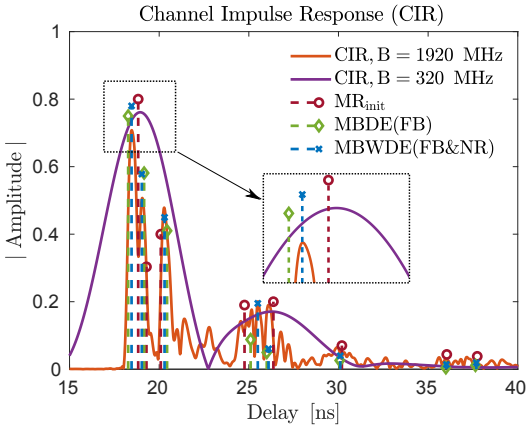

Figure 8.5: Channel impulse response for varying total bandwidth and estimates of the MPCs in a university building.

INFLUENCE OF BAND SELECTION

Next, we analyze the distribution of ranging errors with respect to band selection. We consider scenarios where a single snapshot, i.e., $M = 1$, of CSI measurements is collected in $L = 4$ bands, each with a bandwidth of $B = 40$ MHz. In the first scenario, we collect CSI by taking samples of the CFR in the following bands: $f_i \in \{5.990, 6.070, 6.150, 6.230\}$ GHz, which results in the frequency aperture of 280 MHz. In the second scenario, we decrease the total frequency aperture to 160 MHz and collect CSI in the following consecutive bands $f_i \in \{5.990, 6.030, 6.070, 6.110\}$ GHz. The selected frequencies correspond to the IEEE 802.11be channels in the 6 GHz band (cf. Fig. 8.1). We estimate the ranges between the mobile node and anchors for 484 different locations and compute the ranging errors by comparing estimates with the ground truth. We then estimate the bias as a median value of estimated ranges and compensate for it. Fig. 8.6 shows histograms of bias-free ranging errors normalized to the probability. The histograms are fitted to the Gaussian and Lévy alpha-stable distributions. It is seen that due to the small number of outliers with a high ranging error, the Gaussian distribution does not fit well the histograms. The alpha-stable distribution is more general compared to Gaussian, and its stability parameter α can be tuned to introduce more heavy tails in the PDF to better fit probabilities of outliers [277]. The estimated parameters α for the first and second scenarios are 1.72 and 1.45, respectively. However, for these values of α, the common properties of distributions such as mean and standard deviation are undefined. Therefore, we use the median value to express the bias and 95%-quantile (Q95) to express the accuracy of the estimates. The Q95 is defined as the segment around the median, which contains 95% of the estimates. To calculate Q95, we subtract the 2.5$^{\text{th}}$ percentile from the 97.5$^{\text{th}}$ percentile. The median and Q95 for these scenarios are given in Table 8.1(a). As expected from the results for the larger frequency aperture, i.e., 280 MHz, and as shown in Chapter 4, the resolution of the estimates increases, and Q95 = 19.55 cm. This is approximately two times lower compared to Q95 = 43.32 cm obtained when using the smaller frequency aperture, i.e., 160 MHz.

However, the experiments also show that selecting a too large frequency aperture can

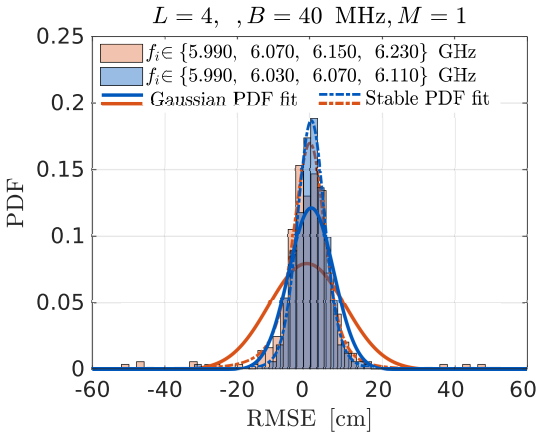

Figure 8.6: Histogram of ranging errors with respect to band selection fitted with Gaussian and Stable PDFs.

Table 8.1: Statistical parameters of ranging errors in a university building for selection of $f_{c,i}$ (a) and B (b)

(a)

$\lvert\hat{d}-d\rvert$		
Scenario	**Median** [cm]	**Q95** [cm]
1.	6.87	19.55
2.	7.74	43.3

(b)

$\lvert\hat{d}-d\rvert$		
Scenario	**Median** [cm]	**Q95** [cm]
1.	7.95	38.37
2.	6.87	19.55
3.	4.05	10.84
4.	0.86	2.89

lead to degradation of delay estimation. This is caused by the frequency dependency of RF scattering, which introduces errors in the model (4.14). The same effect occurs in channel extrapolation for FDD massive MIMO systems [208], where the goal is to infer the CSI of the downlink band from CSI estimates of the uplink band. The frequency dependency is hard to model as it depends on the dimensions and materials of reflecting structures that produce an RF scattering scene [278]. However, these modeling errors are not critical if the frequency aperture is less than 20% of the carrier frequency [275]. We do not optimize the band selection in this thesis with respect to the trade-off between time-delay resolution and modeling errors, and this remains an open question for future research. However, we avoid modeling errors in the experiments by estimating ranges from the CSI measurements collected in the bands that create a frequency aperture smaller than 10% of the carrier frequency, i.e., smaller than 600 MHz.

INFLUENCE OF BANDWIDTH SELECTION

Next, we perform experiments that illustrate the impact of the bandwidth B of the multi-band signal bands on the performance of time-delay estimation. We consider four scenarios where the bandwidth B of $L = 4$ bands is varied, and takes the values $\{20, 40, 80, 160\}$ MHz, and where their central frequencies are set to $\{5.98, 6.06, 6.14, 6.22\}$,

Table 8.2: Statistical properties of the 2-D positioning error in an indoor hospital environment for several choices of the bandwidth parameter B

	$\|\hat{\mathbf{p}}-\mathbf{p}\|_2$			
B [MHz]	**Mean** [cm]	σ_p [cm]	**Q80** [cm]	**Q95** [cm]
20	26.23	17.21	30.23	47.95
40	17.61	11.02	22.91	30.23
80	9.97	6.28	16.87	23.57
160	4.82	2.72	7.06	9.29

$\{5.95, 6.03, 6.15, 6.23\}$, $\{5.97, 6.13, 6.21, 6.37\}$ and $\{6.01, 6.21, 6.37, 6.57\}$ GHz, respectively. Although our motivation is to illustrate the impact of bandwidth on the performance of ranging, we vary both the bandwidth and central frequencies of the probed bands in these scenarios. We do this to avoid outliers in time-delay estimation that are introduced in scenarios where the bandwidth B is low, e.g. 20 or 40 MHz, and the frequency aperture is considerably larger than the bandwidth, e.g. 480 and 720 MHz. In these scenarios, a large aperture improves the resolution of the estimation. However, the overall accuracy of time-delay estimation is deteriorated due to outliers introduced by noise and modeling errors. This is similar to the effects observed in Section 4.5 where we concluded that the band selection comes as a trade-off between resolution and robustness to noise. However, now in this trade-off, modeling errors must also be included.

We repeat the same procedure as previously to compute the median and Q95, and the results are shown in Table 8.1(b). As expected, it is seen that Q95 decreases when the bandwidth is increased, where the accuracy improvement is proportional to the increase in bandwidth. To illustrate the distribution of ranging errors, Fig. 8.7 shows the empirical CDFs for these scenarios. It is seen that in 80% of the cases, the absolute ranging error is smaller than 16, 8, 4, and 1 cm for $B \in \{20, 40, 80, 160\}$ MHz, respectively.

8.4.2. PERFORMANCE OF POSITIONING AND RANGING

To illustrate the performance of ranging and 2-D positioning in a scenario where a mobile node moves over a long trajectory, we use the dataset collected in the hospital environment (cf. Fig 8.4). We start with ranging experiments and compare the results of the MBWDE algorithm with those of the MI-MUSIC, CS(L1), MUSIC, and ESPRIT algorithms.

COMPARISON TO OTHER ALGORITHMS

To compare the MBWDE(FB&NR) algorithm against other algorithms, we consider three scenarios where we vary the bandwidth $B \in \{20, 40, 80\}$ MHz. The carrier frequencies of the bands for MBWDE(FB&NR), MI-MUSIC, and CS(L1), are selected as in Section 8.4.1, while for MUSIC and ESPRIT, a single band with the same total bandwidth is selected starting from 5.925 GHz. The delay grid step is set to 0.15 ns (0.5 cm) for MI-MUSIC, CS(L1), and MUSIC.

We use the previously mentioned algorithms to estimate the ranges between anchor *A2* and the mobile node moving on segment *S1S2S3* of the trajectory (cf. Fig 8.4), where the segment *S3S4* is omitted because of the presence of NLOS propagation. We compute the ranging error and empirical CDFs in the same way as in previous scenarios. These

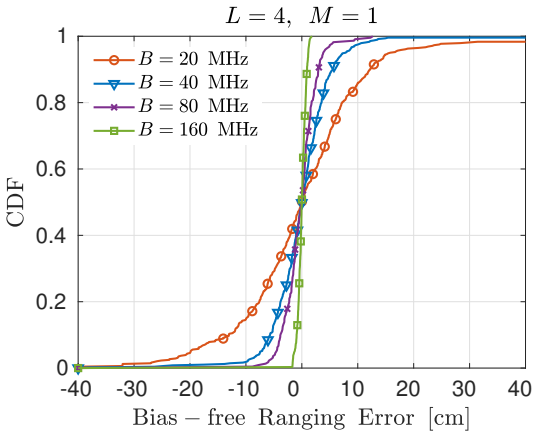

Figure 8.7: Empirical CDFs of the ranging error with respect to the bandwidth parameter B.

empirical CDFs are fitted with a Gaussian CDF and shown in Fig. 8.8. It is seen that in all scenarios, MBWDE(FB&NR) shows the best performance, where the performance of improvement of MBWDE compared to other algorithms is the largest when the bandwidth is the smallest, i.e., $B = 20$ MHz. In scenarios where $B \in \{40, 80\}$, the performance of MI-MUSIC and MBWDE(FB&NR) are almost identical. MUSIC and ESPRIT perform worst for all scenarios compared to algorithms that use multiband CSI due to the smaller frequency aperture.

PERFORMANCE OF 2-D POSITIONING

Finally, we illustrate the performance of 2-D positioning by using range estimates of the MBWDE (FB&NR) algorithm. We define the mobile node position as $\mathbf{p} = [x, y]^T$, where x and y are the node's coordinates. The mobile node positions are estimated using an LS algorithm from the ranges estimated between the mobile node and three anchors (cf. Fig. 8.4). In particular, for the segments *S1S2*, *S2S3*, and *S3S4* the ranges are estimated between the mobile node and anchors {*A1, A2, A3*}, {*A2, A4, A5*} and {*A5, A6, A7*}, respectively. We select the anchors based on the floor map shown in Fig. 8.4 to avoid NLOS propagation and outliers in the 2-D positioning. However, if a floor map is not available, this could be done directly from the measurements as shown in [279].

We estimate the positions for four different scenarios described in Section 8.4.1 where Fig. 8.4 shows the position estimates for the scenarios when $B \in \{80, 160\}$ MHz. It can be seen that for $B = 160$ MHz the position is almost perfectly estimated. To quantify the performance of position estimation, we compute the estimation error as $\text{RMSE}(\hat{\mathbf{p}}) = \|\hat{\mathbf{p}} - \mathbf{p}\|_2$, where $\mathbf{p}$ is the ground truth and $\hat{\mathbf{p}}$ is the estimate. We compute statistical properties of the errors such as mean, standard deviation σ_p, 80%-quantile (Q80), and Q95. The Q80 is computed by subtracting the 10^{th} percentile from the 90^{th} percentile. These properties are given in Table 8.2. As expected, $\text{RMSE}(\hat{\mathbf{p}})$ decreases with increasing bandwidth B. It is seen that with a single snapshot of CSI with a total bandwidth of 320 MHz and using 3 anchor nodes, it is possible to achieve an positioning error below 24 cm in 95% of the cases.

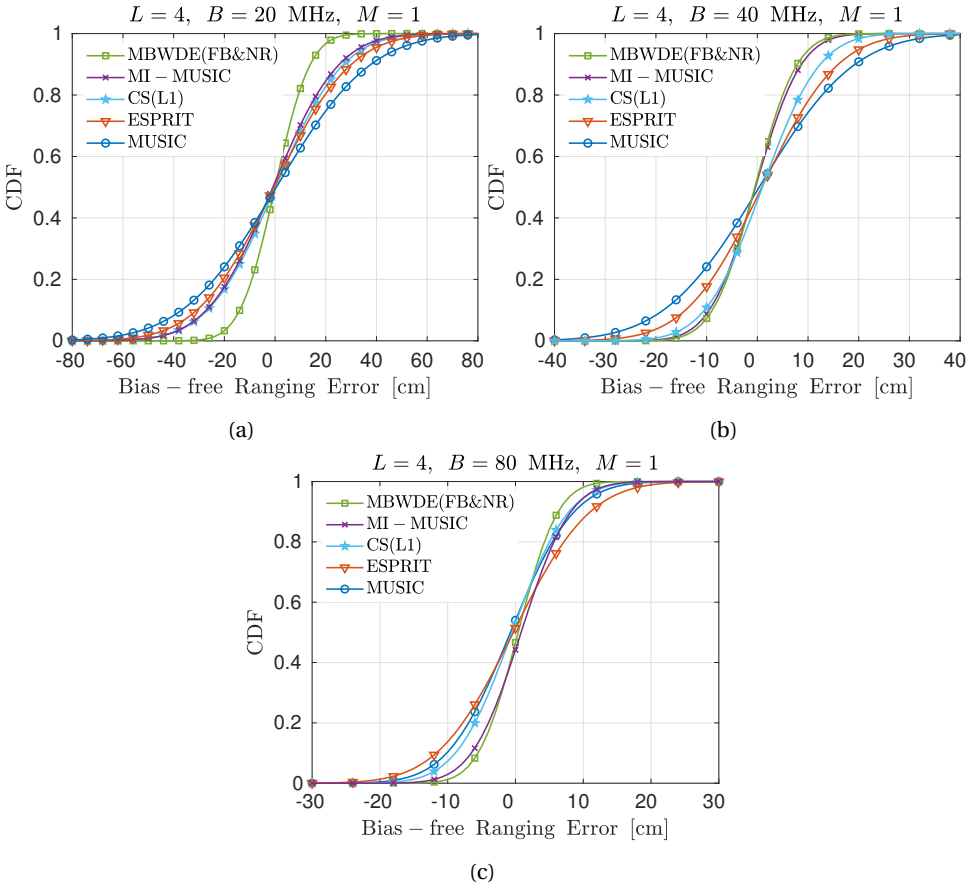

Figure 8.8: The CDFs of the ranging errors of the compared algorithms and choices of the bandwidth parameter B: (a) 20 MHz, (b) 40 (b), and (c) 80 MHz.

8.5. CONCLUSIONS

In this chapter, we have assessed the performance of ranging and 2-D positioning using the MBWDE algorithm by doing experiments with real indoor channel measurements. These results are compared against those when using the MI-MUSIC, CS(L1), MUSIC, and ESPRIT algorithms. The aim of these experiments is to validate the data modeling assumptions and the numerical results presented in Chapters 4 and 5. The results reveal that multiband channel probing and MBWDE improve time-delay resolution compared to single band probing and time-delay estimation methods. This means that smaller total bandwidth needs to be probed when using MBWDE than any single band time-delay estimation method to achieve the same RMSE. The results also show that when the total frequency aperture of multiband CSI is increased to more than ~20% of the carrier frequency, the frequency dependency effects of multipath propagation cause modeling errors that degrade the estimation performance. Therefore, the problem of modeling these frequency dependency effects of multipath propagation remains an open research

question for future work. Accurate modeling of these effects would enable the design of a multiband time-delay estimation algorithm that accounts for these effects, which would allow combining multiband CSI measurements from all available frequency bands.

9

Conclusions and Future Research Directions

"The highest reward for a person's toil is not what they get for it, but what they become by it."

— John Ruskin

9.1. CONCLUSIONS AND SUMMARY OF MAIN RESULTS

The first attempts to localize objects using radio frequency (RF) signals have been made at the beginning of the 20th century. However, the initial localization systems had poor localization accuracy and limited coverage. In Chapter 1, we discussed these matters and have provided historical background and a discussion on the importance of precise radio localization for various popular applications in industry and science. We saw that the emergence of satellite systems paved the way for developing GNSSs that support global coverage with RF positioning signals and high accuracy localization in outdoor environments with a clear view of the sky. These systems became crucial tools for providing accurate navigation and timing in many vital industries, such as transportation and logistics, location-based services, and military and defense, to name a few. However, GNSS signals are unavailable in indoor environments, and GNSS localization performs poorly in multipath propagation environments such as urban canyons. These are often scenarios with extensive human activity and where precise positioning is crucial for assisted living services and localization in the internet-of-things (IoT) networks, or autonomous navigation in urban environments and factories of the future.

The trend of densification of wireless infrastructure in indoor and urban environments in future wireless networks will ensure high SNR at the receiver. At the same time, the need for higher throughput promotes the use of signals with large bandwidth and carrier aggregation. These favorable developments will open the opportunity to utilize existing wireless infrastructure and ambient radio frequency (RF) signals for precise localization in GNSS denied environments. Localization using these signals starts with multipath channel estimation between a mobile node and anchors where parameters of the multipath channel (e.g., time-delays, directions-of-arrival, or complex-amplitudes) encode location information of the mobile node and surrounding RF reflectors.

CHAPTER 2

In Chapter 2 we have provided preliminaries and a general introduction to radio localization. There we discussed the multipath channel model and the relation between its parameters and location information. We then introduced two-step localization and direct localization methods and made a comparison between them.

We saw that the two-step localization methods first estimate the parameters of the line-of-sight (LOS) paths of a number of anchors and then estimate the location of the mobile node from the parameter estimates. The generalized data model for the measurements used in two-step localization methods (e.g., TOAs, TDOAs, DOAs, and RSSs) showed that these measurements are a nonlinear function of the unknown location of the mobile node. Therefore, location estimation using two-step localization methods involves solving nonlinear least squares (NLS) optimization problems. These optimization problems can be solved efficiently using iterative optimization methods such as Gauss-Newton, Levenberg-Marquardt, and steepest descent. However, they require initialization and their performance highly depends on the initial location estimate. We have also presented linear location estimation methods that linearize the nonlinear data models used in two-step localization. After linearizing the model, these methods estimate the location by finding the minimum of least squares (LS) or weighted least squares (WLS) cost functions.

On the other hand, direct location estimation (DLE) methods estimate the location directly from the measurements of the received signal without the intermediate step of first estimating parameters of the LOS path. This approach is statistically more efficient than two-step localization methods. However, DLE methods are highly computationally intensive and require solving complex optimization problems where the number of optimization parameters is proportional to the number of multipath components. Thereby, we concluded that DLE methods are not practical for localization in multipath scenarios. Therefore, in the remainder of this thesis, we have focused on high-resolution time-delay estimation for two-step localization methods.

CHAPTER 3

In Chapter 3, we showed that the problem of high-resolution multipath channel time-delay estimation belongs to the broad family of super-resolution signal processing problems. The super-resolution problems appear in many popular applications such as ultrasound imaging, optical imaging, and radar. We used a single-molecule microscopy problem as an intuitive example to illustrate the main impairments and challenges common for super-resolution problems: the degrading effects of noise and the limited resolution of a measurement device on the observed signals. We then derived the discrete data model for multipath channel measurements, which belongs to the family of 1-D super-resolution problems. In the remainder of this chapter, we have provided preliminaries and related work on popular signal processing frameworks used for 1-D super-resolution estimation. These frameworks include maximum likelihood (ML), subspace-based estimation, and deterministic and Bayesian sparse estimation methods.

CHAPTERS 4 AND 5

Chapters 4 and 5 have been dedicated to high-resolution time-delay estimation of multipath components. In these chapters, the main questions that we have answered are Q1, and its subquestions Q1.1, Q1.2 and Q1.3, as stated in Chapter 1.

In particular, we have proposed multiband channel probing to acquire multipath channel measurements, which allows us to increase the frequency aperture of the measurements while using RF transceivers with limited bandwidth and thus enable high-resolution time-delay estimation. We then derived the data model for these measurements, which showed that after stacking them in a block Hankel matrix, the data has multiple shift-invariance structures. Later we used this property to design algorithms for time-delay estimation based on weighted subspace fitting (WSF) and joint diagonalization, which we called multiband weighted delay estimation (MBWDE) and multiresolution time-delay (MRTD) algorithms, respectively. The MRTD algorithm has a closed-form solution, and it can be used to initialize iterative optimization methods to solve the nonlinear least-squares (NLS) problem present in the MBWDE algorithm. However, the MRTD algorithm limits time-delay estimation to scenarios when multiband channel measurements are collected in two frequency bands.

To evaluate the performance of the proposed algorithms, we used the data model of the multiband channel measurements to derive the Cramér-Rao Bound (CRB) on the root mean square error (RMSE) of their time-delay estimates. We then presented results of extensive numerical simulations that showed that both algorithms are statistically ef-

ficient and achieve the CRB. These results also show that the resolution of time-delay estimation is improved for the measurements collected over a larger frequency aperture. The derived data model is similar to the data models that arise in other signal processing applications, such as radar and ultrasound imaging. Therefore, the algorithms presented in this thesis can be adapted and extended to these and general problems of parameter estimation from data whose models exhibit multiple shift-invariance structures.

CHAPTERS 6 AND 7

Next, in Chapters 6 and 7, we have focused on the problems of joint calibration of RF transceivers and time-delay estimation, answering question Q2. In particular, in Chapters 6 and 7, we have answered its subquestions Q2.1 and Q2.2, respectively.

In Chapter 6, we have provided a solution for joint multiband time-delay estimation and calibration of the RF transceiver response. A wideband RF transceiver often introduces frequency-dependent gain and phase distortions in the multipath channel measurements due to various hardware nonidealities of RF components. If these hardware impairments are not calibrated before time-delay estimation, they can significantly deteriorate its performance. We use the properties of the communication channel and formulate the joint calibration and time-delay estimation as a special case of a covariance matching problem. The resulting problem is severely ill-posed. However, it can be regularized by using the sparse nature of multipath channels and prior knowledge of the basis functions that approximate the frequency response of RF transceivers. The regularization leads to a biconvex optimization problem in the calibration and time-delay parameters. We further recast the biconvex optimization problem into a rank-1 constrained linear system using the *lifting* technique, which can be efficiently solved as a group Lasso problem. We conducted numerical simulations and comparisons with other algorithms for joint calibration and parameter estimation. The results show that the proposed algorithm has better calibration performance than the ALMIN and BLC algorithms, that are used for comparison. At the same time, the proposed algorithm supports high-resolution time-delay estimation.

In Chapter 7, we have solved the problem of joint clock-skew and range estimation from phase difference of arrival (PDoA) measurements collected using narrowband RF transceivers. To achieve this, we have derived a data model that captures the effects of both clock-skew imperfections and narrowband signal propagation on the PDoA measurements. Following the data model, we proposed a communication protocol for collecting PDoA measurements that enables joint clock-skew and range estimation. From the collected measurements, we construct a data matrix that has a structure that calls for a 2-D subspace-based algorithm for estimation of clock-skew and range. The performance of the proposed algorithms is compared against the CRB using numerical simulations, and the results show that the algorithm is asymptotically efficient and approaching the CRB for a sufficiently high signal-to-noise ratio (SNR). When designing the proposed algorithm, we assumed a radio channel with only a LOS path between the anchor and the sensor nodes. However, this algorithm can be extended to joint clock-skew and range estimation in multipath scenarios where the effects of multipath components on the PDoA measurements can not be neglected.

CHAPTER 8

Finally, in Chapter 8, we have evaluated the performance of the multiband time-delay estimation algorithms proposed in Chapters 4 and 5 using real multipath channel measurements. In particular, we have addressed question Q3 and its subquestion Q3.1.

We performed several experiments with radio channel measurements collected in a university building and in a hospital environment to answer these questions. Our experiments consider the problem of time-delay estimation and localization in future WiFi-7 networks defined by the emerging IEEE 802.11be standard. We use this standard to define simulation parameters and experiment scenarios. The results of the experiments with real measurements are in line with the results of the numerical experiments presented in Chapters 4 and 5. However, it is also seen that multipath channels exhibit frequency dependency effects. In [275], a rule of thumb is given, saying that these effects are negligible if the frequency aperture of the channel measurements is less than 20% of the carrier frequency. To avoid modeling errors caused by frequency dependency effects, we constrained the frequency aperture of the multiband channel measurements to be less than 10% of the carrier frequency. However, the problem of modeling the frequency dependency of multipath channels remains an open question.

9.2. SUGGESTIONS FOR FUTURE RESEARCH

The research for this thesis has resulted in several new challenges and research questions, which remain still open. This section concludes the thesis with a list of some of these open problems worth further investigation, including discussion and suggestions on how to approach these problems.

JOINT DETECTION OF MULTIPATH COMPONENTS AND MULTIBAND TIME-DELAY ESTIMATION

In Chapters 4 and 5, we have presented methods for multiband time-delay estimation that assume prior knowledge of the model order, i.e., of the number of multipath components (MPCs)) (K) present in the channel. To estimate the number K in these chapters, we used the modified minimum description length (MDL) criterion [205], which comprises a data fidelity term representing the fitting error and a penalty term that increases with the model order [135]. From the range of possible model orders, the number K is selected by finding the tradeoff between the fitting error and model complexity such that the MDL criterion is minimized. The MDL method and, in general, the information criteria-based model order selection methods (e.g., AIC, BIC) tend to provide a wrong model order in non-asymptotic regimes such as low SNR or a limited number of snapshots. In Figure 4.8, as discussed in Chapter 4, we showed that the performance of the proposed multiband time-delay estimation algorithms deteriorates significantly when the model order is wrongly estimated. This issue is generally related to the two-step parametric estimation methods that separately estimate model order and parameters [82].

Given the discussion above, the interesting question is, can we jointly estimate the model order and multipath time-delay parameters from multiband channel measurements. In particular, it would be useful to formulate the problem of multiband delay es-

timation in the sparse Bayesian framework [180, 183]. That is, it would be interesting to model the multiband channel measurements using the stochastic maximum likelihood (ML) model regularized by sparsity promoting prior on the coefficients of the exponentials. This formulation would allow for joint estimation of the number of MPCs and their time delays.

A BAYESIAN APPROACH TO BAND SELECTION AND TRAINING SIGNAL DESIGN FOR MULTIBAND TIME-DELAY ESTIMATION

In Chapter 4, we did experiments that illustrate the influence of band selection on the root mean square error (RMSE) of multiband time-delay estimation in multipath channels. In particular, Fig. 4.7 shows that selecting frequency bands for channel probing such that the total frequency aperture of the channel measurements is increased, can decrease the RMSE of multiband time-delay estimation. The results of these experiments are following the performance indication given by the Cramér-Rao Bound (CRB) that is derived in Section 4.4. This leads to several interesting questions, such as: "What is optimal selection of frequency bands in terms of RMSE of multiband time-delay estimation?" and "What is the optimal training signal design in terms of the RMSE of multiband time-delay estimation considering power and bandwidth constraints set by spectrum regulations?". There have been several attempts to tackle these and similar problems previously, such as, in [280, 281, 282]. These works select performance criteria for waveform parameter design and band selection based on the CRB.

In particular, in [280], the performance criteria is defined as a combination of the CRB on time-delay estimation for a single-path channel and the bias measure (a so-called measure of dependence for delay estimation) for a two-path channel. However, it is seen that the bias measure depends on the time-delay parameters of the two paths present in the channel. This dependency causes the performance criteria to become a function of the parameters that are to be estimated and leads to optimal band selection only for a specific channel realization and the time-delays considered in it. In Section 4.4, we came to the same conclusion for a general case of the CRB on multiband time-delay estimation in multipath channels.

A promising approach to optimize band selection and the training signal for multiband time-delay estimation for the expected channel realizations is to follow the Bayesian approach [283]. In the Bayesian framework, the time-delays of MPCs are considered as random variables whose probability density function (PDF) characterizes prior constraints on the likelihood of time-delays [284, 285]. This formulation would lead to a performance criteria function based on the Bayesian CRB (also called the global CRB), which does not depend on time-delay parameters, leading to the optimal band selection and training signal design in terms of the chosen PDF function for the time-delays and other optimization constraints. The question of interest is, can such an optimization problem be solved.

JOINT RANGING AND SYNCHRONIZATION FOR NARROWBAND TRANSCEIVERS IN MULTIPATH CHANNELS

In Chapter 7, we focussed on joint ranging and synchronization using narrowband RF transceivers. In particular, we designed a protocol for collecting phase difference of ar-

rival (PDoA) measurements that allows for joint range and clock-skew estimation. When designing the algorithm, we have considered a single path channel with only one dominant, i.e., LOS, path. However, this is rarely the case in practice, and the multipath effects usually cannot be ignored, as otherwise, these effects lead to biased parameter estimation. Therefore, it would be interesting to extend the algorithm presented in Chapter 7 to take into account multipath effects. In multipath channels, joint range and clock-skew estimation can be formulated as the problem of two-dimensional (2-D) parameter estimation of multiple complex exponentials [286], which can be solved using subspace-based [287] and maximum likelihood [113] methods.

MULTIPATH CHANNEL FREQUENCY DEPENDENCY

In Chapter 8, the last chapter of this thesis, we validate the modeling assumptions and the performance of multiband delay estimation algorithms presented in Chapters 4 and 5. These experiments showed that the performance of the derived algorithms follows the theoretical result under the condition that the frequency aperture of the real multiband measurements is not too large. However, if the frequency aperture of the measurements becomes too large, the measurements start to exhibit frequency-dependency effect. This effect is the consequence of frequency-dependent diffraction and scattering of the RF signals on the reflecting structures that create an RF scattering scene [278]. In general, the frequency-dependency is negligible if the frequency aperture is smaller than 20% of the carrier frequency of the band [275].

The data models used to derive algorithms in Chapters 4 and 5 do not capture frequency-dependency effects. Therefore, when they are present in the measurements, the modeling errors are introduced, and the performance of the algorithms starts to deteriorate. To avoid frequency-dependency effects in this thesis, we select the multiband channel measurements such that their frequency aperture is smaller than 10% of the carrier frequency of the band. However, this is not the solution for scenarios where regulatory bodies preallocate frequency bands with a large frequency aperture. Therefore, frequency dependency effects can not always be ignored, and they often appear in many practical multiband communication and radar problems such as multipath channel state information extrapolation in frequency division duplexing (FDD) massive MIMO communications [288, 208] or multiband radars [289]. One possible way to solve this problem is to model the frequency dependency of multipath components and derive new algorithms for multiband time-delay estimation. However, this modeling task is challenging as these effects depend on the materials that create the RF scattering scene [278].

Therefore, an interesting question is, can we design a hybrid data-driven and model-based algorithm [290] for multiband time-delay estimation. This assumes that the model is used to describe multipath propagation phenomena that do not depend on the frequency of the RF signal, while the nonlinear function that models the frequency dependency of RF signal scattering is learned from the channel measurements.

MULTIBAND TIME-DELAY ESTIMATION AND HARDWARE IMPAIRMENTS CALIBRATION

Finally, in Chapter 8 of the thesis we used multiband channel measurements collected using a vector network analyzer (VNA) for the experiments. The parameters of the ex-

periments are selected following the IEEE 802.11be standard. However, the question remains unanswered, what is the performance of the time-delay estimation algorithms presented in this thesis with multiband channel state information (CSI) measurements collected using off-the-shelf IEEE 802.11be transceivers. In particular, it would be interesting to see how significant is the impact of hardware impairments, such as frequency and timing offsets, on the performance of the algorithms presented in this thesis. The answer to this question could potentially motivate new research problems related to the calibration of multiband CSI measurements.

BIBLIOGRAPHY

[1] Zaher Zak M Kassas et al. “I hear, therefore I know where I am: Compensating for GNSS limitations with cellular signals”. In: *IEEE Signal Processing Magazine* 34.5 (2017), pp. 111–124.

[2] Cezary Specht, Adam Weintrit, and Mariusz Specht. “A history of maritime radionavigation positioning systems used in Poland”. In: *The Journal of Navigation* 69.3 (2016), pp. 468–480.

[3] Norman Bonnor Air Commodore. “A brief history of global navigation satellite systems”. In: *The Journal of Navigation* 65.1 (2012), p. 1.

[4] Irving Lachow. “The GPS dilemma: balancing military risks and economic benefits”. In: *International Security* 20.1 (1995), pp. 126–148.

[5] Gonzalo Seco-Granados et al. “Challenges in indoor global navigation satellite systems: Unveiling its core features in signal processing”. In: *IEEE Signal Processing Magazine* 29.2 (2012), pp. 108–131.

[6] Reza Malekian et al. “Design and implementation of a wireless OBD II fleet management system”. In: *IEEE Sensors Journal* 17.4 (2016), pp. 1154–1164.

[7] Y Jade Morton et al. *Position, Navigation, and Timing Technologies in the 21st Century, Volumes 1 and 2: Integrated Satellite Navigation, Sensor Systems, and Civil Applications, Set*. John Wiley & Sons, 2020.

[8] Xiang Sun and Nirwan Ansari. “EdgeIoT: Mobile edge computing for the Internet of Things”. In: *IEEE Communications Magazine* 54.12 (2016), pp. 22–29.

[9] Greg Milner. *Pinpoint: how GPS is changing technology, culture, and our minds*. WW Norton & Company, 2016.

[10] Michael Braasch and Andrew Dempster. “Tutorial: GPS receiver architectures, front-end and baseband signal processing”. In: *IEEE Aerospace and Electronic Systems Magazine* 34.2 (2019), pp. 20–37.

[11] Mark Petovello. “How does a GNSS receiver estimate velocity?” In: *Inside GNSS* (2015), pp. 38–41.

[12] Rigas Themistoklis Ioannides, Thomas Pany, and Glen Gibbons. “Known vulnerabilities of global navigation satellite systems, status, and potential mitigation techniques”. In: *Proceedings of the IEEE* 104.6 (2016), pp. 1174–1194.

[13] Frank Stephen Tromp Van Diggelen. *A-GPS: Assisted GPS, GNSS, and SBAS*. Artech House, 2009.

[14] Grace Xingxin Gao et al. “Protecting GNSS receivers from jamming and interference”. In: *Proceedings of the IEEE* 104.6 (2016), pp. 1327–1338.

[15] Mark L Psiaki and Todd E Humphreys. “GNSS spoofing and detection”. In: *Proceedings of the IEEE* 104.6 (2016), pp. 1258–1270.

[16] Peter JG Teunissen. “A new method for fast carrier phase ambiguity estimation”. In: *Proceedings of 1994 IEEE Position, Location and Navigation Symposium-PLANS'94*. IEEE. 1994, pp. 562–573.

[17] Peter JG Teunissen. “Least-squares estimation of the integer GPS ambiguities”. In: *Invited lecture, section IV theory and methodology, IAG general meeting, Beijing, China*. 1993.

[18] Arash Hassibi and Stephen Boyd. “Integer parameter estimation in linear models with applications to GPS”. In: *IEEE Transactions on signal processing* 46.11 (1998), pp. 2938–2952.

[19] Peiliang Xu. “Voronoi cells, probabilistic bounds, and hypothesis testing in mixed integer linear models”. In: *IEEE Transactions on information theory* 52.7 (2006), pp. 3122–3138.

[20] Ekim Yurtsever et al. “A survey of autonomous driving: Common practices and emerging technologies”. In: *IEEE Access* 8 (2020), pp. 58443–58469.

[21] Xiang Cheng, Liuqing Yang, and Xia Shen. “D2D for intelligent transportation systems: A feasibility study”. In: *IEEE Transactions on Intelligent Transportation Systems* 16.4 (2015), pp. 1784–1793.

[22] Li Da Xu, Wu He, and Shancang Li. “Internet of things in industries: A survey”. In: *IEEE Transactions on industrial informatics* 10.4 (2014), pp. 2233–2243.

[23] Giovanni Acampora et al. “A survey on ambient intelligence in healthcare”. In: *Proceedings of the IEEE* 101.12 (2013), pp. 2470–2494.

[24] Seung-Hyun Kong. “High sensitivity and fast acquisition signal processing techniques for GNSS receivers: From fundamentals to state-of-the-art GNSS acquisition technologies”. In: *IEEE Signal Processing Magazine* 34.5 (2017), pp. 59–71.

[25] *Artificial Intelligence in Logistics*. https://www.ssi-schaefer.com/en-th/best-practices-trends/trends/whitepaper-artificial-intelligence-514320. Accessed: 2021-04-26. 2018.

[26] Mark Galvin. *Precision Agriculture – the Future of Farming*. https://www.cubictelecom.com/blog/precision-agriculture-the-future-of-farming/. Accessed: 2021-04-26. 2020.

[27] Ibrar Yaqoob et al. “Autonomous driving cars in smart cities: Recent advances, requirements, and challenges”. In: *IEEE Network* 34.1 (2019), pp. 174–181.

[28] Hamid Menouar et al. “UAV-enabled intelligent transportation systems for the smart city: Applications and challenges”. In: *IEEE Communications Magazine* 55.3 (2017), pp. 22–28.

[29] Yassen Dobrev et al. “Steady delivery: Wireless local positioning systems for tracking and autonomous navigation of transport vehicles and mobile robots”. In: *IEEE Microwave Magazine* 18.6 (2017), pp. 26–37.

[30] Claudine Badue et al. “Self-driving cars: A survey”. In: *Expert Systems with Applications* (2020), p. 113816.

[31] You Li et al. “What happens for a ToF LiDAR in fog?” In: *IEEE Transactions on Intelligent Transportation Systems* (2020).

[32] Gi-Poong Gwon et al. “Generation of a precise and efficient lane-level road map for intelligent vehicle systems”. In: *IEEE Transactions on Vehicular Technology* 66.6 (2016), pp. 4517–4533.

[33] Anna Syberfeldt et al. “Localizing operators in the smart factory: A review of existing techniques and systems”. In: *2016 International Symposium on Flexible Automation (ISFA)*. IEEE. 2016, pp. 179–185.

[34] Fatih Erden et al. “Sensors in assisted living: A survey of signal and image processing methods”. In: *IEEE Signal Processing Magazine* 33.2 (2016), pp. 36–44.

[35] Klaus Witrisal et al. “High-accuracy localization for assisted living: 5G systems will turn multipath channels from foe to friend”. In: *IEEE Signal Processing Magazine* 33.2 (2016), pp. 59–70.

[36] Fadel Adib et al. “3d tracking via body radio reflections”. In: *11th {USENIX} Symposium on Networked Systems Design and Implementation ({NSDI} 14)*. 2014, pp. 317–329.

[37] Moran Amit et al. “Mass-surveillance technologies to fight coronavirus spread: the case of Israel”. In: *Nature Medicine* (2020), pp. 1–3.

[38] Nuria Oliver et al. *Mobile phone data for informing public health actions across the COVID-19 pandemic life cycle*. 2020.

[39] Kimia Shamaei, Joe Khalife, and Zaher M Kassas. “Exploiting LTE signals for navigation: Theory to implementation”. In: *IEEE Transactions on Wireless Communications* 17.4 (2018), pp. 2173–2189.

[40] Erik Leitinger et al. “Evaluation of position-related information in multipath components for indoor positioning”. In: *IEEE Journal on Selected Areas in communications* 33.11 (2015), pp. 2313–2328.

[41] Hassan Naseri and Visa Koivunen. “Cooperative simultaneous localization and mapping by exploiting multipath propagation”. In: *IEEE Transactions on Signal Processing* 65.1 (2016), pp. 200–211.

[42] Benjamin Kempke et al. “Surepoint: Exploiting ultra wideband flooding and diversity to provide robust, scalable, high-fidelity indoor localization”. In: *Proceedings of the 14th ACM Conference on Embedded Network Sensor Systems CD-ROM*. 2016, pp. 137–149.

[43] M Shahwaiz Afaqui, Eduard Garcia-Villegas, and Elena Lopez-Aguilera. “IEEE 802.11 ax: Challenges and requirements for future high efficiency WiFi”. In: *IEEE Wireless Communications* 24.3 (2016), pp. 130–137.

[44] Richard B Ertel et al. “Overview of spatial channel models for antenna array communication systems”. In: *IEEE personal communications* 5.1 (1998), pp. 10–22.

[45] Ruonan Zhang et al. “Two-dimensional DoA estimation for multipath propagation characterization using the array response of PN-sequences”. In: *IEEE Transactions on Wireless Communications* 15.1 (2015), pp. 341–356.

[46] Okan Yurduseven et al. “Frequency-diverse computational direction of arrival estimation technique”. In: *Scientific reports* 9.1 (2019), pp. 1–12.

[47] Navid Tadayon et al. “Decimeter ranging with channel state information”. In: *IEEE Transactions on Wireless Communications* 18.7 (2019), pp. 3453–3468.

[48] Reza Zekavat and R Michael Buehrer. *Handbook of position location: Theory, practice and advances*. Vol. 27. John Wiley & Sons, 2011.

[49] Faheem Zafari, Athanasios Gkelias, and Kin K Leung. “A survey of indoor localization systems and technologies”. In: *IEEE Communications Surveys & Tutorials* 21.3 (2019), pp. 2568–2599.

[50] Sinan Gezici et al. “Localization via ultra-wideband radios: a look at positioning aspects for future sensor networks”. In: *IEEE signal processing magazine* 22.4 (2005), pp. 70–84.

[51] Slavisa Tomic, Marko Beko, and Rui Dinis. “RSS-based localization in wireless sensor networks using convex relaxation: Noncooperative and cooperative schemes”. In: *IEEE Transactions on Vehicular Technology* 64.5 (2014), pp. 2037–2050.

[52] Biao Zhou et al. “DoA-based rigid body localization adopting single base station”. In: *IEEE Communications Letters* 23.3 (2019), pp. 494–497.

[53] Heidi Steendam, Marc Moeneclaey, and Herwig Bruneel. “An ML-based estimate and the Cramer-Rao bound for data-aided channel estimation in KSP-OFDM”. In: *EURASIP Journal on Wireless Communications and Networking* 2008 (2007), pp. 1–9.

[54] Sangwoo Park, Erchin Serpedin, and Khalid Qaraqe. “Gaussian assumption: The least favorable but the most useful [lecture notes]”. In: *IEEE Signal Processing Magazine* 30.3 (2013), pp. 183–186.

[55] Petre Stoica and Prabhu Babu. “The Gaussian data assumption leads to the largest Cramér-Rao bound [lecture notes]”. In: *IEEE Signal Processing Magazine* 28.3 (2011), pp. 132–133.

[56] Regina Kaune. “Accuracy studies for TDOA and TOA localization”. In: *2012 15th International Conference on Information Fusion*. IEEE. 2012, pp. 408–415.

[57] Raj Thilak Rajan and Alle-Jan van der Veen. “Joint ranging and synchronization for an anchorless network of mobile nodes”. In: *IEEE Transactions on Signal Processing* 63.8 (2015), pp. 1925–1940.

[58] Sundeep Prabhakar Chepuri, Geert Leus, and Alle-Jan van der Veen. “Joint localization and clock synchronization for wireless sensor networks”. In: *Signals, Systems and Computers (ASILOMAR), 2012 Conference Record of the Forty Sixth Asilomar Conference on*. IEEE. 2012, pp. 1432–1436.

[59] William A Gardner and Chad M Spooner. “Comparison of autocorrelation and cross-correlation methods for signal-selective TDOA estimation”. In: *IEEE Transactions on signal processing* 40.10 (1992), pp. 2606–2608.

[60] Hailong Shi, Hao Zhang, and Xiqin Wang. “A TDOA technique with super-resolution based on the volume cross-correlation function”. In: *IEEE Transactions on Signal Processing* 64.21 (2016), pp. 5682–5695.

[61] Hing Cheung So, Yiu Tong Chan, and Frankie Kit Wing Chan. “Closed-form formulae for time-difference-of-arrival estimation”. In: *IEEE Transactions on Signal Processing* 56.6 (2008), pp. 2614–2620.

[62] Mohammad Reza Gholami, Reza Monir Vaghefi, and Erik G Ström. “RSS-based sensor localization in the presence of unknown channel parameters”. In: *IEEE Transactions on Signal Processing* 61.15 (2013), pp. 3752–3759.

[63] Neal Patwari et al. “Locating the nodes: cooperative localization in wireless sensor networks”. In: *IEEE Signal processing magazine* 22.4 (2005), pp. 54–69.

[64] Alan J Coulson, Allan G Williamson, and Rodney G Vaughan. “A statistical basis for lognormal shadowing effects in multipath fading channels”. In: *IEEE Transactions on Communications* 46.4 (1998), pp. 494–502.

[65] Y Hu. “Signal strength based localization and path-loss exponent self-estimation in wireless networks”. PhD thesis. Delft University of Technology, 2017.

[66] Yue Wang and KC Ho. “An asymptotically efficient estimator in closed-form for 3-D AOA localization using a sensor network”. In: *IEEE Transactions on Wireless Communications* 14.12 (2015), pp. 6524–6535.

[67] Yimao Sun, KC Ho, and Qun Wan. “Eigenspace solution for AOA localization in modified polar representation”. In: *IEEE Transactions on Signal Processing* 68 (2020), pp. 2256–2271.

[68] Keke Hu, Sundeep Prabhakar Chepuri, and Geert Leus. “Near-field source localization: Sparse recovery techniques and grid matching”. In: *2014 IEEE 8th Sensor Array and Multichannel Signal Processing Workshop (SAM)*. IEEE. 2014, pp. 369–372.

[69] Alessio Fascista et al. “A localization algorithm based on V2I communications and AOA estimation”. In: *IEEE Signal Processing Letters* 24.1 (2016), pp. 126–130.

[70] Kerry Gallagher and Malcolm Sambridge. “Genetic algorithms: a powerful tool for large-scale nonlinear optimization problems”. In: *Computers & Geosciences* 20.7-8 (1994), pp. 1229–1236.

[71] Konstantinos E Parsopoulos and Michael N Vrahatis. “On the computation of all global minimizers through particle swarm optimization”. In: *IEEE Transactions on evolutionary computation* 8.3 (2004), pp. 211–224.

[72] Steven M Kay. *Estimation theory*. Prentice Hall PTR, 2010.

[73] Anthony J Weiss. “Direct position determination of narrowband radio frequency transmitters”. In: *IEEE Signal Processing Letters* 11.5 (2004), pp. 513–516.

[74] Liran Tzafri and Anthony J Weiss. “High-resolution direct position determination using MVDR”. In: *IEEE Transactions on Wireless Communications* 15.9 (2016), pp. 6449–6461.

[75] Oded Bialer, Dan Raphaeli, and Anthony J Weiss. “Maximum-likelihood direct position estimation in dense multipath”. In: *IEEE Transactions on Vehicular Technology* 62.5 (2012), pp. 2069–2079.

[76] Pau Closas and Adria Gusi-Amigo. “Direct position estimation of GNSS receivers: Analyzing main results, architectures, enhancements, and challenges”. In: *IEEE Signal Processing Magazine* 34.5 (2017), pp. 72–84.

[77] Saleh Al-Jazzar, Mounir Ghogho, and Desmond McLernon. “A joint TOA/AOA constrained minimization method for locating wireless devices in non-line-of-sight environment”. In: *IEEE transactions on vehicular technology* 58.1 (2008), pp. 468–472.

[78] Lorenzo Taponecco, Antonio Alberto D’Amico, and Umberto Mengali. “Joint TOA and AOA estimation for UWB localization applications”. In: *IEEE Transactions on Wireless Communications* 10.7 (2011), pp. 2207–2217.

[79] Fang Shang, Benoit Champagne, and Ioannis N Psaromiligkos. “A ML-based framework for joint TOA/AOA estimation of UWB pulses in dense multipath environments”. In: *IEEE Transactions on Wireless Communications* 13.10 (2014), pp. 5305–5318.

[80] Jihao Yin et al. “A simple and accurate TDOA-AOA localization method using two stations”. In: *IEEE Signal Processing Letters* 23.1 (2015), pp. 144–148.

[81] Slavisa Tomic, Marko Beko, and Rui Dinis. “Distributed RSS-AoA based localization with unknown transmit powers”. In: *IEEE Wireless Communications Letters* 5.4 (2016), pp. 392–395.

[82] Petre Stoica, Randolph L Moses, et al. *Spectral analysis of signals*. Pearson Prentice Hall Upper Saddle River, NJ, 2005.

[83] Yonina C Eldar and Gitta Kutyniok. *Compressed sensing: theory and applications*. Cambridge university press, 2012.

[84] Tarik Kazaz et al. “Joint blind calibration and time-delay estimation for multiband ranging”. In: *ICASSP 2020-2020 IEEE International Conference on Acoustics, Speech and Signal Processing (ICASSP)*. IEEE. 2020, pp. 4846–4850.

[85] Tarik Kazaz et al. “Analysis of multipath channel delay estimation using subspace fitting”. In: *2020 54th Asilomar Conference on Signals, Systems, and Computers*. IEEE. 2020, pp. 1237–1241.

[86] Joseph W Goodman. *Introduction to Fourier optics*. Roberts and Company Publishers, 2005.

[87] Richard Baraniuk and Philippe Steeghs. “Compressive radar imaging”. In: *2007 IEEE radar conference*. IEEE. 2007, pp. 128–133.

[88] Qiong Huang et al. “UWB through-wall imaging based on compressive sensing”. In: *IEEE Transactions on Geoscience and Remote Sensing* 48.3 (2009), pp. 1408–1415.

[89] Sunil Rudresh and Chandra Sekhar Seelamantula. “Finite-rate-of-innovation-sampling-based super-resolution radar imaging”. In: *IEEE Transactions on Signal Processing* 65.19 (2017), pp. 5021–5033.

[90] Ronen Tur, Yonina C Eldar, and Zvi Friedman. “Innovation rate sampling of pulse streams with application to ultrasound imaging”. In: *IEEE Transactions on Signal Processing* 59.4 (2011), pp. 1827–1842.

[91] Noam Wagner, Yonina C Eldar, and Zvi Friedman. “Compressed beamforming in ultrasound imaging”. In: *IEEE Transactions on Signal Processing* 60.9 (2012), pp. 4643–4657.

[92] Michaela C Vanderveen, A-J Van der Veen, and Arogyaswami Paulraj. “Estimation of multipath parameters in wireless communications”. In: *IEEE Transactions on Signal Processing* 46.3 (1998), pp. 682–690.

[93] Hlaing Minn and Naofal Al-Dhahir. “Optimal training signals for MIMO OFDM channel estimation”. In: *IEEE transactions on wireless communications* 5.5 (2006), pp. 1158–1168.

[94] Anum Ali, Nuria González-Prelcic, and Robert W Heath. “Millimeter wave beam-selection using out-of-band spatial information”. In: *IEEE Transactions on Wireless Communications* 17.2 (2017), pp. 1038–1052.

[95] Christian R Berger et al. “Sparse channel estimation for multicarrier underwater acoustic communication: From subspace methods to compressed sensing”. In: *IEEE Transactions on Signal Processing* 58.3 (2009), pp. 1708–1721.

[96] Yuejie Chi and Maxime Ferreira Da Costa. “Harnessing sparsity over the continuum: Atomic norm minimization for superresolution”. In: *IEEE Signal Processing Magazine* 37.2 (2020), pp. 39–57.

[97] Veniamin I Morgenshtern and Emmanuel J Candes. “Super-resolution of positive sources: The discrete setup”. In: *SIAM Journal on Imaging Sciences* 9.1 (2016), pp. 412–444.

[98] Martin Vetterli, Pina Marziliano, and Thierry Blu. “Sampling signals with finite rate of innovation”. In: *IEEE transactions on Signal Processing* 50.6 (2002), pp. 1417–1428.

[99] Kfir Gedalyahu, Ronen Tur, and Yonina C Eldar. “Multichannel sampling of pulse streams at the rate of innovation”. In: *IEEE Transactions on Signal Processing* 59.4 (2011), pp. 1491–1504.

[100] Cheng-Rung Tsai, Yu-Hsin Liu, and An-Yeu Wu. “Efficient compressive channel estimation for millimeter-wave large-scale antenna systems”. In: *IEEE Transactions on Signal Processing* 66.9 (2018), pp. 2414–2428.

[101] Hamid Krim and Mats Viberg. “Two decades of array signal processing research: the parametric approach”. In: *IEEE signal processing magazine* 13.4 (1996), pp. 67–94.

[102] Yonina C Eldar. *Sampling theory: Beyond bandlimited systems*. Cambridge University Press, 2015.

[103] Omer Bar-Ilan and Yonina C Eldar. “Sub-Nyquist radar via Doppler focusing”. In: *IEEE Transactions on Signal Processing* 62.7 (2014), pp. 1796–1811.

[104] J Bohme. “Estimation of source parameters by maximum likelihood and nonlinear regression”. In: *ICASSP'84. IEEE International Conference on Acoustics, Speech, and Signal Processing*. Vol. 9. IEEE. 1984, pp. 271–274.

[105] Petre Stoica et al. “Maximum likelihood array processing for stochastic coherent sources”. In: *IEEE Transactions on Signal Processing* 44.1 (1996), pp. 96–105.

[106] Björn Ottersten et al. “Exact and large sample maximum likelihood techniques for parameter estimation and detection in array processing”. In: *Radar array processing*. Springer, 1993, pp. 99–151.

[107] Petre Stoica and Arye Nehorai. “Performance study of conditional and unconditional direction-of-arrival estimation”. In: *IEEE Transactions on Acoustics, Speech, and Signal Processing* 38.10 (1990), pp. 1783–1795.

[108] Harry L Van Trees. *Optimum array processing: Part IV of detection, estimation, and modulation theory*. John Wiley & Sons, 2004.

[109] Fredrik Athley. “Threshold region performance of maximum likelihood direction of arrival estimators”. In: *IEEE Transactions on Signal Processing* 53.4 (2005), pp. 1359–1373.

[110] Ya-Xiang Yuan. “Recent advances in numerical methods for nonlinear equations and nonlinear least squares”. In: *Numerical algebra, control & optimization* 1.1 (2011), p. 15.

[111] Philip E Gill and Walter Murray. “Algorithms for the solution of the nonlinear least-squares problem”. In: *SIAM Journal on Numerical Analysis* 15.5 (1978), pp. 977–992.

[112] Gene Golub and Victor Pereyra. “Separable nonlinear least squares: the variable projection method and its applications”. In: *Inverse problems* 19.2 (2003), R1.

[113] Yoram Bresler and Albert Macovski. “Exact maximum likelihood parameter estimation of superimposed exponential signals in noise”. In: *IEEE Transactions on Acoustics, Speech, and Signal Processing* 34.5 (1986), pp. 1081–1089.

[114] Mati Wax and Ilan Ziskind. “Detection of the number of coherent signals by the MDL principle”. In: *IEEE Transactions on Acoustics, Speech, and Signal Processing* 37.8 (1989), pp. 1190–1196.

[115] Joao Paulo CL da Costa et al. “Enhanced model order estimation using higher-order arrays”. In: *2007 Conference Record of the Forty-First Asilomar Conference on Signals, Systems and Computers*. IEEE. 2007, pp. 412–416.

[116] Alle-Jan van der Veen, Jac Romme, and Ye Cui. “Rank detection thresholds for Hankel or Toeplitz data matrices”. In: *2020 28th European Signal Processing Conference (EUSIPCO)*. IEEE. 2020, pp. 1911–1915.

[117] Fu Li and Richard J Vaccaro. “Unified analysis for DOA estimation algorithms in array signal processing”. In: *Signal Processing* 25.2 (1991), pp. 147–169.

[118] Sergios Theodoridis and Rama Chellappa. *Academic Press library in signal processing: communications and radar signal processing*. Academic Press, 2013.

[119] Ralph Schmidt. "Multiple emitter location and signal parameter estimation". In: *IEEE transactions on antennas and propagation* 34.3 (1986), pp. 276–280.

[120] Min Lin and Luxi Yang. "Blind calibration and DOA estimation with uniform circular arrays in the presence of mutual coupling". In: *IEEE Antennas and Wireless Propagation Letters* 5 (2006), pp. 315–318.

[121] Monson H Hayes. *Statistical digital signal processing and modeling*. John Wiley & Sons, 2009.

[122] Arthur Barabell. "Improving the resolution performance of eigenstructure-based direction-finding algorithms". In: *ICASSP'83. IEEE International Conference on Acoustics, Speech, and Signal Processing*. Vol. 8. IEEE. 1983, pp. 336–339.

[123] Petre Stoica and Kenneth C Sharman. "Maximum likelihood methods for direction-of-arrival estimation". In: *IEEE Transactions on Acoustics, Speech, and Signal Processing* 38.7 (1990), pp. 1132–1143.

[124] Richard Roy and Thomas Kailath. "ESPRIT-estimation of signal parameters via rotational invariance techniques". In: *IEEE Transactions on acoustics, speech, and signal processing* 37.7 (1989), pp. 984–995.

[125] Yingbo Hua and Tapan K Sarkar. "On SVD for estimating generalized eigenvalues of singular matrix pencil in noise". In: *1991., IEEE International Sympoisum on Circuits and Systems*. IEEE. 1991, pp. 2780–2783.

[126] Y. Hua. "Estimating two-dimensional frequencies by matrix enhancement and matrix pencil". In: *IEEE Transactions on Signal Processing* 40.9 (1992), pp. 2267–2280. DOI: 10.1109/78.157226.

[127] Anders Eriksson and Petre Stoica. "Optimally weighted ESPRIT for direction estimation". In: *Signal processing* 38.2 (1994), pp. 223–229.

[128] Martin Haardt and Josef A Nossek. "Unitary ESPRIT: How to obtain increased estimation accuracy with a reduced computational burden". In: *IEEE transactions on signal processing* 43.5 (1995), pp. 1232–1242.

[129] A-J Van Der Veen, ED F Deprettere, and A Lee Swindlehurst. "Subspace-based signal analysis using singular value decomposition". In: *Proceedings of the IEEE* 81.9 (1993), pp. 1277–1308.

[130] S Unnikrishna Pillai and Byung Ho Kwon. "Forward/backward spatial smoothing techniques for coherent signal identification". In: *IEEE Transactions on Acoustics, Speech, and Signal Processing* 37.1 (1989), pp. 8–15.

[131] Fuxi Wen et al. "5G positioning and mapping with diffuse multipath". In: *IEEE Transactions on Wireless Communications* 20.2 (2020), pp. 1164–1174.

[132] Keyong Han and Arye Nehorai. "Improved source number detection and direction estimation with nested arrays and ULAs using jackknifing". In: *IEEE Transactions on Signal Processing* 61.23 (2013), pp. 6118–6128.

[133] Ahmad Bazzi, Dirk TM Slock, and Lisa Meilhac. “Detection of the number of superimposed signals using modified MDL criterion: A random matrix approach”. In: *2016 IEEE International Conference on Acoustics, Speech and Signal Processing (ICASSP)*. IEEE. 2016, pp. 4593–4597.

[134] Bhaskar D Rao and KVS Hari. “Weighted subspace methods and spatial smoothing: analysis and comparison”. In: *IEEE Transactions on Signal Processing* 41.2 (1993), pp. 788–803.

[135] Petre Stoica and Yngve Selen. “Model-order selection: a review of information criterion rules”. In: *IEEE Signal Processing Magazine* 21.4 (2004), pp. 36–47.

[136] David L Donoho. “Superresolution via sparsity constraints”. In: *SIAM journal on mathematical analysis* 23.5 (1992), pp. 1309–1331.

[137] Michael E Tipping. “Sparse Bayesian learning and the relevance vector machine”. In: *Journal of machine learning research* 1.Jun (2001), pp. 211–244.

[138] David L Donoho. “Compressed sensing”. In: *IEEE Transactions on information theory* 52.4 (2006), pp. 1289–1306.

[139] Emmanuel J Candès and Michael B Wakin. “An introduction to compressive sampling”. In: *IEEE signal processing magazine* 25.2 (2008), pp. 21–30.

[140] David P Wipf and Bhaskar D Rao. “Sparse Bayesian learning for basis selection”. In: *IEEE Transactions on Signal processing* 52.8 (2004), pp. 2153–2164.

[141] Robert Tibshirani. “Regression shrinkage and selection via the lasso”. In: *Journal of the Royal Statistical Society: Series B (Methodological)* 58.1 (1996), pp. 267–288.

[142] Shaobing Chen and David Donoho. “Basis pursuit”. In: *Proceedings of 1994 28th Asilomar Conference on Signals, Systems and Computers*. Vol. 1. IEEE. 1994, pp. 41–44.

[143] Stephen Boyd, Stephen P Boyd, and Lieven Vandenberghe. *Convex optimization*. Cambridge university press, 2004.

[144] Zai Yang et al. “Sparse methods for direction-of-arrival estimation”. In: *Academic Press Library in Signal Processing, Volume 7*. Elsevier, 2018, pp. 509–581.

[145] Emmanuel Candes and Justin Romberg. “l1-magic: Recovery of sparse signals via convex programming”. In: *URL: www. acm. caltech. edu/l1magic/downloads/l1magic. pdf* 4 (2005), p. 14.

[146] Michael Lustig, David Donoho, and John M Pauly. “Sparse MRI: The application of compressed sensing for rapid MR imaging”. In: *Magnetic Resonance in Medicine: An Official Journal of the International Society for Magnetic Resonance in Medicine* 58.6 (2007), pp. 1182–1195.

[147] Yu Nesterov. “Smooth minimization of non-smooth functions”. In: *Mathematical programming* 103.1 (2005), pp. 127–152.

[148] Stephen Becker, Jérôme Bobin, and Emmanuel J Candès. “NESTA: A fast and accurate first-order method for sparse recovery”. In: *SIAM Journal on Imaging Sciences* 4.1 (2011), pp. 1–39.

[149] Stephen Boyd, Neal Parikh, and Eric Chu. *Distributed optimization and statistical learning via the alternating direction method of multipliers*. Now Publishers Inc, 2011.

[150] E. van den Berg and M. P. Friedlander. "Probing the Pareto frontier for basis pursuit solutions". In: *SIAM Journal on Scientific Computing* 31.2 (2008), pp. 890–912. DOI: 10.1137/080714488. URL: http://link.aip.org/link/?SCE/31/890.

[151] E. van den Berg and M. P. Friedlander. *SPGL1: A solver for large-scale sparse reconstruction*. https://friedlander.io/spgl1. Sept. 2019.

[152] Dmitry Malioutov, Müjdat Cetin, and Alan S Willsky. "A sparse signal reconstruction perspective for source localization with sensor arrays". In: *IEEE transactions on signal processing* 53.8 (2005), pp. 3010–3022.

[153] Waheed U Bajwa et al. "Compressed channel sensing: A new approach to estimating sparse multipath channels". In: *Proceedings of the IEEE* 98.6 (2010), pp. 1058–1076.

[154] J. Meng et al. "Compressive Sensing Based High-Resolution Channel Estimation for OFDM System". In: *IEEE Journal of Selected Topics in Signal Processing* 6.1 (2012), pp. 15–25.

[155] Georg Taubock et al. "Compressive estimation of doubly selective channels in multicarrier systems: Leakage effects and sparsity-enhancing processing". In: *IEEE Journal of selected topics in signal processing* 4.2 (2010), pp. 255–271.

[156] Yuejie Chi et al. "Sensitivity to basis mismatch in compressed sensing". In: *IEEE Transactions on Signal Processing* 59.5 (2011), pp. 2182–2195.

[157] Kevin P Murphy. *Machine learning: a probabilistic perspective*. MIT press, 2012.

[158] ACFME Tipping and A Faul. "Analysis of sparse Bayesian learning". In: *Advances in neural information processing systems* 14 (2002), pp. 383–389.

[159] Sergios Theodoridis. *Machine learning: a Bayesian and optimization perspective*. Academic press, 2015.

[160] Niels Lovmand Pedersen. "Bayesian Inference Methods for Sparse Channel Estimation". English. PhD thesis. July 2013. ISBN: 978-87-7152-035-4.

[161] Dmitriy Shutin and Bernard H Fleury. "Sparse variational Bayesian SAGE algorithm with application to the estimation of multipath wireless channels". In: *IEEE Transactions on signal processing* 59.8 (2011), pp. 3609–3623.

[162] Jordan Frecon et al. "Bayesian-driven criterion to automatically select the regularization parameter in the L1-Potts model". In: *2017 IEEE International Conference on Acoustics, Speech and Signal Processing (ICASSP)*. IEEE. 2017, pp. 3839–3843.

[163] Zhilin Zhang and Bhaskar D Rao. "Sparse signal recovery with temporally correlated source vectors using sparse Bayesian learning". In: *IEEE Journal of Selected Topics in Signal Processing* 5.5 (2011), pp. 912–926.

[164] Dmitriy Shutin et al. “Fast variational sparse Bayesian learning with automatic relevance determination for superimposed signals”. In: *IEEE Transactions on Signal Processing* 59.12 (2011), pp. 6257–6261.

[165] Ranjitha Prasad, Chandra R Murthy, and Bhaskar D Rao. “Joint approximately sparse channel estimation and data detection in OFDM systems using sparse Bayesian learning”. In: *IEEE Transactions on Signal Processing* 62.14 (2014), pp. 3591–3603.

[166] Petre Stoica and Prabhu Babu. “Sparse estimation of spectral lines: Grid selection problems and their solutions”. In: *IEEE Transactions on Signal Processing* 60.2 (2011), pp. 962–967.

[167] Hao Zhu, Geert Leus, and Georgios B Giannakis. “Sparsity-cognizant total least-squares for perturbed compressive sampling”. In: *IEEE Transactions on Signal Processing* 59.5 (2011), pp. 2002–2016.

[168] Badri Narayan Bhaskar, Gongguo Tang, and Benjamin Recht. “Atomic norm denoising with applications to line spectral estimation”. In: *IEEE Transactions on Signal Processing* 61.23 (2013), pp. 5987–5999.

[169] Zai Yang, Cishen Zhang, and Lihua Xie. “Robustly stable signal recovery in compressed sensing with structured matrix perturbation”. In: *IEEE Transactions on Signal Processing* 60.9 (2012), pp. 4658–4671.

[170] Zai Yang, Lihua Xie, and Cishen Zhang. “Off-grid direction of arrival estimation using sparse Bayesian inference”. In: *IEEE Transactions on Signal Processing* 61.1 (2012), pp. 38–43.

[171] Jisheng Dai et al. “Root sparse Bayesian learning for off-grid DOA estimation”. In: *IEEE Signal Processing Letters* 24.1 (2016), pp. 46–50.

[172] Haoyue Tang, Jintao Wang, and Longzhuang He. “Off-grid sparse bayesian learning-based channel estimation for mmwave massive mimo uplink”. In: *IEEE Wireless Communications Letters* 8.1 (2018), pp. 45–48.

[173] Dmitriy Shutin, Wei Wang, and Thomas Jost. “Incremental sparse Bayesian learning for parameter estimation of superimposed signals”. In: *10th International Conference on Sampling Theory and Applications*. 1. 2013, pp. 6–9.

[174] Lei Hu et al. “Compressed sensing of complex sinusoids: An approach based on dictionary refinement”. In: *IEEE Transactions on Signal Processing* 60.7 (2012), pp. 3809–3822.

[175] Petre Stoica et al. “Gridless compressive-sensing methods for frequency estimation: Points of tangency and links to basics”. In: *2014 22nd European Signal Processing Conference (EUSIPCO)*. IEEE. 2014, pp. 1831–1835.

[176] Zai Yang and Lihua Xie. “On gridless sparse methods for line spectral estimation from complete and incomplete data”. In: *IEEE Transactions on Signal Processing* 63.12 (2015), pp. 3139–3153.

[177] Carlos Fernandez-Granda. “Super-resolution of point sources via convex programming”. In: *Information and Inference: A Journal of the IMA* 5.3 (2016), pp. 251–303.

[178] Emmanuel J Candès and Carlos Fernandez-Granda. “Super-resolution from noisy data”. In: *Journal of Fourier Analysis and Applications* 19.6 (2013), pp. 1229–1254.

[179] Emmanuel J Candès and Carlos Fernandez-Granda. “Towards a mathematical theory of super-resolution”. In: *Communications on pure and applied Mathematics* 67.6 (2014), pp. 906–956.

[180] Mihai-Alin Badiu, Thomas Lundgaard Hansen, and Bernard Henri Fleury. “Variational Bayesian inference of line spectra”. In: *IEEE Transactions on Signal Processing* 65.9 (2017), pp. 2247–2261.

[181] Thomas Lundgaard Hansen. “Sparsity-Based Algorithms for Line Spectral Estimation”. English. PhD thesis. 2018. DOI: 10.5278/vbn.phd.tech.00037.

[182] Thomas Lundgaard Hansen et al. “An iterative receiver for OFDM with sparsity-based parametric channel estimation”. In: *IEEE Transactions on Signal Processing* 66.20 (2018), pp. 5454–5469.

[183] Thomas Lundgaard Hansen, Bernard Henri Fleury, and Bhaskar D Rao. “Superfast line spectral estimation”. In: *IEEE Transactions on Signal Processing* 66.10 (2018), pp. 2511–2526.

[184] Slavche Pejoski and Venceslav Kafedziski. “Estimation of sparse time dispersive channels in pilot aided OFDM using atomic norm”. In: *IEEE Wireless Communications Letters* 4.4 (2015), pp. 397–400.

[185] Hongyun Chu, Le Zheng, and Xiaodong Wang. “Semi-blind millimeter-wave channel estimation using atomic norm minimization”. In: *IEEE Communications Letters* 22.12 (2018), pp. 2535–2538.

[186] Henk Wymeersch et al. “A machine learning approach to ranging error mitigation for UWB localization”. In: *IEEE transactions on communications* 60.6 (2012), pp. 1719–1728.

[187] Xinrong Li and Kaveh Pahlavan. “Super-resolution TOA estimation with diversity for indoor geolocation”. In: *IEEE Transactions on Wireless Communications* 3.1 (2004), pp. 224–234.

[188] Feng-Xiang Ge et al. “Super-resolution time delay estimation in multipath environments”. In: *IEEE Transactions on Circuits and Systems I: Regular Papers* 54.9 (2007), pp. 1977–1986.

[189] M. Vetterli, P. Marziliano, and T. Blu. “Sampling signals with finite rate of innovation”. In: *IEEE Transactions on Signal Processing* 50.6 (2002), pp. 1417–1428.

[190] Yann Barbotin et al. “Estimation of sparse MIMO channels with common support”. In: *IEEE Transactions on Communications* 60.12 (2012), pp. 3705–3716.

[191] Jie Xiong, Karthikeyan Sundaresan, and Kyle Jamieson. “Tonetrack: Leveraging frequency-agile radios for time-based indoor wireless localization”. In: *Proceedings of the 21st Annual International Conference on Mobile Computing and Networking*. 2015, pp. 537–549.

[192] Deepak Vasisht, Swarun Kumar, and Dina Katabi. “Decimeter-level localization with a single WiFi access point”. In: *13th USENIX Symposium on Networked Systems Design and Implementation (NSDI 16)*. 2016, pp. 165–178.

[193] Chen Chen et al. “Achieving centimeter-accuracy indoor localization on WiFi platforms: A frequency hopping approach”. In: *IEEE Internet of Things Journal* 4.1 (2016), pp. 111–121.

[194] Mahdi Barzegar Khalilsarai et al. “WiFi-based indoor localization via multi-band splicing and phase retrieval”. In: *2019 IEEE 20th International Workshop on Signal Processing Advances in Wireless Communications (SPAWC)*. IEEE. 2019, pp. 1–5.

[195] A Lee Swindlehurst et al. “Multiple invariance ESPRIT”. In: *IEEE Transactions on Signal Processing* 40.4 (1992), pp. 867–881.

[196] Mats Viberg and Bjorn Ottersten. “Sensor array processing based on subspace fitting”. In: *IEEE Transactions on signal processing* 39.5 (1991), pp. 1110–1121.

[197] David López-Pérez et al. “IEEE 802.11 be extremely high throughput: The next generation of Wi-Fi technology beyond 802.11 ax”. In: *IEEE Communications Magazine* 57.9 (2019), pp. 113–119.

[198] Camillo Gentile et al. “Methodology for Benchmarking Radio-Frequency Channel Sounders through a System Model”. In: *IEEE Transactions on Wireless Communications* 19.10 (2020), pp. 6504–6519.

[199] M. Luise, R. Reggiannini, and G. M. Vitetta. “Blind equalization/detection for OFDM signals over frequency-selective channels”. In: *IEEE Journal on Selected Areas in Communications* 16.8 (1998), pp. 1568–1578.

[200] Ove Edfors et al. “OFDM channel estimation by singular value decomposition”. In: *IEEE Transactions on communications* 46.7 (1998), pp. 931–939.

[201] Pepijn Boer et al. “Performance of High-Accuracy Phase-Based Ranging in Multipath Environments”. In: *2020 IEEE 91st Vehicular Technology Conference (VTC2020-Spring)*. IEEE. 2020, pp. 1–5.

[202] Tarik Kazaz, Gerard JM Janssen, and Alle-Jan van der Veen. “Time Delay Estimation from Multiband Radio Channel Samples in Nonuniform Noise”. In: *2019 53rd Asilomar Conference on Signals, Systems, and Computers*. IEEE. 2019, pp. 1237–1241.

[203] Tarik Kazaz et al. “Multiresolution time-of-arrival estimation from multiband radio channel measurements”. In: *ICASSP 2019-2019 IEEE International Conference on Acoustics, Speech and Signal Processing (ICASSP)*. IEEE. 2019, pp. 4395–4399.

[204] Mati Wax and Thomas Kailath. “Detection of signals by information theoretic criteria”. In: *IEEE Transactions on acoustics, speech, and signal processing* 33.2 (1985), pp. 387–392.

[205] Abdo Gaber and Abbas Omar. “A study of wireless indoor positioning based on joint TDOA and DOA estimation using 2-D matrix pencil algorithms and IEEE 802.11 ac”. In: *IEEE Transactions on Wireless Communications* 14.5 (2014), pp. 2440–2454.

[206] A Lee Swindlehurst and Thomas Kailath. “A performance analysis of subspace-based methods in the presence of model error. II. Multidimensional algorithms”. In: *IEEE Transactions on Signal Processing* 41.9 (1993), pp. 2882–2890.

[207] Petre Stoica and Arye Nehorai. “MUSIC, maximum likelihood, and Cramer-Rao bound”. In: *IEEE Transactions on Acoustics, speech, and signal processing* 37.5 (1989), pp. 720–741.

[208] François Rottenberg et al. “Performance Analysis of Channel Extrapolation in FDD Massive MIMO Systems”. In: *IEEE Transactions on Wireless Communications* 19.4 (2020), pp. 2728–2741.

[209] Niels Lovmand Pedersen et al. “Analysis of smoothing techniques for subspace estimation with application to channel estimation”. In: *2011 IEEE International Conference on Communications (ICC)*. IEEE. 2011, pp. 1–6.

[210] Marco Driusso et al. “Performance analysis of time of arrival estimation on OFDM signals”. In: *IEEE Signal Processing Letters* 22.7 (2014), pp. 983–987.

[211] Wasim Q Malik, David J Edwards, and Christopher J Stevens. “Frequency dependence of fading statistics for ultrawideband systems”. In: *IEEE Transactions on Wireless Communications* 6.3 (2007), pp. 800–804.

[212] Tarik Kazaz et al. “Analysis of Multipath Channel Delay Estimation Using Subspace Fitting”. In: *2020 54th Asilomar Conference on Signals, Systems, and Computers*. 2020, pp. 1070–1074. DOI: 10.1109/IEEECONF51394.2020.9443360.

[213] Yuan Shen and Moe Z Win. “Fundamental limits of wideband localization—Part I: A general framework”. In: *IEEE Transactions on Information Theory* 56.10 (2010), pp. 4956–4980.

[214] A Lee Swindlehurst, Petre Stoica, and Magnus Jansson. “Exploiting arrays with multiple invariances using MUSIC and MODE”. In: *IEEE Transactions on Signal Processing* 49.11 (2001), pp. 2511–2521.

[215] Jorge J Moré. “The Levenberg-Marquardt algorithm: implementation and theory”. In: *Numerical analysis*. Springer, 1978, pp. 105–116.

[216] Allen A Goldstein. “On steepest descent”. In: *Journal of the Society for Industrial and Applied Mathematics, Series A: Control* 3.1 (1965), pp. 147–151.

[217] Aweke N Lemma, A-J Van der Veen, and Ed F Deprettere. “Multiresolution ESPRIT algorithm”. In: *IEEE Transactions on signal processing* 47.6 (1999), pp. 1722–1726.

[218] Petr Tichavsky and Arie Yeredor. “Fast approximate joint diagonalization incorporating weight matrices”. In: *IEEE Transactions on Signal Processing* 57.3 (2008), pp. 878–891.

[219] Cheng Qian et al. “Enhanced PUMA for direction-of-arrival estimation and its performance analysis”. In: *IEEE Transactions on Signal Processing* 64.16 (2016), pp. 4127–4137.

[220] Jens Steinwandt, Florian Roemer, and Martin Haardt. “Generalized least squares for ESPRIT-type direction of arrival estimation”. In: *IEEE Signal Processing Letters* 24.11 (2017), pp. 1681–1685.

[221] Irena Maravic and Martin Vetterli. “Sampling and reconstruction of signals with finite rate of innovation in the presence of noise”. In: *IEEE Transactions on Signal Processing* 53.8 (2005), pp. 2788–2805.

[222] Alle-Jan van der Veen, P Bas Ober, and Ed F Deprettere. “Azimuth and elevation computation in high resolution DOA estimation”. In: *IEEE Transactions on Signal Processing* 40.7 (1992), pp. 1828–1832.

[223] Gilles Chabriel et al. “Joint matrices decompositions and blind source separation: A survey of methods, identification, and applications”. In: *IEEE Signal Processing Magazine* 31.3 (2014), pp. 34–43.

[224] Tarik Kazaz et al. “Delay estimation for ranging and localization using multiband channel state information”. In: *IEEE Transactions on Wireless Communications* (2021).

[225] Klaus Witrisal et al. “Noncoherent ultra-wideband systems”. In: *IEEE Signal Processing Magazine* 26.4 (2009).

[226] Ahmad Bazzi, Laura Cottatellucci, and Dirk Slock. “Blind on board wideband antenna RF calibration for multi-antenna satellites”. In: *2017 IEEE International Conference on Acoustics, Speech and Signal Processing (ICASSP)*. IEEE. 2017, pp. 6294–6298.

[227] Kfir Gedalyahu and Yonina C Eldar. “Time-delay estimation from low-rate samples: A union of subspaces approach”. In: *IEEE Transactions on Signal Processing* 58.6 (2010), pp. 3017–3031.

[228] Martin Vetterli, Pina Marziliano, and Thierry Blu. *Sampling signals with finite rate of innovation*. Tech. rep. EPFL, 2001.

[229] Thomas Zwick, Troy J Beukema, and Haewoon Nam. “Wideband channel sounder with measurements and model for the 60 GHz indoor radio channel”. In: *IEEE transactions on Vehicular technology* 54.4 (2005), pp. 1266–1277.

[230] Anthony J Weiss and Benjamin Friedlander. “Eigenstructure methods for direction finding with sensor gain and phase uncertainties”. In: *Circuits, Systems and Signal Processing* 9.3 (1990), pp. 271–300.

[231] Arogyaswami Paulraj and Thomas Kailath. “Direction of arrival estimation by eigenstructure methods with unknown sensor gain and phase”. In: *ICASSP’85. IEEE International Conference on Acoustics, Speech, and Signal Processing*. Vol. 10. IEEE. 1985, pp. 640–643.

[232] Keyong Han, Peng Yang, and Arye Nehorai. “Calibrating nested sensor arrays with model errors”. In: *IEEE Transactions on Antennas and Propagation* 63.11 (2015), pp. 4739–4748.

[233] Stefan J Wijnholds et al. “Calibration challenges for future radio telescopes”. In: *IEEE Signal Processing Magazine* 27.1 (2009), pp. 30–42.

[234] Stefan J Wijnholds and Alle-Jan Van Der Veen. “Multisource self-calibration for sensor arrays”. In: *IEEE Transactions on Signal Processing* 57.9 (2009), pp. 3512–3522.

[235] Alle-Jan van der Veen, Stefan J Wijnholds, and Ahmad Mouri Sardarabadi. “Signal Processing for Radio Astronomy”. In: *Handbook of Signal Processing Systems*. Springer, 2019, pp. 311–360.

[236] Pim van der Meulen et al. “Calibration techniques for single-sensor ultrasound imaging with a coding mask”. In: *2018 52nd Asilomar Conference on Signals, Systems, and Computers*. IEEE. 2018, pp. 1641–1645.

[237] Björn Ottersten, Peter Stoica, and Richard Roy. “Covariance matching estimation techniques for array signal processing applications”. In: *Digital Signal Processing* 8.3 (1998), pp. 185–210.

[238] Haolu Xie et al. “Single-chip multiband EGPRS and SAW-less LTE WCDMA CMOS receiver with diversity”. In: *IEEE Transactions on Microwave Theory and Techniques* 60.5 (2012), pp. 1390–1396.

[239] Shuyang Ling and Thomas Strohmer. “Self-calibration and biconvex compressive sensing”. In: *Inverse Problems* 31.11 (2015), p. 115002.

[240] Benjamin Friedlander and Thomas Strohmer. “Bilinear compressed sensing for array self-calibration”. In: *2014 48th Asilomar Conference on Signals, Systems and Computers*. IEEE. 2014, pp. 363–367.

[241] Emmanuel J Candes, Thomas Strohmer, and Vladislav Voroninski. “Phaselift: Exact and stable signal recovery from magnitude measurements via convex programming”. In: *Communications on Pure and Applied Mathematics* 66.8 (2013), pp. 1241–1274.

[242] Ali Ahmed, Benjamin Recht, and Justin Romberg. “Blind deconvolution using convex programming”. In: *IEEE Transactions on Information Theory* 60.3 (2013), pp. 1711–1732.

[243] Mark A Davenport and Justin Romberg. “An overview of low-rank matrix recovery from incomplete observations”. In: *IEEE Journal of Selected Topics in Signal Processing* 10.4 (2016), pp. 608–622.

[244] Krishnaprasad Nambur Ramamohan et al. “Blind calibration of sparse arrays for DOA estimation with analog and one-bit measurements”. In: *ICASSP 2019-2019 IEEE International Conference on Acoustics, Speech and Signal Processing (ICASSP)*. IEEE. 2019, pp. 4185–4189.

[245] Y Bistritz and G Langholz. “Model reduction by Chebyshev polynomial techniques”. In: *IEEE Transactions on Automatic Control* 24.5 (1979), pp. 741–747.

[246] Yoram Bresler. “Maximum likelihood estimation of a linearly structured covariance with application to antenna array processing”. In: *Fourth Annual ASSP Workshop on Spectrum Estimation and Modeling*. IEEE. 1988, pp. 172–175.

[247] E. van den Berg and M. P. Friedlander. *SPGL1: A solver for large-scale sparse reconstruction*. http://www.cs.ubc.ca/labs/scl/spgl1. June 2007.

[248] Yik-Chung Wu, Qasim Chaudhari, and Erchin Serpedin. “Clock synchronization of wireless sensor networks”. In: *IEEE Signal Processing Magazine* 28.1 (2011), pp. 124–138.

[249] Moe Z Win et al. “Efficient multisensor localization for the Internet of Things: Exploring a new class of scalable localization algorithms”. In: *IEEE Signal Processing Magazine* 35.5 (2018), pp. 153–167.

[250] Yiyin Wang, Xiaoli Ma, and Geert Leus. “Robust time-based localization for asynchronous networks”. In: *IEEE Transactions on Signal Processing* 59.9 (2011), pp. 4397–4410.

[251] Raj Thilak Rajan and Alle-Jan van der Veen. “Joint ranging and clock synchronization for a wireless network”. In: *Computational Advances in Multi-Sensor Adaptive Processing (CAMSAP), 2011 4th IEEE International Workshop on*. IEEE. 2011, pp. 297–300.

[252] Sundeep Prabhakar Chepuri et al. “Joint clock synchronization and ranging: Asymmetrical time-stamping and passive listening”. In: *IEEE Signal Processing Letters* 20.1 (2013), pp. 51–54.

[253] Mathias Pelka, Christian Bollmeyer, and Horst Hellbrück. “Accurate radio distance estimation by phase measurements with multiple frequencies”. In: *Indoor Positioning and Indoor Navigation (IPIN), 2014 International Conference on*. IEEE. 2014, pp. 142–151.

[254] Georg von Zengen et al. “No-Cost distance estimation using standard WSN radios”. In: *Computer Communications, IEEE INFOCOM 2016-The 35th Annual IEEE International Conference on*. IEEE. 2016, pp. 1–9.

[255] Omotayo Oshiga, Stefano Severi, and Giuseppe TF de Abreu. “Superresolution multipoint ranging with optimized sampling via orthogonally designed Golomb rulers”. In: *IEEE Transactions on Wireless Communications* 15.1 (2016), pp. 267–282.

[256] Thomas Watteyne, M Palattella, and L Grieco. *Using IEEE 802.15. 4e time-slotted channel hopping (TSCH) in the internet of things (IoT): Problem statement*. Tech. rep. 2015.

[257] Stephanie Rouquette and Mohamed Najim. “Estimation of frequencies and damping factors by two-dimensional ESPRIT type methods”. In: *IEEE Transactions on signal processing* 49.1 (2001), pp. 237–245.

[258] Hing-Cheung So and Frankie KW Chan. “A generalized weighted linear predictor frequency estimation approach for a complex sinusoid”. In: *IEEE Transactions on Signal Processing* 54.4 (2006), pp. 1304–1315.

[259] Hing-Cheung So et al. “An efficient approach for two-dimensional parameter estimation of a single-tone”. In: *IEEE Transactions on Signal Processing* 58.4 (2010), pp. 1999–2009.

[260] Elad Tzoreff, Ben-Zion Bobrovsky, and Anthony J Weiss. “Single Receiver Emitter Geolocation Based on Signal Periodicity With Oscillator Instability.” In: *IEEE Trans. Signal Processing* 62.6 (2014), pp. 1377–1385.

[261] Yiyin Wang, Zijian Tang, and Geert Leus. “Clock skewcalibration for UWB ranging”. In: *2012 IEEE International Conference on Acoustics, Speech and Signal Processing (ICASSP)*. IEEE. 2012, pp. 3013–3016.

[262] Behzad Razavi. *RF Microelectronics (2Nd Edition) (Prentice Hall Communications Engineering and Emerging Technologies Series)*. 2nd. Upper Saddle River, NJ, USA: Prentice Hall Press, 2011. ISBN: 9780137134731.

[263] David Tse and Pramod Viswanath. *Fundamentals of wireless communication*. Cambridge university press, 2005.

[264] Hariharan Shankar Rahul, Swarun Kumar, and Dina Katabi. “JMB: scaling wireless capacity with user demands”. In: *Proceedings of the ACM SIGCOMM 2012 conference on Applications, technologies, architectures, and protocols for computer communication*. ACM. 2012, pp. 235–246.

[265] Peishuo Li et al. “An adaptive channel selection scheme for reliable TSCH-based communication”. In: *2015 International Symposium on Wireless Communication Systems (ISWCS)*. IEEE. 2015, pp. 511–515.

[266] Tomas Lennvall, Stefan Svensson, and Fredrik Hekland. “A comparison of WirelessHART and ZigBee for industrial applications”. In: *2008 ieee international workshop on factory communication systems*. IEEE. 2008, pp. 85–88.

[267] Yuriy S Shmaliy. “Von Mises/Tikhonov-based distributions for systems with differential phase measurement”. In: *Signal Processing* 85.4 (2005), pp. 693–703.

[268] Michael P Clark and Louis L Scharf. “Two-dimensional modal analysis based on maximum likelihood”. In: *IEEE Transactions on Signal Processing* 42.6 (1994), pp. 1443–1452.

[269] Hing-Cheung So and KW Chan. “Approximate maximum-likelihood algorithms for two-dimensional frequency estimation of a complex sinusoid”. In: *IEEE Transactions on Signal Processing* 54.8 (2006), pp. 3231–3237.

[270] Jun Liu, Xiangqian Liu, and Xiaoli Ma. “First-order perturbation analysis of singular vectors in singular value decomposition”. In: *IEEE Transactions on Signal Processing* 56.7 (2008), pp. 3044–3049.

[271] S. Kay and R. Nekovei. “An efficient two-dimensional frequency estimator”. In: *IEEE Transactions on Acoustics, Speech, and Signal Processing* 38.10 (Oct. 1990), pp. 1807–1809. ISSN: 0096-3518. DOI: 10.1109/29.60114.

[272] Cailian Deng et al. “IEEE 802.11 be Wi-Fi 7: New challenges and opportunities”. In: *IEEE Communications Surveys & Tutorials* 22.4 (2020), pp. 2136–2166.

[273] J Romme et al. “Measurement and analysis of UWB radio channel for indoor localization in a hospital environment”. In: *2014 IEEE International Conference on Ultra-WideBand (ICUWB)*. IEEE. 2014, pp. 274–279.

[274] P. Meissner, E. Leitinger, S. Hinteregger, J. Kulmer, M. Lafer, K. Witrisal. Accessed Jan. 10, 2021. MeasureMINT UWB database, Graz University of Technology. URL: www.spsc.tugraz.at/tools/UWBmeasurements.

[275] Andreas F Molisch. “Ultra-wide-band propagation channels”. In: *Proceedings of the IEEE* 97.2 (2009), pp. 353–371.

[276] Yonghao Zhao et al. “Calibration-free indoor positioning using crowdsourced data and multidimensional scaling”. In: *IEEE Transactions on Wireless Communications* 19.3 (2019), pp. 1770–1785.

[277] Yingjie Liang and Wen Chen. “A survey on computing Lévy stable distributions and a new MATLAB toolbox”. In: *Signal Processing* 93.1 (2013), pp. 242–251.

[278] Katsuyuki Haneda, Andreas Richter, and Andreas F Molisch. “Modeling the frequency dependence of ultra-wideband spatio-temporal indoor radio channels”. In: *IEEE transactions on antennas and propagation* 60.6 (2012), pp. 2940–2950.

[279] Zhuoling Xiao et al. “Non-line-of-sight identification and mitigation using received signal strength”. In: *IEEE Transactions on Wireless Communications* 14.3 (2014), pp. 1689–1702.

[280] Han Dun et al. “Design of Sparse Multiband Signal for Precise Positioning With Joint Low-Complexity Time Delay and Carrier Phase Estimation”. In: *IEEE Transactions on Vehicular Technology* 70.4 (2021), pp. 3552–3567.

[281] Michael D Larsen, Gonzalo Seco-Granados, and A Lee Swindlehurst. “Pilot optimization for time-delay and channel estimation in OFDM systems”. In: *2011 IEEE International Conference on Acoustics, Speech and Signal Processing (ICASSP)*. IEEE. 2011, pp. 3564–3567.

[282] Rafael Montalban, Gonzalo Seco-Granados, and A Lee Swindlehurst. “Suboptimal method for pilot and data power allocation in combined positioning and communications OFDM systems”. In: *2012 Conference Record of the Forty Sixth Asilomar Conference on Signals, Systems and Computers (ASILOMAR)*. IEEE. 2012, pp. 1041–1045.

[283] Harry L Van Trees and Kristine L Bell. *Bayesian bounds for parameter estimation and nonlinear filtering/tracking*. Wiley-IEEE press New York, 2007.

[284] Ulkü Oktel and Randolph L Moses. “A Bayesian approach to array geometry design”. In: *IEEE transactions on signal processing* 53.5 (2005), pp. 1919–1923.

[285] Oliver Lange and Bin Yang. “Optimization of array geometry for direction-of-arrival estimation using a priori information”. In: *Advances in Radio Science* 8.C. 1 (2010), pp. 87–94.

[286] Frankie KW Chan, Hing-Cheung So, and Weize Sun. “Subspace approach for two-dimensional parameter estimation of multiple damped sinusoids”. In: *Signal Processing* 92.9 (2012), pp. 2172–2179.

[287] Aweke N Lemma, A-J Van der Veen, and Ed F Deprettere. “Joint angle-frequency estimation using multi-resolution ESPRIT”. In: *Acoustics, Speech and Signal Processing, 1998. Proceedings of the 1998 IEEE International Conference on*. Vol. 4. IEEE. 1998, pp. 1957–1960.

[288] Yuwen Yang et al. “Deep Transfer Learning-Based Downlink Channel Prediction for FDD Massive MIMO Systems”. In: *IEEE Transactions on Communications* 68.12 (2020), pp. 7485–7497.

[289] Ying Zhang et al. “Multiple radar subbands fusion algorithm based on support vector regression in complex noise environment”. In: *IEEE Transactions on Antennas and Propagation* 66.1 (2017), pp. 381–392.

[290] Nir Shlezinger et al. “Model-Based Machine Learning for Communications”. In: *arXiv preprint arXiv:2101.04726* (2021).

GLOSSARY

NOTATION

SETS

$\mathbb{N}$	Natural numbers.
$\mathbb{N}_+$	Positive natural numbers.
$\mathbb{Z}$	Integer numbers.
$\mathbb{R}$	Real numbers.
$\mathbb{R}_+$	Nonnegative real numbers.
$\mathbb{R}^N$	Real length-N vectors.
$\mathbb{R}^{M\times N}$	Real $M \times N$ matrices.
$\mathbb{C}$	Complex numbers.
$\mathbb{C}^N$	Complex length-N vectors.
$\mathbb{C}^{M\times N}$	Complex $M \times N$ matrices.

VECTORS AND MATRICES

x, X	Plain lowercase and uppercase letters denote scalar.
$\mathbf{x}$	Lowercase boldface letters denote vectors.
$\mathbf{X}$	Uppercase boldface letters denote matrices.
$\mathbf{X}^T$	Transpose of matrix $\mathbf{X}$.
$\mathbf{X}^*$	Complex conjugate of the elements in matrix $\mathbf{X}$.
$\mathbf{X}^H$	Complex conjugate transpose, i.e., Hermitian, of matrix $\mathbf{X}$.
$\mathrm{diag}(\mathbf{x})$	Diagonal matrix with entries on the main diagonal collected in $\mathbf{x}$.
$\mathbf{0}_N$	$N \times 1$ vector of all ones.
$\mathbf{0}_{N,M}$	$N \times M$ matrix of all zeros.
$\mathbf{I}_N$	$N \times N$ matrix of all ones.
$\mathrm{Tr}(\mathbf{X})$	Trace of matrix $\mathbf{X}$.
$\det(\mathbf{X})$	The determinant of square matrix $\mathbf{X}$.
$\mathbf{X}^{-1}$	Inverse of matrix $\mathbf{X}$.
$\mathbf{X}^\dagger := (\mathbf{X}^H\mathbf{X})^{-1}\mathbf{X}^H$	Pseudo inverse (or the left-inverse) of a full-column rank tall matrix $\mathbf{X}$.
$\mathbf{X} \succcurlyeq \mathbf{Y}$	$\mathbf{X}-\mathbf{Y}$ is a positive semidefinite matrix.
$\mathbf{X} \odot \mathbf{Y}$	Hadamard product of matrix $\mathbf{X}$ and matrix $\mathbf{Y}$.
$\mathbf{X} \otimes \mathbf{Y}$	Kronecker product of matrix $\mathbf{X}$ and matrix $\mathbf{Y}$.
$\mathbf{X} \circ \mathbf{Y}$	Khatri-Rao product of matrix $\mathbf{X}$ and matrix $\mathbf{Y}$.

vec($\mathbf{X}$)	$MN \times 1$ vector formed by stacking the columns of an $M \times N$ matrix $\mathbf{X}$.
unvec($\mathbf{X}$)	$M \times N$ matrix formed by the inverse vec($\mathbf{X}$) operation on an $MN \times 1$ vector.
range($\mathbf{X}$)	The range of matrix vec($\mathbf{X}$).

NORMS

$\|\mathbf{x}\|_0$	ℓ_0-(quasi) norm, i.e., number on non-zero entries of vector $\mathbf{x}$.
$\|\mathbf{x}\|_1$	ℓ_1-norm of vector $\mathbf{x}$.
$\|\mathbf{x}\|_2$	Euclidean (or ℓ_2-)norm of vector $\mathbf{x}$.
$\|\mathbf{X}\|_{2,1} := \sum_{i=1}^{N} \|\mathbf{x}_i\|_2$	$\ell_{2,1}$ norm of matrix $\mathbf{X}$ that has columns $\mathbf{x}_i, i = 1, \ldots, N$.
$\|\mathbf{X}\|_F := \sqrt{\mathrm{Tr}(\mathbf{X}\mathbf{X}^H)}$	Forbenious norm of matrix $\mathbf{X}$.
$\|\mathbf{X}\|_*$	Nuclear norm of matrix $\mathbf{X}$.

STOCHASTIC PROCESSES

$\mathbb{E}(\mathbf{x})$	Expected value of random vector $\mathbf{x}$.
$\mathcal{N}(\boldsymbol{\mu}, \boldsymbol{\Sigma})$	Gaussian distribution with mean vector $\boldsymbol{\mu}$ and covariance matrix $\boldsymbol{\Sigma}$.
Lap$(x, \boldsymbol{\mu}, b)$	Laplace distribution of variable x with location and scale parameters denoted by μ and b.
$p(x; \boldsymbol{\theta})$	Probability density function of x parameterized by $\boldsymbol{\theta}$.

ABBREVIATIONS

ADC	analog-to-digital-converter
AGC	automatic gain control
AOA	angle of arrival
cf.	confer (compare)
CFR	channel frequency response
CIR	channel impusle response
CRB	Cramér–Rao bound
CS	compressive sensing
CSI	channel state information
DAC	digital-to-analog-converter
EHT	extremly high throughput
EVD	eigenvalue decomposition
e.g.	exempli gratia (for example)
FIM	Fisher information matrix
GNSS	global navigation satellite system
GPS	global positioning system
i.e.	id est (that is)
i.i.d	independent and identically distributed

LS	least squares
LTF	long training field
MBWDE	multiband weighted delay estimation
MI	multiple invariance
MPC	multipath component
MRTDE	multiresolution time-delay estimation
MSE	mean square error
NLS	nonlinear least squares
PDF	probability density function
PDoA	phase difference of arrival
RF	radio frequency
RMSE	root mean square error
RSS	received signal strength
STF	short training field
SVD	singular value decomposition
TDOA	time difference of arrival
TOA	time of arrival
UWB	ultra-wideband
VNA	vector network analyzer
WLS	weighted least squares
WSF	weighted subspace fitting

ACKNOWLEDGMENTS

"Life is a succession of lessons
which must be lived to be understood."
— Ralph Waldo Emerson

All the life journies need to end. However, they become part of us. They leave marks and shape who we are and what we will be. As usual, what makes these journeys interesting is the people that accompany us through them. Now that my Ph.D. journey is about to end, it is time to make an attempt to reflect on it and thank all those who influenced, supported, and accompanied me on my way through it.

Alle-Jan and Gerard, thank you for giving me the opportunity to write this thesis and be part of Circuits and Systems (CAS) group and SuperGPS project.

Alle-Jan, my motivation to apply for a PhD in CAS developed after reading two of your publications on subspace-based signal analysis and joint angle and delay estimation a few years before I even applied. In other words, I first met your work and then you. I have always been inspired while reading your publications, and now at the end of my Ph.D., I feel that I have been truly lucky and privileged to be supervised by you. You have provided direction to my Ph.D. and have taught me the essence of signal processing during it. Beyond your technical and scientific support, I have also greatly benefited from your guidance when dealing with general life and project-related challenges. I admire your ethics and integrity when handling such situations. Further, I would like to thank you for the care and effort that you have put into making CAS feel like home for every one of its members.

Gerard, thank you for providing me guidance as well as freedom in my research choices, and having patience and trust in me. Now that I am back in the industry, I truly appreciate that you took care that we find the balance between practice and signal processing theory in this thesis. I am also grateful for your prompt and acute feedback on drafts of my publications and thesis, and for having infinite tolerance for my missing "the"s and "a"s.

Jac, I have been fortunate that you have been part of our group. During my Ph.D., not many researchers in CAS worked on problems related to RF signal processing and localization. Therefore, our occasional discussions and your presentations were essential to make me feel less lonely in my research. I also want to thank you for your collaboration and providing us datasets, as these were very beneficial for our joint work and this thesis. I am also very grateful and happy that you accepted to be part of my doctoral committee.

I am grateful to Prof. Alexander Yarovoy, Prof. Fernando Kuipers, Prof. Heidi Steendam, Prof. Klaus Witrisal and Prof. Mark Bentum for accepting to read my thesis and take part in my doctoral committee.

During my Ph.D., I had the opportunity to work on the NWO-funded SuperGPS

project with several other researchers. Christian, Cherif, Han, and Farnaz, thank you for our discussions and collaboration.

Doing any work without a nice environment is not pleasant or fun. I have been fortunate enough to share the 17th floor of the EEMCS building with some great individuals. Well, at least this was the case until the COVID pandemic came, but finally we survived through it. I would like to thank Geert, Raj, Rene and Alexander for occasional scientific and technical discussions. Raj, thank you also for being a great office-mate. With some of my colleagues, I got to share even more than I could imagine. Pim, thank you for being a fantastic friend and making my wedding amazing. None expected those moves from a Dutch man. Mario, thank you for the great scientific discussions and collaborations. I truly appreciate having shared an office with you, our hang-outs and sports time in general. The research group is changing fast, and for some of my colleagues, I wish they had joined the group a bit earlier. However, when two personalities match, you do not need much time to grow it into a friendship. Sofia, Vincent, Anurodh and Mari, thank you for being great friends, making the Netherlands feel like home, and for all the support. I also thank Hanie, Alberto, Sharzad, Elvin, Krishna, Jamal, Sumeet, Sundeep, Amir, Jorge, Jie, Venkat, Jeroen, Ellen, Tom, Andreas, Aydin, Didem, David, Costas, Jiani, Selin, Metin, Patrick, Jorn, Miao, Aydin, Bahar, Borbola, Richard, Nick, Rob and Mostafa for occasional dinners, BBQs, coffee corner talks and Friday sports events. I am also thankful for all the support that I got from Brigitte, Minaksie, Irma, Rosario, Alexander, Antoon and Wim when dealing with a wide range of administrative and technical issues.

At the end of my PhD, I started to feel that the Netherlands had become my home. Therefore, I decided to learn Dutch language intensively. During this process, I got to meet some great people who thought me the language, but also provided a necessary distraction from my research. Lissy, Tineke and Helgert, thank you for being great teachers and making our lessons and talks fun and interesting. The language skills learned during these courses were very useful when translating the summary of this thesis. However, my Dutch is far from fluent, and I needed help with this task. Jeroen, thank you for reading and correcting the translation of the summary.

Last but not least, the most important acknowledgment goes to my family. Above all, I thank my mother and father for all the effort and commitment that they made to rise me and my brother into normal persons during abnormal times. During my PhD, I have been lucky to meet my wife, Aybüke. Aybüke, thank you for being my best friend and for all your patience and love. This thesis would never be finished without your support and understanding. With Aybüke, I got extra parents in my life. Ayten and Faruk, thank you for being there for us, for accepting me as your son, and for all the care and love during the last two years.

Tarik
Eindhoven, May 2022

CURRICULUM VITÆ

TARIK KAZAZ was born in Teslić, north-central Bosnia and Herzegovina (Yugoslavia at the time). At the age of three, due to the war circumstances and dramatic events in his hometown, with his parents, he escaped to Tešanj, a town where he spent most of his young years. He earned his B.Sc. and M.Sc. degrees, both with honors, at Department of Telecommunications, Faculty of Electrical Engineering, University of Sarajevo, Sarajevo, Bosnia and Herzegovina, in 2010 and 2012, respectively. During his M.Sc. studies and after completing the studies until 2015, he was a teaching assistant for courses RF Engineering, Mobile Communications, Systems and Services of Mobile Communications at the Faculty of Electrical Engineering. In 2014, he joined BH Mobile, Sarajevo, where he worked as an RF Engineer. In 2015, he moved to Ghent, Belgium, and joined IMEC, IDLab, as a signal processing and digital design researcher. During this period, he has worked on designing and implementing flexible wireless transceivers and has participated in several H2020 research projects such as Flex5Gware, WISHFUL and ORCA. In 2017, in search of fundamental signal processing knowledge, he moved to Delft, the Netherlands, and joined Circuits and Systems (CAS) research group of Delft University of Technology (TU Delft) as PhD student on SuperGPS project supported by NWO. From June 2021 until April 2022, he worked at Fugro Innovation and Technology, Nootdorp, the Netherlands, as a signal processing research and development engineer. During this period, he has designed signal processing algorithms and a receiver for precise low Earth orbit (LEO) satellite positioning. Since April 2022, he has been part of NXP, Eindhoven, the Netherlands, where he works as a signal processing architect and scientist for automotive radar applications. His general research interests lie in the areas of statistical signal processing, array signal processing, linear algebra, machine learning, RF sensing, and wireless communications. Tarik is very passionate about reading books, cooking and sports such as calisthenics and running. Therefore you will find him exercising for at least 12 hours during an average week.